Doctoral Thesis

Structure–Activity Relationship in Non-Precious Metal Catalysts for the Hydrogen Evolution Reaction

Bora Seo

Department of Chemistry

Graduate School of UNIST

2018

Structure–Activity Relationship in Non-Precious Metal Catalysts for the Hydrogen Evolution Reaction

Bora Seo

Department of Chemistry

Graduate School of UNIST

Structure–Activity Relationship in Non-Precious Metal Catalysts for the Hydrogen Evolution Reaction

A thesis/dissertation
submitted to the Graduate School of UNIST
in partial fulfillment of the
requirements for the degree of
Doctor of Philosophy

Bora Seo

11. 30. 2017 of submission
Approved by

Advisor
Sang Hoon Joo

ULSAN NATIONAL INSTITUTE OF
SCIENCE AND TECHNOLOGY

Structure–Activity Relationship in Non-Precious Metal Catalysts for the Hydrogen Evolution Reaction

Bora Seo

This certifies that the dissertation of Bora Seo is approved.

11. 30. 2017 of submission

Sang Hoon Joo
Advisor: Sang Hoon Joo

Hyeon Suk Shin

Moon
Hoi Ri Moon

Sang Kyu Kwak

Ji-Wook Jang

Abstract

This dissertation describes the development of electrocatalysts for the hydrogen evolution reaction (HER), which is a key reaction of clean and environmentally benign water electrolysis. Currently, Pt-based nanomaterials are used commercially as HER catalysts with very high efficiency. However, their high cost and scarcity are severe obstacles for the widespread application in water electrolysis. Hence, significant efforts have been devoted to replacing Pt catalysts with non-precious metal catalysts such as transition metal sulfides and transition metal phosphides, which have shown promising HER activity and stability in acidic media. When designing non-precious metal-based HER electrocatalysts, a fundamental understanding of the structural factors responsible for catalytic properties is crucial. In this context, this dissertation focuses on establishing the catalyst structure–activity correlation and providing a guideline for the design of advanced HER electrocatalysts. For this purpose, various structural features of catalysts, including size, shape, and composition, have been controlled, and their structural effects have been scrutinized using multiple characterization techniques combined with electrochemical measurements.

We investigated the growth of two transition metal sulfides, MoS_2 and WS_2, within the confined nanopores of porous carbons, and the catalytic activity of the resulting composites for the HER. Confined growth using a carbon nanostructure is appealing as it could limit the nanoscale growth of transition metal sulfides, thereby exposing a high density of active edge sites, as well as endowing conductivity. Layer number-controlled MoS_2 was successfully prepared with monolayer precision and was applied as a model system to investigate layer-dependent HER activity. Experimental and theoretical calculations revealed that the HER activity increases with decreasing MoS_2 layer numbers in a quasi-linear manner. In contrast to MoS_2, WS_2 maintains a monolayer morphology with increasing WS_2 loadings. The different growth behavior investigated by theoretical calculations revealed that MoS_2 and WS_2 prefer basal and edge plane bonding with the carbon surface, thereby growing into monolayer and multilayer structures, respectively.

The modification of the oxidation state of transition metal sulfides could be used to enhance the catalytic activity. To investigate the oxide effect on HER performance, WS_2 nanorods encasing a tungsten oxide core layer ($W_{18}O_{49}$@WS_2 NRs) were prepared *via* a controlled sulfidation reaction of $W_{18}O_{49}$ NRs. Prolonged sulfidation resulted in fully sulfided WS_2 nanotubes (NTs). Electrochemical measurements revealed that the partially sulfided $W_{18}O_{49}$@WS_2 NRs exhibited higher HER activity than that of the fully sulfided WS_2 NTs. Furthermore, electrochemically-induced surface oxidation significantly enhanced the HER activity of WS_2. The results suggest that the oxide layer at the surface and core facilitates electron transfer at the interface between the catalyst and the electrode without the aid of additional conductive supports.

The morphological effect of metal sulfide materials on HER activity was investigated. For this purpose, shell thickness-controlled rhodium sulfide hollow nanoparticles (Rh_2S_3 HNPs) were employed as HER catalysts. Rh_2S_3 HNPs were prepared *via* one-step formation of core-shell copper sulfide-Rh_2S_3 nanoparticles ($Cu_{1.94}S@Rh_2S_3$ NPs), followed by selective etching of the core. The importance of hollow morphology was confirmed by the superior HER activity of Rh_2S_3 HNPs compared to that of non-etched $Cu_{1.94}S@Rh_2S_3$ NPs. Among the shell thickness-controlled HNPs, thick-shell HNPs could have larger void volumes because of their better structural rigidity, which meant that they retained the hollow morphology better, than thin-shell HNPs. As a result, the HNPs with the thickest shell showed the best HER activity, emphasizing the importance of a wide cavity for facilitating mass transport along with the enhanced catalytic active sites originating from both the inside and outside of the hollow structure. Notably, the Rh_2S_3 HNPs showed unprecedented activity enhancement after 10000 potential cycles. The electrolysis further removed the inactive Cu impurities that remained in the HNPs even after core etching.

The shape effect of nanoparticle catalysts in HER electrocatalysis is presented. Shape-controlled NPs can selectively expose the desired crystallographic surfaces, and can thus serve as excellent model catalysts for investigating the correlations between surface structures and activity and/or selectivity in the HER. For this scope, Ni_2P NPs with spherical and rod shapes were prepared and applied as HER catalysts. Spherical Ni_2P NPs, mainly exposing the $Ni_2P(001)$ surface, showed higher HER activity than rod-shaped Ni_2P NPs with a predominantly exposed $Ni_2P(210)$ surface. The results imply that the $Ni_2P(001)$ surface shows preferential interaction with hydrogen atoms for the HER and a lower activation barrier for the initial hydrogen adsorption, activating the overall HER. This study suggests that the crystallographic facets of Ni_2P NPs play a key role in dictating the HER performance.

Molecular MoS_x was investigated as the HER catalyst since a well-defined molecular catalyst can serve as an appropriate model system for elucidating genuine active sulfur sites for hydrogen adsorption in the HER. It was found that a commercially available inorganic molecule, thiomolybdate (MoS_4^{2-}), which is commonly used as the precursor for preparing MoS_x catalysts, can catalyze the HER with high efficiency. The excellent activity of MoS_4^{2-} could be attributed to the S^{2-} ligands mimicking the unsaturated S^{2-} species observed in active MoS_2-based nanocatalysts. Furthermore, its activity and stability were enhanced by immobilization on the surface of Au nanocrystals. The resulting $Au@MoS_4^{2-}$ hybrid enhanced the HER activity and effectively prevented MoS_4^{2-} dissolution in a strongly acidic environment.

Contents

Chapter 1. GENERAL INTRODUCTION

Chapter 2. CHARACTERIZATION METHODS

Chapter 3. NANOSCALE SIZE EFFECTS OF MOLYBDENUM SULFIDE CATALYSTS FOR THE HYDROGEN EVOLUTION REACTION

Chapter 4. HORIZONTAL GROWTH OF TUNGSTEN SULFIDE ON CARBON AND INSIGHT INTO ACTIVE SULFUR SITE FOR THE HYDROGEN EVOLUTION REACTION

Chapter 5. IMPACT OF OXIDE CORE IN TUNGSTEN SULFIDE CATALYSTS ON THE HYDROGEN EVOLUTION REACTION

Chapter 6. HIGHLY ACTIVE AND ROBUST HOLLOW RHODIUM SULFIDE CATALYSTS FOR THE HYDROGEN EVOLUTION REACTION

Chapter 7. SHAPE EFFECTS OF NICKEL PHOSPHIDE CATALYSTS ON THE HYDROGEN EVOLUTION REACTION

Chapter 8. MONOMERIC MoS_4^{2-} ADHERED ON GOLD NANOCRYSTALS FOR EFFICIENT HYDROGEN EVOLUTION REACTION

Chapter 9. SUMMARY AND SUGGESTIONS FOR FUTURE WORKS

List of Figures

List of Tables

List of Abbreviations

AR-TEM	Atomic-Resolution Trasmission Electron Microscopy
α	Transfer Coefficient
BET	Brunauer–Emmett–Teller
BJH	Barrett–Joyner–Halenda
C_{dl}	Double Layer Capacitance
c_{O}	Concentration of Oxidized Species
c_{R}	Concentration of Reduced Species
CN	Coordination Number
CV	Cyclic Voltammetry
DFT	Density Functional Theory
η	Overpotential for the HER
η_c	Overpotential for the cathode
E_a	Potential for Anode, OER
E_c	Potential for Cathode, HER
EXAFS	Extended X-ray Absorption Fine Structure
ECSA	Electrochemically Active Surface Area
EDS	Energy-Dispersive X-ray Spectroscopy
EIS	Electrochemical Impedance Spectroscopy
F	Faraday Constant
FFT	Fast Fourier Transformation
FWHM	Full-Width-at-Half-Maximum
GC	Glassy Carbon
ΔG_{H}	Gibbs Free Energy
H_{ad}	Adsorbed Hydrogen Atom
HAADF-STEM	High Angle Annular Dark Field-Scanning Transmission Electron Microscopy
HER	Hydrogen Evolution Reaction
HRTEM	High-Resolution Transmission Electron Microscopy
I	Current Density
i_0	Exchange Current Density
ICP-OES	Inductively Coupled Plasma Optical Emission Spectrometry
iR	Ohmic Potential Loss
JCPDS	Joint Commission for Powder Diffraction Standard
LSV	Linear Sweep Voltammetry

N	Number of Electrons Involved in an Electrode Reaction
NP	Nanoparticle
NR	Nanorod
NS	Nanosphere
NT	Nanotube
OCP	Open Circuit Potential
OER	Oxygen Evolution Reaction
OMC	Ordered Mesoporous Carbon
OMS	Ordered Mesoporous Silica
PEM	Proton Exchange Membrane or Polymer Electrolyte Membrane
PMA	Phosphomolybdic Acid Hydrate
PTA	Phosphotungstic Acid Hydrate
R	Gas Constant
RDF	Radial Distribution Function
RHE	Reversible Hydrogen Electrode
RRDE	Rotating Ring Disk Electrode
SEM	Scanning Electron Microscopy
R_s	Series Resistance
TEM	Transmission Electron Microscopy
TMD	Transition Metal Dichalcogenide
TMP	Transition Metal Phosphide
TOF	Turnover Frequency
V_{act}	Activation Voltage Loss
V_{cell}	Cell Voltage
V_{Ohm}	Ohmic Voltage Loss
V_{trans}	Mass Transport Voltage Loss
XANES	X-ray Absorption Near Edge Spectroscopy
XAS	X-ray Absorption Spectroscopy
XRD	X-ray Diffraction
XPS	X-ray Photoelectron Spectroscopy
2D	Two-Dimensional

1

GENERAL INTRODUCTION

1.1. Water Electrolysis

1.1.1. Hydrogen Energy

According to International Energy Agency (IEA), global energy demand is estimated to increase rapidly from 18 TW in 2013 to 27 TW by 2040, due to the ever-increasing worldwide population and societal developments.[1] Currently, the majority (~80%) of energy requirement is supplied by fossil fuels such as oil, coal and natural gas, none of which is renewable (**Figure 1.1a**). Massive industrial use of the fossil fuels has increased the atmospheric concentration of carbon dioxide (CO_2), which is largely responsible for global warming and climate change.[2] In addition, reserves of fossil fuels have been continuously depleted every year.[3] Thus, the demand for sustainable and clean energy sources has been accelerated due to the ongoing problem of greenhouse gas emission and the depletion of fossil fuel. A large number of alternative fuels have been suggested, including biomass, methanol, ethanol, hydrogen, and Fischer-Tropsch fuels.[4] As the most promising candidate, hydrogen has received a great deal of attention because of its high gravimetric energy density (142 MJ/kg, nearly three times higher than that of gasoline) and carbon-neutral combustion (**Figure 1.1b**).[5–7] In addition, hydrogen has multiple advantageous properties as a combustible fuel, such as a wide flammability range, low ignition energy (0.02 MJ), high ignition temperature, high flame speed, and high diffusivity.[4] Moreover, it holds great promise as a fuel to make electricity in fuel cells for a variety of applications, including transportation, back-up power, and grid stabilization.[8] Hydrogen has already been used in the global market, including in petroleum refinery, and in the production of ammonia and other chemicals.[9]

Although hydrogen is the most abundant element in the universe, it does not naturally exist in its molecular state, and this must be produced by means of an energy input. Thus, hydrogen is considered as an energy carrier, and not a primary energy source, unlike fossil fuels. Currently, more than 50 million tons of hydrogen are produced globally each year. The majority of the hydrogen is produced by steam methane reforming, partial oxidation of hydrocarbons and coal gasification processes.[10–12] However, steam reforming of fossil fuels generates low purity hydrogen, releasing a high concentration of carbonaceous by-products such as carbon monoxide. In addition, when the reformate hydrogen is used as fuel cell feed, the poisonous CO and CO_2 present in the hydrogen fuel can cause the overall cell performance to deteriorate severely.[13] To escape the strong reliance on fossil fuels and the associated environmental emissions, hydrogen production should be conducted without adverse environmental impacts. Moreover, to be competitive with fossil fuel, hydrogen storage and transportation techniques have been developed together to keep pace with the progress of hydrogen production.

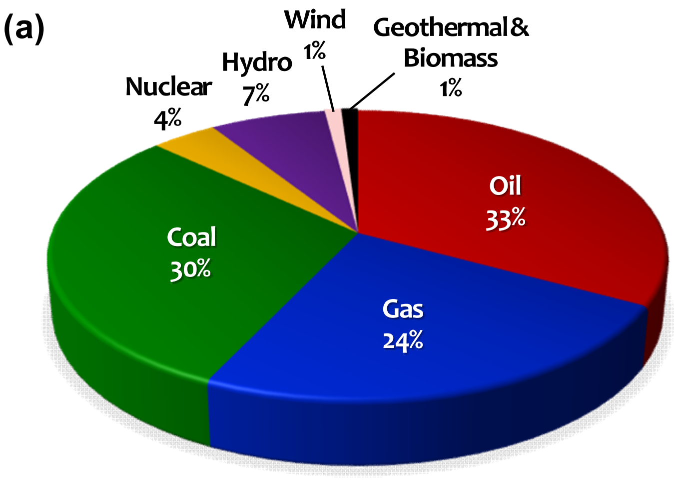

Fossil fuels occupy 87% of global energy consumption in 2013

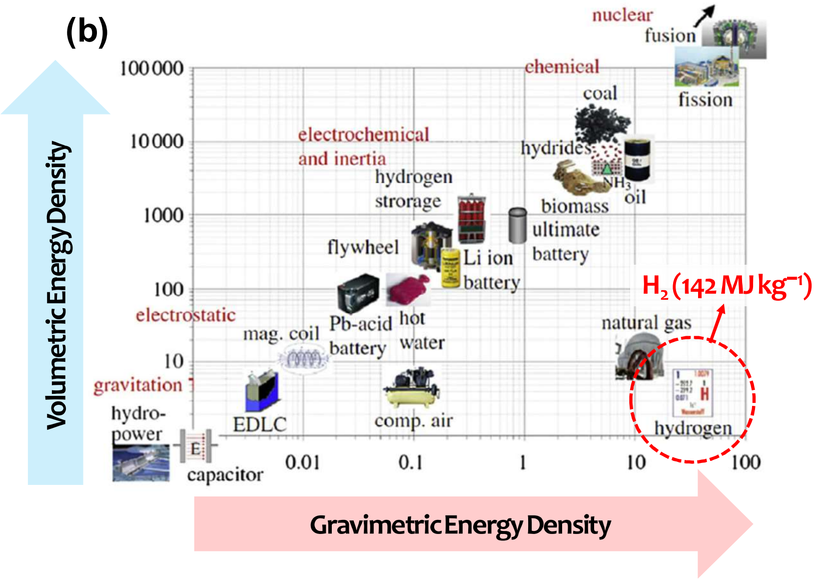

Figure 1.1. (a) Global energy consumption in 2013. This chart is based on statistical data from multiple sources, including IEA, EIA, and BP Statistical review of World Energy. (b) Volumetric versus gravimetric energy density of the energy carriers. Figure (b) was reproduced with permission from ref. 7. Copyright 2011 Hydrogen Energy Publications, LLC. Published by Elsevier Ltd.

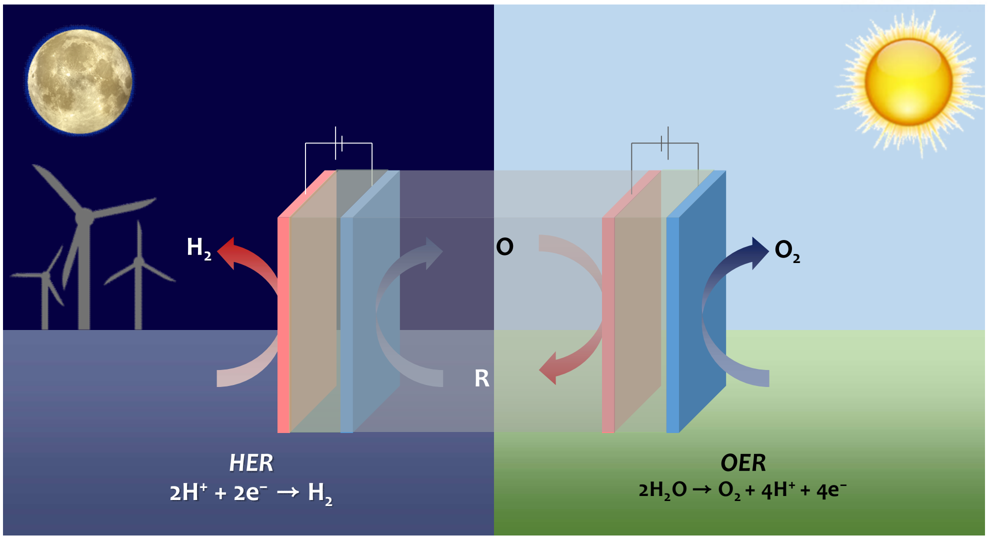

Figure 1.2. Illustration for water electrolysis based on hydrogen- and oxygen-evolving half-reactions derived from wind (during the night) and solar energy (during the day), respectively. This figure was drawn based on Figure 1 in ref. 15 with permission. Copyright 2013 Macmillan Publishers Ltd.

Hydrogen production *via* water electrolysis is the most environmentally benign and sustainable route to obtain high purity hydrogen with net zero total emissions (**Figure 1.2**).[14–16] As the input energy, renewable energy sources like solar and wind energy have received significant attention due to their growing capacity, which surpasses the GW range. The sunlight continuously provides 4.3×10^{20} J of energy to the Earth in 1 h, [17] which corresponds to 120,000 TW and far exceeds the global energy consumption for a whole year (18 TW, 2013). However, renewable energy sources are intermittent, causing a mismatch between supply and demand. Water electrolysis combined with renewable energy sources could overcome the challenge by storing surplus renewable energy in the form of chemical bonds through the oxygen evolution reaction (OER) at the anode, and the conversion of chemical energy into hydrogen fuel *via* the hydrogen evolution reaction (HER) at the cathode. At present, only 4% of hydrogen is produced *via* water electrolysis. For widespread implementation, the cost-effectiveness and efficiency of the system should be improved. The HER, which is the cathodic reaction of water electrolysis, typically involves the use of Pt-based materials as electrocatalysts. However, the dominant use of Pt-based catalysts significantly impedes widespread utilization of the technology due to their high cost (~\$30/g Pt in November 2017)[18] and scarcity. Only 142 tons of Pt was produced by mining and recycling in 2016.[19] A large portion of the cost required to operate the industrial proton-exchange-membrane (PEM) electrolyzer is due to the cost of the membrane-electrode-assembly, and half of this cost comprises the Pt price. Current state of the art hydrogen production costs about \$4–5/kg H_2 (\$4.20/kg H_2 for 2011 status).[20] The U. S. Department of Energy (DOE) has set a cost target for hydrogen production at \$2.30/kg H_2 until 2020. Therefore, the development of highly efficient electrocatalysts made of non-precious materials is of prime importance for realizing a hydrogen-based future infrastructure, the so-called hydrogen economy.

1.1.2. Water Electrolyzer

Since the electrolysis phenomenon was first discovered by Troostwijk and Diemann in 1789,[21] there have been numerous milestones in the development of water electrolyzers. Among the many different electrolyzers developed, the alkaline electrolyzer has been developed extensively and constitutes the most extended electrolytic technology for hydrogen production at a commercial level worldwide. However, the alkaline electrolyzer has several problems associated with the low partial load range, limited current density and low operating pressure.[22,23] Most drawbacks of the alkaline electrolyzer were overcome with the development of the proton exchange membrane or polymer electrolyte membrane (PEM) electrolyzer.[22,23] The polymer electrolyte membrane (Nafion®) used in the PEM electrolyzer allows high proton conductivity (0.1 ± 0.02 S cm^{-1}),[24] low gas crossover, compact system design and high-pressure operation. For this reason, the PEM electrolyzer can operate at much higher current densities, reducing the overall operating cost. Problems related with PEM electrolysis are also present. Due to the corrosive acidic environment, the choice of catalytic materials is limited. Therefore, the development of catalysts that are highly durable in strongly acidic environments is an important issue in PEM electrolysis. Generally, carbon nanostructures are adopted as the catalyst support because they exhibit strong corrosion resistance to acid, and also endow conductivity. The two types of water electrolyzers are depicted in **Figure 1.3**.

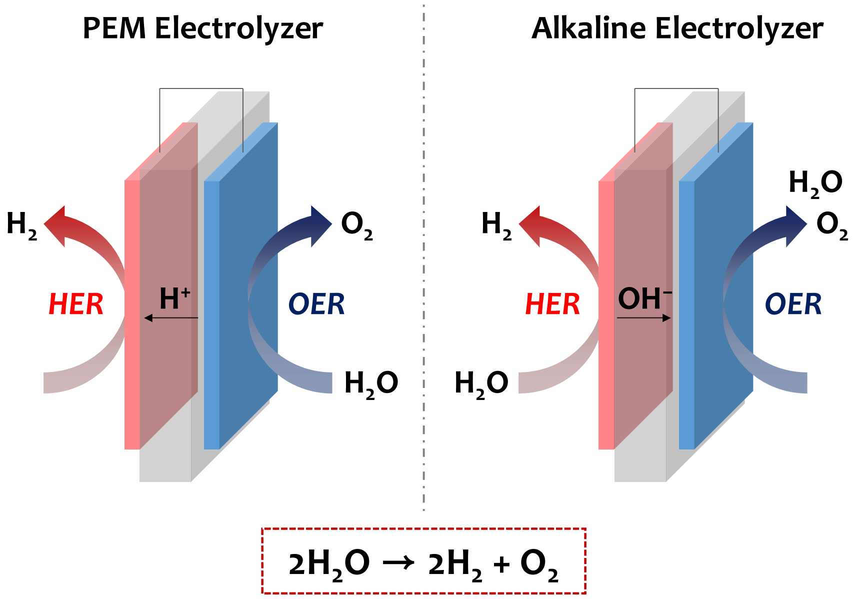

Figure 1.3. Illustration depicting PEM and alkaline water electrolyzers.

Water electrolysis comprises two half reactions, producing oxygen at the anode and hydrogen at the cathode. The detailed mechanisms are different in acidic and alkaline environments.

In an acidic electrolyte, the water molecule is split to produce oxygen and protons *via* the OER at the anode. The protons generated are delivered to the cathode *via* the proton-conducting electrolyte, and then the electrons provided by the external electric circuit are used to produce molecular hydrogen *via* the HER at the cathode. The reactions and standard equilibrium potentials are as follows:

Anode: $2H_2O \leftrightarrow O_2 + 4H^+ + 4e^-$ (OER)
$E_a = 1.23$ V (*vs.* reversible hydrogen electrode, RHE)

Cathode: $4H^+ + 4e^- \leftrightarrow 2H_2$ (HER)
$E_c = 0$ V (*vs.* RHE)

In an alkaline electrolyte, the water molecule is split to produce hydrogen and hydroxide ions *via* the HER at the cathode. The hydroxide ions generated are delivered to the anode *via* the electrolyte (generally a liquid for the alkaline electrolyzer), and then oxidized to produce oxygen and water *via* the OER at the anode. The reactions and standard equilibrium potentials are as follows:

Anode: $4OH^- \leftrightarrow O_2 + 2H_2O + 4e^-$ (OER)
$E_a = 0.40$ V (*vs.* RHE)

Cathode: $4H_2O + 4e^- \leftrightarrow 2H_2 + 4OH^-$ (HER)
$E_c = -0.83$ V (*vs.* RHE)

In both cases, the total water splitting reaction and thermodynamic cell voltage (V_{cell}) are given by:

$$2H_2O \leftrightarrow 2H_2 + O_2,\ V_{cell} = E_a - E_c$$

The theoretical water decomposition V_{cell} is 1.23 V. However, the practical voltages of water electrolysis in industrial cells are much higher, reaching about 1.8–2.6 V. The discrepancy mainly originates from three potential losses, namely activation losses, mass transport losses and Ohmic losses (**Figure 1.4**), as given by:[25,26]

$$V_{cell} = E + V_{act} + V_{trans} + V_{Ohm}$$

V_{act} is the activation loss, which is noticeable in the low current region. The activation loss mainly occurs due to the slow electrochemical reactions at the interface between the electrode and electrolyte, where the surface species undergo redox reactions. It is directly proportional to the increase in current flow, as given by:

$$V_{act} = \frac{RT}{\alpha nF}\ln(\frac{i}{i_0})$$

V_{tras} is the mass transport loss. It is dominant in the high current region, as the reactant gas is consumed near the electrode, resulting in a concentration gradient. The mass transport loss is mainly attributed to the slow diffusion of the gas products in the electrode, the concentration gradient of reactants in the electrolyte, and the blocking of the electrode with the ionomer used as the binder in the catalyst layer. In the HER particularly, the H_2 bubbles generated significantly influence the mass transport of the reactant and product, increasing the voltage loss. A porous electrode structure could facilitate the mass transport.

$$V_{trans} = \frac{RT}{nF}\ln(1-\frac{i}{i_0})$$

V_{Ohm} is the ohmic loss. It originates from the internal resistance of the cell components, arising mainly from the resistance to the ionic flow in the electrolyte and electronic flow through the electrodes and the external circuit. It can be reduced by decreasing the distance between the electrodes, enhancing the ionic conductivity, and by decreasing the thickness of the catalyst layer. This loss follows Ohm's law and has a linear relationship with the current density, as given by:

$$V_{Ohm} = IR_C$$

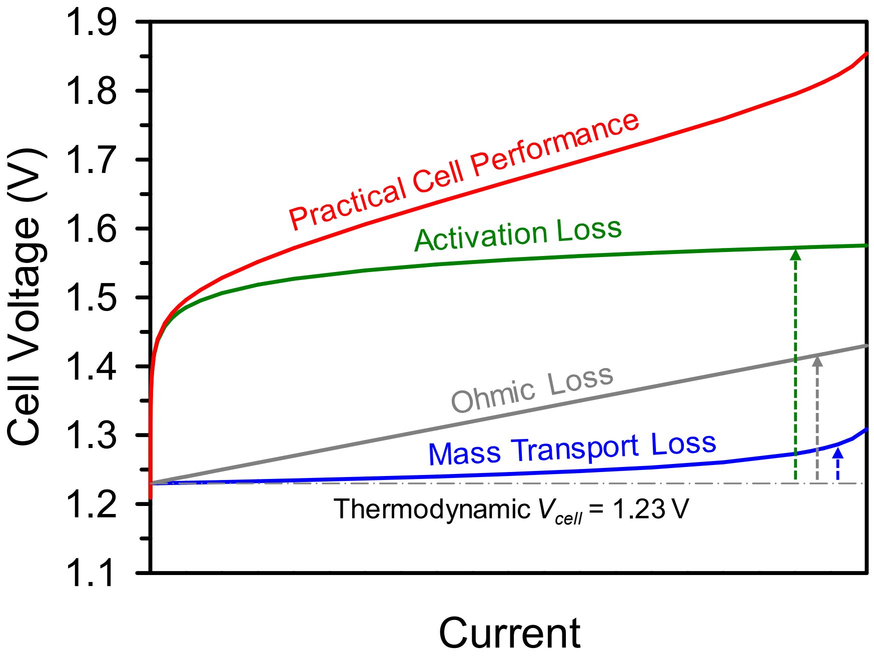

Figure 1.4. Cell voltage versus cell current, depicting the three major performance losses.

Considering the compatibility with solar cell devices operated in acidic media, the development of efficient and stable HER catalysts for the PEM electrolyzer in an acidic environment is more suitable for commercial viability. In addition, considering the different reaction mechanisms of the HER at different pHs, an acidic electrolyte is more favorable for the initial proton adsorption step as there are enough protons in the electrolyte. In contrast, water must be decomposed to provide protons in alkaline media.

1.1.3. Hydrogen Evolution Reaction

This dissertation focuses on the electrocatalysis of the HER taking place in an acidic environment. Thermodynamically, the HER occurs with 0 V (*vs.* RHE) of applied potential, as shown in **Figure 1.5**.[27] However, for practical operation, an excess potential, which is referred to as overpotential (η_c), is indispensable to overcome the energy barrier. Incorporation of highly efficient HER catalysts can significantly reduce the overpotential.

In water electrolysis, the HER at the cathode, is a simple reaction where two protons and two electrons combine to form a hydrogen molecule, as given by:

$$2H^+ + 2e^- \leftrightarrow H_2$$

The HER proceeds by the initial adsorption of a hydrogen atom on the catalyst surface, which is referred to as the Volmer step, as given by:[28]

$$H^+_{(aq)} + e^- \leftrightarrow H_{ad} \text{ (discharge reaction)}$$

where H^+, e^-, and H_{ad} designate the hydrated proton, the electron from the external circuit, and the adsorbed hydrogen atoms on the catalyst surface, respectively. Subsequently, molecular hydrogen is produced *via* the chemical recombination of two adsorbed hydrogen atoms (the so-called Tafel reaction), or through a second electron transfer (the so-called Heyrovsky reaction), as given by:[28]

$$\text{Tafel reaction: } 2H_{ad} \leftrightarrow H_{2(g)} \text{ (chemical combination reaction)}$$

$$\text{Heyrovsky reaction: } H^+_{(aq)} + H_{ad} + e^- \leftrightarrow H_{2\,(g)} \text{ (ion + atom reaction)}$$

Therefore, the HER could follow one of two possible reaction mechanisms, namely the Volmer–Tafel or the Volmer–Heyrovsky pathway, depending on the catalyst surface. In both cases, the Volmer reaction (discharge reaction) is fast. The rate-determining steps are the Tafel reaction (chemical combination reaction) and the Heyrovsky reaction (ion+atom reaction) in the Volmer-Tafel and Volmer-Heyrovsky mechanisms, respectively. If the discharge reaction is rate-determining, the overall reaction kinetics are much slower than those in the other two cases. The HER mechanism can be assessed with Tafel analysis, as discussed in section 1.2.2.

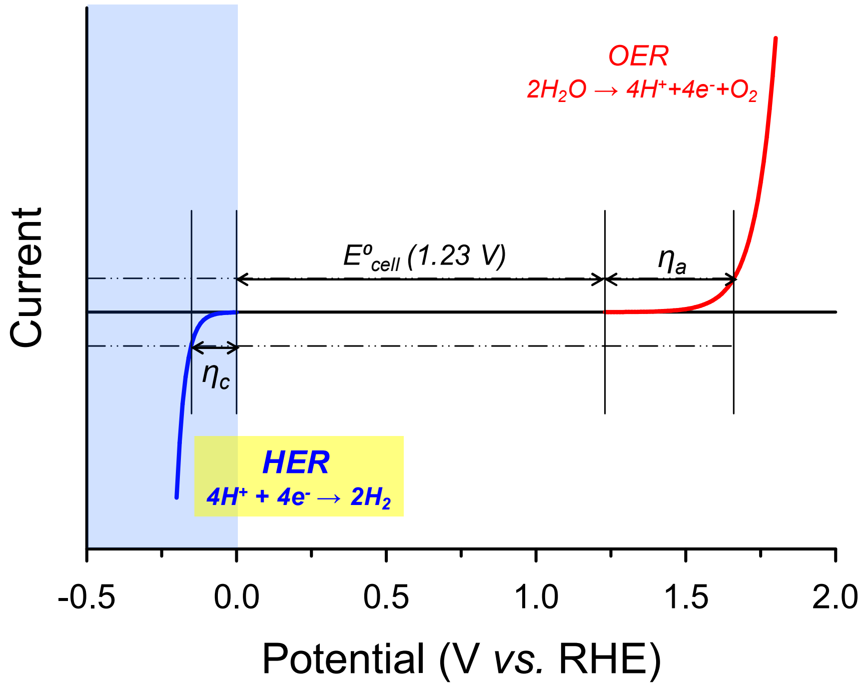

Figure 1.5. *I–V* polarization curve depicting overall water electrolysis. This figure was reused with permission from ref. 27. Copyright 2016 SpringerOpen.

1.2. HER Activity Parameters

1.2.1. Overpotential to drive a current density of −10 mA cm^{-2}

Generally, the comparison of HER activities has been made in terms of the overpotential at a current density of −10 mA cm^{-2}. This current density corresponds to an efficiency of approximately 10% in solar-to-fuel devices,[29] and the derivation is as follows:

(1) American Society for Testing and Materials (ASTM) defined the standard solar spectral irradiance at air mass 1.5 (AM 1.5G).[30] Integration of the solar spectrum (AM1.5G) yields a value of 100 mW cm^{-2}, which is typically referred to as “1 sun”.

(2) As the redox potential for water oxidation is ~1.2 V, a 100% efficient solar-to-fuel device would give (100 (mA V) cm^{-2})/(1.2 V) = 83 mA cm^{-2} under AM1.5G.

(3) Thus, a 10% efficient solar-to-fuel device would give 8.3 mA cm^{-2}.

Therefore, the ranking of HER catalysts by comparison of the overpotentials required to drive a current density of −10 mA cm^{-2} is reasonable in a practical context.

1.2.2. Tafel Slope and Exchange Current Density

The Tafel slope is a kinetic parameter that is used to evaluate reaction mechanisms, and it can be derived from the classical Butler–Volmer equation as shown here:[31]

$$i = i_0 \left(c_\mathrm{R} \mathrm{e}^{\frac{(1-\alpha) nF\eta}{RT}} - c_\mathrm{O} \mathrm{e}^{\frac{-\alpha nF\eta}{RT}} \right)$$

where i is the measured current density; i_0 is the exchange current density; c_O and c_R are the concentrations of the species being reduced and oxidized, respectively; α is the electrochemical transfer coefficient; n is the number of electrons involved in the electrode reaction; F is the Faraday constant; η is the overpotential; R is the ideal gas constant; and T is the absolute temperature. When the reaction is out of equilibrium, the measured current will be dominated by either the cathodic or the anodic current. The logarithm of the equation results in a plot of the overpotential as a function of current density.

$$|\eta| = \frac{2.3RT}{\alpha nF} \log \frac{i}{i_0}$$

From the above equation, the Tafel slope is defined as $2.3RT/\alpha nF$ and bears the units mV dec^{-1}. The Tafel slope is therefore determined from the linear regression line of the Tafel plots (η *vs.* $\log|i|$), which can be derived from the I–V polarization curve. In the case of plotting the $\log|i|$ *vs.* η, the Tafel slope was the reciprocal of the slope ($\alpha nF/2.3RT$) as shown in **Figure 1.6**. The Tafel slope has been used to assess the HER mechanism. More specifically, in an acid, an HER occurring *via* the Volmer–Tafel and the Volmer–Heyrovsky mechanisms gives rise to Tafel slopes of 29 and 38 mV dec^{-1}, respectively (see section 1.1.2 for details of HER mechanism). In both cases, the combination of two hydrogen atoms is the rate-determining step, because if the Volmer step is the rate-determining step or the catalyst surface coverage is close to 1, the Tafel slope increases to 116 mV dec^{-1}.

The i_0 is also used as the figure of merit for HER activity comparison as the i_0 is related to the electron-transfer rate of the reaction, reflecting the intrinsic catalytic activity. From the Tafel plots, i_0 can be determined from the y-intercept ($\log i_0$) (**Figure 1.6**). However, i_0 values can be different even with the same catalyst materials, depending on the measurement conditions. For example, Gasteigher *et al*. reported i_0 values of 235–600 mA cm^{-2} for Pt NPs,[32] which is two orders of magnitude higher than the 0.8–1.4 mA cm^{-2} reported by Markovic and co-workers.[33] They used different catalysis systems; in the former case the i_0 was measured with a membrane electrode assembly, and in the latter case the i_0 was evaluated with single crystals using a rotating disc electrode in a liquid electrolyte. Therefore, it is important to evaluate both i_0 and Tafel slope for reliable activity comparison.

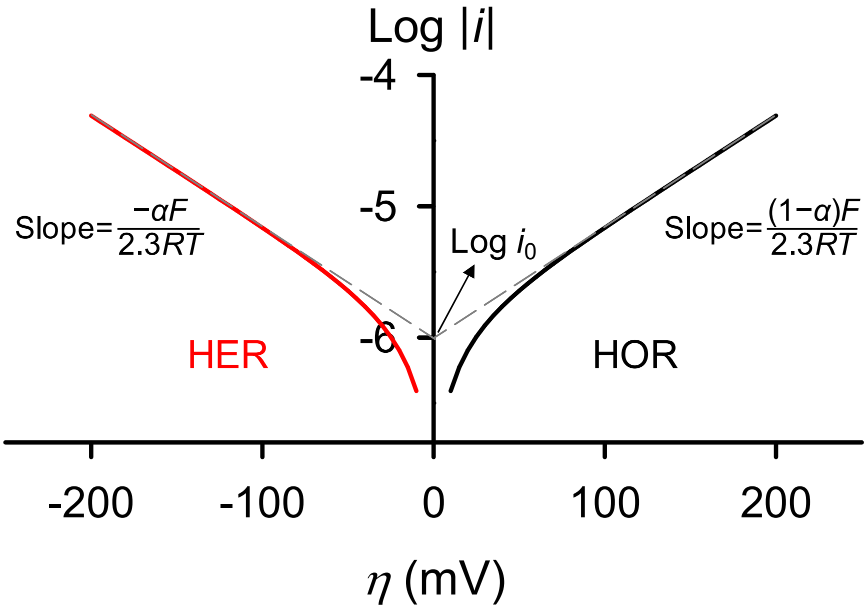

Figure 1.6. Tafel plots for anodic and cathodic reactions of the log|i|–η curve with $\alpha = 0.5$, $T = 298$ K, and $j_0 = 10^{-6}$ A cm^{-2}.[31]

1.2.3. Turnover Frequency

The precise evaluation of activity per active site is important to obtain a fundamental understanding of the origin of catalytic activity. The intrinsic activity can be assessed by calculating turnover frequency (TOF), which is defined as the turnover rate per active site. The general equation for TOF calculations is given by:

$$\text{TOF} = i(\text{A}) \times \frac{1\text{H}_2}{2\text{e}^-} \times \frac{1\text{e}^-}{1.602 \times 10^{-19}\,\text{C}} \div (\text{Number of active sites})$$

While the comparison of TOFs is meaningful, a fair comparison of TOFs has not yet been made due to variations in methods for counting the active sites in addition to the issues associated with different catalyst structures. For example, only edge sites are active in 2H-MoS_2, while both edge and basal sites are active in 1T-MoS_2. Furthermore, the active sites present in amorphous MoS_x catalysts are unclear due to complexity of their structures. For this reason, TOF should be more carefully determined for fair comparison of these catalysts.

Depending on which sites are assigned as the active centers, the TOF can vary by many orders of magnitude. Theoretically, it is widely accepted that hydrogen atoms bind to the surface S sites in transition metal sulfides-based HER catalysts.[34] However, the majority of studies have calculated TOFs by assuming that the surface Mo atoms are the active sites, as the multiple chemical states possible for S render the calculation difficult. In this dissertation, I will briefly introduce three possible methods for measuring catalytically active surface sites.

Firstly, the lower bound TOF can be calculated by assuming that all the atoms loaded on the electrode are active. In this case, the number of active sites can be simply calculated with catalyst loading, as given by:

$$\text{Number of active sites} = \frac{m}{MW} \times N_\text{A}$$

where m is the amount (g) of catalyst loaded on the electrode, MW is the molecular weight of the catalyst, and N_A is Avogadro's number. This method is specifically appropriate for molecular catalysts because all the loaded catalysts are expected to expose their active sites and participate in the catalysis. An example is described in section 8.3.

Secondly, the number of active sites can be calculated using a geometric model. The geometric model can be determined from theoretical calculations or the crystal information of the catalysts. An example is described in section 3.3.1.[35]

Thirdly, the electrochemically active surface area (ECSA) can be used for determining the active sites. ECSA is commonly obtained with double layer capacitance measurements (see section 2.2.4 for measurement details), which can probe all electrochemically assessible surface sites, except the inert areas. Indeed, among the three methods, ECSA-derived TOFs are closest to the upper bound. An example is described in section 7.3.[36] In this case, the surface occupancy was calculated based on the molar volume of the catalyst materials, and the # of active sites was determined as follows:

$$\text{Number of active sites} = \text{ECSA (cm}^2\text{)} \times \text{Surface occupancy (atoms cm}^{-2}\text{)}$$

In addition to the three methods used in this study, there are many routes to measure the catalytically active sites. A commonly adopted method is to use microscopy technique.[37–39] Nevertheless, there remains room for calculating more upper bound TOFs that are closer to genuine values with more accurate counts of catalytic active sites. The establishment of a general route that is affordable with all kinds of electrocatalysts would allow a fairer comparison between different catalytic materials.

Moreover, it should be noted that the TOF values are highly dependent on the geometric catalyst loadings. Jaramillo and co-workers reported that $[Mo_3S_{13}]^{2-}$ clusters show increasing TOFs (at −200 mV) with decreasing catalyst loadings from 100 μg cm^{-2} to 20 μg cm^{-2}.[39] Further decrease of the catalysts loadings from 20 μg cm^{-2} to 10 μg cm^{-2}, however, decreases the TOFs. The results suggested that the optimum thickness of the catalyst film on the electrode is important for the accurate measurement of the HER current in the aspect of catalyst accessibility and full utilization. Ideally, the full utilization of loaded catalysts is possible with preparation of ultrathin catalyst films in which all catalysts on the electrode surface are accessible.

1.2.4. Gibbs Free Energy

The Gibbs free energy (ΔG_H) for adsorption of atomic hydrogen has been adopted as an activity metric for the HER. According to the Sabatier principle, too strong or weak interactions between reaction intermediates and the catalyst surface can deteriorate the overall catalyst performance, thereby exhibiting a volcano-shaped relationship between i_0 and ΔG_H (**Figure 1.7**).[40–42] Specifically, if the adsorption binding is too weak, the reactant will not adsorb onto the catalyst surface, and if the adsorption binding is too strong, the product cannot escape from the catalyst surface. Therefore, negative and positive ΔG_H means that the activity will be governed by the desorption rate of products and the adsorption rate of reactants, respectively. Among HER catalysts of various compositions, Pt-based catalysts exhibit the highest i_0, with a ΔG_H value close to zero. This indicates that an optimal binding strength is important to adsorb the reactant and desorb the product. In this regard, ΔG_H has been commonly employed as the figure-of-merit for evaluating the HER performance of a newly developed electrocatalyst. Generally, ΔG_H values are calculated using a theoretical model to mimic the real catalysts.

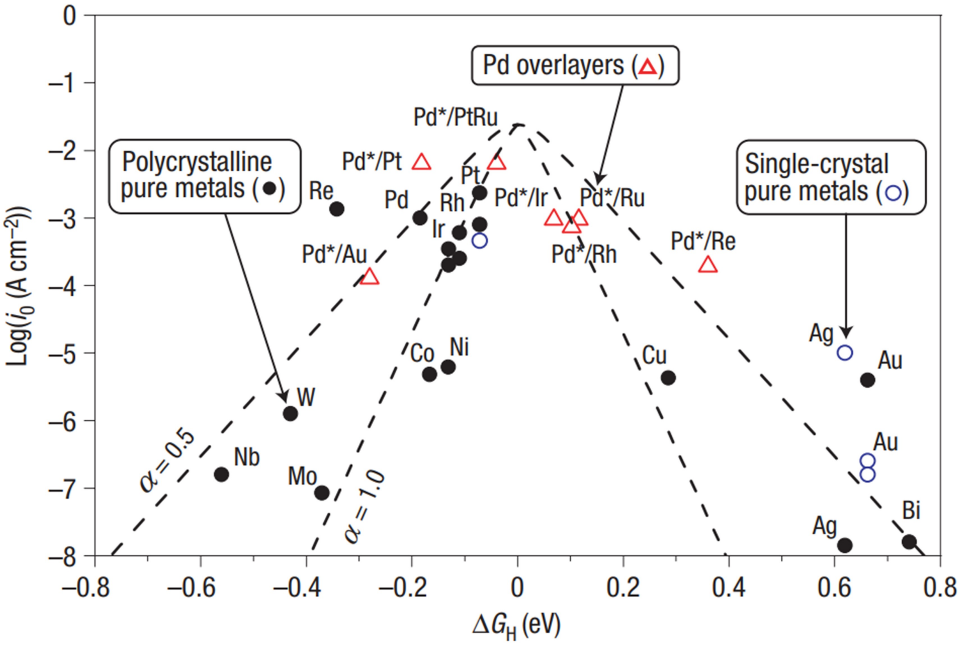

Figure 1.7. Volcano plot of i_0 as a function of density functional theory (DFT)-calculated ΔG_H for atomic hydrogen adsorption. This figure was reprinted with permission from ref. 41. Copyright 2006 Nature Publishing Group.

1.3. ELECTROCATALYSTS FOR HER

Many significant advances have been made in the development of highly active non-precious electrocatalysts to replace expensive Pt-based HER catalysts. Notable examples of non-precious metal catalysts include metal sulfides, phosphides, carbides, and heteroatom-doped carbons.[16,43–46] In this section, the progress that has been made in the development of non-precious electrocatalysts for the HER, primarily in acidic electrolytes that are relevant to the PEM electrolysis system, is highlighted. Additionally, some representative synthetic strategies for enhancing their HER performance are discussed.

1.3.1. Transition Metal Sulfides

Among the various classes of materials, two-dimensional (2D) layered transition metal dichalcogenides (TMDs) have emerged as a promising class of catalytic materials owing to their tunable electronic structures.[47] As representatives of 2D TMDs, nanostructured molybdenum sulfides (MoS_2) have been the forefront of non-precious HER catalysts, owing to their high activities, stabilities, and precious metal-free compositions.[35,37,39,42,48–76] Although bulk MoS_2 exhibits negligible catalytic performance for the HER,[77] nanostructured 2D TMDs are capable of catalyzing the HER with very high efficiency by exposing a high density of catalytically active edge sites.[42,48]

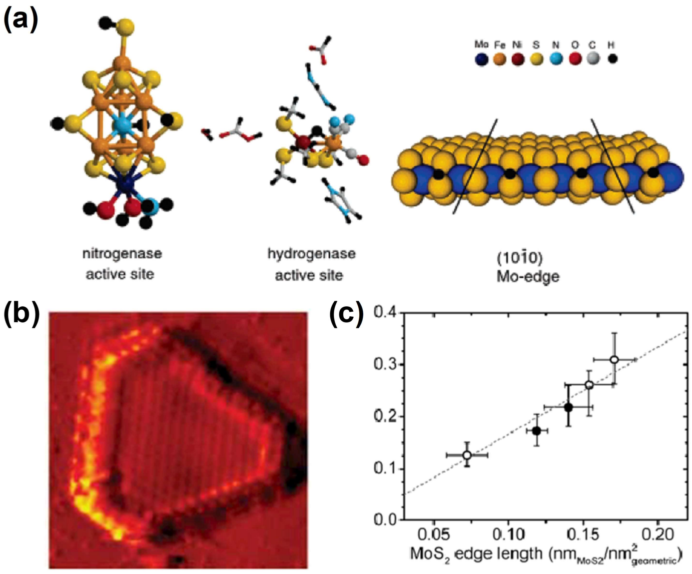

Figure 1.8. (a) Active sites of nitrogenase and hydrogenase, and depiction of the Mo-edge on MoS_2 slab. Figure (a) was reprinted with permission from ref. 48. Copyright 2005 American Chemical Society. (b) STM image of MoS_2 nanoparticles on a Au(111) crystal surface. (c) Exchange current density versus MoS_2 edge length. Figures (b),(c) were reprinted with permission from ref. 42. Copyright 2007 American Association for the Advancement of Science.

The active edge sites of MoS_2-based HER catalysts bear a remarkable resemblance to those of the nitrogenase and hydrogenase enzymes, which are the most active molecular catalysts in the natural HER system (**Figure 1.8a**).[48] To date, considerable progress has been made to synthesize highly active and stable heterogeneous electrocatalysts whose structures mimic the active sites of such natural catalysts.[39,49–51] In 2005, theoretical calculations by Nørskov and coworkers revealed that the $Mo(10\bar{1}0)$ edge of MoS_2 exhibits a ΔG_H of 0.08 eV, close to the optimal value of 0 eV, suggesting that the MoS_2 edge is a highly plausible active site for the HER.[48] In stark contrast, the basal plane shows a ΔG_H of 1.92 eV.[52] Indeed, this was demonstrated experimentally using a model catalyst comprising MoS_2 nanoparticles (NPs) grown on a Au(1 1 1) surface (**Figure 1.8b**).[42] This work revealed that the electrochemical HER activity exhibits a linear correlation with the edge length of MoS_2 (**Figure 1.8c**). These pioneering works have provided important evidence that the active sites of MoS_2 are located at the edge planes.

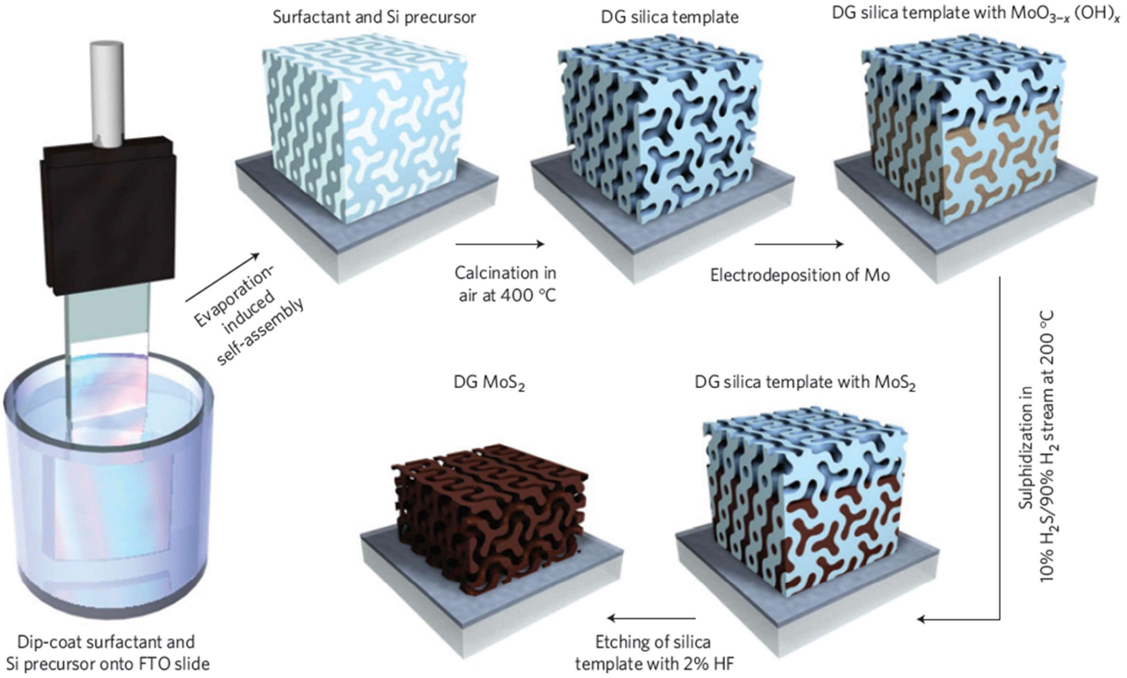

Figure 1.9. Synthesis procedure and structural model for DG MoS_2. This figure was reprinted with permission from ref. 53. Copyright 2012 Macmillan Publishers Ltd.

Since the edges of MoS_2 were proposed as the catalytic active sites, a variety of strategies have been employed to maximize the edge site densities *via* structural modifications, including space-confined growth,[35,53–55] vertical alignment,[37] and the design of molecular catalysts.[39,49–51] Reducing the particle size of MoS_2 is the most straightforward method that can increase the density of active edge sites. However, thermodynamics tends to favor growth through the basal plane because the formation of edge sites is highly energetic due to the under-coordinated atomic configuration. To overcome this challenge, confinement growth within a nanospace has been reported.[35,53–55] Jaramillo and co-workers reported a mesoporous MoS_2 structure synthesized using a silica template with double-gyroid (DG) morphology (**Figure 1.9**).[53] The DG MoS_2 structure exhibited a high surface curvature, thereby exposing a large fraction of active edge sites. DG MoS_2 exhibited a higher HER performance than high aspect-ratio core-shell MoO_3-MoS_2 nanowires.[56] In addition, DG MoS_2 gives a Tafel slope of 50 mV dec^{-1}, which is relatively low compared to those of the previously reported MoS_2-based HER catalysts. The result indicates that space confinement growth paves the way to controlling the surface structure and the size of MoS_2 at the nanoscale to ultimately develop effective catalysts with high densities of active edge sites at the surface.

The active sites, long been limited to the edges of MoS_2, have recently been expanded to basal surfaces *via* several strategies, such as phase engineering from the 2H phase to the metallic 1T phase,[57–60] heteroatom doping,[61,62] defect site generation on the basal surfaces,[63–67] and strain engineering.[68] Phase engineering from trigonal prismatic (2H-MoS_2) to metallic octahedral (1T-MoS_2) structures (**Figure 1.10a,b**) have significantly increased the active sites in the basal surface.[57–60] For example, Jin group reported that the chemical exfoliation of 2H-MoS_2 using n-butyllithium remarkably enhanced the HER activity through the formation of metallic 1T-MoS_2.[57] The 1T-MoS_2 nanosheets exhibited a low overpotential of 187 mV to drive a current density of −10 mA cm^{-2}, compared to ~313 mV for 2H-MoS_2.[57] Furthermore, the Tafel slope of 43 mV dec^{-1} for 1T-MoS_2 was significantly lower than that of 2H-MoS_2 (i.e., 110 mV dec^{-1}), indicating fast HER kinetics in 1T-MoS_2. This was explained by the fact that the electronic conductivity in 1T-MoS_2 is six orders of magnitude greater than that of 2H-MoS_2. However, the preparation of 1T-MoS_2 is more complicated than that of 2H-MoS_2, due to its metastable nature (**Figure 1.10c**). In this regard, significant efforts have been directed to prepare the stable and highly pure 1T-MoS_2 polymorph using chemical Li-intercalation,[57,58] electrochemical Li-intercalation,[59] and a pressurized hydrothermal process.[60] After much effort, Chhowalla and coworkers prepared the 1T phase MoS_2 through an exfoliation reaction using lithium borohydride, where a significantly higher yield was obtained than that obtained using n-butyllithium (i.e., 80% *vs.* ~50%).[58] In this work, the main active sites of the two polymorphs, i.e., 2H-MoS_2 and 1T-MoS_2, were compared. Upon partial oxidation of the edges, the HER activity of 2H-MoS_2 was significantly reduced, while that of 1T-MoS_2 remained unaffected, suggesting that the main active site of the 2H-MoS_2 polymorph is located at the edge sites, while that of 1T MoS_2 may be located at basal surface (**Figure 1.10d,e**). The origin of HER activity has not yet been completely elucidated. Decoupling of the intrinsic activities of the 1T phase from the overall HER activity is required to reach a fundamental understanding of the active sites present in MoS_2 polymorphs.

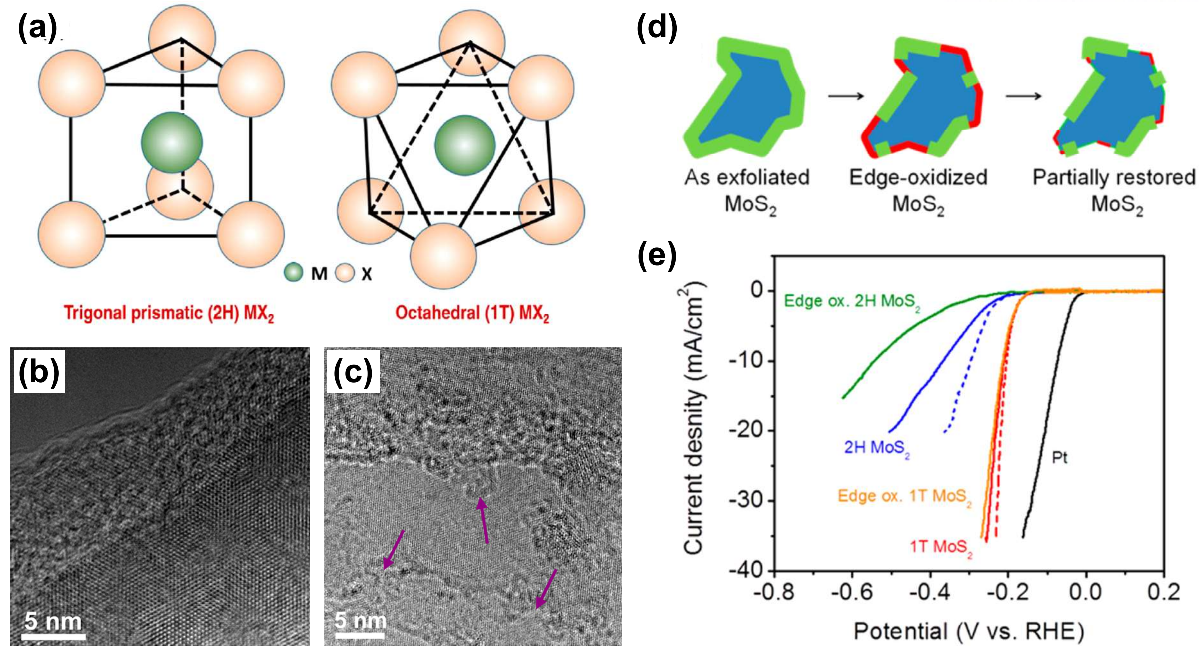

Figure 1.10. (a) Unit cell structures of 2H-MoS_2 and 1T-MoS_2. Figure (a) was reprinted with permission from ref. 47 Copyright 2014 American Chemical Society. HRTEM images of (b) 2H-MoS_2 and (c) 1T-MoS_2. Figures (b),(c) were reprinted with permission from ref. 57 Copyright 2014 American Chemical Society. (d) Schematic representation of the oxidation process and partial restoration of the MoS_2 edges after several voltammetric cycles. (e) HER polarization curves of 1T and 2H-MoS_2 before and after the edge oxidation. Dashed lines indicate the *iR*-corrected polarization curves. Figures (d),(e) were reprinted with permission from ref 58. Copyright 2013 American Chemical Society.

The incorporation of heteroatoms into the basal surface of MoS_2 nanosheets also significantly enhanced the HER performance by modifying the electronic structure of the in-plane S atoms neighboring the heteroatom, thereby altering the adsorption strength of H atoms.[61,62] More specifically, Du and co-workers suggested that doping MoS_2 with a heteroatom in combination with a small compressive strain can yield an ideal ΔG_H for hydrogen binding in the HER.[62] Bao and co-workers reported the doping of single Pt atoms into the in-plane domain of MoS_2 nanosheets (Pt-MoS_2),[61] where the resulting Pt-MoS_2 exhibited an enhanced HER performance compared with the undoped MoS_2. Furthermore, they also screened the HER activities of MoS_2 doped with many transition metals, resulting in a volcano-shaped relationship with the adsorption free energy of the H atoms (ΔG_H). Heteroatom doping is a novel method for activating the inert in-plane domain of MoS_2 catalysts, which may also be extended to other 2D materials applicable in a variety of catalytic reactions.

The inert basal surfaces of 2H-MoS_2 have also been successfully activated by creating defect sites and/or inducing strain.[63–67] The first example of defect engineering conducted by Xie and co-workers focused on the exposure of additional active edge planes by forming cracks on the surfaces of nanosheets.[63] They reported that defect-rich MoS_2 exhibited a significantly enhanced HER performance compared with defect-free MoS_2. In addition, Ajayan and co-workers demonstrated that oxygen plasma treatment and H_2 annealing introduced additional active sites within the MoS_2 monolayer, significantly improving the HER activity.[64] Recently, more rational and controllable defect modulation has been reported through combined experimental and theoretical studies.[65–67] Allwood and co-workers prepared MoS_2 nanocrystals and activated the Mo atoms in the basal surface of MoS_2 nanocrystals by S depletion,[65] with the resulting activated MoS_2 exhibiting a very high HER performance (~150 mV at −10 mA cm^{-2} and a Tafel slope of ~29 mV dec^{-1}). Cao and co-workers also verified the importance of S vacancies on the catalytic activity for the HER,[66] estimating the intrinsic TOFs of the edge sites, S vacancies, and grain boundaries as approximately 7.5 s^{-1}, 3.2 s^{-1}, and 0.1 s^{-1}, respectively. Finally, the Zheng and Nørskov groups reported that straining of the S-vacancies further enhances the HER activity.[68] The experimental results were further verified with theoretical results showing that the optimum level of strain and S-vacancy can tune ΔG_H close to zero, guaranteeing the highest intrinsic HER activity.

Despite significant investigations into the structural engineering of MoS_2-based electrocatalysts to enhance the HER performance, a number of questions remain regarding the active sites and reaction mechanisms. Specifically, the identification of active sulfur sites for proton reduction in the HER has not yet been clarified due to the diverse chemical species of S, namely; bridging S_2^{2-}, terminal S_2^{2-}, apical S^{2-}, and unsaturated S^{2-} (**Figure 1.11a**).[39,69–71] In this context, exploiting molecular analogues to MoS_2 edges is an attractive approach, as well-defined molecular catalysts selectively possess desirable sulfur sites, and hence, serve as an appropriate model system for deciphering genuine active sulfur sites for atomic hydrogen adsorption. For instance, $[Mo_2S_{12}]^{2-}$ catalysts that only contain bridging and terminal S_2^{2-} sites[51] showed higher HER performance than trimeric $[Mo_3S_{13}]^{2-}$ clusters containing apical S^{2-} sites together with bridging and terminal S_2^{2-} sites. The results suggest that the apical S^{2-} species is catalytically inert for the HER compared to the bridging or terminal S_2^{2-} sites. Recent *in situ* Raman study of MoS_x catalysts suggested that the bridging S_2^{2-} sites are transformed into unsaturated S^{2-} species under the HER potential.[69] In addition, molecular mimics could expose active edge sites with maximum extent, enhancing the efficiency of HER. Representative molecular mimics to MoS_2 edges include trimeric clusters of $[Mo_3S_4]^{4+}$ and $[Mo_3S_{13}]^{2-}$,[39,49] a dimeric $[Mo_2S_{12}]^{2-}$ cluster,[51] and an exquisitely designed molybdenum complex, $[(PY5Me_2)MoS_2]^{2+}$ ($PY5Me_2$ = 2,6-bis(1,1-bis(2-pyridyl)ethyl)pyridine) (**Figure 1.11b**).[50]

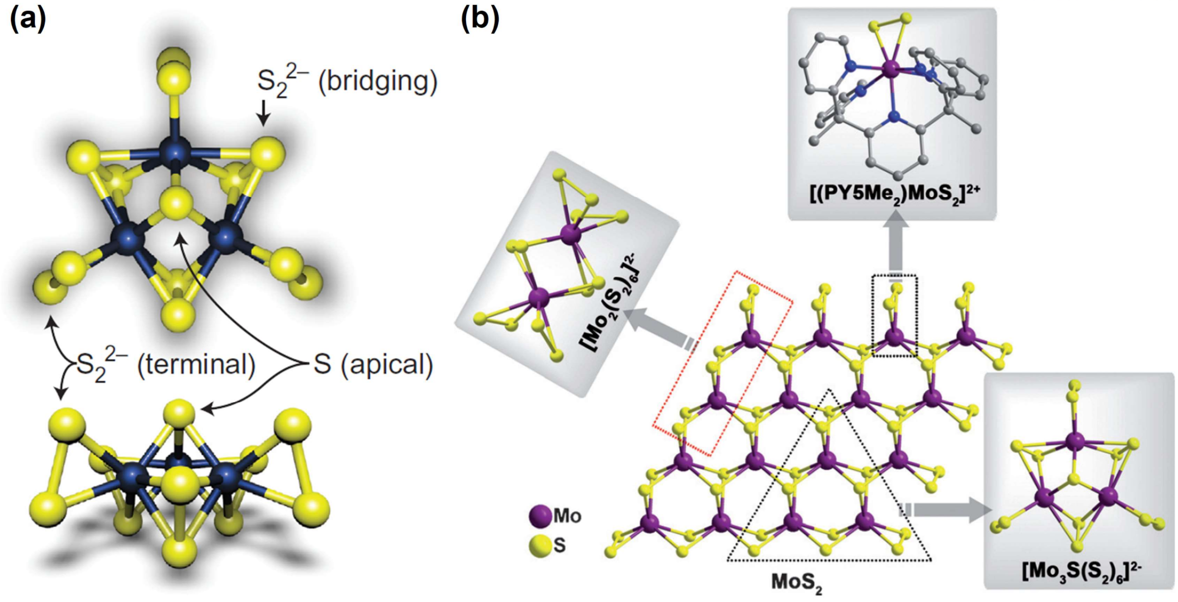

Figure 1.11. (a) Model of a single $[Mo_3S_{13}]^{2-}$ cluster with bridging S_2^{2-}, terminal S_2^{2-}, and the apical S^{2-} species. Figure (a) was reprinted with permission from ref 39. Copyright 2014 Macmillan Publishers Ltd. (b) The relationship of the MoS_x-based molecular HER catalysts to the monolayer MoS_2 with sulfur-rich edges. Top: the discrete analogue $[(PY5Me_2)MoS_2]^{2+}$. Left: the dimeric analogue $[Mo_2S_{12}]^{2-}$. Right: the trimeric analogue $[Mo_3S_{13}]^{2-}$. Figure (b) was reprinted with permission from ref 51. Copyright 2015 Wiley-VCH Verlag GmbH & Co. KGaA, Weinheim.

Amorphous MoS_x, which contains short-range atomic arrangements with molecular clusters as building units, has attracted significant attention due to its facile preparation under mild conditions, such as wet chemical synthesis,[72] and electrodeposition.[71,73,74] Unlike MoS_2, amorphous MoS_x have received little attention due to the complex polymeric structure of such compounds.[71] The question of active sulfur sites on amorphous MoS_x has also been unavoidably and continuously raised. Yeo and co-workers provided an important clue for revealing the active sulfur sites for proton reduction by establishing a linear correlation between TOFs for the HER and the percentage of S species with higher electron binding energies using X-ray photoelectron spectroscopy (**Figure 1.12**).[70] This work suggested bridging S_2^{2-} species as the potential catalytic active sites. In addition, Yano and Hu and co-workers investigated the structural changes taking place in the amorphous MoS_x under HER conditions using *in situ* X-ray absorption spectroscopy.[75] They proposed a reaction mechanism, where the catalytic species is similar to MoS_2, which corroborates an earlier result by Nilsson and Jaramillo and co-workers.[76] Although significant efforts have been devoted to revealing the active sites for proton reduction, the identification and confirmation of genuine catalytically active sulfur sites remain elusive.

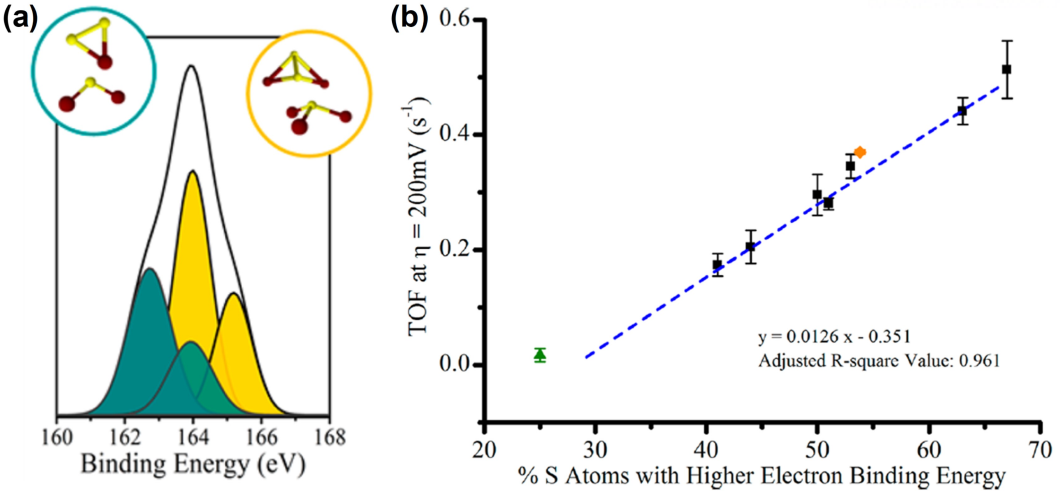

Figure 1.12. (a) A typical XPS spectrum for amorphous MoS_x. The green- and yellow colored peaks at lower and higher binding energies, mainly originating from terminal S_2^{2-}/unsaturated S^{2-} and bridging S_2^{2-}/apical S^{2-} species, respectively. (b) TOFs versus the percentage of S atoms with a high electron binding energy. Figures were reprinted with permission from ref 70. Copyright 2016 American Chemical Society.

1.3.2. Transition Metal Phosphides

Along with the TMDs, transition metal phosphides (TMPs) have recently been identified as a promising class of non-precious metal catalysts for the HER.[78,79] Like MoS_2, the potential of TMPs as the HER catalysts originates from the structural commonalities with the active centers in hydrogenase and nitrogenase enzymes. Among diverse compositions of metal phosphides, nickel phosphide-based catalysts have shown very high HER activity.[36,80–83] As phosphorus has a higher electronegativity compared to Ni, it can provide many proton acceptor sites on the nearby Ni. In addition, phosphorus atoms can optimize the adsorption strength of hydrogen atoms on the Ni surface. Like the metal sulfides, the crystal structure of metal phosphides is based on prismatic building blocks, but is more isotropic, thereby affording a large number of coordinatively unsaturated surface sites. For this reason, TMPs could exhibit intrinsically higher HER performance than TMDs. In 2005, Rodriguez and co-workers employed DFT calculations to investigate the HER activity over a series of HER catalysts including [NiFe] hydrogenase, analogue metal complexes, and Pt(111), Ni(111), and Ni_2P(001) single crystal surfaces.[80] The hollow sites of Ni_2P(001) surface poisoned with H (**Figure 1.13a**) showed superior HER activity to the Pt(111) surface, and even displayed a comparable HER activity to [NiFe] hydrogenase, which had the highest HER activity among the catalysts.[80] In 2013, Schaak and co-workers demonstrated the translation of theoretical prediction to nanoscale catalysts by preparing Ni_2P NPs containing a high density of Ni_2P(001) surfaces, which showed excellent HER activity (**Figure 1.13b–d**).[81] Following these pioneering studies, nickel phosphide NPs have become the recent focus of attention as advanced HER catalysts.

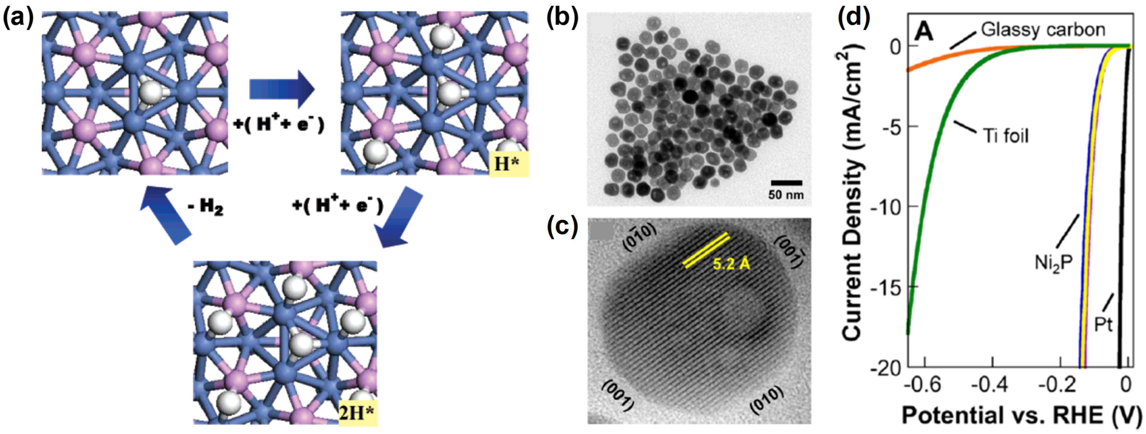

Figure 1.13. (a) A catalytic cycle for the HER on a H-poisoned $Ni_2P(001)$ surface (white, H; navy, Ni; purple, P). Figure (a) was reprinted with permission from ref. 80. Copyright 2005 American Chemical Society. (b) TEM image and (c) HRTEM image of a representative Ni_2P NP, highlighting the exposed $Ni_2P(001)$ facet and the lattice fringes that correspond to the (010) planes. (d) LSV curves of glassy carbon, Ti foil, Ni_2P and Pt. Figures (b),(c),(d) were reprinted with permission from ref. 81. Copyright 2013 American Chemical Society.

Besides Ni_2P, other phases of nickel phosphide with different crystal structure were also explored as HER catalysts.[82,83] For example, Sundaram and co-workers investigated the effect of phosphorus content on the HER activity and stability in an acidic electrolyte.[82] They varied the Ni content from 8 at% to 33 at%, yielding different stoichiometry. The electrochemical measurements showed that the sample with higher phosphorus content was more active and stable for the HER in acid. In addition to nickel phosphide, the Schaak group synthesized various metal phosphides *via* solution-phase reaction using tri-n-octylphosphine (TOP) as a phosphorus source.[81,84–86] However, the reaction is highly corrosive and flammable due to the use of high boiling-point organic solvent inevitable for the decomposition of TOP. In this context, diverse synthesis strategies for metal phosphides have been employed, including the gas-solid reaction using NaH_2PO_2,[87–89] electrodeposition at room temperature,[90] and the hydrothermal reaction using white and red phosphorus with metal salts.[91] Sun group made notable contributions in this field by directly using metal phosphides with a three-dimensional (3D) structure as the cathode without a binder.[87–89] Among the 3D-structured metal phosphides, FeP nanowires grown on Ti achieved very high HER performance with an overpotential of 55 mV at -10 mA cm^{-2} and a Tafel slope of 38 mV dec^{-1}.[88] These studies greatly expanded the field of metal phosphide catalysts for the HER.

1.3.3. Transition Metal Carbides

The tremendous research attention toward transition metal carbides as HER catalysts was initiated by the discovery that tungsten carbide showed Pt-like catalytic behavior for the HER because of its similar d-band electronic structure to Pt.[92] Since the report, varied transition metal carbides have been explored as HER electrocatalysts.[93–95] In 2012, Hu *et al*. reported that commercially available β-Mo_2C can catalyze the HER with unexpectedly good efficiency in both acidic and alkaline media.[93] However, gas phase carbide synthesis, which has been widely used, has several issues, including the use of a toxic gas as the carbon source, and the generation of a char during the synthesis, which blocks the catalytic active sites on the carbide surface. Some recent studies suggest that solid carbon nanostructures could serve as the carbon source, as well as a conductive support for as-formed metal carbide NPs.[94–96] This approach can prevent severe agglomeration of metal carbide NPs by maximizing the anchoring sites, hence enhancing the overall HER performance. For example, Adzic and co-workers used carbon nanotubes and carbon blacks as the carbon sources and supports, synthesizing a high-performance β-Mo_2C-nanocarbon composites *via* in situ carburization.[94] The β-Mo_2C supported on carbon nanotubes exhibits 152 mV of overpotential at −10 mA cm^{-2} with a Tafel slope of 55.2 mV dec^{-1}. Further activity enhancement of metal carbide was achieved with a metal-organic framework (MOF)-assisted strategy yielding exceptionally high surface area. Lou *et al*. prepared mesoporous molybdenum carbide nano-octrahedrons using copper-based MOF as the HER catalysts. It shows 142 mV of overpotential at −10 mA cm^{-2} with a low Tafel slope of 53 mV dec^{-1}.[95]

1.3.4. Heteroatom-Doped Carbons

As carbon materials are catalytically inert for the HER, they have been commonly adopted as the catalyst support with the purpose of enhancing conductivity. Recently, heteroatom-doped carbon nanomaterials have showed significant catalytic activity for the HER.[96–99] Qiao *et al*. reported nitrogen (N) and phosphorus (P) dual-doped graphene as HER catalysts.[96] In this work, theoretical calculations revealed that pyridinic N and P dual-doped graphene has a Gibbs free energy close to zero (0.08 eV). Moreover, electrochemical measurements showed that N, P dual-doped graphene showed higher HER performance than those of single-doped graphenes. The dual-doped graphene exhibited 423 mV of overpotential at −10 mA cm^{-2} with a Tafel slope of 91 mV dec^{-1}. The same group improved the HER activity of nitrogen-doped graphene by forming a hybrid with graphitic carbon nitride (g-C_3N_4).[97,98] The hybrid of g-C_3N_4/N-graphene can operate the HER with a very low overpotential of 80 mV at −10 mA cm^{-2} and with a low Tafel slope of 49.1 mV dec^{-1}.[98] The results demonstrate that carbon nanomaterials are particularly promising as non-metal HER catalysts.

1.4. OUTLINE OF THE DISSERTATION

This dissertation deals with non-precious electrocatalysts for the HER, and establishes the correlations between the catalyst structure and the electrochemical properties to reveal the determining factors dictating the HER performance, as summarized in **Figure 1.14**. The outline is as follows.

Chapter 2 includes more detailed descriptions of the characterization and electrochemical measurement methods utilized in the following works.

In **Chapter 3**, layer number-dependent HER activity was investigated using a representative layered material of TMD, MoS_2 as the model catalyst. A confined growth approach was introduced to control the layer numbers with monolayer precision at the nanoscale. Finally, the layer number dependent-TOF trends were deduced. To explain the activity trend, the structural features that changed with layer numbers were investigated with multiple characterization techniques and theoretical calculations. Additionally, the general synthetic approach to cobalt-doped MoS_2 nanoplates was introduced.

In **Chapter 4**, the growth behavior of WS_2 on a carbon surface was explored and compared with that of MoS_2 using experimental and computational demonstrations. In this study, further insight into the active sulfur sites for the HER was provided with WS_x nanostructures.

In **Chapter 5**, the impact of oxidation states in WS_x nanostructures on the HER activity was investigated using WS_2 and a WS_2-containing tungsten oxide core ($WS_2@W_{18}O_{49}$). In addition, the surface oxidation effect was also explored using electrochemical pretreatment.

In **Chapter 6**, Rh_2S_3 hollow NPs were applied as highly active and stable HER catalysts and their cavity size effects toward the HER were scrutinized. Together with the hollow morphology effect, the impact of chemical and electrochemical leaching of the core impurities was also investigated.

In **Chapter 7**, shape-controlled Ni_2P NPs were utilized as model systems to investigate the shape effects on the HER. In this work, exposed crystalline surfaces of shape-controlled NPs were inspected closely with TEM and XRD analyses. Finally, this work revealed the impact of the exposed crystallographic facets, mainly determined by the shape of NPs on the HER performance.

In **Chapter 8**, commercially available thiomolybdate; monomeric MoS_4^{2-} catalysts were adopted as HER catalysts, demonstrating the potential use of the smallest molecular catalyst as the active HER catalysts. This work could also elucidate the genuine active sulfur sites for proton reduction in the HER in nanostructured and molecular catalysts, which are linked at the atomic scale.

Chapter 9 summarizes the main results presenting the significance of this work, and suggest future work.

These studies aim to reveal the structural features responsible for the catalytic activity and stability. Establishment of the structure–activity relationship could provide fundamental insight towards the design of new electrocatalysts, thereby enhancing the overall efficiency of water electrolysis, and enabling widespread utilization. Moreover, these insights can be applied to other emerging and promising electrocatalytic reactions, such as hydrogen peroxide production, carbon dioxide reduction, and nitrogen reduction. Finally, I have attached my curriculum vitae and acknowledgements at the end of this dissertation.

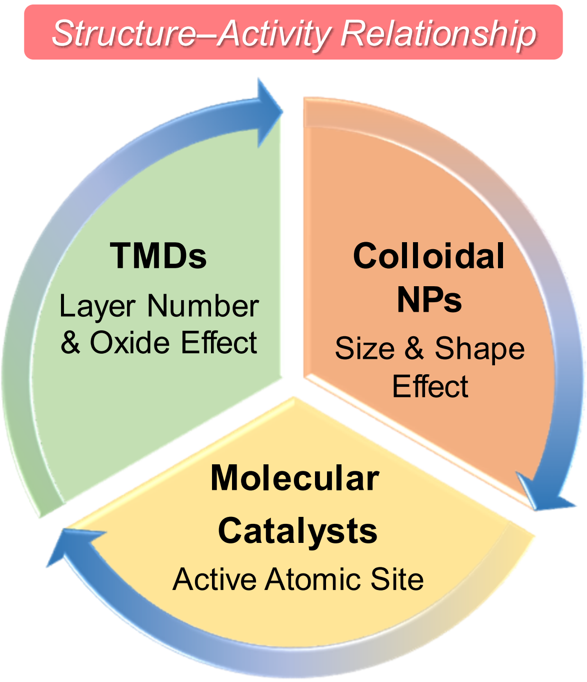

Figure 1.14. Outline of the dissertation revealing the structural factors responsible for HER performance with TMDs, colloidal NPs, and molecular catalysts.

1.5. REFERENCES

1. World Energy Outlook 2015, *International Energy Agency* **2015**
2. Asefi-Najafabady, S.; Rayner, P. J.; Gurney, K. R.; McRobert, A.; Song, Y.; Coltin, K.; Huang, J.; Elvidge, C.; Baugh, K. *J. Geophys. Res. Atmos.* **2014**, *119*, 10,213–10,231.
3. Annual Coal Report, *U. S. Energy Information Administration* **2017**
4. Balat, M. *Int. J. Hydrogen Energy* **2008**, *33*, 4013–4029.
5. Turner J. A. *Science* **2004**, *305*, 972–974.
6. Nørskov, J. K.; Christensen, C. H. *Science* **2006**, *312*, 1322–1323.
7. Lan, R.; Irvine, J. T. S.; Tao, S. *Int. J. Hydrogen Energy* **2012**, *37*, 1482–1494.
8. Report of the Hydrogen Production Expert Panal: A Subcommitte of the Hydrogen & Fuel Cell Technical Advisory Committee, *U. S. Department of Energy* **2013**.
9. Bakenne, A.; Nuttall, W.; Kazantzis, N. *Int. J. Hydrogen Energy* **2016**, *41*, 7744–7753.
10. Armor, J. N. *Appl. Catal. A* **1999**, *176*, 159–176.
11. Haryanto, A.; Fernando, S.; Murali, N.; Adhikari, S. *Energy Fuels* **2005**, *19*, 2098–2106.
12. Paster, M. D.; Ahluwalia, R. K.; Berry, G.; Elgowainy, A.; Lasher, S.; Mckenney, K.; Gardiner, M. *Int. J. Hydrogen Energy* **2011**, *36*, 14534–14551.
13. Cheng, X.; Shi, Z.; Glass, N.; Zhang, L.; Zhang, J.; Song, D.; Liu, Z.-S.; Wang, H.; Shen, J. *J. Power Socurces* **2007**, *165*, 739–756.
14. Ivy, J. Summary of Electrolytic Hydrogen Production Milestone Completion Report, *U. S. Department of Energy* **2004**.
15. Mallouk, T. E. *Nat. Chem.* **2013**, *5*, 362–363.
16. Anantharaj, S.; Ede, S. R.; Sakthikumar, K.; Karthick, K.; Mishra, S.; Kundu, S. *ACS Catal.* **2016**, *6*, 8069–8097.
17. Agrafiotis, C.; Roeb, M.; Konstandopoulos, A. G.; Nalbandian, L.; Zaspalis, V. T.; Sattler, C.; Stobbe, P.; Steele, A. M. *Sol. Energy* **2005**, *79*, 409–421.
18. https://www.jmbullion.com
19. Mineral Commodity Summaries, *U. S. Geological Survey* **2017**
20. https://energy.gov/eere/fuelcells/doe-technical-targets-hydrogen-production-electrolysis
21. Trasatti, S. *J. Electroanal. Chem.* **1999**, *476*, 90–91.
22. Ursua, A.; Gandia, L. M.; Sanchis, P. *Proc. IEEE.* **2012**, *100*, 410–426.
23. Carmo, M.; Fritz, D. L.; Mergel, J.; Stolten, D. *Int. J. Hydrogen Energy* **2013**, *38*, 4901–4934.
24. Slade, S.; Campbell, S. A.; Ralph, T. R.; Walsh, F. C. *J. Electrochem. Soc.* **2002**, *149*, A1556–A1564.
25. Dau, H.; Limberg, C.; Reier, T.; Risch, M.; Roggan, S.; Strasser, P. *ChemCatChem.* **2010**, *2*, 724–761.
26. Badwal, S. P. S.; Giddey, S.; Ciacchi, F. T. *Ionics* **2006**, *12*, 7–14.

27. Seo, B.; Joo, S. H. *Nano Convergence* **2017**, *4*, 19.
28. Merki, D.; Hu, X. *Energy Environ. Sci.* **2011**, *4*, 3878–3888.
29. Gorlin, Y.; Jaramillo, T. F. *J. Am. Chem. Soc.* **2010**, *132*, 13612–13614.
30. http://rredc.nrel.gov/solar/spectra/am1.5/
31. Bard, A. J.; Faulkner, L. R. Kinetics of Electrode Reaction. In *Electrochemical Methods*, 2; Harris, D.; Swain, E.; Aiello, E., Eds.; John Wiley & Sons, Inc: Hoboken, NJ, **2001**; pp 92–104.
32. Neyerlin, K. C.; Gu, W. B.; Jorne, J.; Gasteiger, H. A. *J. Electrochem. Soc.* **2007**, *154*, B631–B635.
33. Markovic, N. M.; Grgur, B. N.; Ross, P. N. *J. Phys. Chem. B* **1997**, *101*, 5405–5413.
34. Raybaud, P.; Hafner, J.; Kresse, G.; Kasztelan, S.; Toulhoat, H. *J. Catal.* **2000**, *189*, 129–146.
35. Seo, B.; Jung, G. Y.; Sa, Y. J.; Jeong, H. Y.; Chen, J. Y.; Lee, J. H.; Kim, H. Y.; Kim, J. C.; Shin, H. S.; Kwak, S. K.; Joo, S. H. *ACS Nano* **2015**, *9*, 3728–3739.
36. Seo, B.; Baek, D. S.; Sa, Y. J.; Joo, S. H. *CrystEngComm.* **2016**, *18*, 6083–6089.
37. Kong, D.; Wang, H.; Cha, J. J.; Pasta, M.; Koski, K. J.; Yao, J.; Cui, Y. *Nano Lett.* **2013**, *13*, 1341–1347.
38. Wu, Z.; Fang, B.; Wang, Z.; Wang, C.; Liu, Z.; Liu, F.; Wang, W.; Alfantazi, A.; Wang, D.; Wilkinson, D. P. *ACS Catal.* **2013**, *3*, 2101–2107.
39. Kibsgaard, J.; Jaramillo, T. F.; Besenbacher, F. *Nat. Chem.* **2014**, *6*, 248–253.
40. Parsons, R. *Trans. Fraday Soc.* **1958**, *54*, 1053–1063.
41. Greeley, J.; Jaramillo, T. F.; Bonde, J.; Chorkendorff, I.; Nørskov, J. N. *Nat. Mater.* **2006**, *5*, 909–913.
42. Jaramillo, T. F.; Jørgensen, K. P.; Bonde, J.; Nielsen, J. H.; Horch, S.; Chorkendorff, I. *Science*, **2007**, *317*, 100–102.
43. Vesborg, P. C. K.; Segar, B.; Chorkendorff, I. *J. Phys. Chem. Lett.* **2015**, *6*, 951–957.
44. Zou, X.; Zhang, Y. *Chem. Soc. Rev.* **2015**, *44*, 5148–5180.
45. Zheng, Y.; Jiao, Y.; Jaroniec, M.; Qiao, S. Z. *Angew. Chem. Int. Ed.* **2015**, *54*, 52–65.
46. Wang, J.; Xu, F.; Jin, H.; Chen, Y.; Wang, Y. *Adv. Mater.* **2017**, *29*, 1605838.
47. Lv, R.; Robinson, J. A.; Schaak, R. E.; Sun, D.; Sun, Y.; Mallouk, T. E.; Terrones, M. *Acc. Chem. Res.* **2015**, *48*, 56–64.
48. Hinnemann, B.; Moses, P. G.; Bonde, J.; Jørgensen, K. P.; Nielsen, J. H.; Horch, S.; Chorkendorff, I.; Nørskov, J. K. *J. Am. Chem. Soc.* **2005**, *127*, 5308–5309.
49. Jaramillo, T. F.; Bonde, J.; Zhang, J.; Ooi, B.-L.; Andersson, K.; Ulstrup, J.; Chorkendorff, I. *J. Phys. Chem. C* **2008**, *112*, 17492–17498.
50. Karunadasa, H. I.; Montalvo, E.; Sun, Y.; Majda, M.; Long, J. R.; Chang, C. J. *Science* **2012**, *335*, 698–702.
51. Huang, Z.; Luo, W.; Ma, L.; Yu, M.; Ren, X.; He, M.; Polen, S.; Click, K.; Garrett, B.; Lu, J.;

Amine, K.; Hadad, C.; Chen, W.; Asthagiri, A.; Wu, Y. *Angew. Chem. Int. Ed.* **2015**, *54*, 15181–15185.

52. Tsai, C.; Chan, K. R.; Nørskov, J. K.; Abild-Pedersen, F. *Surf. Sci.* **2015**, *640*, 133–140.
53. Kibsgaard, J.; Chen, Z.; Reinecke, B. N.; Jaramillo, T. F. *Nat. Mater.* **2012**, *11*, 963–969.
54. Zhu, C.; Mu, X.; van Aken, P. A.; Yu, Y.; Maier, J. *Angew. Chem. Int. Ed.* **2014**, *53*, 2152–2156.
55. Zheng, X.; Xu, J.; Yan, K.; Wang, H.; Wang, Z.; Yang, S. *Chem. Mater.* **2014**, *26*, 2344–2353.
56. Chen, Z.; Cummins, D.; Reinecke, B. N.; Clark, E.; Sunkara, M. K.; Jaramillo, T. F. *Nano Lett.* **2011**, *11*, 4168–4175.
57. Lukowski, M. A.; Daniel, A. S.; Meng, F.; Forticaux, A.; Li, L.; Jin, S. *J. Am. Chem. Soc.* **2013**, *135*, 10274–10277.
58. Voiry, D.; Salehi, M.; Silva, R.; Fujita, T.; Chen, M.; Asefa, T.; Shenoy, V. B.; Eda, G.; Chhowalla, M. *Nano Lett.* **2013**, *13*, 6222–6227.
59. Wang, H.; Lu, Z.; Kong, D.; Sun, J.; Hymel, T. M.; Cui, Y. *ACS Nano* **2014**, *8*, 4940–4947.
60. Geng, X.; Sun, W.; Wu, W.; Chen, B.; Al-Hilo, A.; Benamara, M.; Zhu, H.; Watanabe, F.; Cui, J.; Chen, T. 2016, *Nat. Commun.* **2016**, *7*, 10672.
61. Deng, J.; Li, H.; Xiao, J.; Tu, Y.; Deng, D.; Yang, H.; Tian, H.; Li, J.; Ren, P.; Bao, X. *Energy Environ. Sci.* **2015**, *8*, 1594–1601.
62. Gao, G.; Sun, Q.; Du, A. *J. Phys. Chem. C* **2016**, *120*, 16761–16766.
63. Xie, J.; Zhang, H.; Li, S.; Wang, R.; Sun, X.; Zhou, M.; Zhou, J.; Lou, X. W.; Xie, Y. *Adv. Mater.* **2013**, *25*, 5807–5813.
64. Ye, G.; Gong, Y.; Lin, J.; Li, B.; He, Y.; Pantelides, S. T.; Zhou, W.; Vajtai, R.; Ajayan, P. M. *Nano Lett.* **2016**, *16*, 1097–1103.
65. Lin, L.; Miao, N.; Wen, Y.; Zhang, S.; Ghosez, P.; Sun, Z.; Allwood, D. A. *ACS Nano* **2016**, *10*, 8929–8937.
66. Li, G.; Zhang, D.; Qiao, Q.; Yu, Y.; Peterson, D.; Zafar, A.; Kumar, R.; Curtarolo, S.; Hunte, F.; Shannons, S.; Zhu, Y.; Yang, W.; Cao, L. *J. Am. Chem. Soc.* **2016**, *138*, 16632–16638.
67. Tsai, C.; Li, H.; Park, S.; Park, J.; Han, H. S.; Nørskov, J. K.; Zheng, X.; Abild-Pedersen, F. *Nat. Commun.* **2017**, *8*, 15113.
68. Li, H.; Tasi, C.; Koh, A. L.; Cai, L.; Contryman, A. W.; Fragapane, A. H.; Zhao, J.; Han, H. S.; Manoharam, H. C.; Abild-Pederson, F.; Nørskov, J. K.; Zheng, X. *Nat. Mater.* **2016**, *15*, 48–53.
69. Deng, Y.; Ting, L. R. L.; Neo, P. H. L.; Zhang, Y.-J.; Peterson, A. A.; Yeo, B. S. *ACS Catal.* **2016**, *6*, 7790–7798.
70. Ting, L. R. L.; Deng, Y.; Ma, L.; Zhang, Y.-J.; Peterson, A. A.; Yeo, B. S. *ACS Catal.* **2016**, *6*, 861–867.
71. Tran, P. D.; Tran, T. V.; Orio, M.; Torelli, S.; Truong, Q. D.; Nayuki, K.; Sasaki, Y.; Chiam, S. Y.; Yi, R.; Honma, I.; Barber, J.; Artero, V. *Nat. Mater.* **2016**, *15*, 640–646.

72. Benck, J. D.; Chen, Z.; Kuritzky, L. Y.; Forman, A. J.; Jaramillo, T. F. *ACS Catal.* **2012**, *2*, 1916–1923.
73. Merki, D.; Fierro, S.; Vrubel, H.; Hu, X. *Chem. Sci.* **2011**, *2*, 1262–1267.
74. Vrubel, H.; Hu, X. *ACS Catal.* **2013**, *3*, 2002–2011.
75. Lassalle-Kaiser, B.; Merki, D.; Vrubel, H.; Gul, S.; Yachandra, V. K.; Hu, X.; Yano, J. *J. Am. Chem. Soc.* **2015**, *137*, 314–321.
76. Sanchez Casalongue, H. G.; Benck, J. D.; Tsai, C.; Karlsson, R. K. B.; Kaya, S.; Ng, M. L.; Pettersson, L. G. M.; Abild-Pedersen, F.; Nørskov, J. K.; Ogasawara, H.; Jaramillo, T. F.; Nilsson, A. *J. Phys. Chem. C* **2014**, *118*, 29252–29259.
77. Tributsch, H.; Bennett, J. C. *J. Electroanal. Chem. Interfacial Electrochem.* **1977**, *81*, 97–111.
78. Callejas, J. F.; Read, C. G.; Roske, C. W.; Lewis, N. S.; Schaak, R. E. *Chem. Mater.* **2016**, *28*, 6017–6044.
79. Shi, Y.; Zhang, B. *Chem. Soc. Rev.* **2016**, *45*, 1529–1541.
80. P. Liu and J. A. Rodriguez, *J. Am. Chem. Soc*. **2005**, *127*, 14871–14878.
81. Popczun, E. J.; Mckone, J. R.; Read, C. G.; Biacchi, A. J.; Wiltrout, A. M.; Lewis, N. S.; Schaak, R. E. *J. Am. Chem. Soc.* **2013**, *135*, 9267–9270.
82. Kucernak, A. R. J.; Sundaram, V. N. N. *J. Mater. Chem. A* **2014**, *2*, 17435–17445.
83. Pan, Y.; Liu, Y.; Zhao, J.; Yang, K.; Liang, J.; Liu, D.; Hu, W.; Liu, D.; Liu, Y.; Liu, C. *J. Mater. Chem. A* **2015**, *3*, 1656–1665.
84. Callejas, J. F.; McEnaney, J. M.; Read, C. G.; Crompton, J. C.; Biacchi, A. J.; Popczun, E. J.; Gordon, T. R.; Lewis, N. S.; Schaak, R. E. *ACS Nano* **2014**, *8*, 11101–11107.
85. Popczun, E. J.; Read, C. G.; Roske, C. W.; Lewis, N. S.; Schaak, R. E. *Angew. Chem. Int. Ed.* **2014**, *53*, 5427–5430.
86. McEnaney, J. M.; Crompton, J. C.; Callejas, J. F.; Popczun, E. J.; Biacchi, A. J.; Lewis, N. S.; Schaak, R. E. *Chem. Mater.* **2014**, *26*, 4826–4831.
87. Tian, J.; Liu, Q.; Asiri, A. M.; Sun, X. *J. Am. Chem. Soc.* **2014**, *136*, 7587–7590.
88. Jiang, P.; Liu, Q.; Liang, Y.; Tian, J.; Asiri, A. M.; Sun, X. *Angew. Chem. Int. Ed.* **2014**, *53*, 12855–12859.
89. Liang, Y.; Liu, Q.; Asiri, A. M.; Sun, X.; Luo, Y. *ACS Catal.* **2014**, *4*, 4065–4069.
90. Saadi, F. H.; Carim, A. I.; Verlage, E.; Hemminger, J. C.; Lewis, N. S.; Soriaga, M. P. *J. Phys. Chem. C* **2014**, *118*, 29294–29300.
91. Wang, X.; Kolen'ko, Y. V.; Liu, L. *Chem. Commun.* **2015**, *51*, 6738–6741.
92. Levy, R. B.; Boudart, M. *Science* **1973**, *181*, 547–549.
93. Vrubel, H.; Hu, X. *Angew. Chem. Int. Ed.* **2012**, *51*, 12703–12706.
94. Chen, W.-F.; Wang, C.-H.; Sasaki, K.; Marinkovic, N.; Xu, W.; Muckerman, J. T.; Zhu, Y.; Adzic, R. R. *Energy Environ. Sci.* **2013**, *6*, 943–951.

95. Wu, H. B.; Xia, B. Y.; Yu, L.; Yu, X.-Y.; Lou, X. W. *Nat. Commun.* **2016**, *6*, 6512.
96. Zheng, Y.; Jiao, Y.; Li, L. H.; Xing, T.; Chen, Y.; Jaroniec, M.; Qiao, S. Z. *ACS Nano* **2014**, *8*, 5290–5296.
97. Zheng, Y.; Jiao, Y.; Zhu, Y.; Li, L. H.; Han, Y.; Chen, Y.; Du, A.; Jaroniec, M.; Qiao, S. Z. *Nat. Commun.* **2014**, *5*, 3783.
98. Duan, J.; Chen, S.; Jaroniec, M. Qiao, S. Z. *ACS Nano* **2015**, *9*, 931–940.
99. Ito, Y.; Cong, W.; Fujita, T.; Tang, Z.; Chen, M. *Angew. Chem. Int. Ed.* **2015**, *54*, 2131–2136.

2

CHARACTERIZATION METHODS

2.1. STRUCTURE CHARACTERIZATION

2.1.1. Electron Microscopy

Scanning electron microscopy (SEM) analysis was conducted on a field emission scanning electron microscope (Nanonova 230, FEI) or a Hitachi S-4800 scanning electron microscope operating at 10 kV. High-resolution transmission electron microscopy (HRTEM) images, bright-field (BF), high-angle annular dark-field (HAADF) scanning TEM (STEM) images, and energy dispersive X-ray spectroscopy (EDS) mapping images were taken on a JEOL JEM-2100F field emission electron microscope at an acceleration voltage of 200 kV. Atomic-resolution TEM and STEM images were taken with FEI Titan^3 G2 60-300 with a double Cs corrector at an acceleration voltage of 80 and 200 kV. As an exception, the TEM and HRTEM images displayed in **Figures 6.2–6.4** were taken on a TECNAI G2 20 S-Twin operated at 200 kV and TECNAI G2 F30 operated at 300 kV, respectively. The HAADF-STEM and EDS elemental maps in **Figures 6.2 and 6.3** were acquired with the TECNAI G2 F30 ST.

2.1.2. X-ray Diffraction

X-ray diffraction (XRD) patterns were obtained with a high-power X-ray diffractometer (Rigaku) equipped with Cu K_α radiation, and operated at 40 kV and 200 mA. Low-angle and wide-angle XRD patterns were measured in a 2θ range from 0.5° to 5° and from 10° to 90° with a scan rate of 0.5, and 4° min^{-1}, respectively. XRD patterns were indexed with reference to the Joint Commission for Powder Diffraction Standard (JCPDS).

2.1.3. Nitrogen Sorption

The porous and textural properties of porous materials were examined using a nitrogen sorption analyzer (BEL BELSORP-MAX) at liquid-nitrogen temperatures. The total pore volume was determined at a relative pressure of 0.98–0.99, and the specific surface area was calculated using the Brunauer–Emmett–Teller (BET) equation in a relative pressure range of 0.05–0.2. The pore size was determined from the adsorption branch using the Barrett–Joyner–Halenda (BJH) method.

2.1.4. X-ray Photoelectron Spectroscopy

XPS analysis was conducted with an X-ray photoelectron spectrometer (K-alpha, ThermoScientific) equipped with a monochromatic Al K_α X-ray source (1486.6 eV). The curve fitting of the XPS spectra was performed using XPSpeak41 software. The baseline of the XPS spectra was corrected by the Shirley-type background with a zero slope. Peaks in the XPS spectra were deconvoluted using a Gaussian–Lorentzian mixed function (70% Gaussian and 30% Lorentzian). Full-width-at-half-maximum (FWHM) values for the major peaks were constrained to a specific value. A typical example is shown in **Figure 2.1**. Deconvolution of XPS spectra for the S 2p region show three main doublets with a broad peak. The FWHM values of the three major doublets are constrained to 1.5 eV. For each doublet, the peak area for S $2p_{1/2}$ was set around one-half to two-thirds of that for S $2p_{3/2}$. The broad peaks for sulfate groups appearing around 168 eV are not constrained.

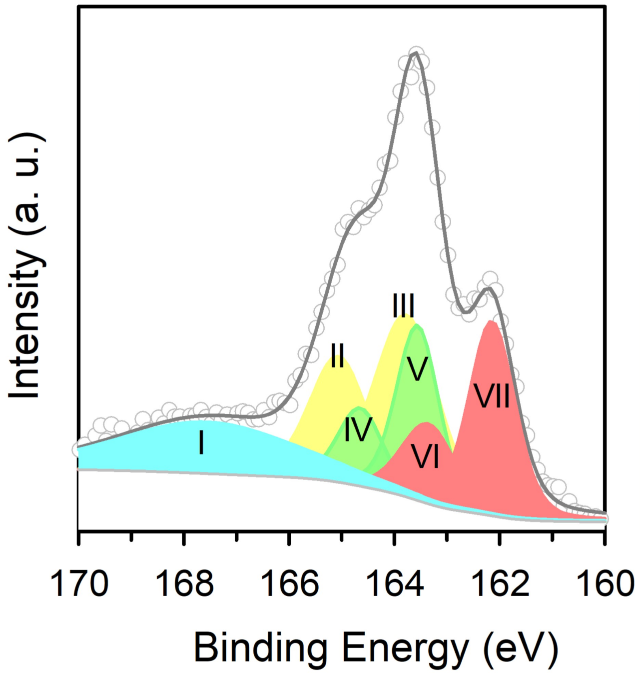

Peak	*Position*	*Area*	*FWHM*
I	167.6	0.54	4.1
II	165.1	0.42	1.3
III	163.8	0.66	1.4
IV	164.6	0.20	1.0
V	163.6	0.43	0.96
VI	163.4	0.24	1.2
VII	162.1	0.51	1.0

Figure 2.1. Typical deconvoluted XPS spectra for the S 2p region with tabulated numerical data for peak position, area, and FWHM.

2.1.5. Raman Spectroscopy

The Raman spectra were obtained using a WITec alpha300R couple with a He-Ne laser of 532 nm at a specific power. The laser power was modulated depending on the catalyst material. For example, as thiomolybdate could be damaged from the laser power, it was set lower than 0.5 mW (Chapter 8).[1,2] In this dissertation, Raman analysis was used to reveal the monolayer features of WS_2 nanoplates (**Figure 4.4b**) and to reveal the electronic structures of MoS_4^{2-} ligands (**Figure 8.3, 8.4 and 8.10**).

2.1.6. X-ray Absorption Spectroscopy

XAS experiments were performed on the Beamline 6D and 10C of the Pohang Accelerator Laboratory (PAL) in South Korea, with a beam energy and current of around 3 GeV and 300 mA, respectively. The beam energy and current were changed depending on the beam condition. X-ray photon energy was monochromatized by a Si(1 1 1) double-crystal monochromator, which was detuned by around 15–30% to remove high-order harmonics. Samples were prepared as pellets using a home-made pelletizer (**Figure 2.2**). As the pellet thickness influences the absorption intensity, the thickness was optimized to yield an edge step of 0.8–1.5. Depending on the catalyst material, the transmittance or fluorescence detection mode was adopted. Background removal and normalization of the XAS spectra was carried out using IFEFFIT (Athena) software. The extended X-ray absorption fine structure (EXAFS) spectra were k^3-weighted and Fourier-transformed to a radial distribution function (RDF) over a k range (generally, 3−14 Å^{-1}), and an R range (generally 1.5−3.4 Å) using a Hanning window. The k and R ranges were modulated depending on the raw data quality for accurate analysis. The RDF was fitted with a known crystal structure, using IFEFFIT (Artemis) software.[3]

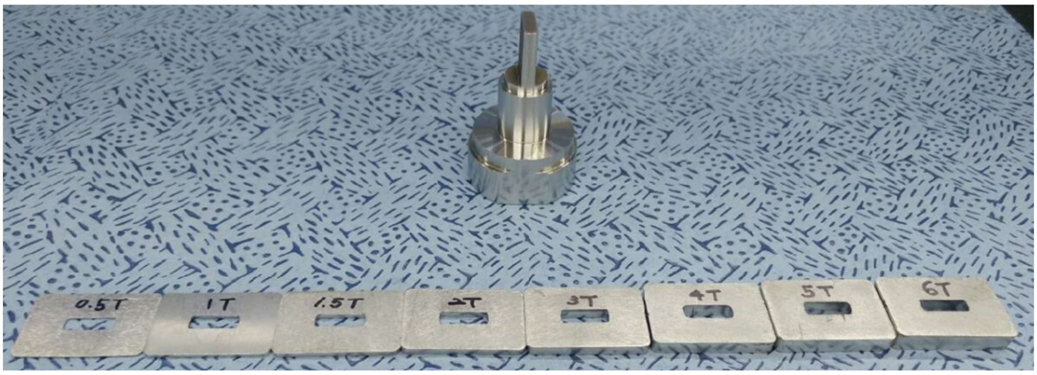

Figure 2.2. Home-made pelletizer set used to make pellet with powder specimen for XAS analysis. The thickness of the sample holder was controlled to optimize the absorption intensity.

2.2. ELECTROCHEMICAL CHARACTERIZATION

2.2.1. Electrochemical Setup

All electrochemical measurements were performed on an IviumStat electrochemical analyzer at room temperature and under atmospheric pressure using a three-electrode electrochemical cell. A graphite rod and Ag/AgCl (in saturated KCl solution) were used as the counter and reference electrodes, respectively. In alkaline media, Hg/HgO was used as the reference electrode. All potentials quoted in this dissertation are presented on the RHE scale. For electrochemical measurement, a rotating ring-disk electrode (RRDE) containing glassy carbon (GC) as the central disk (4-mm diameter, 0.126 cm^2 area) was used as the working electrode (**Figure 2.3**). The RRDE was polished with a 1.0-μm alumina suspension, and then with a 0.3-μm suspension to generate a mirror finish before use. Catalyst inks were prepared by mixing the catalyst with Nafion (5 wt.% in isopropanol and deionized (DI) water (Sigma-Aldrich) in a solution of DI water (18.2 MΩ) and ethanol (EtOH, 99.9%). The mixture was sonicated for 30 min to produce a homogeneous slurry. The catalyst ink was then dropped onto the GC electrode, and dried at 60 °C. The ink composition and drying conditions were different depending on the catalyst materials. Carbon paper (CP) can replace the RRDE for demonstration of relatively large-scale H_2 production (see section 7.2.4).[4]

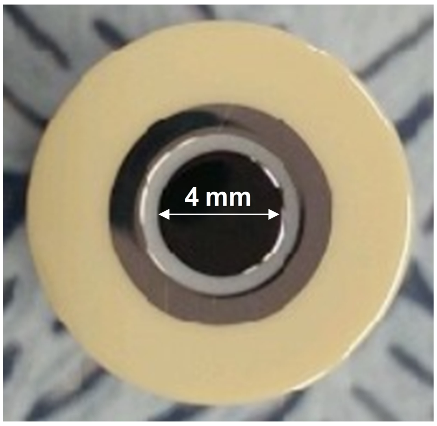

Figure 2.3. An RRDE containing a GC as the central disk (4-mm diameter, 0.126 cm^2 area).

2.2.2. Activity Test for HER Using Linear Sweep Voltammetry

Before electrochemical measurements, 0.5 M H_2SO_4 electrolyte was deaerated by bubbling N_2 for 20 min followed by conducting cyclic voltammetry (CV) for electrochemical cleaning. The cleaning conditions were changed depending on the catalyst materials. For two-dimensional transition metal dichalcogenides (2D TMDs) hybridized with mesoporous carbons, this consisted of 20 repetitions in a potential range between −0.3 and 0.6 V (*vs.* RHE) at a scan rate of 100 mV s^{-1}. For Rh_2S_3 HNPs, the 20 CV repetitions were performed in a potential range between 0.01 and 1.2 V (*vs.* RHE) at a scan rate of 50 mV dec^{-1}. In the case for a benchmark catalyst, 20 wt.% Pt/C (Johnson-Matthey, HiSPEC-3000), electrochemical cleaning was conducted in a potential range between 0.05 V and 1.2 V (*vs.* RHE) at a scan rate of 500 mV s^{-1}, followed by three CVs at a scan rate of 50 mV s^{-1}. Linear sweep voltammetry (LSV) for the hydrogen evolution reaction (HER) was conducted by cathodic potential sweep from 0.1 V to −0.4 V (*vs.* RHE) at a scan rate of 2 mV s^{-1} with a rotating speed of 1500 rpm in N_2 or H_2-purged 0.5 M H_2SO_4. For the CP electrode, rotation was not possible. The LSV of each sample was measured several times, and the average of the data were used for reliability.

2.2.3. Electrochemical Impedance Spectroscopy

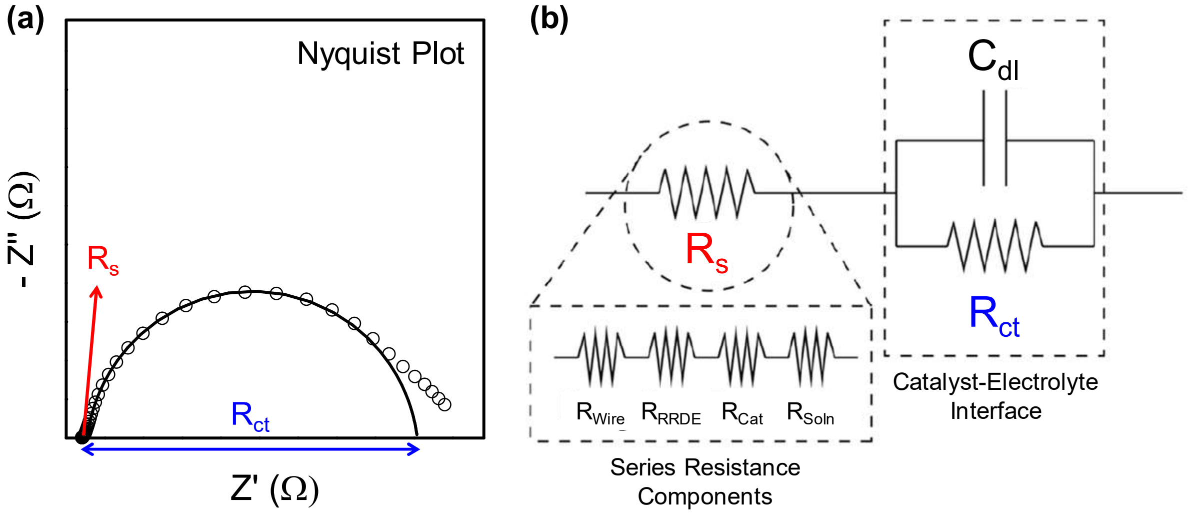

Figure 2.4. (a) A Nyquist plot and (b) simplified Randles equivalent circuit model. R_s, C_{dl}, and R_{ct} represent the series resistance, double layer capacitance, and charge transfer resistance, respectively. R_s is a combination of resistances from electrical wiring, RRDE, catalyst itself, and electrolyte solution. The circuit model was reproduced with permission from ref. 5. Copyright 2011 American Chemical Society.

Electrochemical impedance spectroscopy (EIS) was performed on the same electrochemical system. Nyquist plots were measured in a frequency range of 100 kHz to 0.01 Hz (or 10 kHz to 1 Hz) at an overpotential of 100 mV (**Figure 2.4a**). The resulting impedance spectra were fitted to a simplified equivalent Randles circuit model using Zview software (**Figure 2.4b**). A series resistance

(R_s) arises from a combination of resistance in solution, resistance in the catalysts themselves, and resistance in the glassy carbon substrate, and the charge-transfer resistance (R_{ct}) results from the resistance in the catalyst–electrolyte interface.[6] The LSVs displayed in this dissertation were plotted after compensating the ohmic drops with R_s values unless notified.

2.2.4. Electrochemical Active Surface Area Measurement

The electrochemical active surface area (ECSA) was determined from the double layer capacitance (C_{dl}) of the catalyst surface.[7,8] C_{dl} was determined by measuring CVs with multiple scan rates in the non-faradaic potential region. In this potential region, all measured currents are assumed to be associated with double-layer charging. Typically, CVs were measured in a potential range centered at the open-circuit potential (OCP) with a potential window of 0.1 V at multiple scan rates (**Figure 2.5a**). The measured charging current (i_C) is equal to the product of the scan rate (v) and the C_{dl}, as given by equation **(1)**.

$$i_C = vC_{dl} \cdots\cdots \textbf{(1)}$$

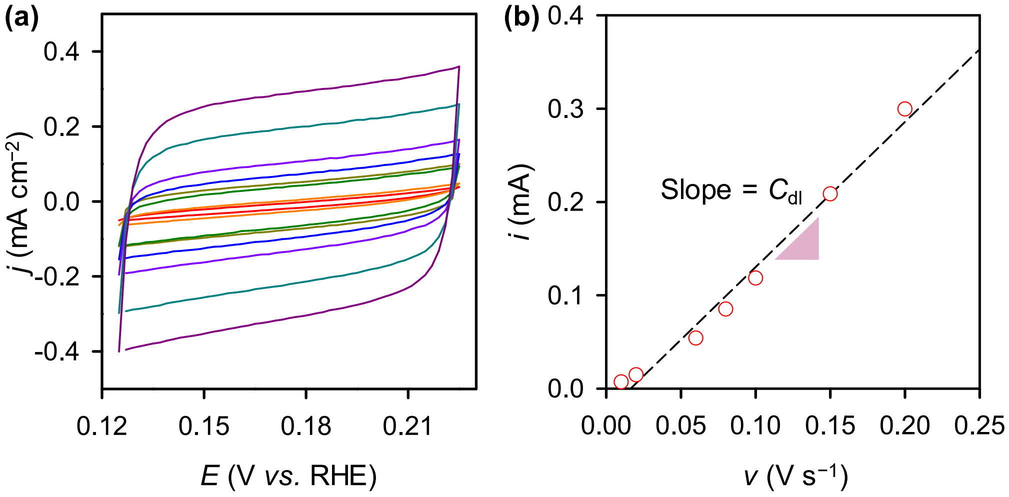

Figure 2.5. (a) Typical CV scans with different scan rates in the non-faradaic regime. (b) Corresponding linear plot for the cathodic current versus scan rate (v, V s^{-1}).

Therefore, the slope was derived from a plot of i_C as a function of v equal to the C_{dl} (**Figure 2.5b**). The ECSA of a catalyst is calculated by dividing C_{dl} with the specific capacitance of the sample according to equation **(2)**.

$$\mathrm{ECSA} = \frac{C_{\mathrm{dl}}}{C_{\mathrm{s}}} \quad \cdots\cdots \ \textbf{(2)}$$

Jaramillo *et al*. suggest general specific capacitances of C_{s} based on reported values.[7]

2.2.5. Electrochemical Durability and Stability Tests

A long-term durability test was conducted by performing consecutive CV measurements between 0.1 and −0.3 V (*vs.* RHE) at a sweep rate of 50 mV s^{-1} with a rotation speed of 1500 rpm. LSV curves were recorded before and after the cycling test. Before measuring the LSV after the cycling test, the electrolyte was replaced with a fresh one. A long-term stability test was performed with chronopotentiommetry measurements exerting a static current of −10 mA cm^{-2}. Structural characterization after the electrochemical durability and stability tests could give information for the structural changes of catalyst materials made during electrolysis (see the examples in **Figures 6.8, 7.5 and 7.6**).

2.3. REFERENCES

1. Huang, Z.; Luo, W.; Ma, L.; Yu, M.; Ren, X.; He, M.; Polen, S.; Click, K.; Garrett, B.; Lu, J.; Amine, K.; Hadad, C.; Chen, W.; Asthagiri, A.; Wu, Y. *Angew. Chem. Int. Ed.* **2015**, *54*, 15181–15185.
2. Tran, P. D.; Tran, T. V.; Orio, M.; Torelli, S.; Truong, Q. D.; Nayuki, K.; Sasaki, Y.; Chiam, S. Y.; Yi, R.; Honma, I.; Barber, J.; Artero, V. *Nat. Mater.* **2016**, *15*, 640–646.
3. Ravel, B.; Newville, M. *J. Synchrotron Radiat.* **2005**, *12*, 537–541.
4. Seo, B.; Baek, D. S.; Sa, Y. J.; Joo, S. H. *CrystEngComm.* **2016**, *18*, 6083–6089.
5. Chen, Z.; Cummins, D.; Reinecke, B. N.; Clark, E.; Sunkara, M. K.; Jaramillo, T. F. *Nano Lett.* **2011**, *11*, 4168–4175.
6. Helveg, S.; Lauritsen, J. V.; Lægsgaard, E.; Stensgaard, I.; Nørskov, J. K.; Clausen, B. S.; Topsøe, H.; Besenbacher, F. *Phys. Rev. Lett.* **2000**, *84*, 951.
7. McCrory, C. C. L.; Jung, S.; Peters, J. C.; Jaramillo, T. F. *J. Am. Chem. Soc.* **2013**, *135*, 16977–16987.
8. McCrory, C. C. L.; Jung, S.; Ferrer, I. M.; Chatman, S. M.; Peters, J. C.; Jaramillo, T. F. *J. Am. Chem. Soc.* **2015**, *137*, 4347–4357.

3

NANOSCALE SIZE EFFECTS OF MOLYBDENUM SULFIDE CATALYSTS FOR THE HYDROGEN EVOLUTION REACTION

This chapter includes the published content: Seo, B.; Jung, G. Y.; Sa, Y. J.; Jeong, H. Y.; Cheon, J. Y.; Lee, J. H.; Kim, H. Y.; Kim, J. C.; Shin, H. S.; Kwak, S. K.; Joo, S. H. *ACS Nano* **2015**, *9*, 3728−3739. Reproduced with permission. Copyright 2015 American Chemical Society.

3.1. INTRODUCTION

Layered two-dimensional (2D) transition metal dichalcogenides (TMDs) have emerged as a promising class of materials owing to their widespread utility in electronics, photonics, energy storage, and catalysis.[1–5] Metal sulfide nanostructures represent a novel class of the 2D TMDs, and constitute a topic of tremendous current interest. Burgeoning research regarding metal sulfide nanostructures primarily stems from their intriguing physicochemical properties such as tunable electronic and optical characteristics as well as their broad applicability as transistors, topological insulators, batteries, and catalysts.[1–5] Notably, metal sulfide-based nanostructured materials have emerged as promising catalysts for the hydrogen evolution reaction (HER), and significant progress has been achieved in enhancing their activity and durability for the HER.[4,6–40]

The understanding of particle size-dependent catalytic activities can suggest critical information regarding catalytic reactivity, providing the scientific basis for the design of advanced catalysts.[41–43] In particular, studies utilizing catalysts below 5 nm, where the structural and electronic properties of nanoparticles exhibit the most drastic changes, can suggest compelling evidence. Hence, particle size effects have been a topic of keen interests during the last several decades, which have consequently led to the identification of molecular factors responsible for the reactivity.[44–48] However, the nanoscale size effects in metal sulfide-based HER catalysts have not yet been established fully, due to the synthetic difficulty in controlling the size of metal sulfide structures on the nanometer scale in the basal and edge plane directions; the anisotropic nature of layered MoS_2 dictates the energetically favorable horizontal growth, thus resulting in sheet or film-like structures.

In this work, MoS_2 nanoplates were prepared with monolayer precision, and their size-dependent catalytic activity trends in the HER was discovered. We prepared MoS_2 nanoplates embedded in ordered mesoporous carbon (MoS_2@OMC) nanostructures using ordered mesoporous silica (OMS) as a template (**Figure 3.1**). In this design, the layer number of the MoS_2 nanoplates could be controlled precisely from one to four layers in a layer-by-layer manner by varying the MoS_2 loading, while the basal plane size was maintained below 5 nm. On the basis of density functional theory (DFT) calculations, the most favorable single-, double-, and triple-layer MoS_2 model structures were identified for the HER, and elementary step energetics of the HER over these three model structures were calculated. The electrochemical and theoretical analyses revealed that the turnover frequency (TOF) of MoS_2 nanoplates in the HER increases in a quasi-linear manner with decreased layer numbers. Cobalt-promoted MoS_2 nanoplates also exhibited similar HER activity trend. The higher HER activity of smaller metal sulfide nanoplates was attributed to the higher degree of oxidation, higher Mo–S coordination number (CN), formation of the 1T phase, and lower activation energy required to overcome transition state. This insight into the nanoscale size-dependent HER activity trend will facilitate the design of advanced HER catalysts as well as other hydrotreating catalysts.

3.2. SYNTHESIS OF CATALYSTS

3.2.1. Synthesis of SBA-15 OMS template

The SBA-15 OMS template was synthesized by the previously reported method,[49,50] with some modifications. 8.00 g of P123 (Sigma-Aldrich), 251.4 g of deionized (DI) water (18.2 MΩ), and 48.6 g of HCl (35%, Samchun) were mixed in a 500-mL polypropylene (PP) bottle, and the solution was stirred at 35 °C until P123 was completely dissolved. 17.0 g of tetraethyl orthosilicate (TEOS, 98%, Sigma-Aldrich) was immediately added to the P123 solution and was stirred for 5 min at 35 °C; the solution was kept at 35 °C overnight without stirring. The slurry was then transferred to a Teflon-lined stainless steel autoclave and aged at 150 °C for 24 h, and subsequently cooled to room temperature (RT). White precipitates were filtered and subsequently washed with DI water, and dried in an oven at 60 °C for 24 h. 250 mL of ethanol (EtOH, 94.5%, Samchun) and 5 g of HCl were mixed with the dried product, and the mixture was stirred for 30 min, followed by filtering and washing with EtOH, and then drying at 60 °C. Finally, the resulting powder was calcined in a box furnace at 550 °C for 5 h.

3.2.2. Synthesis of MS_2@OMC (M=Mo and CoMo)

The general synthetic procedure for MS_2@OMC (M = Mo and CoMo) nanostructures consists of (i) partial filling of mesopores of SBA-15 OMS template with carbon structure, (ii) subsequent formation of metal sulfide nanostructures inside the void spaces of carbon-SBA-15 composites, and (iii) etching of the SBA-15 template (**Figure 3.1**). The preparation of MoS_2@OMC is described as follows. 6.10 g of sucrose (Samchun) was dissolved in 20 g of DI water in a PP bottle, and 0.69 g of H_2SO_4 (95%, Samchun) was added to the solution. Then, 4.0 g of SBA-15 was added to the sucrose solution, and the mixture was gently agitated to make a homogeneous paste. This paste was heated to 100 °C and maintained at this temperature for 6 h, then was subsequently kept at 160 °C for 2 h under air. The brownish product was then carbonized at 400 °C for 4 h, and at 900 °C for 2 h under N_2 gas at a flow rate of 1 L min^{-1}. To the resulting carbon-SBA-15 composite, the molybdenum precursor was impregnated and sulfided to generate MoS_2–carbon–silica composites. A specific amount (0.056, 0.11, 0.22, 0.45, 0.66, or 1.11 g) of phosphomolybdic acid hydrate (PMA, Sigma-Aldrich) was dissolved in 5 g of absolute EtOH, and 1.15 g of the as-synthesized carbon-SBA-15 composite was added to the solution. The mixture was stirred at 35 °C to evaporate the solvent, and finely ground in an agate mortar. The resulting powder was sulfided by raising the temperature to 600 °C at a heating rate of 2 °C min^{-1} and maintained at 600 °C for 5 h under 10% H_2S (balanced with Ar) gas at a flow rate of 200 mL min^{-1}. After sulfidation, the furnace was cooled to RT under N_2 gas flow. Finally, in order to etch the SBA-15 OMS template, the MoS_2–carbon–silica composite was mixed with 1:1=EtOH:10 wt.% HF solution (J. T. Baker), stirred for 30 min, filtered, and washed with EtOH. The etching process was repeated once, and the product was dried. The nominal loadings of MoS_2, based on the quantities of PMA precursor listed above, were 5, 10, 15, and 20 wt.%. The synthesis of cobalt-doped $CoMoS_2$@OMC nanostructures was carried out in the same manner as MoS_2@OMC, but with a mixture of cobalt and molybdenum precursors. Specified amounts of cobalt(II) nitrate hexahydrate ($Co(NO_3)_2{\cdot}6H_2O$, Sigma-Aldrich) and PMA at a fixed molar ratio of Co:Mo=1:3 were used.

3.2.3. Synthesis of Mesoporous MoS_2

The ordered mesoporous material, composed of molybdenum disulfides (Meso-MoS_2), was prepared using SBA-15 OMS as a template, following the previously reported method.[51] First, 2 g of PMA was dissolved in 7.5 mL of absolute EtOH. Then, 0.5 g of SBA-15 was added to the solution. The mixture was stirred at 35 °C to evaporate the EtOH. The dried powder was sulfided by gradually heating to 600 °C at a heating rate of 2 °C min^{-1}, and was then maintained at each set temperature for 5 h under 10% H_2S (balanced with Ar) gas at a flow rate of 200 mL min^{-1}. Finally, the SBA-15 OMS template was etched with HF solution in the same manner as above. It was confirmed that 72 wt.% of the PMA was converted to MoS_2. This percent yield for the MoS_2 product was used as a basis for calculating the amount of precursor for the preparation of metal disulfide nanoplates embedded in the ordered mesoporous carbons, which is described in detail above.

3.2.4. Synthesis of Sulfur-Doped OMC

For comparative purposes, sulfur-doped OMC (S-OMC) was also prepared by synthesizing CMK-3 mesoporous carbon,[52] followed by sulfidation. 5.5 g of sucrose was dissolved in 20 g of DI water in a PP bottle, and 0.62 g of H_2SO_4 was added to the solution. Then, 4.0 g of SBA-15 was added to this solution, and a homogeneous paste was formed. The paste was then heated at 100 °C for 6 h, and subsequently heated at 160 °C for 2 h under air. The brownish composite was impregnated again with the solution comprising 3.3 g of sucrose, 20 g of DI water, and 0.37 g of H_2SO_4. The mixture was then heated to 100 °C then 160 °C under air, in the same manner as above. The brownish product was subsequently carbonized at 400 °C for 4 h, and continuously heated at 900 °C for 2 h under N_2 at a flow rate of 1 L min^{-1}. The OMC was obtained by etching the silica template, which entailed two consecutive 30-min washings with HF solution. Finally, the resulting OMC was sulfided at 600 °C to produce S-OMC, using the same sulfidation scheme as with the MS_2@OMC nanostructures.

3.3. COMPUTATIONAL DETAILS

3.3.1. Turnover Frequency Calculations

The turnover frequency (TOF) (s^{-1}), defined as the HER rate per active site and per time, was derived from the following equation **(1)**.

$$\mathrm{TOF}(\mathrm{s}^{-1}) = \left\{ j(\mathrm{A\,cm^{-2}}) \times S(\mathrm{cm^{2}}) \times \frac{1\mathrm{H_2}}{2\mathrm{e^-}} \times \frac{1\mathrm{e^-}}{q_\mathrm{e}} \right\} \div N_{active} \quad \cdots\cdots \ \textbf{(1)}$$

Here, the current density (*j*) was derived from the current generated during HER, *S* is the geometric surface area of working electrode (0.126 cm^2 in our case), and q_e is the electron charge of 1.602×10^{-19} C. N_{active} is the number of Mo atoms at the Mo-edges, which were assumed as active sites. For counting N_{active}, we suggest two possible geometric models based on Gibbs free energy (**Figure 3.8a**) and binding energy (**Figure 3.10a**) calculations. Complying with the geometric models, N_{active} was obtained by the following equation:

$$N_{active} = \left\{ \frac{m \times S(\mathrm{cm^{2}}) \times (\mathrm{wt\%\ of\ MoS_2}) \times N_\mathrm{A}}{MW \text{ of } \mathrm{MoS_2}} \right\} \times F_{active} \quad \cdots\cdots \ \textbf{(2)}$$

Here, *m* is the loading of catalyst on the electrode. In our case, 300 µg cm^{-2} of catalyst was deposited on the GC. The wt.% of MoS_2 was estimated by inductively coupled plasma optical emission spectrometry (ICP-OES) analysis, as summarized in **Table 3.1**. F_{active} is the fraction of active sites versus total Mo atoms in a MoS_2 sheet. The F_{active} was calculated by the following equation:

$$F_{active} = \frac{n_{Mo}}{n_{Mo,total}} \quad \cdots\cdots \textbf{(3)}$$

Here, n_{Mo} and $n_{Mo,total}$ are the number of Mo atoms at the Mo-edges (50% S) and the total Mo atoms in a MoS_2 sheet, respectively. The n_{Mo} and $n_{Mo,total}$ were obtained using the crystallite sizes for the (002) plane determined from transmission electron microscopy (TEM) analysis (**Table 3.2**). These crystallite sizes correspond to the diagonal length of the basal plane. The number of S atoms in the diagonal line was readily obtained by dividing this length with the S–S bond length, which is 0.315 nm.[53] From that, the number of S atoms in one edge (equal to half of the number of S atoms in the diagonal line) in a MoS_2 sheet was obtained, which was designated as a in the following equations and used to calculate the n_{Mo}, $n_{Mo,total}$ and F_{active} as follows.

$$n_{Mo} = 3a \cdots\cdots \textbf{(4)}$$

$$n_{Mo,total} = 3a + 3(a-1)^2 + 3(a-1) \cdots\cdots \textbf{(5)}$$

$$F_{active} = \frac{n_{Mo}}{n_{Mo,total}} = \frac{3a}{3a + 3(a-1)^2 + 3(a-1)} \quad \cdots\cdots \textbf{(6)}$$

Equation **(6)** was based on the structural models, which were generated using DFT calculations of the Gibbs free energy and the binding energy of hydrogen on the MoS_2. The resulting fraction was integrated into equation **(2)**, thus affording the number of active sites (N_{active}) of each sample. Finally, the TOFs were calculated by inserting the result into the equation **(1)**.

The TOFs for the HER were also calculated in an alternative way assuming S atoms on the Mo-edges as the active sites, as the HER is initiated by the adsorption of H atoms on such unsaturated S atoms. In this case, the equations for N_{active} and F_{active} were modified as follows.

$$N_{active} = \left\{ \frac{m \times S(\text{cm}^2) \times (\text{wt\% of MoS}_2) \times N_A}{MW \text{ of MoS}_2} \times 2 \right\} \times F_{active} \quad \cdots\cdots \textbf{(7)}$$

$$F_{active} = \frac{n_{S,H-adsorb}}{n_{S,total}} \quad \cdots\cdots \textbf{(8)}$$

Here, $n_{S,H-adsorb}$ and $n_{S,total}$ are the number of S atoms at the Mo-edges and the total S atoms in a MoS_2 sheet, respectively. The $n_{S,H-adsorb}$ and $n_{S,total}$ can be determined by the following equations.

$$n_{S,H-adsorb} = 3a - 3 \cdots\cdots \textbf{(9)}$$

$$F_{active} = \frac{n_{S,H-adsorb}}{n_{S,total}} = \frac{3a-3}{7.5a + 6(a-1)^2 + 6(a-1)} \quad \cdots\cdots \textbf{(10)}$$

$$F_{active} = \frac{n_{S,H-adsorb}}{n_{S,total}} = \frac{3a-3}{9a-3+6(a-1)^2+6(a-1)} \cdots\cdots \textbf{(11)}$$

Equation **(10)** and **(11)** were based on the structural models, which were generated using DFT calculations of the Gibbs free energy and the binding energy of hydrogen on the MoS_2, respectively. The resulting fraction was integrated into equation **(8)**, thus affording the number of active sites (N_{active}) of each sample using equation **(7)**. Finally, the TOFs were calculated by inserting the result into the equation **(1)**.

The third method for TOF calculations assumed that the S atoms in both the Mo- and S-edges were involved in the HER, as the S-edges can also be involved in the HER. In this case, the calculations for $n_{S,H\text{–}adsorb}$ and F_{active} were modified as follows.

$$n_{S,H-adsorb} = 6a-3 \cdots\cdots \textbf{(12)}$$

$$F_{active} = \frac{n_{S,H-adsorb}}{n_{S,total}} = \frac{6a-3}{7.5a-3+6(a-1)^2+6(a-1)} \cdots\cdots \textbf{(13)}$$

$$F_{active} = \frac{n_{S,H-adsorb}}{n_{S,total}} = \frac{6a-3}{9a-3+6(a-1)^2+6(a-1)} \cdots\cdots \textbf{(14)}$$

Equation **(13)** and **(14)** were based on the structural models, which were generated using DFT calculations of the Gibbs free energy and the binding energy of hydrogen on the MoS_2, respectively. The resulting fraction was integrated into equation **(8)**, thus affording the number of active sites (N_{active}) of each sample using equation **(7)**. Finally, the TOFs were calculated by inserting the result into the equation **(1)**.

3.3.2. Computation Methods

We used DFT calculation using DMol^3,[54,55] under the generalized gradient approximation (GGA) with the Perdew–Burke–Ernzerhof (PBE) functional.[56] The semi-empirical DFT-D method for dispersion correction[57] was included to accommodate van der Waals (vdW) interactions in the multi-layer structure. Unrestricted spin-polarized calculations were performed with the Brillouin-zone integration of a 4 × 1 × 1 Monkhorst-Pack k-point grid[58] and basis set of DNP 4.4. The convergence criteria for the geometry optimization were 2.0×10^{-5} Ha for energy, 0.004 Ha/Å for force, and 0.005 Å for displacement. The self-consistent field convergence was less than 1.0×10^{-5} Ha and the electron smearing value was set to 0.005 Ha. The relativistic effect of all electrons on core electrons was also included in our DFT calculation. To dissect the HER process on the MoS_2 layers, the detailed elementary step energetics for the hydrogen adsorption and the desorption (Heyrovsky reaction) processes of H_2 were calculated: the first by energy calculation and the second by estimating the reaction path.

3.3.3. Energy Calculations

The hydrogen adsorption process was studied in terms of both the binding energy (ΔE_{H}) and the change of Gibbs free energy ($\Delta G_{\mathrm{H}}^{0}$), which predict the structural stability of H adsorbed on MoS_2 and probabilities of adsorption and desorption of hydrogen, respectively. The binding energy, which represents the adsorption energy of hydrogen, is calculated by

$$\Delta E_{H} = E_{\mathrm{MoS_2+nH}} - E_{\mathrm{MoS_2+(n-1)H}} - \frac{1}{2} E_{H_2} \quad \cdots\cdots \textbf{(15)}$$

where n is the number of hydrogens; $E_{\mathrm{MoS_2+nH}}$ is the total electronic energy of the nH-MoS_2 system, with n hydrogens adsorbed on an optimized MoS_2; $E_{\mathrm{MoS_2+(n-1)H}}$ is the total electronic energy of the (n−1)H-MoS_2 system, with (n−1) hydrogens adsorbed on an optimized MoS_2; and E_{H_2} is the electronic energy of a hydrogen molecule. The adsorption for hydrogen here is chemisorption, which is assumed only to occur on the edges because of energetically unfavorable adsorption on the basal plane. For $\Delta G_{\mathrm{H}}^{0}$, a prior study[11] used a uniform energy value as a sum of the zero-point energy and the half value of the entropy of a gaseous H_2 at the standard condition (^{0}), regardless of sulfur coverage. It is assumed that the change of the vibrational frequency as a function of sulfur coverage is negligible in their treatment. However, we have calculated the enthalpy and entropy of the reaction of a hydrogen with MoS_2 at 298 K, with varying sulfur coverage, to precisely predict the adsorption and desorption of hydrogen. The formalism is expressed as follows,

$$\Delta G_{\mathrm{H}}^{0} = \Delta H_{\mathrm{H}}^{0} - T\Delta S_{\mathrm{H}}^{0} \quad \cdots\cdots \textbf{(16)}$$

where $\Delta H_{\mathrm{H}}^{0}$ and $\Delta S_{\mathrm{H}}^{0}$ are the changes of enthalpy and entropy in the adsorption process, respectively, at T = 298 K. The notion and derivation of Equation **(16)** are presented in detail below, and $\Delta G_{\mathrm{H}}^{0}$ can be expanded as

$$\Delta G_{\mathrm{H}}^{0} = H_2^0 - H_1^0 - T(S_2^0 - S_1^0)$$

$$= (U_2 + P_2 V_2) - (U_1 + P_1 V_1) - T(S_2^0 - S_1^0) \quad \cdots\cdots \textbf{(17)}$$

where U is molar internal energy, P is pressure, V is molar volume, and the subscripts 1 and 2 represent pre- and post-adsorptions of hydrogen, respectively. By introducing motional degrees of freedom (i.e. vibration, rotation, and translation) and ΔE_H, equation **(17)** can be rewritten as follows,

$$\Delta G_{\mathrm{H}}^{0} = \Delta E_{\mathrm{H}} + U_2^{'} - U_1^{'} - P_1 V_1 - T(S_2^0 - S_1^0) \quad \cdots\cdots \textbf{(18)}$$

where $U_2^{'} = E_{2,vib}$, $U_1^{'} = E_{1,vib} + E_{1,trans}$, $\mathrm{S}_2^0 = \mathrm{S}_{2,vib}^0$, $\mathrm{S}_1^0 = \mathrm{S}_{1,vib}^0 + \mathrm{S}_{1,trans}^0$, and $P_1 V_1 = RT$ (where R is the ideal gas constant). Note that the following thermodynamic values are neglected: $E_{2,trans}$, $E_{2,rot}$, and $S_{2,trans}^0$, $S_{2,rot}^0$ of adsorbed H atoms on MoS_2; $E_{1,trans}$, $E_{1,rot}$, and $S_{1,trans}^0$ of MoS_2; $E_{1,rot}$, $E_{1,vib}$, and $S_{1,vib}^0$ of H; and P_2. With the assumption of ideal H atoms, the translation energy and entropy can be obtained by

$$E_{trans} = \frac{3}{2}RT \quad \cdots\cdots \textbf{(19)}$$

$$S_{trans} = \frac{5}{2}R\ln T + \frac{3}{2}R\ln M_w - R\ln P - 2.31482 \quad \cdots\cdots \textbf{(20)}$$

where M_{w} is molecular weight.[59] By using Equation **(18)**, the enthalpy and entropy contribution in hydrogen adsorption at 298 K has been calculated, and it was observed that $\Delta G_{\mathrm{H}}^{0}$ without adsorption energy showed differences of around 0.36–0.49 eV for the systems of interest, unlike the uniform value of 0.29 eV found in previous work.[11]

3.3.4. Estimation of an Energy Diagram and Reaction Coordinates

The desorption (Heyrovsky reaction) process of H_2 was studied with the edge configurations of Mo-edge(50% S) and S-edge(75% S) in 1L, 2L, and 3L models, with adsorbed hydrogen(s). To study the effect of the energetics of the desorption process depending on hydrogen coverage, 1L, 2L, 3L with Mo-edge(50%S), where one or two hydrogen(s) are attached at the edge site, was used. The implicit water environment is applied at the model system by conductor-like screening model (COSMO) calculation.[60] The reaction path was investigated by linear and quadratic synchronous transit (LST/QST) methods, combined with the conjugated gradient (CG) refinement.[61] The former was used to approximate the transition state and the latter was iteratively applied where the position of hydrogen was adjusted so that the minimum-energy structure emerged at a stationary point for each reaction coordinate.

3.4. RESULTS AND DISCUSSION

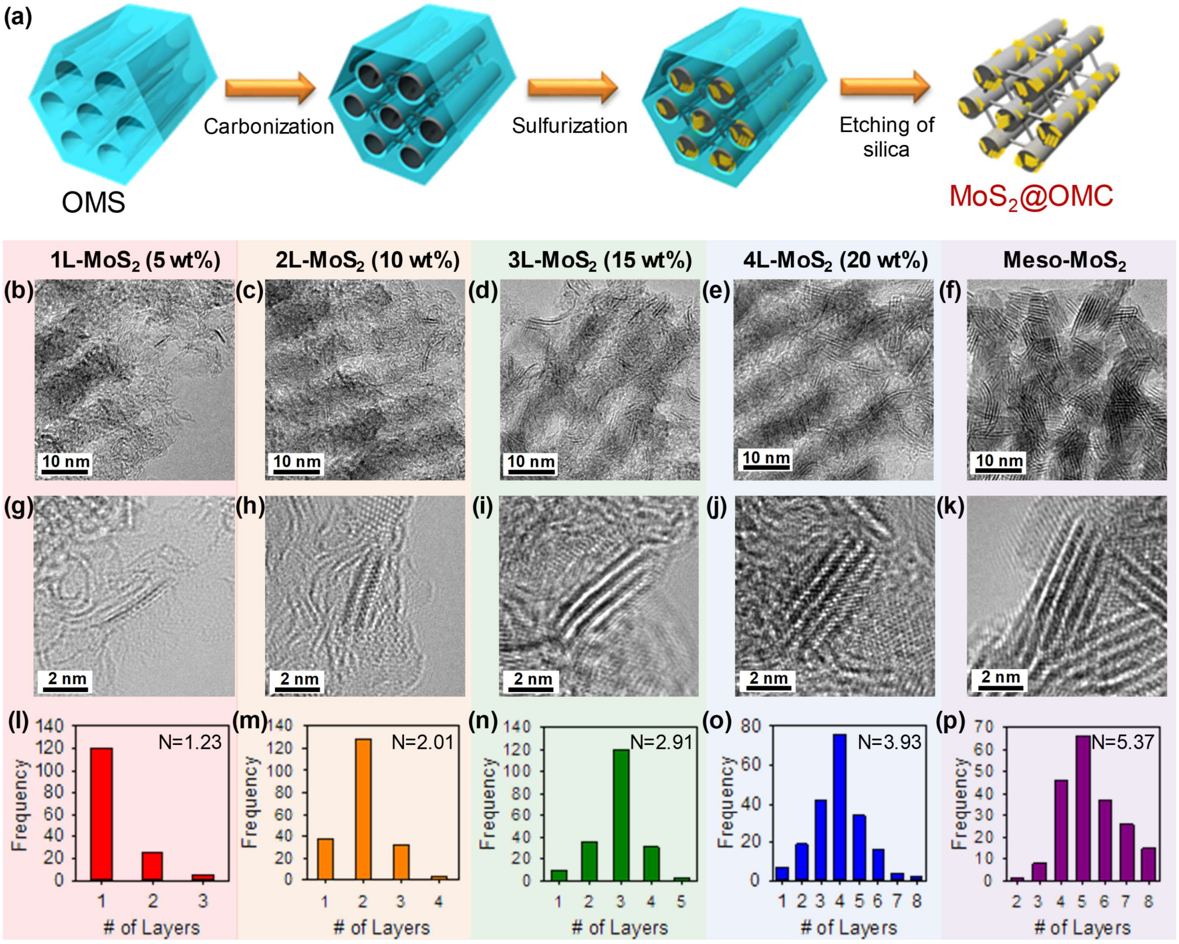

Figure 3.1. (a) Schematic illustration for preparation of MoS_2@OMC. (b–f) TEM images of (b) 1L-MoS_2@OMC, (c) 2L-MoS_2@OMC, (d) 3L-MoS_2@OMC, (e) 4L-MoS_2@OMC, and (f) Meso-MoS_2. (g–k) Corresponding AR-TEM images and (l–p) histograms for layer number distribution. The average layer number of MoS_2 nanoplates is denoted as 'N' in (l–p).

Figure 3.1a shows a schematic illustration for preparation of MoS_2@OMC nanostructures. The first step involved partial filling of the pores of the OMS template with carbon nanostructures, which was carried out *via* a similar method to that used in the synthesis of CMK-3 mesoporous carbon,[52] except for the decreased amount of the carbon source. The silica–carbon composite was then impregnated with a molybdenum precursor, followed by drying and sulfidation using H_2S gas. The etching of silica from the silica–carbon–MoS_2 ternary composite afforded the MoS_2@OMC nanostructures. On the basis of previous reports for the preparation of mesoporous MoS_2 (Meso-MoS_2),[51,62] the sulfidation temperature was set at 600 °C for the preparation of MoS_2@OMC nanostructures. The detailed synthetic procedure for the MoS_2@OMCs is described in section 3.2.

Table 3.1. Contents of metals and MoS_2 in MoS_2@OMC and $CoMoS_2$@OMC nanostructures, determined by ICP-OES analysis.

Sample	Co (wt.%)	Mo (wt.%) [a]	MoS_2 (wt.%) [b]
1L-MoS_2@OMC	-	2.66	4.43
2L-MoS_2@OMC	-	6.71	11.2
3L-MoS_2@OMC	-	9.11	15.2
4L-MoS_2@OMC	-	12.7	21.2
2.5L-$CoMoS_2$@OMC	0.45	6.95	11.6
3.5L-$CoMoS_2$@OMC	0.98	12.1	20.2

[a] The contents of Mo were obtained by averaging four ICP-OES results.
[b] The contents of MoS_2 were calculated by assuming that all Mo exist in the form of MoS_2.

Table 3.2. Crystallite sizes in the (100) and (002) directions, and number of MoS_2 layers in the MoS_2@OMC, Meso-MoS_2 and $CoMoS_2$@OMC nanostructures, determined by TEM images.

Sample	Crystallite size in (100) direction [a]	Crystallite size in (002) direction [a]	Number of layers [a]
1L-MoS_2@OMC	3.85	0.80	1.23
2L-MoS_2@OMC	4.49	1.27	2.01
3L-MoS_2@OMC	4.22	1.86	2.91
4L-MoS_2@OMC	4.36	2.50	3.93
Meso-MoS_2	5.12	3.45	5.37
2.5L-$CoMoS_2$@OMC	4.01	1.55	2.45
3.5L-$CoMoS_2$@OMC	4.27	2.24	3.51

[a] Crystallite sizes and number of layers were measured on the particles in TEM images. The values were obtained by averaging the measured sizes over one hundred of particles.

The nominal content of MoS_2 was controlled from 5 to 20 wt.%, ICP-OES analysis indicated successful incorporation of the desired amount of the MoS_2 (**Table 3.1**). TEM images of the MoS_2@OMCs (**Figure 3.1b–e**) showed that the MoS_2 nanoplates were successfully embedded and uniformly distributed within the carbon nanorod arrays. From the TEM images, it can be seen that the layer number (or edge plane size) of the MoS_2 nanoplates increased with increasing MoS_2 content, while the basal plane size remains below 5 nm regardless of the MoS_2 content (**Table 3.2**). Significantly, atomic resolution TEM (AR-TEM) image (**Figure 3.1g**) and layer number distribution

(**Figure 3.1l**) showed that the lowest MoS_2 loading (5 wt.%) sample consisted mostly of monolayer MoS_2 nanoplates (the calculated average layer number (N) was 1.2). The increase in the MoS_2 content to 10, 15, and 20 wt.% in the MoS_2@OMC nanostructures led to layer number growth while preserving the basal plane size, leading to the formation of 2.0, 2.9, and 3.9 layers MoS_2 nanoplates (**Figure 3.1h–j** for AR-TEM images and **Figure 3.1m–o** for layer number distributions). Hereafter, these materials are denoted as 1L-, 2L-, 3L-, and 4L-MoS_2@OMCs according to the MoS_2 layer number. From the TEM observations, it was found that at the initial stage, MoS_2 growth preferentially occurred in the thermodynamically favorable basal plane direction, which was limited by the confined nanopore space of the silica–carbon composite; with increased MoS_2 loading, the crystal growth took place *via* the layer-by-layer stacking of MoS_2 layers, leading to a gradual increase in the layer number. The average crystallite size of the basal and edge planes of MoS_2 nanoplates and their layer numbers, determined using TEM images, are summarized in **Table 3.2**. Notably, in the AR-TEM images of the MoS_2@OMC nanostructures (**Figure 3.1h–j**), the interlayer spacing of the (002) planes of MoS_2 was 0.64 nm, which was slightly larger than that of bulk MoS_2 (0.61 nm).[63] The extended spacing could result from the curvatures and distortions of the (002) planes induced by the confined growth of the MoS_2 nanoplates within the limited pore space of silica–carbon composite. In addition, the TEM characterization of Meso-MoS_2 (**Figure 3.1f,k,p**) revealed that it was composed of 5.4 layer nanoplates. Overall, we demonstrated the preparation of discrete size MoS_2 nanoplates with monolayer precision, which featured a high percentage of catalytically active edge sites and a distorted (002) plane.

The structures of MoS_2@OMC were further characterized by X-ray diffraction (XRD) and nitrogen adsorption analyses. The high-angle XRD patterns of the MoS_2@OMCs (**Figure 3.2a**) were commensurate with that of the hexagonal MoS_2 standard (JCPDS No. 75-1539). The edge plane direction (002) diffraction peak at $2\theta = 14.1°$ became sharper as the layer number increased. It is noteworthy that 1L- and 2L-MoS_2@OMCs exhibited featureless (002) diffraction peaks, indicating formation of nearly single layer MoS_2. The XRD patterns were in good agreement with the TEM observations. The small-angle XRD patterns of the MoS_2@OMCs (**Figure 3.2b**) exhibited distinct XRD peaks below 2°, indicating a periodic mesostructure. The porous structure of the MoS_2@OMCs was analyzed by nitrogen adsorption–desorption isotherms (**Figure 3.2c,d**). The MoS_2@OMCs have uniform mesopores, large Brunauer–Emmett–Teller (BET) surface areas (as high as 1090 $m^2\ g^{-1}$), and large pore volumes (**Table 3.3**). As expected, the increase in MoS_2 content in MoS_2@OMCs resulted in a decrease in BET surface area and pore volume.

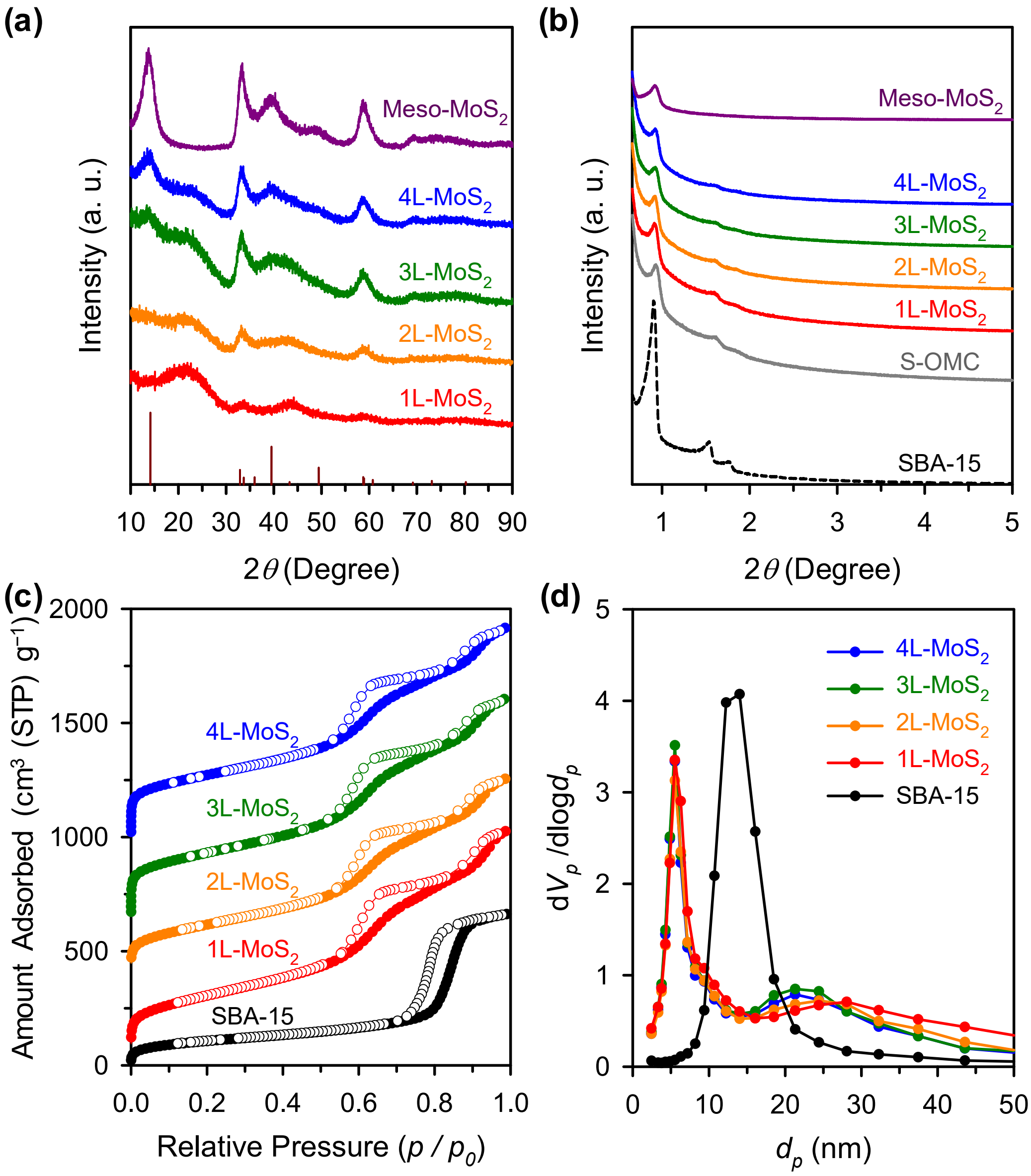

Figure 3.2. (a) Wide-angle XRD patterns with reference pattern for 2H MoS_2 crystal structure (JCPDS No. 75-1539) displayed as vertical bars. (b) Small-angle XRD patterns of SBA-15, S-OMC, MoS_2@OMCs and Meso-MoS_2. (c) Nitrogen adsorption–desorption isotherms of SBA-15 and MoS_2@OMCs. Filled circles and empty circles represent adsorption and desorption branches, respectively. The isotherms of the 2L-, 3L-, and 4L-MoS_2@OMC were offset by 350, 650, and 1000 cm^3 g^{-1}, respectively, for clarity. (d) BJH pore size distributions obtained from the adsorption branches of their isotherms.

Table 3.3. BET surface areas, total pore volumes, and pore sizes obtained from nitrogen adsorption–desorption analysis.

Sample	BET surface area [a] ($m^2\ g^{-1}$)	Pore volume [b] ($cm^3\ g^{-1}$)	Pore size [c] (nm)
SBA-15	388	1.02	14
1L-MoS_2@OMC	1089	1.59	5.5, 28.1
2L-MoS_2@OMC	951	1.40	5.5, 24.4
3L-MoS_2@OMC	1004	1.48	5.5, 21.3
4L-MoS_2@OMC	972	1.42	5.5, 21.3
Meso-MoS_2	105	0.19	6.3
S-OMC	1192	1.79	5.5, 24.4
2.5L-$CoMoS_2$@OMC	1092	1.63	5.5, 18.5
3.5L-$CoMoS_2$@OMC	1052	1.42	5.5, 18.5

[a] BET surface area was obtained in the relative pressure range of 0.05–0.2.
[b] Pore volume was determined at the relative pressure of 0.98–0.99.
[c] Pore size was obtained by using BJH method from the adsorption branch.

The local coordination environment of MoS_2 in MoS_2@OMCs was scrutinized by extended X-ray absorption fine structure (EXAFS) analysis. The Fourier transformed k^3-weighted Mo K-edge EXAFS spectra (**Figure 3.3a and Table 3.4**) exhibited two main peaks at 1.96 and 2.81 Å, which correspond to Mo–S and Mo–Mo bonds, respectively. With decreased layer numbers in MoS_2, the peak intensity for Mo–S bond relative to that for Mo–Mo bond increased, thus resulting in increased the CN ratio of Mo–S to Mo–Mo (N_s/N_{Mo}) (**Figure 3.3b**). The electronic structures of the samples were accessed with X-ray photoelectron spectroscopy (XPS) analysis (**Figure 3.3c,d**). In the Mo 3d XPS spectra (**Figure 3.3c**), the peaks at 229.3–229.4 eV (Mo $3d_{5/2}$) and 232.4–233.0 eV (Mo $3d_{3/2}$) (shown in blue) were mainly observed, which are consistent with the oxidation state of Mo^{4+}.[31] The two doublets at higher binding energies, corresponding to Mo^{5+} (red) and Mo^{6+} (purple) oxidation states were also observed. The oxide species appear to be generated during HF etching of silica and subsequent exposure to air.[31] The slight surface oxidation can contribute to formation of pits, exposing more edge sites, which is known to be advantageous for HER catalysis.[52] The oxide peaks gradually intensified as the MoS_2 layer number decreased, presumably due to the more surface oxidation in the smaller MoS_2 nanoplates. Notably, the intensity of the doublet peaks around 228.3 and 231.4 eV increased with decrease in the layer number suggesting the evolution of structurally distorted 1T phase MoS_2.[39,40] In the deconvoluted spectra of the S 2p region (**Figure 3.3d**), the bulk MoS_2 and

Meso-MoS_2 samples showed main peaks at 162.1–162.3 eV (S $2p_{3/2}$) and 163.3–163.5 eV (S $2p_{1/2}$) that correspond to the S^{2-} species.[21] For the MoS_2@OMC nanostructures, the peaks for S_2^{2-} ligands at higher binding energies (163.9–164.1 eV and 164.9–165.2 eV for S $2p_{3/2}$ and S $2p_{1/2}$, respectively) progressively evolved as the MoS_2 layer numbers decreased, at the expense of S^{2-} species. The gradual increase of the S_2^{2-} peak indicates an increase in the number of bridging S_2^{2-} sites correlated with the active sites.[35,64] Moreover, a peak corresponding to sulfuric oxide (SO_x) species are the strongest in 1L-MoS_2@OMC among the MoS_2@OMC nanostructures, indicating the most oxidized state. Overall, EXAFS and XPS suggested the increased N_s/N_{Mo}, increased number of S_2^{2-} sites, and enhanced surface oxidation with decreased layer numbers in MoS_2 nanoplates.

Table 3.4. Fitting parameters obtained by EXAFS analysis. [a]

Sample	**Pair**	**Distance (Å)**	**Coordination number (CN)**	**Debye-Waller factor (σ^2) (10^{-3} Å^2)**	**ΔE_0 (eV)**	**N_s/N_{Mo} [b]**
1L-MoS_2@OMC	Mo–S Mo–Mo	2.41 3.16	5.71 3.93	4.1 4.2	2.08	1.45
2L-MoS_2@OMC	Mo–S Mo–Mo	2.41 3.16	5.82 4.44	3.8 4.3	1.24	1.31
3L-MoS_2@OMC	Mo–S Mo–Mo	2.41 3.16	5.81 4.36	3.7 4.0	1.43	1.33
4L-MoS_2@OMC	Mo–S Mo–Mo	2.41 3.17	5.83 4.53	3.6 4.0	1.37	1.29
Meso-MoS_2	Mo–S Mo–Mo	2.41 3.16	5.64 4.42	3.6 4.0	1.57	1.28
Bulk-MoS_2	Mo–S Mo–Mo	2.41 3.17	6.05 6.41	3.3 3.5	2.17	0.94
2.5L-$CoMoS_2$@OMC	Mo–S Mo–Mo	2.40 3.16	5.30 4.29	3.4 4.4	0.33	1.24
3.5L-$CoMoS_2$@OMC	Mo–S Mo–Mo	2.41 3.17	5.57 4.69	3.3 4.3	1.02	1.19

[a] Uncertainties in fitting parameters: < ± 0.003 Å for distance, < ± 8% for CN, < ± 0.5×10^{-3} Å^2 for σ^2 for undoped MoS_2@OMCs; < ± 0.005 Å for distance, < ± 20% for CN, < ± 0.9×10^{-3} Å^2 for σ^2 for Co-doped MoS_2@OMCs.

[b] N_s: CN of Mo–S, N_{Mo}: CN of Mo–Mo.

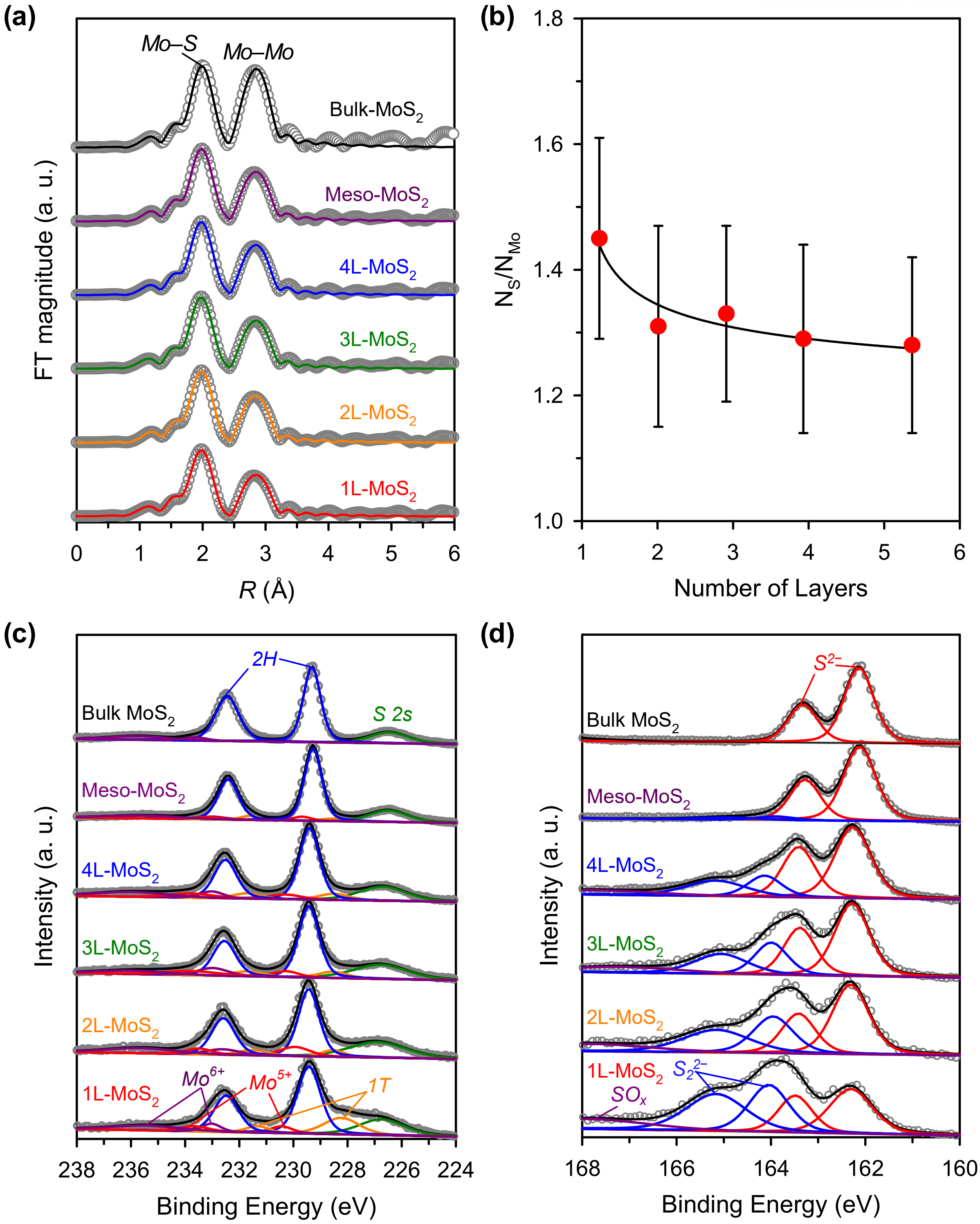

Figure 3.3. (a) Mo K-edge EXAFS fitting spectra. (b) N_S/N_{Mo} ratio of MoS_2@OMCs with respect to number of layers (N_S: CN of Mo–S, N_{Mo}: CN of Mo–Mo, obtained from EXAFS analysis). XPS spectra for (c) Mo 3d and S 2s, and (d) S 2p regions.

We theoretically explored the Gibbs free energy of hydrogen adsorption on MoS_2 structures in vacuum condition by DFT calculations. This calculation was designed to estimate appropriate coverage of sulfur on Mo- and S-edges. Importantly, we investigated single- and double-layer MoS_2 structures,[12,65] as well as previously unexplored triple-layer MoS_2 structures, thereby providing an unprecedented level of insights into the energetics of hydrogen adsorption on MoS_2. **Figure 3.4a** shows the structural models for $\mathrm{Mo}\,(10\bar{1}0)$ and $\mathrm{S}\,(\bar{1}010)$ edges with varying sulfur coverage. Models A and A' correspond to Mo-edge structures covered with 50 % and 100 % S atoms, respectively, whereas Models B and B' represent S-edge structures with 75% and 100 % S atoms, respectively. **Figure 3.4b** shows the representative slab models for single-, double-, and triple-layer (denoted as 1L, 2L, and 3L, respectively) MoS_2. We found Model B', which is a more stable form than those used in previous studies.[66–68] We point out that the temperature effect was included for more accurate calculations of $\Delta G_{\mathrm{H}}^{0}$. A $\Delta G_{\mathrm{H}}^{0}$ near zero suggests superior HER activity.[11]

The calculation of $\Delta \mathrm{G}_{\mathrm{H}}^{0}$ with 1L MoS_2 models showed that, for Mo- and S-edge structures, Models A (50% S) and B (75% S) are favorable structures for the HER, respectively (**Figure 3.4c**). In the calculation of $\Delta G_{\mathrm{H}}^{0}$ using the 2L MoS_2 models (**Figure 3.4d**), the bond stability was affected by the sulfur coverage of the H-adsorbed layer as well as the edge configurations of adjacent layers on the same side. The Mo-edge (0% S) was not used to construct the 2L models, since the Mo-edge (0% S) is known to be unstable and the adsorbed hydrogen on this layer shows strong adsorption, indicating difficult desorption.[69] By considering the inclusion of assorted energies induced from the temperature effect, the $\Delta G_{\mathrm{H}}^{0}$ of Model A-B where hydrogen adsorbed on the B layer was found to be the most suitable structure for the HER.

Next, DFT calculations were extended to the 3L MoS_2 models built on the above 2L models that were proved to be favorable for the HER. For the 3L MoS_2 models, hydrogen can be adsorbed on the 2nd layer or 3rd layer (equivalent to 1st layer). Hence, 3L(2nd) and 3L(3rd) models were considered, and their calculated $\Delta G_{\mathrm{H}}^{0}$s are shown in **Figure 3.4e and 3.4f**, respectively. The $\Delta G_{\mathrm{H}}^{0}$s of 3L(3rd) models were similar to those of the 2L models with either type of edge. Also, it was revealed that regardless of whether bonding occurs at the 2nd or 3rd layer, the S-edge produces a more thermo-neutral S–H bond (that is, close to a zero energy) than the Mo-edge. Comparing the two 3L models, the adsorption at the 2nd layer produces a more thermo-neutral S–H bond than the 3rd layer for the Mo-edge and a comparable thermo-neutral bond for the S-edge.

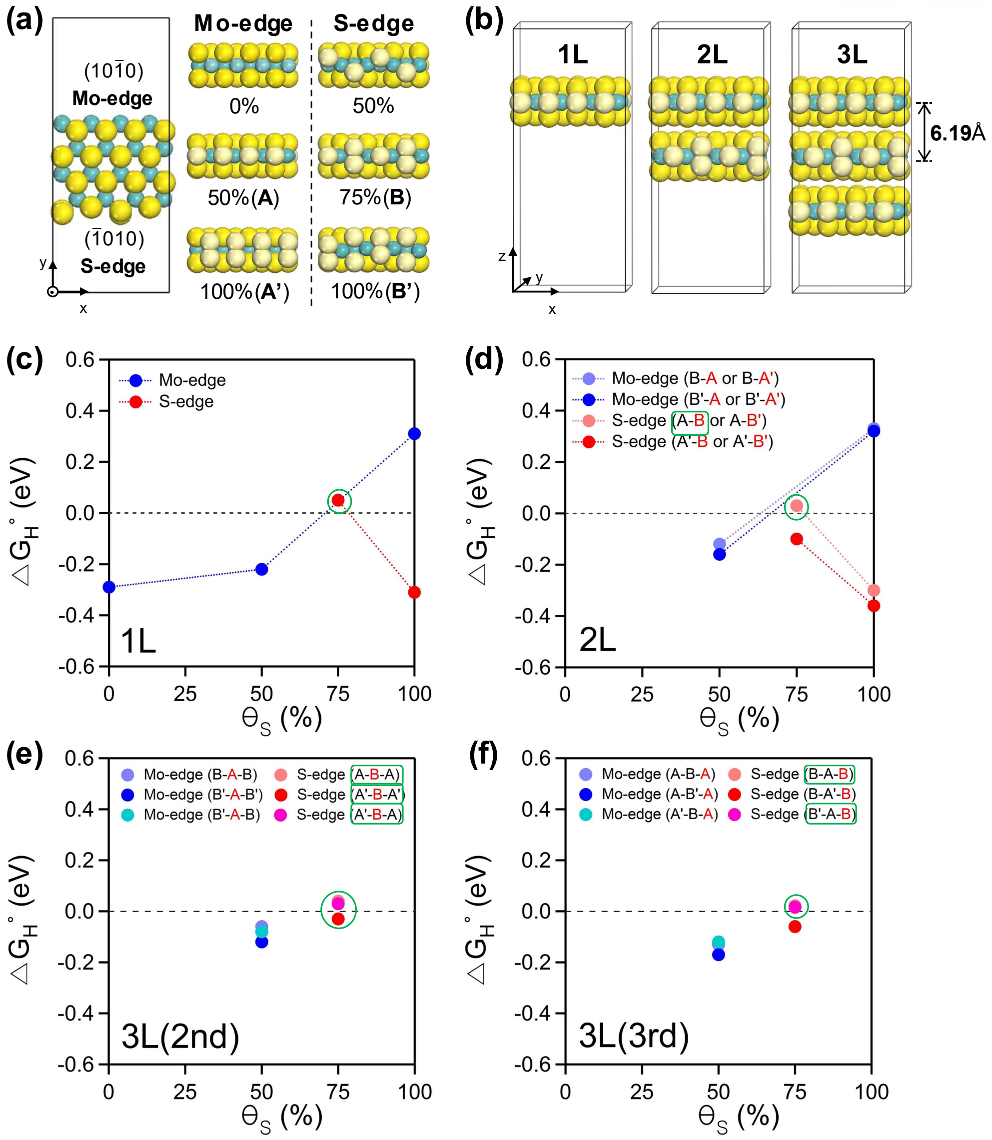

Figure 3.4. DFT calculations of the Gibbs free energy for H adsorption on the MoS$_2$ structures. (a) Top and side views of the semi-infinite slab models of Mo- and S-edge sites in MoS$_2$ with different sulfur coverage. The S atoms along the edge and at terrace sites are displayed as light and dark yellow spheres, respectively, and Mo atoms are presented as blue-green spheres. A supercell structure (*i.e.* x:12.84 Å, y:30.0 Å, z:30.0 Å) was created by four Mo atoms in the x, y directions. The slab model is only periodic in the x direction, and the Mo-and S-edges are exposed in the y direction. The terms, A, A', B, and B' represent Mo-edge (50% S), Mo-edge (100% S), S-edge (75% S), and S-edge (100% S) structures, respectively. (b) Representative layer models for 1L, 2L, and 3L MoS$_2$. The slab models for 2L and 3L are stacked with a layer center-to-center distance of 6.19 Å, and a vacuum space is introduced above and below the layer models. (c–f) The Gibbs free energy ($\Delta G_{\mathrm{H}}^{0}$) for hydrogen adsorption on the (c) 1L, (d) 2L, (e) 3L(2nd), and (f) 3L(3rd) MoS$_2$ models with varying degree of sulfur coverage (θ_S). '2nd' and '3rd' indicate that hydrogen adsorption occurs at the 2nd layer and 3rd layer (equivalent to the 1st layer) in the 3L models, respectively. The green boxes in the legends and green circles in the plots match each other and represent the most suitable points for the HER. The red letters in the legends indicate the location of the layers where hydrogen adsorption occurs.

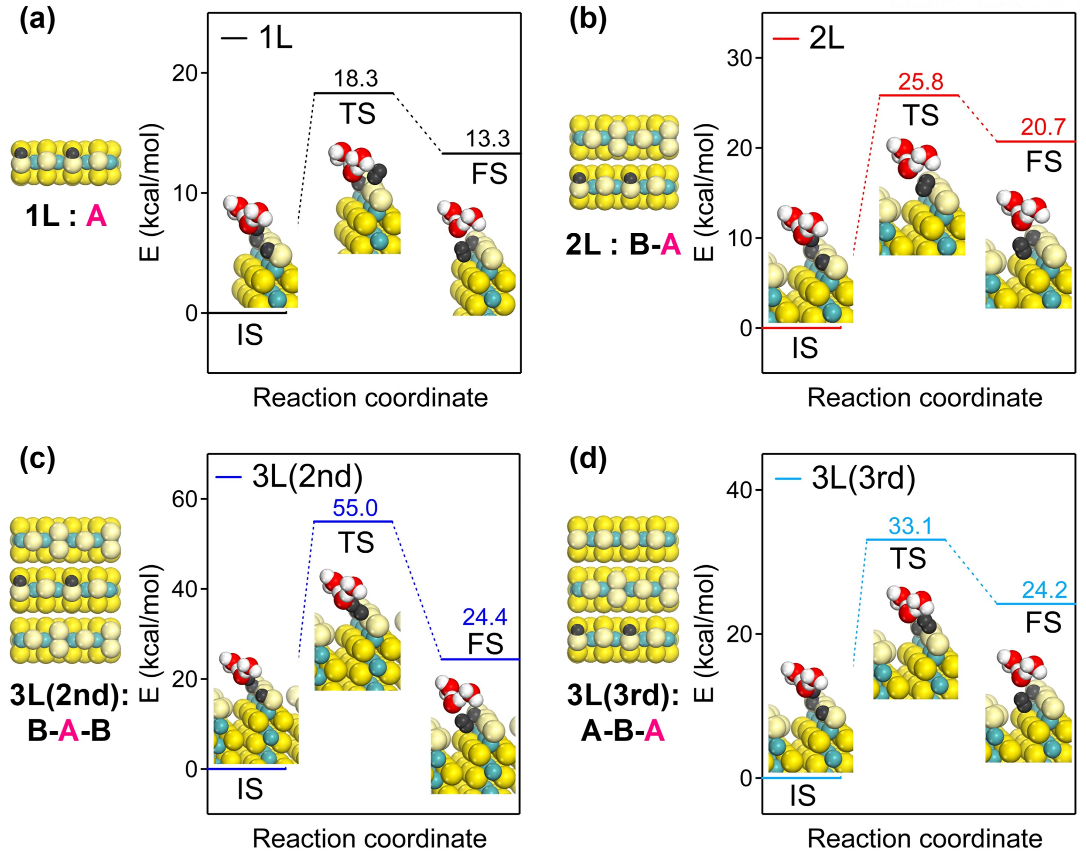

Figure 3.5. DFT calculations of the reaction paths on the Mo-edge layer models during the Heyrovsky reaction. The energy diagrams of the reaction paths on the Mo-edge (50%S) for a hydrogen coverage of 50% in the (a) 1L, (b) 2L, (c) 3L(2nd), and (d) 3L(3rd) models with respect to the reaction coordinate. The acronyms IS, TS, and FS represent the initial, transition, and final states, respectively. The numerical values represent the relative energies of each state based on that of the IS. The black spheres represent either adsorbed H or desorbed H_2. The pink letter indicates a layer with adsorbed hydrogen atoms.

From the aforementioned Gibbs free energy calculations, we could deduce the most energy-efficient MoS_2 models (*i.e.* Mo-edge (50% S) and S-edge (75% S)) for the HER. Next, the energetics of elementary steps in the HER was calculated by tracking the reaction pathway in each MoS_2 model. As previous studies revealed, MoS_2 catalysts followed the Volmer-Heyrovsky mechanism during HER.[15,26,33–34] Heyrovsky reaction, which is the electrochemical desorption step, includes the combination of one adsorbed hydrogen atom and one proton freely floating in electrolyte. The latter proton must be introduced in water environments.[70,71] Thus, we modeled the solvated proton, which was originated from H_2SO_4, with two adjacent water molecules seizing the hydronium ion on both sides (*i.e.* $H_3O^+(H_2O)_2$), and applied the implicit water environment by using the COSMO method.[60] With the simplified models, we investigated the energetics of the reaction paths for Heyrovsky reaction on Mo-edge first depending on the hydrogen coverage. We found that the heats of reaction and activation energies of 50% coverage of hydrogen are lower, thus more favorable than 25%

coverage of hydrogen regardless of the layer numbers. Within the 50% coverage, separately adsorbed hydrogen atoms are more favorable than closely adsorbed ones since the former case shows smaller $\Delta G_{\mathrm{H}}^{0}$, thus more thermo-neutral. Based on the results, the most possible case for the HER of our interest was determined to be the 50% coverage of hydrogen, where two hydrogen atoms were separately adsorbed.

For further study on the effect of layer numbers on the HER, the energetics during the elementary reaction paths of two separately adsorbed hydrogen atoms at the Mo-edge in 1L (Model A), 2L (Model B-A), 3L(2nd) (Model B-A-B), and 3L(3rd) (Model A-B-A) models were calculated (**Figure 3.5**). As the number of layers was increased, the heat of reaction and activation energy at transition state (TS), where the adsorbed hydrogen atom combines with a proton in H_3O^+ at the edge site, was clearly increased because of the van der Waals (vdW) effect from adjacent S-edge layer(s). Similar activation energies of 2L and 3L(3rd) models revealed no significant influence of the top layer in the 3L(3rd) system. However, a clear difference in the activation energies between 3L(2nd) and 3L(3rd) models exists because of more vdW effects of adjacent S-edge layers located at both sides. In the case of the S-edge, the activation energy was increased as the number of layer was increased. Unlike the case of Mo-edge, both activation energies of 3L(2nd) and 3L(3rd) models were high since the S-edge top layer could exert the vdW effect on the adsorption S-edge layer at the bottom in the 3L(3rd) model. Even though increasing trend of the heat of reaction and activation energy was similar with the cases of Mo-edges, HER on S-edge of 1L model was not favored in comparison to that on Mo-edge due to larger heat of reaction and activation energy. Therefore, by evaluating the Mo- and S-edge cases, some important conclusions were drawn, which might be crucial for predicting HER activity; (i) the Mo-edge plays a major role in the HER, (ii) the S-edge can, in principle, be involved in HER in view of the thermo-neutral $\Delta G_{\mathrm{H}}^{0}$, yet little involved in view of Heyrovsky reaction (iii) S-edge-type layers may severely hinder HER that occurs on the Mo-edge layer, and (iv) given the major role of the Mo-edge in HER with a little contributions from the S-edge, the best order for the HER might be $3L < 2L \leq 1L$.

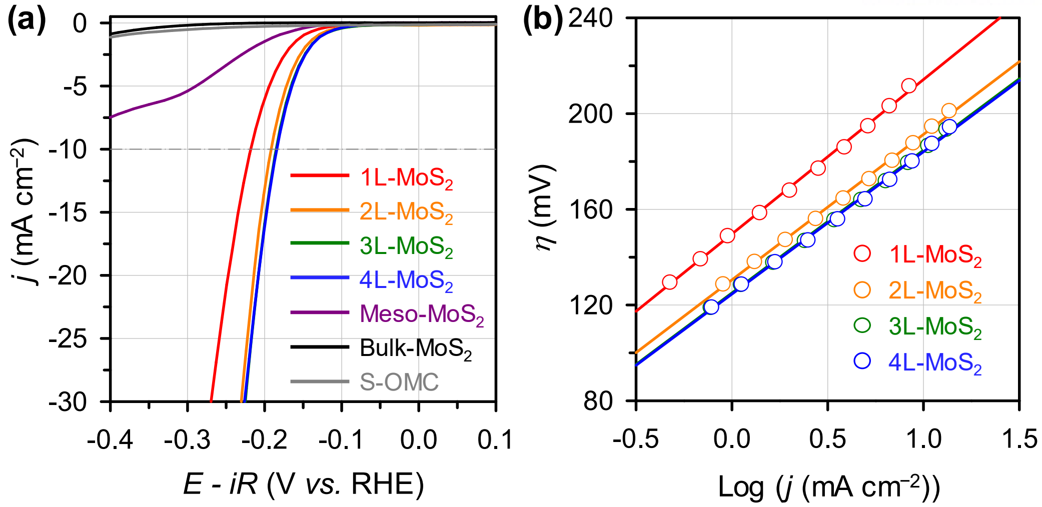

Figure 3.6. (a) LSV curves of MoS_2@OMCs, Meso-MoS_2, Bulk-MoS_2, and S-OMC for the HER. (b) Corresponding Tafel plots for MoS_2@OMCs.

Table 3.5. HER activities of MoS_2@OMC and $CoMoS_2$@OMC nanostructures, expressed in terms of overpotential at 10 mA cm^{-2}, Tafel slope, exchange current density, and TOF.

Sample	**Overpotential at 10 mA cm^{-2} (V)**	**Tafel slope ^{a} (mV dec^{-1})**	**Exchange current density ^{b} (A cm^{-2})**	**TOF (s^{-1}) ^{c}**
1L-MoS_2@OMC	0.215	65	4.82 x 10^{-6}	2.32
2L-MoS_2@OMC	0.189	61	7.14 x 10^{-6}	2.32
3L-MoS_2@OMC	0.182	60	8.04 x 10^{-6}	1.95
4L-MoS_2@OMC	0.182	60	8.07 x 10^{-6}	1.45
2.5L-$CoMoS_2$@OMC	0.166	60	1.70 x 10^{-5}	5.13
3.5L-$CoMoS_2$@OMC	0.170	73	4.69 x 10^{-5}	2.30

[a,b] The Tafel slopes and exchange current densities were derived from the linear portion of the corresponding Tafel plots.

[c] The TOFs were determined with current densities at overpotential of 200 mV. The TOF (s^{-1}) per Mo atom in Mo-edges (50% S coverage) was calculated using the structural model based on theoretically calculated Gibbs free energy, the details of which has been described in section 3.3.1.

The preparation of MoS_2 nanoplates with monolayer-precision allowed us to investigate layer number effects on catalytic properties. We examined the electrocatalytic properties of MoS_2@OMC nanostructures in the HER (**Figure 3.6**). For comparison, the HER activities of Meso-MoS_2, bulk-MoS_2, and sulfur-doped OMC (S-OMC) were also measured. The details of the electrochemical measurements are described in section 2.2. For all samples, the LSV curves were measured five times and the average data were used. For the MoS_2@OMC nanostructures, the LSV data were presented after the *iR* correction, for which series resistances were measured using electrochemical impedance spectroscopy (EIS) (See section 2.2.3 for details). As shown in **Figure 3.6a**, only a negligible amount of current was derived from the bulk-MoS_2 and S-OMC even at high overpotential greater than 300 mV; such low catalytic activity could originate from the low intrinsic conductivity of bulk-MoS_2 and the small number of active sites in S-OMC. In contrast, the MoS_2@OMC catalysts showed on-set potentials in the range of 120–132 mV with comparatively low overpotentials. In addition, the MoS_2@OMC catalysts exhibited a current density of −10 mA cm^{-2} in the overpotential range 178–192 mV (**Table 3.5**). The Tafel slopes of the MoS_2@OMC catalysts were between 60 and 65 mV dec^{-1} (**Figure 3.6b**), which were similar to those of other metal sulfide catalysts, such as MoS_2 NPs on Au surface (55–60 mV dec^{-1}),[13] amorphous molybdenum sulfide (60 mV dec^{-1}),[22] and $[Mo_3S_{13}]^{2-}$ clusters on highly oriented pyrolytic graphite (HOPG) (57 mV dec^{-1}).[35]

To gain further insight into the HER activity, the TOFs of the MoS_2@OMC catalysts were calculated. While the overpotential of catalysts has relevance to their practical device applicability, TOFs can reveal an intrinsic turnover rate of single active site in MoS_2 nanoplates. In the TOF calculations, a MoS_2 model (**Figure 3.7a**), which was constructed based on the Gibbs free energy calculation-optimized layers (Model A and B in **Figure 3.4a**), was used. With the MoS_2 model and the measured sizes of MoS_2 nanoplates from TEM images, the number of each type of atoms in each type of edges could be calculated (see section 3.3.1 for details). Firstly, Mo atoms at the Mo-edges were considered as active sites, similar to that in previous works.[9,13,35] Among the compared catalysts, the 1L- and 2L-MoS_2@OMC catalysts showed the highest HER activity, with a TOF of 2.32 s^{-1} at an overpotential of 200 mV (**Figure 3.7b and Table 3.5**). Comparison with the TOFs of previously reported MoS_2-based catalysts at the same overpotential indicates the very high TOF of 1L- and 2L-MoS_2@OMCs, which approached the TOF of $[Mo_3S_{13}]^{2-}$ clusters on HOPG (~3 s^{-1}) reported by Besenbacher and co-workers,[35] and was higher than the TOFs of MoS_2 on reduced graphene oxide,[15] electrodeposited amorphous MoS_3,[21] and double gyroid structured MoS_2.[31] Upon examination of the HER activity trend of the MoS_2@OMC catalysts, the TOF value decreased nonlinearly with increased layer numbers in MoS_2 nanoplates (**Figure 3.7c**). While the HER activity was nearly preserved from 1L- to 2L-MoS_2@OMC, it rapidly diminished upon stacking additional MoS_2 layers. The more remarkable change of TOFs from 2L to 3L compared to that from 1L to 2L can be explained by the energetics of the HER. A similar trend is observed for the change of activation energy required to overcome the TS in **Figure 3.5**. The activation energy increases more rapidly from 2L to 3L than from 1L to 2L, demonstrating that the increase in activation energy at the TS with layer numbers owing to the vdW effect could play an important role in governing the HER activity. In addition, the increasing trend in HER activity with decreased MoS_2 layer number can be explained by a combination of several factors, including the increased number of edge sulfur sites, their enhanced surface oxidation, and the evolution of the 1T phase, as confirmed by EXAFS and XPS analyses.

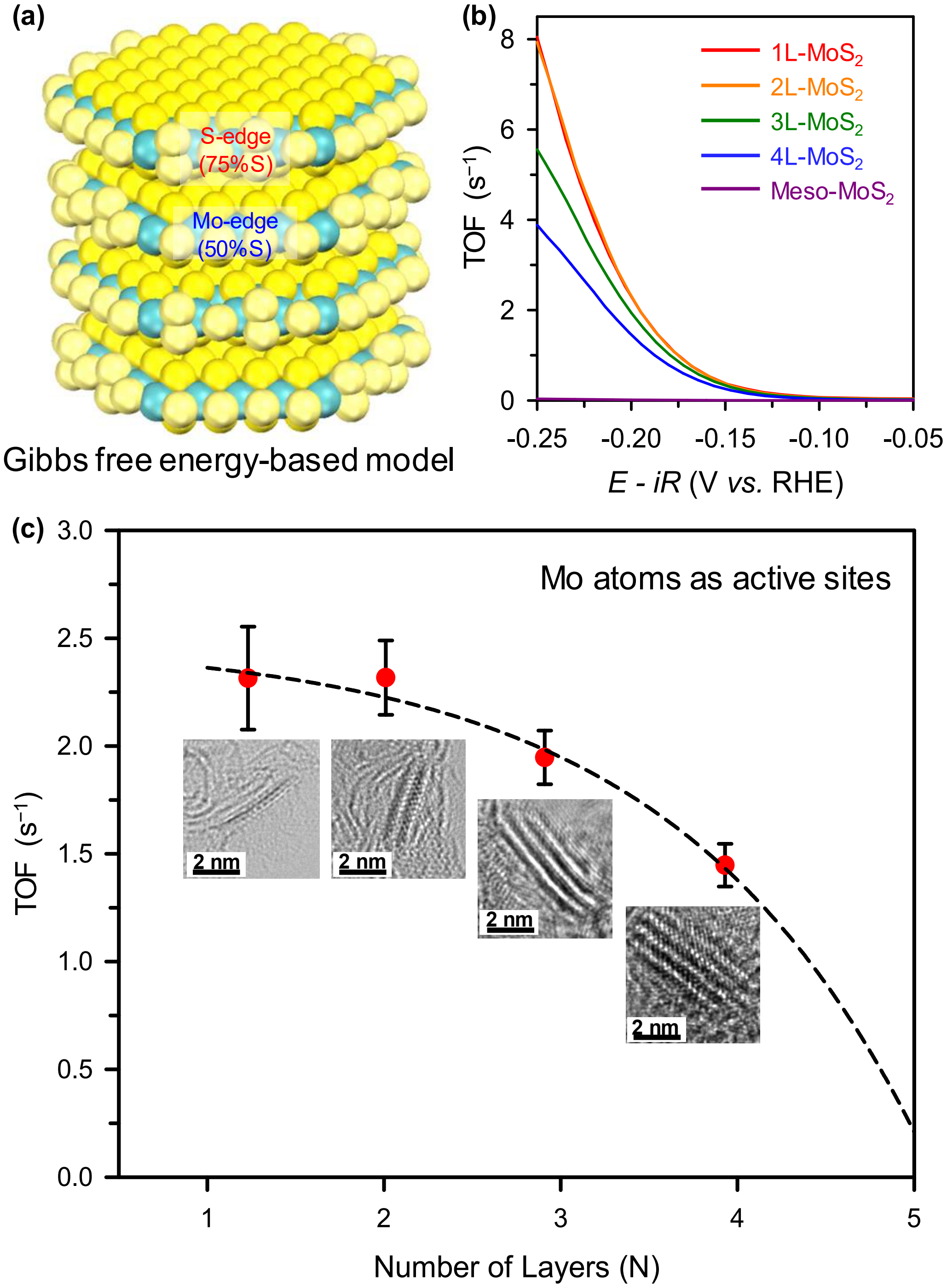

Figure 3.7. TOF calculations assuming Mo atoms at the Mo-edge as active sites. (a) MoS_2 structural model most suitable for the HER based on DFT calculations of the Gibbs free energy of hydrogen adsorption on MoS_2. (b) TOFs with respect to potential. (c) TOFs at −200 mV (*vs.* RHE) with respect to the number of layers (inset: TEM images of corresponding MoS_2 nanoplates in MoS_2@OMCs).

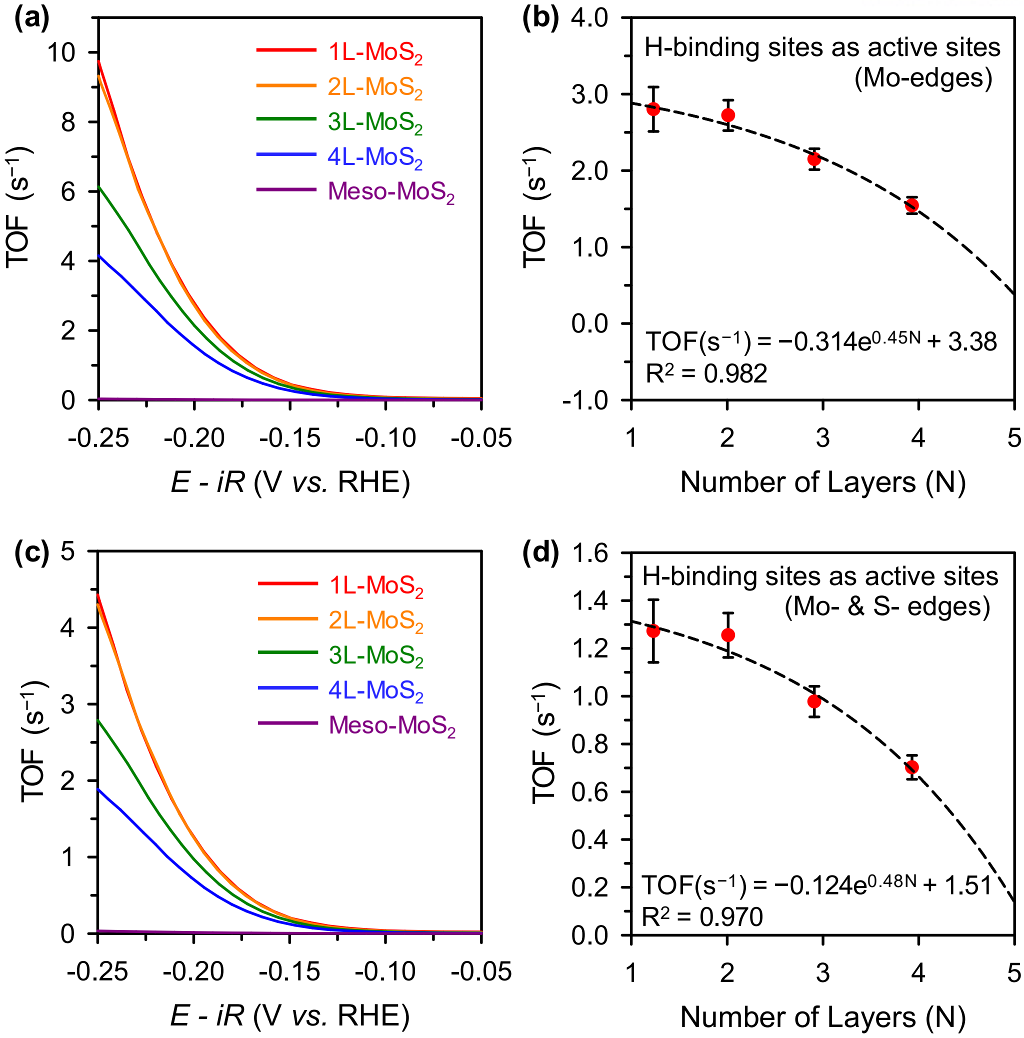

Figure 3.8. TOF calculations on MoS_2@OMCs and Meso-MoS_2 using the structural model based on the Gibbs free energy calculations (**Figure 3.7a**). (a,b) TOF calculations assuming H-binding sites (S atoms) at the Mo-edge as active sites: (a) TOFs with respect to potential and (b) TOFs at −200 mV (*vs.* RHE) with respect to the number of layers. (c,d) TOF calculations assuming H-binding sites at both the Mo- and S-edges as active sites: (c) TOFs with respect to potential and (d) TOFs at −200 mV (*vs.* RHE) with respect to the number of layers.

We also carried out TOF calculations, assuming S atoms on the Mo-edges as the active sites, as the HER is initiated by the adsorption of H atoms on S atoms (**Figure 3.8a,b**). The HER activity trend for the MoS_2@OMC catalysts was similar to the above calculation, but the TOF values in this case were lower. In addition, as the S-edges can also be involved in the HER, the TOFs were calculated, assuming that the S atoms in both the Mo- and S-edges were involved in the HER (**Figure 3.8c,d**).

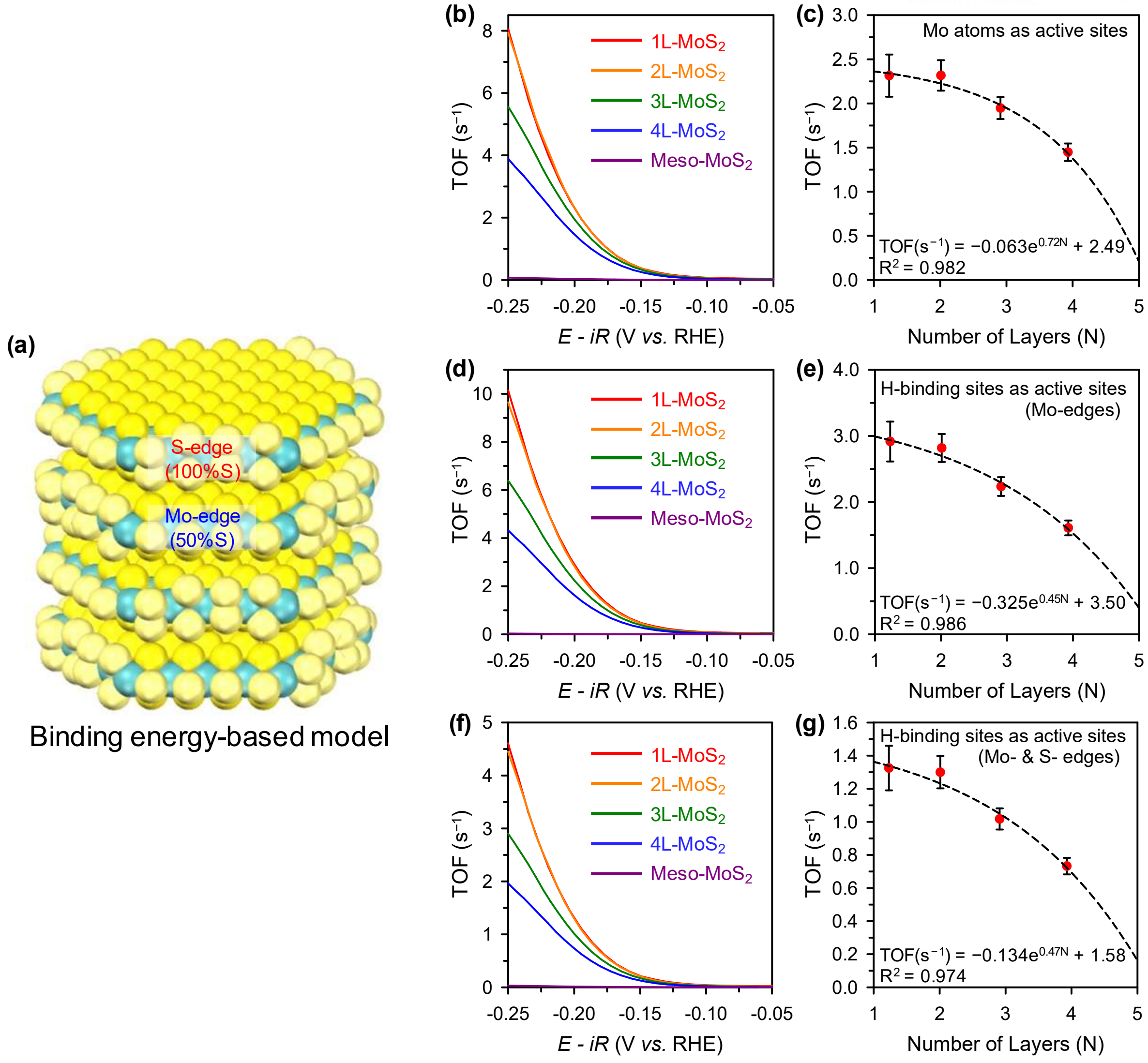

Figure 3.9. TOF calculations using (a) a structural model based on the binding energy calculations. (b,c) TOF calculations assuming Mo atoms at the Mo-edge as active sites: (b) TOFs with respect to potential and (c) TOFs at −200 mV (*vs.* RHE) with respect to the number of layers. (d,e) TOF calculations assuming H-binding sites (S atoms) at the Mo-edge as active sites: (d) TOFs with respect to potential and (e) TOFs at −200 mV (*vs.* RHE) with respect to the number of layers. (f,g) TOF calculations assuming H-binding sites at both the Mo- and S-edges as active sites: (f) TOFs with respect to potential and (g) TOFs at −200 mV (*vs.* RHE) with respect to the number of layers.

In addition, the TOF calculations were conducted using the structural model deduced from the binding energy calculations (**Figure 3.9a**). With this model, the TOFs were calculated by assuming that the active sites were (i) Mo atoms in the Mo-edge (**Figures 3.9b,c**), (ii) S atoms in the Mo-edge (**Figures 3.9d,e**), and (iii) S atoms in the Mo- and S-edges (**Figures 3.9f,g**). All TOF calculations consistently shown that HER activity was reduced in a quasi-linear manner as the MoS_2 layer number increased.

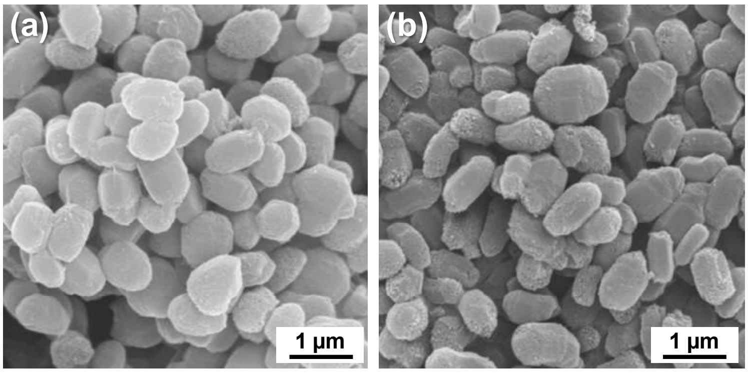

Figure 3.10. SEM images of (a) 2.5L- and (b) 3.5L-$CoMoS_2$@OMCs.

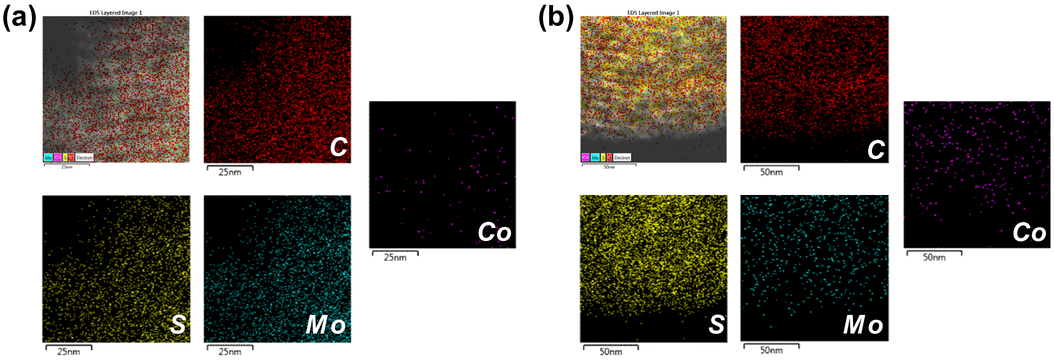

Figure 3.11. EDS elemental mapping images of (a) 2.5L- and (b) 3.5L-$CoMoS_2$@OMCs.

To generalize the nanopore-confined synthesis of metal sulfide nanoplates and to confirm the HER activity trend, we prepared cobalt-doped MoS_2@OMC ($CoMoS_2$@OMC) nanostructures. Previously, it was shown that the addition of Co atoms to MoS_2 could increase the HER activity.[26] The characterizations of the two $CoMoS_2$@OMC nanostructures by scanning electron microscopy (SEM), energy-dispersive X-ray spectroscopy (EDS) elemental mapping, XRD, nitrogen adsorption (**Figures 3.10–3.12**), and ICP-OES analysis (**Table 3.1**) clearly revealed the successful formation of mesoporous structures with large surface area and homogeneous distributions of the respective elements of the $CoMoS_2$ nanoplates.

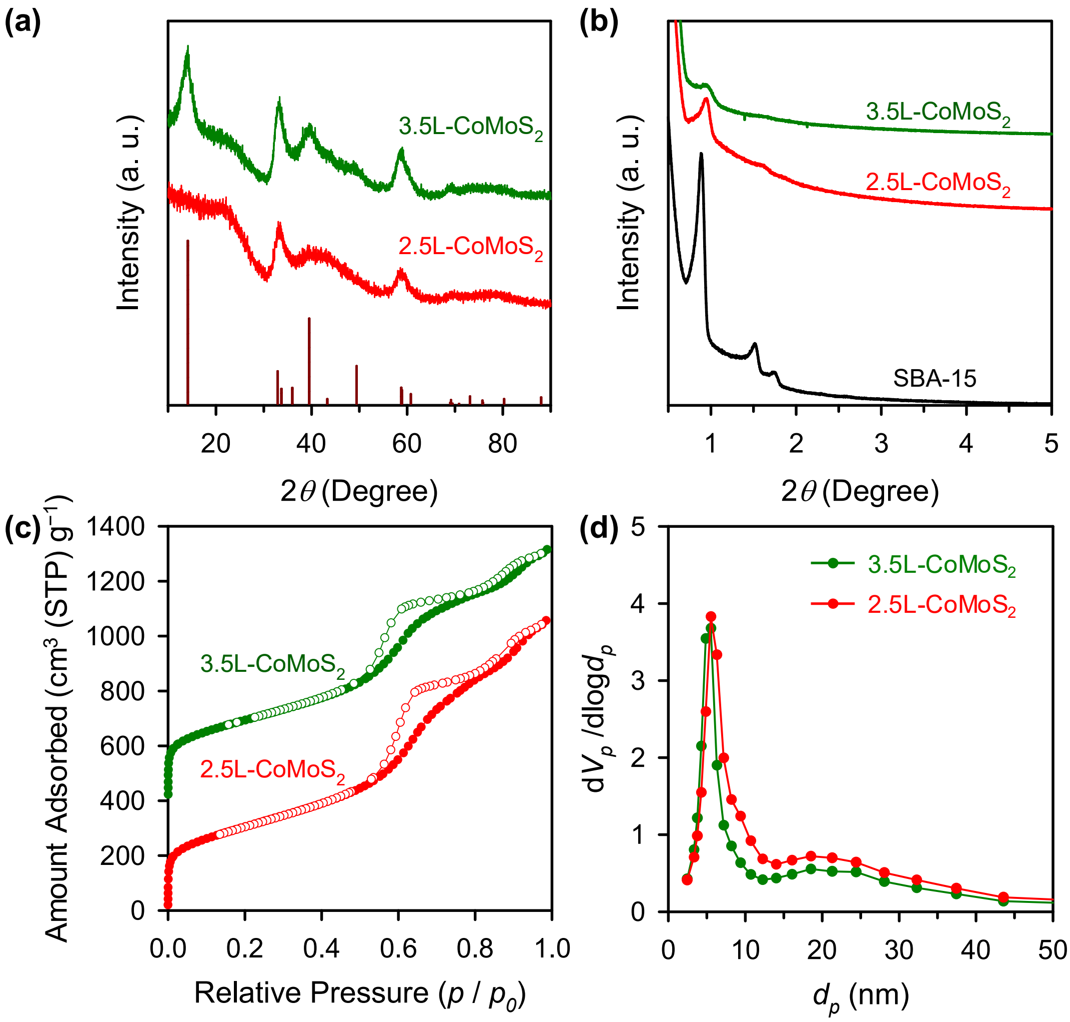

Figure 3.12. (a) Wide-angle and (b) small-angle XRD patterns of CoMoS$_2$@OMCs. (c) Nitrogen adsorption–desorption isotherms of CoMoS$_2$@OMCs. Filled circles and empty circles represent adsorption and desorption branches, respectively. The isotherm of the 3.5L-CoMoS$_2$@OMC was offset by 400 cm^3 g^{-1}, for clarity. (d) BJH pore size distributions of CoMoS$_2$@OMCs obtained from the adsorption branches of their isotherms.

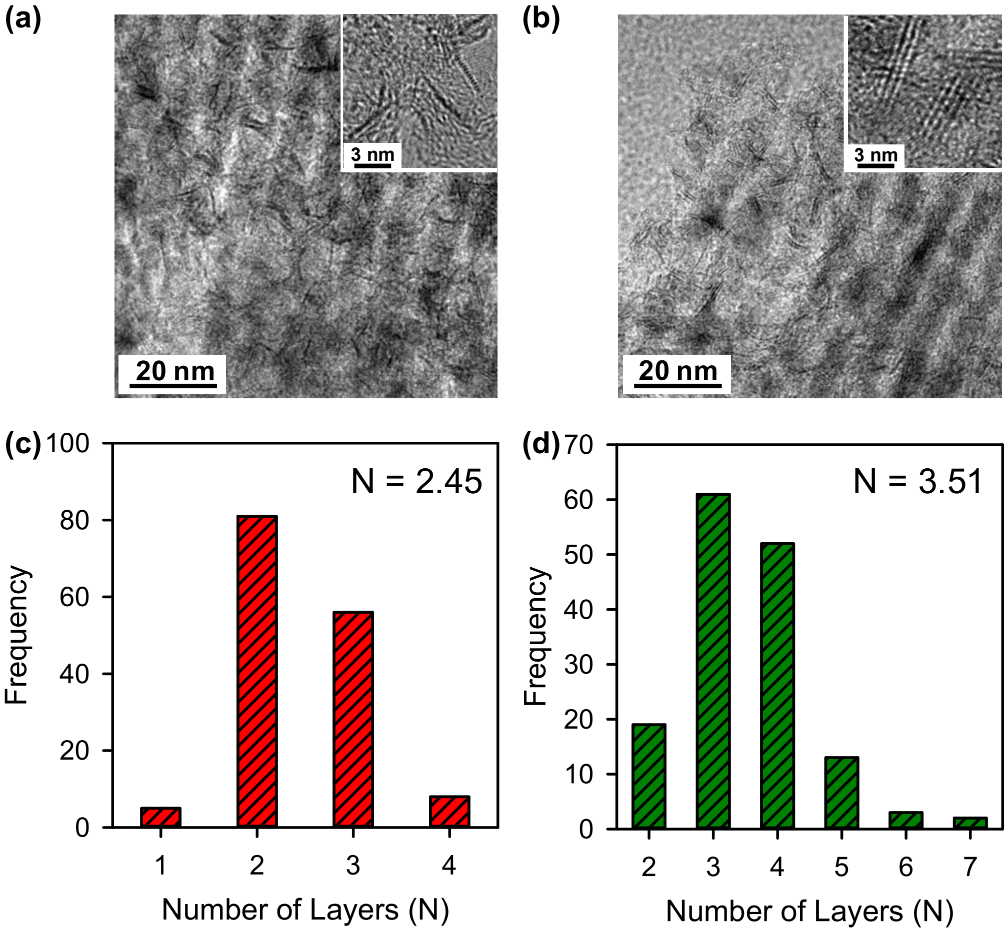

Figure 3.13. TEM images of (a) 2.5L- and (b) 3.5L-$CoMoS_2$@OMCs. Inset images in (a) and (b) are HRTEM images. Layer number distributions of the nanoplates in (c) 2.5L- and (d) 3.5L-$CoMoS_2$@OMCs.

TEM images of $CoMoS_2$@OMCs (**Figures 3.13a,b**) showed that the $CoMoS_2$ nanoplates were successfully inserted into the OMC arrays, like the MoS_2 nanoplates in the MoS_2@OMC nanostructures. The TEM images and layer number distributions (**Figures 3.13c,d and Table 3.2**) revealed that the two $CoMoS_2$ nanoplates in the $CoMoS_2$@OMC composites with different $CoMoS_2$ loadings had an average 2.5 and 3.5 layers (hereafter denoted as 2.5L-$CoMoS_2$@OMC and 3.5L-$CoMoS_2$@OMC, respectively).

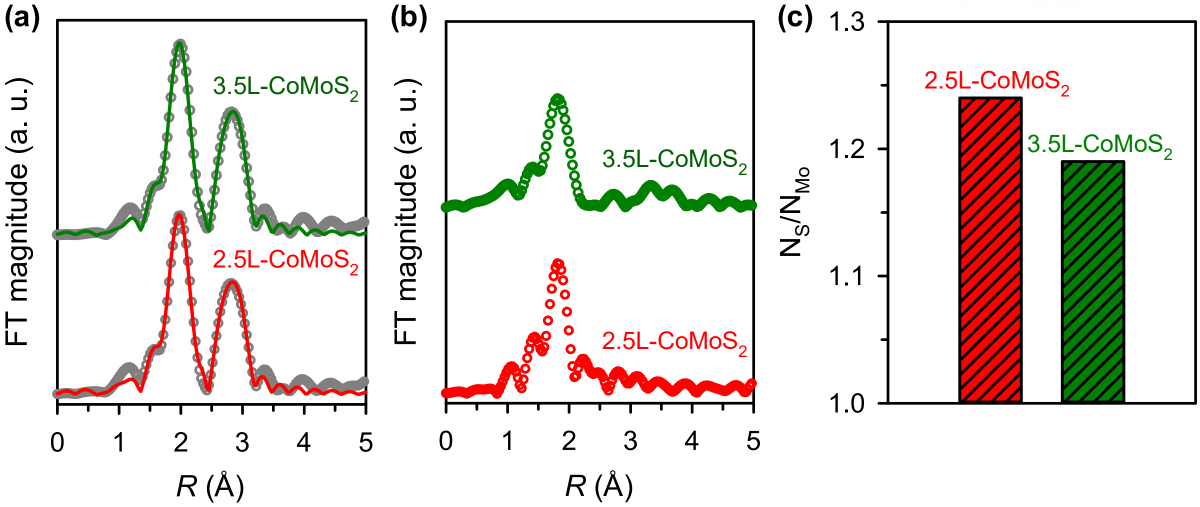

Figure 3.14. (a) Mo K-edge and (b) Co K-edge EXAFS spectra of $CoMoS_2$@OMCs. Empty circles and solid lines are raw data and fitting results, respectively. (c) The resulting N_s/N_{Mo} ratio plotted as vertical bars with respect to the composition (N_s: CN of Mo−S, N_{Mo}: CN of Mo−Mo).

The Mo K-edge EXAFS fitting spectra of the $CoMoS_2$@OMC nanostructures (**Figure 3.14a**) exhibited very similar peak positions and intensities for Mo–S and Mo–Mo bonds to those of MoS_2@OMCs. The Co K-edge EXAFS spectra (**Figure 3.14b**) revealed the absence of Co–Co and Co–Mo bonds, indicating that Co was atomically incorporated into the MoS_2 nanoplates, and that most Co atoms were located on the edge sites rather than the basal plane, as suggested by Hu and co-workers.[26]

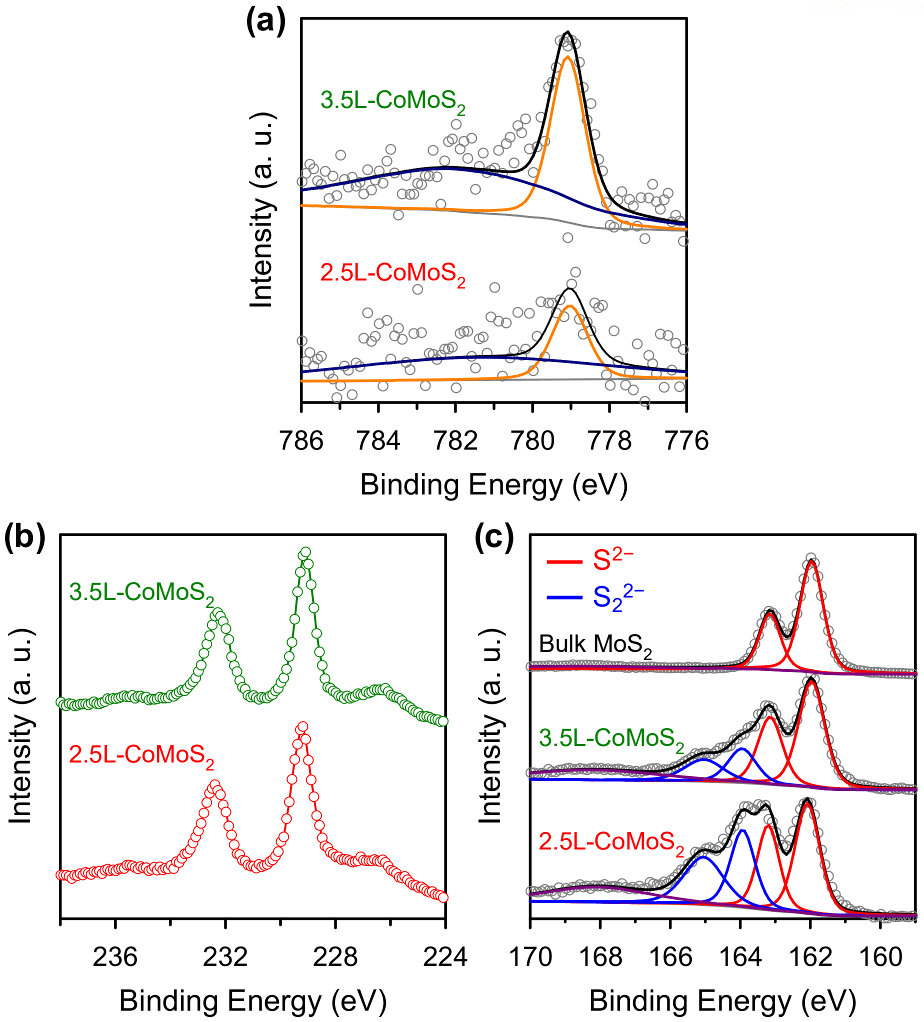

Figure 3.15. (a) Mo 3d, (b) Co 2p, and (c) S 2s XPS spectra. Peak intensities are normalized by setting the maximum intensity to one and the minimum intensity to zero.

The EXAFS results were further substantiated by Co 2p XPS spectra (**Figure 3.15a**), as characteristic peaks corresponding to Co_9S_8 and CoMo alloys were not observed.[29] The Mo 3d and S 2p XPS spectra of $CoMoS_2$@OMC nanostructures (**Figures 3.15b,c**) showed similar trends with those of MoS_2@OMCs; the peaks assigned to the Mo^{5+}, Mo^{6+} and S_2^{2-} oxidation states became more pronounced as the $CoMoS_2$ layer number decreased, indicating enhanced surface oxidation and an increased population of S_2^{2-} species.

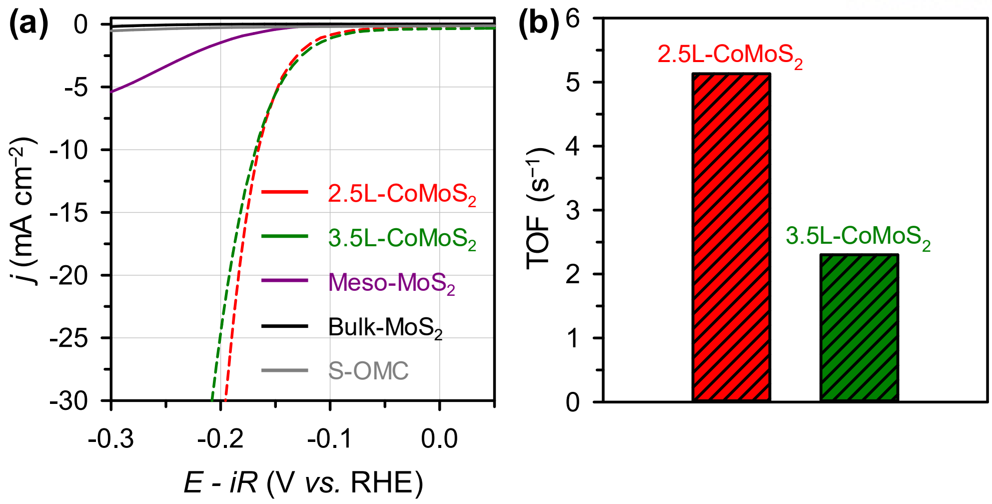

Figure 3.16. (a) LSV curves of CoMoS$_2$@OMCs, Meso-MoS$_2$, Bulk-MoS$_2$ and S-OMC for the HER. (b) TOFs at −200 mV (*vs*. RHE).

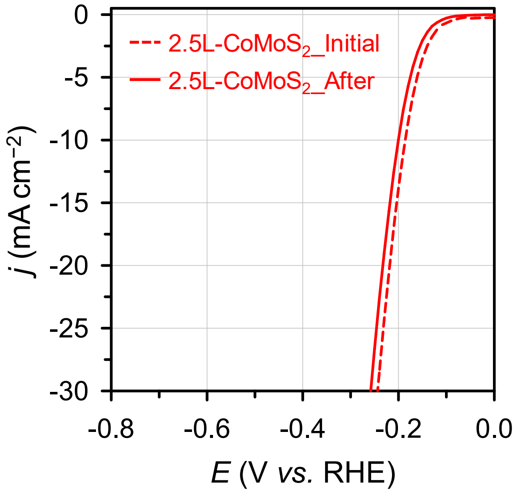

Figure 3.17. LSV curves of 2.5L-CoMoS$_2$@OMC before and after 1000 potential sweeps between −0.3 V and 0.1 V (*vs*. RHE) in 0.5 M H$_2$SO$_4$ at a scan rate of 50 mV s^{-1} without *iR* correction.

The HER activities of CoMoS$_2$@OMC catalysts were investigated and exceeded those of undoped MoS$_2$@OMC catalysts; an overpotential of 166–170 mV at a current density of −10 mA cm^{-2} (**Figure 3.16a and Table 3.5**) was observed. The enhanced catalytic performance was demonstrated by the EIS, as the Nyquist plots for the CoMoS$_2$@OMC catalysts showed substantially reduced charge transfer resistance as compared to MoS$_2$@OMCs (**Table 3.5**). The TOFs of CoMoS$_2$@OMC were calculated using the Gibbs free energy calculation-driven structural model, by assuming the Mo edge atoms as active sites (**Figure 3.16b**). The TOFs of 2.5L- and 3.5L-CoMoS$_2$@OMC catalysts were 5.13 and 2.30 s^{-1}, respectively, which were higher than those of MoS$_2$@OMCs, confirming the promotion effect of the Co dopant. The enhanced HER activity of CoMoS$_2$@OMC catalysts was due to the involvement of the Co-promoted S-edges in the HER.[12,26] Significantly, $CoMoS_2$@OMC exhibited a similar tendency to increase HER activity as the layer number of $CoMoS_2$ decreased, as in the case of the MoS_2@OMC catalysts (**Figure 3.16b and Table 3.5**). Finally, the durability of the 3.5L-$CoMoS_2$@OMC catalyst, which showed the best activity, was evaluated with 1000 potential cycles between −0.3 V and 0.1 V. The LSV of 2.5L-$CoMoS_2$@OMC after cycling showed only a marginal negative shift in the potential (**Figure 3.17**), indicating the durability of the catalysts upon prolonged operation in acidic medium.

3.5. CONCLUSION

We prepared MoS_2 nanoplates with discrete layer numbers *via* nanopore-confined synthesis, which enabled the investigation of nanoscale layer number effects in the HER. The most favorable single-, double-, and triple-layer MoS_2 model structures for the HER were deduced using DFT calculations; using these models, the detailed energetics of elementary reactions during the HER were calculated. By combining the measured HER currents with the energetically favorable MoS_2 model, we found that the TOFs of MoS_2@OMC for the HER decreased in a quasi-linear manner with an increase in the layer number of MoS_2 nanoplates. The enhanced activity in smaller MoS_2 nanoplates originate from a combination of several factors, including the high ratio of edge sulfur sites, tendency towards enhanced surface oxidation, propensity towards 1T phase formation, and lower activation energy required to overcome the TS. Even though it was not considered in this work, electron hopping efficiency between layers has recently been suggested as being another important factor influencing the HER performance.[72] Such trend of HER activity was generalized with $CoMoS_2$@OMC nanostructures. The nanopore-confined synthesis strategy that combined controllability with monolayer-precision and suitability for large-scale synthesis can be generalized to other metal chalcogenides. We believe that the improvement of synthetic procedure would yield MoS_2 nanoplates with more narrow size distribution, which in turn can be used as more reliable platform for investigating the nanoscale size effect. In addition, to interrogate the origin of HER activity in our catalysts, the behavior of active species during HER will be investigated by using *in situ* electrochemical X-ray absorption methods combined with theoretical calculations. Finally, the discernments gleaned from this work can provide crucial information for designing advanced HER catalysts, and may also be applied to other metal sulfide-catalyzed reactions such as hydrodesulfurization.[73]

3.6. REFERENCES

1. Tenne, R. *Nat. Nanotechnol.* **2006**, *1*, 103–111.
2. Geim, A. K.; Grigorieva, I. V. *Nature* **2013**, *499*, 419–425.
3. Nicolosi, V.; Chhowalla, M.; Kanatzidis, M. G.; Strano, M. S.; Coleman, J. N. *Science* **2013**, *340*, 1420–1438.
4. Chhowalla, M.; Shin, H. S.; Eda, G.; Li, L.-J.; Loh, K. P.; Zhang, H. *Nat. Chem.* **2013**, *5*, 263–275.
5. Butler, S. Z.; Hollen, S. M.; Cao, L.; Cui, Y.; Gupta, J. A.; Gutiérrez, H. R.; Heinz, T. F.; Hong, S. S.; Huang, J.; Ismach, A. F.; Johnston-Halperin, E.; Kuno, M.; Plashnitsa, V. V.; Robinson, R. D.; Ruoff, R. S.; Salahuddin, S.; Shan, J.; Shi, L.; Spencer, M. G.; Terrones, M.; Windl, W.; Goldberger, J. E. *ACS Nano* **2013**, *7*, 2898–2926.
6. Merki, D.; Hu, X. *Energy Environ. Sci.* **2011**, *4*, 3878–3888.
7. Laursen, A. B.; Kegnæs, S.; Dahl, S.; Chorkendorff, I. *Energy Environ. Sci.* **2012**, *5*, 5577–5591.
8. Yan, Y.; Xia, B.; Xu, Z.; Wang, X. *ACS Catal*. **2014**, *4*, 1693–1705.
9. Morales-Guio, C. G.; Hu, X. *Acc. Chem. Res.* **2014**, *47*, 2671–2681.
10. Yang, J.; Shin, H. S. *J. Mater. Chem. A* **2014**, *2*, 5979–5985.
11. Hinnemann, B.; Moses, P. G.; Bonde, J.; Jørgensen, K. P.; Nielsen, J. H.; Horch, S.; Chorkendorff, I.; Nørskov, J. K. *J. Am. Chem. Soc.* **2005**, *127*, 5308–5309.
12. Bonde, J.; Moses, P. G.; Jaramillo, T. F.; Nørskov, J. K.; Chorkendorff, I. *Faraday Discuss.* **2008**, *140*, 219–231.
13. Jaramillo, T. F.; Jørgensen, K. P.; Bonde, J.; Nielsen, J. H.; Horch, S.; Chorkendorff, I. *Science* **2007**, *317*, 100–102.
14. Karunadasa, H. I.; Montalvo, E.; Sun, Y.; Majda, M.; Long, J. R.; Chang, C. J. *Science* **2012**, *335*, 698–702.
15. Li, Y.; Wang, H.; Xie, L.; Liang, Y.; Hong, G.; Dai, H. *J. Am. Chem. Soc.* **2011**, *133*, 7296–7299.
16. Firmiano, E. G. S.; Cordeiro, M. A. L.; Rabelo, A. C.; Dalmaschio, C. J.; Pinheiro, A. N.; Pereira, E. C.; Leite, E. R. *Chem. Commun.* **2012**, *48*, 7687–7689.
17. Laursen, A. B.; Vesborg, P. C. K.; Chorkendorff, I. *Chem. Commun.* **2013**, *49*, 4965–4967.
18. Chang, Y.-H.; Lin, C.-T.; Chen, T.-Y.; Hsu, C.-L.; Lee, Y.-H.; Zhang, W.; Wei, K.-H.; Li, L.-J. *Adv. Mater.* **2013**, *25*, 756–760.
19. Yan, Y.; Ge, X.; Liu, Z.; Wang, J.-Y.; Lee, J.-M.; Wang, X. *Nanoscale* **2013**, *5*, 7768–7771.
20. Liao, L.; Zhu, J.; Bian, X.; Zhu, L.; Scanlon, M. D.; Girault, H. H.; Liu, B. *Adv. Funct. Mater.* **2013**, *23*, 5326–5333.

21. Merki, D.; Fierro, S.; Vrubel, H.; Hu, X. *Chem. Sci.* **2011**, *2*, 1262–1267.
22. Benck, J. D.; Chen, Z.; Kuritzky, L. Y.; Forman, A. J.; Jaramillo, T. F. *ACS Catal.* **2012**, *2*, 1916–1923.
23. Vrubel, H.; Merki, D.; Hu, X. *Energy Environ. Sci.* **2012**, *5*, 6136–6144.
24. Vrubel, H.; Hu, X. *ACS Catal.* **2013**, *3*, 2002–2011.
25. Lu, Z.; Zhang, H.; Zhu, W.; Yu, X.; Kuang, Y.; Chang, Z.; Lei, X.; Sun, X. *Chem. Commun.* **2013**, *49*, 7516–7518.
26. Merki, D.; Vrubel, H.; Rovelli, L.; Fierro, S.; Hu, X. *Chem. Sci.* **2012**, *3*, 2515–2525.
27. Tran, P. D.; Nguyen, M.; Pramana, S. S.; Bhattacharjee, A.; Chiam, S. Y.; Fize, J.; Field, M. J.; Artero, V.; Wong, L. H.; Loo, J.; Barber, J. *Energy Environ. Sci.* **2012**, *5*, 8912–8916.
28. Kim, J.; Byun, S.; Smith, A. J.; Yu, J.; Huang, J. *J. Phys. Chem. Lett.* **2013**, *4*, 1227–1232.
29. Tran, P. D.; Chiam, S. Y.; Boix, P. P.; Ren, Y.; Pramana, S. S.; Fize, J.; Artero, V.; Barber, J. *Energy Environ. Sci.* **2013**, *6*, 2452–2459.
30. Sun, X.; Dai, J.; Guo, Y.; Wu, C.; Hu, F.; Zhao, J.; Zeng, X.; Xie, Y. *Nanoscale* **2014**, *6*, 8359–8367.
31. Kibsgaard, J.; Chen, Z.; Reinecke, B. N.; Jaramillo, T. F. *Nat. Mater.* **2012**, *11*, 963–969.
32. Wu, Z.; Fang, B.; Wang, Z.; Wang, C.; Liu, Z.; Liu, F.; Wang, W.; Alfantazi, A.; Wang, D.; Wilkinson, D. P. *ACS Catal.* **2013**, *3*, 2101–2107.
33. Xie, J.; Zhang, H.; Li, S.; Wang, R.; Sun, X.; Zhou, M.; Zhou, J.; Lou, X. W.; Xie, Y. *Adv. Mater.* **2013**, *25*, 5807–5813.
34. Xie, J.; Zhang, J.; Li, S.; Grote, F.; Zhang, X.; Zhang, H.; Wang, R.; Lei, Y.; Pan, B.; Xie, Y. *J. Am. Chem. Soc.* **2013**, *135*, 17881–17888.
35. Kibsgaard, J.; Jaramillo, T. F.; Besenbacher, F. *Nat. Chem.* **2014**, *6*, 248–253.
36. Chung, D. Y.; Park, S.-K.; Chung, Y.-H.; Yu, S.-H.; Lim, D.-H.; Jung, N.; Ham, H. C.; Park, H.-Y.; Piao, Y.; Yoo, S. J.; Sung, Y.-E. *Nanoscale* **2014**, *6*, 2131–2136.
37. Lukowski, M. A.; Daniel, A. S.; Meng, F.; Forticaux, A.; Li, L.; Jin, S. *J. Am. Chem. Soc.* **2013**, *135*, 10274–10277.
38. Voiry, D.; Yamaguchi, H.; Li, J.; Silva, R.; Alves, D. C. B.; Fujita, T.; Chen, M.; Asefa, T.; Shenoy, V. B.; Eda, G.; Chhowalla, M. *Nat. Mater.* **2013**, *12*, 850–855.
39. Voiry, D.; Salehi, M.; Silva, R.; Fujita, T.; Chen, M.; Asefa, T.; Shenoy, V. B.; Eda, G.; Chhowalla, M. *Nano Lett.* **2013**, *13*, 6222–6227.
40. Wang, H.; Lu, Z.; Xu, S.; Kong, D.; Cha, J. J.; Zheng, G.; Hsu, P.-C.; Yan, K.; Bradshaw, D.; Prinz, F. B.; Cui, Y. *Proc. Natl. Acad. Sci. U.S.A.* **2013**, *110*, 19701–19706.

41. Boudart, M. *Adv. Catal.* **1969**, *20*, 153–166.
42. Van Santen, R. A. *Acc. Chem. Res.* **2009**, *42*, 57–66.
43. Koper, M. T. M. *Nanoscale* **2011**, *3*, 2054–2073.
44. Chen, M. S.; Goodman, D. W. *Science* **2004**, *306*, 252–255.
45. Kaden, W. E.; Wu, T.; Kunkel, W. A.; Anderson, S. L. *Science* **2009**, *326*, 826–829.
46. Joo, S. H.; Park, J. Y.; Renzas, J. R.; Butcher, D. R.; Huang, W.; Somorjai, G. A. *Nano Lett.* **2010**, *10*, 2709–2713.
47. Yamamoto, K.; Imaoka, T.; Chun, W.-J.; Enoki, O.; Katoh, H.; Takenaga, M.; Sonoi, A. *Nat. Chem.* **2009**, *1*, 397–402.
48. Nesselberger, M.; Ashton, S.; Meier, J. C.; Katsounaros, I.; Mayrhofer, K. J. J.; Arenz, M. *J. Am. Chem. Soc.* **2011**, *133*, 17428–17433.
49. Zhao, D.; Feng, J.; Huo, Q.; Melosh, N.; Fredrickson, G. H.; Chmelka, B. F.; Stucky, G. D. *Science* **1998**, *279*, 548–552.
50. Kruk, M.; Jaroniec, M.; Ko, C. H.; Ryoo, R. *Chem. Mater.* **2000**, *12*, 1961–1968.
51. Shi, Y.; Wan, Y.; Liu, R.; Tu, B.; Zhao, D. *J. Am. Chem. Soc.* **2007**, *129*, 9522–9531.
52. Jun, S.; Joo, S. H.; Ryoo, R.; Kruk, M.; Jaroniec, M.; Liu, Z.; Ohsuna, T.; Terasaki, O. *J. Am. Chem. Soc.* **2000**, *122*, 10712–10713.
53. Helveg, S.; Lauritsen, J. V.; Lægsgaard, E.; Stensgaard, I.; Nørskov, J. K.; Clausen, B. S.; Topsøe, H.; Besenbacher, F. *Phys. Rev. Lett.* **2000**, *84*, 951–954.
54. Delley, B. *J. Chem. Phys.* **1990**, *92*, 508–517.
55. Delley, B. *J. Chem. Phys.* **2000**, *113*, 7756–7764.
56. Perdew, J. P.; Burke, K.; Ernzerhof, M. *Phys. Rev. Lett.* **1996**, *77*, 3865–3868.
57. Grimme, S. *J. Comput. Chem.* **2006**, *27*, 1787–1799.
58. Monkhorst, H. J.; Pack, J. D. *Phys. Rev. B* **1976**, *13*, 5188–5192.
59. Hirano, T. In *MOPAC Manual,* Seventh Edition; Stewart, J. J. P., Eds.; 1993; pp 71–76.
60. Klamt, A.; Schuurmann, G. *J. Chem. Soc. Perk. Trans. 2* **1993**, 799–805.
61. Halgren, T. A.; Lipscomb, W. N. *Chem. Phys. Lett.* **1977**, *49*, 225–232.
62. Liu, H.; Su, D.; Zhou, R.; Sun, B.; Wang, G.; Qiao, S. Z. *Adv. Energy Mater.* **2012**, *2*, 970–975.
63. Chen, Z.; Cummins, D.; Reinecke, B. N.; Clark, E.; Sunkara, M. K.; Jaramillo, T. F. *Nano Lett.* **2011**, *11*, 4168–4175.
64. Yan, Y.; Xia, B.; Ge, X.; Liu, Z.; Wang, J.-Y.; Wang, X. *ACS Appl. Mater. Interfaces*, **2013**, *5*, 12794–12798.

65. Tsai, C.; Abild-Pedersen, F.; Nørskov, J. K. *Nano Lett.* **2014**, *14*, 1381–1387.

66. Bollinger, M. V.; Jacobsen, K. W.; Norskov, J. K. *Phys. Rev. B* **2003**, *67*, 085410.

67. Hinnemann, B.; Norskov, J. K.; Topsoe, H. *J. Phys. Chem. B* **2005**, *109*, 2245–2253.

68. Prodhomme, P. Y.; Raybaud, P.; Toulhoat, H. *J. Catal.* **2011**, *280*, 178–195.

69. Raybaud, P.; Hafner, J.; Kresse, G.; Kasztelan, S.; Toulhoat, H. *J. Catal.* **2000**, *189*, 129–146.

70. Skulason, E.; Karlberg, G. S.; Rossmeisl, J.; Bligaard, T.; Greeley, J.; Jonsson, H.; Norskov, J. K. *Phys. Chem. Chem. Phys.* **2007,** *9*, 3241–3250.

71. Wei, G. F.; Fang, Y. H.; Liu, Z. P. *J. Phys. Chem. C* **2012,** *116*, 12696–12705.

72. Yu, Y.; Huang, S.-Y.; Li, Y.; Steinmann, S. N.; Yang, W.; Cao, L. *Nano Lett.* **2014**, *14*, 553–558.

73. Lauritsen, J. V.; Nyberg, M.; Nørskov, J. K.; Clausen, B. S.; Topsøe, H.; Lægsgaard, E.; Besenbacher, F. *J. Catal.* **2004**, *224*, 94–106.

4

HORIZONTAL GROWTH OF TUNGSTEN SULFIDE ON CARBON AND INSIGHT INTO ACTIVE SULFUR SITE FOR THE HYDROGEN EVOLUTION REACTION

4.1. INTRODUCTION

The structural features of transition metal dichalcogenides (TMDs), such as their lateral size and layer number, have been shown to greatly influence on their physiochemical properties.[1–5] When the size of TMDs is scaled down to the nanometer-regime, unique electronic, optical, and mechanical properties appear owing to quantum confinement effects. In particular, reducing the layer number of TMDs to a single layer can give rise to unusual structural and physicochemical properties compared to the multilayer counterparts.[5–8] In catalysis, TMDs with smaller basal plane sizes as well as reduced layer numbers have been shown to be effective in enhancing catalytic performances in energy conversion reactions.[4,9–11] Hence, the preparation of mono- or few-layer TMDs at the nanoscale is important.

Mono- and few-layer TMDs have been commonly prepared by mechanical exfoliation,[12] wet chemical exfoliation,[13] and chemical vapor deposition (CVD).[14] Chemical exfoliation enables the production of large amounts of monolayer TMDs, but the obtained TMDs commonly show irregular distributions in their lateral size. CVD can produce highly pure monolayer TMDs; however, CVD is unsuitable for high-throughput production. Recently, confinement effects within carbon nanostructures has attracted attention for generating mono- or few-layer TMDs.[10,15–17] This method is particularly appealing for electrocatalysis, because carbon nanostructures can limit the growth of TMDs in the basal and edge plane directions, and serve as conductive supports as well. Furthermore, TMDs imprisoned within carbon nanostructures could possess a large number of defect sites due to highly strained TMD surfaces; recent examples have demonstrated that defect sites increase the catalytic activity of the inert basal surface of TMDs.[18,19] However, the formation mechanism for mono- or few-layer TMD within or on carbon supports is not completely understood.

Mono- and few-layer TMDs hold great promise as alternatives to expensive precious metal-based catalysts in the renewable energy conversion reactions. As the representative two-dimensional

(2D) TMD catalysts, MoS_2 and WS_2 have been demonstrated to be affordable nonprecious metal electrocatalysts for the hydrogen evolution reaction (HER).[9,10,16–49] Several strategies have been established to tailor the structural features of the TMDs to enhance their HER activity and durability. Structural engineering to maximize the active edge sites of the TMDs has significantly improved the catalytic activity in the HER.[26,28,29] In particular, a molecular catalyst based on subnanometer $[Mo_3S_{13}]^{2-}$ clusters showed large active edge site density, thereby exhibiting excellent HER performance.[29] More interestingly, well-designed molecular catalysts can selectively possess desirable sulfur sites, and hence can serve as appropriate model catalysts for revealing genuine active sulfur sites.

Herein, we report the preferential horizontal growth of tungsten sulfides (WS_x) within micro- and mesopores of carbon nanostructures to yield monolayer WS_2 nanoplates, and their structural effects on the HER performance. WS_x initially form ultrasmall subnanometer-sized clusters and subsequently grow in the horizontal direction along the carbon surface, yielding monolayer WS_2 nanoplates. Interestingly, a TMD analogue, MoS_2 showed a starkly different growth behavior (see chapter 3 for details); MoS_2 continuously stacks layer vertically on the carbon surface to increase layer numbers with increasing MoS_x contents.[10] The contrasting growth behavior of the two TMDs was corroborated by density functional theory (DFT) calculations, which revealed that basal plane bonding and horizontal growth is favored for WS_x on carbon surfaces, whereas edge plane bonding and subsequent layer stacking dominantly occurs for MoS_2. Sulfidation time-dependent growth experiments combined with X-ray absorption spectroscopy (XAS) analysis further corroborated the growth behavior of WS_x. The coordination numbers (CN) for the W–S and W–W bonds increased with increasing sulfidation time, proving the gradual formation of WS_2 nanoplates (CN = 6) with consumption of WS_x nanoclusters (CN < 6). In the HER, the catalyst comprised of ultrasmall WS_x nanoclusters exhibited a three-fold higher exchange current density than the sample enriched with WS_2 nanoplates, indicating faster electron-transfer rates in the HER. Electrochemical and X-ray photoelectron spectroscopy (XPS) results suggested that bridging S_2^{2-} species abundant in the nanoclusters were relevant to catalytically active sites. These results provide important clues into active sulfur species in WS_x-based electrocatalysts for the HER.

4.2. SYNTHESIS OF CATALYSTS

4.2.1. Synthesis of WS_x@OMC

First, SBA-15 ordered mesoporous silica (OMS) template was synthesized by the previously reported methods with some modification (see section 3.2.1 for details).[10,50] The general synthetic procedure for WS_x nanostructures embedded in ordered mesoporous carbon (WS_x@OMC) consisted of (i) partial filling of the mesopores in the OMS with a carbon structure, (ii) subsequent formation of metal sulfide nanostructures inside the void spaces of the carbon–SBA-15 composites, and (iii) etching the OMS. Sucrose (7.70 g, Samchun) was dissolved in deionized (DI) water (25 g) in a polypropylene bottle, and H_2SO_4 (0.87 g, 95%, Samchun) was added to the solution. Then, SBA-15 (5.0 g) was added to the sucrose solution, and the mixture was gently agitated to make a homogeneous paste. The paste was heated to 100 °C and maintained at this temperature for 6 h, then was kept at 160 °C for 2 h in air. The brown product was then carbonized in an N_2 atmosphere (flow rate of 1 L min^{-1}) at 400 °C for 4 h, then at 900 °C for 2 h. The resulting carbon–SBA-15 composites were impregnated with tungsten precursor and sulfided to generate WS_x–carbon–silica composites. The desired amount (0.0036, 0.0095, 0.019, 0.031 or 0.044 g) of phosphotungstic acid hydrate (PTA, Sigma-Aldrich) was dissolved in absolute ethanol (EtOH) (2 g) and the as-synthesized carbon–SBA-15 composite (0.90 g) was added to the solution. The mixture was stirred at 35 °C to evaporate the solvent and then finely ground in an agate mortar. The resulting powder was sulfided by heating at 600 °C using a heating rate of 2 °C min^{-1} and maintaining the temperature at 600 °C for 5 h under 10% H_2S (balanced with Ar) at a flow rate of 200 mL min^{-1}. After sulfidation, the furnace was cooled to room temperature (RT) under an N_2 gas flow. Finally, the SBA-15 silica template was etched with a solution of EtOH (94.5%, Samchun):10 wt.% HF (J. T. Baker) (1:1), stirred for 30 min, filtered, and washed with EtOH. The etching process was repeated once, and the product was dried. The nominal loadings of the WS_x, based on the quantities of the PTA precursor, were 2, 5, 10, 15, and 20 wt.%.

4.2.2. Synthesis of Sulfur-Doped OMC

Sulfur-doped OMC (S-OMC) was prepared by sulfidation of carbon–SBA-15 composites, which is used as a template for the preparation of WS_x@OMC. The carbon–SBA-15 composites was sulfided at 600 °C using the same sulfidation scheme as for the WS_x@OMC nanostructures. The S-OMC was obtained by etching the silica template, by two consecutive 30 min washing steps using the HF solution described earlier.

4.3. COMPUTATIONAL DETAILS

4.3.1. Computation Methods

DFT calculations were performed using DMol^3.[51–53] The generalized gradient approximation (GGA) with the Perdew-Burke-Ernzerhof (PBE)[54] functional was used to describe the exchange-correlation energy of electrons. Semi-empirical dispersion-correction by Tkatchenko and Scheffler's scheme[55] and spin-polarized calculations with the DNP 4.4 basis set were included for all systems. All electron relativistic effects were included in the core treatment by using a smearing value of 0.005 Ha. The Monkhorst-Pack[56] was utilized to sample the Brillouin-zone as follows: 5 × 5 × 2 *k*-point for the unit cell structure, and 1 × 1 × 1 Γ-point for all supercell structures. The convergence criteria for the geometry optimization were set to 1.0×10^{-5} Ha for energy, 0.002 Ha/Å for force, and 0.005 Å for displacement, respectively.

4.3.2. Adhesion Energy Calculation

Two binding models of MS_2 were considered (M = W and Mo) in the adhesion energy calculations. When the MS_2 sheets were parallel to the support surface ("basal bonding"), the periodic 2D monolayers consisting of four and six M atoms in the *x*-, and *y*-directions, respectively, were considered (*i.e.*, *x*- : 12.54 Å, *y*- : 16.29 Å, *z*- : 50.0 Å for WS_2 and *x*- : 12.68 Å, *y*- : 16.47 Å, *z*- : 50.0 Å for MoS_2, respectively). When the edges of MS_2 sheets were attached to the support ("edge bonding"), a slab model consisting of four and six M atoms in the *x*-, and *z*-directions, respectively, was employed. A configuration in which the M-edge covered with 50% S atoms and S-edge covered with 100% S atoms was chosen because this edge configuration was the most stable.[60] The amorphous carbon support was first constructed using the same size periodic box as used for each of the MS_2 sheets. Energy minimizations were performed to find the stable configurations for the structure. The M-edges were only considered in the adhesion energy calculations because the S-edges with 100% S atoms are relatively inert (i.e. difficult to form chemical linkages to the support). The adhesion energy ($\Delta E_{adhesion}$) of MS_2 on carbon support was calculated as follows,

$$\Delta E_{adhesion} = E_{\mathrm{MS_2+C}} - E_{\mathrm{MS_2}} - E_{\mathrm{C}}$$

where $E_{\mathrm{MS_2+C}}$ is the total energy of the MS_2 sheets adsorbed on the carbon support, $E_{\mathrm{MS_2}}$ is the total energy of an isolated MS_2 sheet in an adsorbed state, and E_{C} is the total energy of an isolated carbon support with adsorbed geometry.

4.3.3. Stacking Energy Calculation

We explored the energetics of MS_2 models with varying nucleation sizes to investigate the tendency for growth orientation of each MS_2 nanoplates. Free-standing single-layer models of MS_2 were initially constructed with different nucleation sizes, with $(MS_2)_n$ clusters where n=3, 12, 27, and bulk state, respectively. In a previous study, Hansen *et al* reported that multilayer MoS_2 nanocrystals are formed by the successive growth of additional layers (so-called 'layer-by-layer growth'), rather than by the migration and coalescence of 1L nanocrystals (so-called 'layer-on-layer growth').[57] Based on the experimental observations, 'on-top' double layer models of MS_2 were constructed on the 2D-periodic bottom MS_2 layer (*i.e.,* a 6 × 6 × 1 supercell structure). We used the unit potential energy ($\mu^n_{\mathrm{MS_2}}$) to describe the stability of each MS_2 sheet,[58,59] which is defined as follows,

$$\mu^n_{MS_2} = \frac{1}{n}(E_{\mathrm{MS_2}/Surf} - E_{Surf}) - E_{\mathrm{MS_2}(vac)}$$

where $E_{\mathrm{MS_2}/Surf}$ is the total energy of the system, which consists of the adsorbed MS_2 sheet and 2D-periodic bottom MS_2 layer; E_{Surf} is the total energy of the bare MS_2 bottom layer, n is the number of MS_2 clusters, and $E_{\mathrm{MS_2}(vac)}$ is the total energy of a single MS_2 cluster in vacuum. The stacking energy ($\Delta E_{stacking}$), which describes the interaction between interlayers, was calculated as follows,

$$\Delta E_{stacking} = \mu^n_{\mathrm{MS_2}}(\mathrm{2L}) - \mu^n_{\mathrm{MS_2}}(\mathrm{1L})$$

where $\mu^n_{\mathrm{MS_2}}(\mathrm{2L})$ is the unit potential energy of the 'on-top' 2L cluster model and $\mu^n_{\mathrm{MS_2}}(\mathrm{1L})$ is the unit potential energy of the 'free-standing' 1L cluster model.

4.4. RESULTS AND DISCUSSION

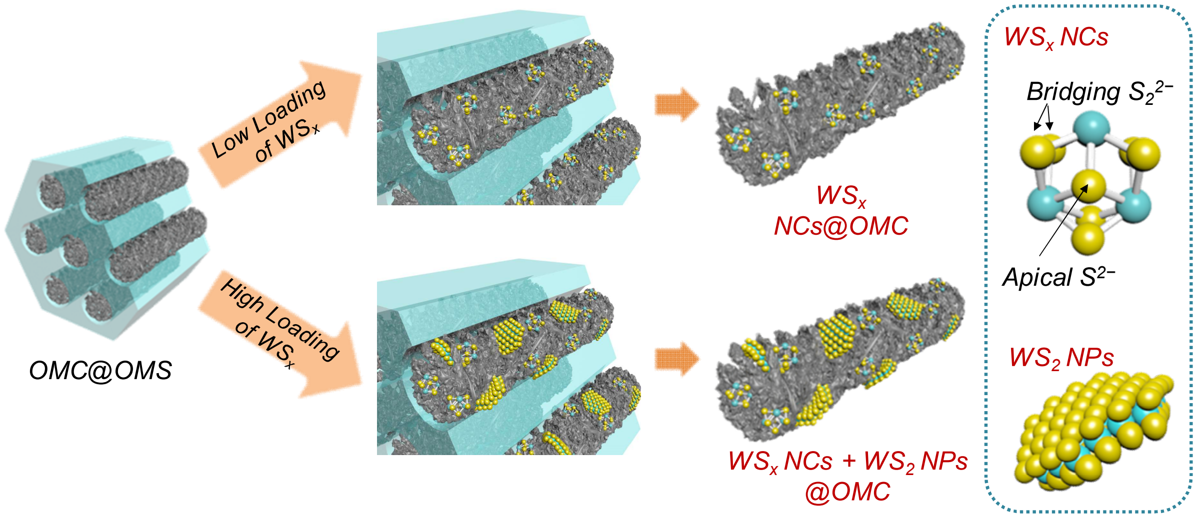

Figure 4.1. (a) Schematic illustration for preparation of WS_x@OMC. Depending on the WS_x loading, WS_x nanocluster (NC)-rich or WS_2 nanoplate (NP)-rich WS_x@OMC composites can be prepared. Dotted box shows the structural models for WS_x NC (top) and WS_2 NP (bottom), respectively. Sulfur species located at the edges of WS_2 NPs were omitted due to their multiple chemical states (*e.g.*, bridging S_2^{2-}, terminal S_2^{2-}, and unsaturated S^{2-}).

Table 4.1. Contents (wt.%) of W, S, and C in WS_x@OMC, determined by quantitative EDS analysis.[a]

Sample	Nominal loading [b]	W	S [c]	C
2% WS_x@OMC	2	1.1 ± 0.3	6.0 ± 1.4	92.9 ± 1.2
5% WS_x@OMC	5	2.7 ± 1.0	6.9 ± 0.9	90.4 ± 1.6
10% WS_x@OMC	10	6.2 ± 0.7	5.7 ± 0.7	88.1 ± 1.0
15% WS_x@OMC	15	8.1 ± 0.9	6.1 ± 1.2	85.8 ± 2.0
20% WS_x@OMC	20	12.0 ± 2.5	5.5 ± 0.7	82.5 ± 2.7

[a] The contents were determined by averaging seven quantitative EDS results measured on different sites.
[b] The nominal loading was determined by the quantity of PTA precursor used in the synthesis.
[c] S species can exist as WS_x and S–C.

To investigate the growth behavior of WS_x on carbon surfaces at the nanoscale, WS_x structures were grown within micro and mesopores of porous carbon nanorod arrays, following synthetic strategy introduced in chapter 3 (**Figure 4.1**).[10] In this case, PTA was used as the tungsten precursor. First, the mesopores of an OMS template were partially filled with carbon. The tungsten precursor was then incorporated into the residual spaces between the OMS frameworks and carbogenic structures. Subsequent sulfidation and etching of the OMS template yielded WS_x@OMC nanostructures. The sulfidation time was fixed at 5 h, and was increased to 20 h in a control experiment (*vide infra*). Detailed synthetic procedures for the WS_x@OMCs are described in section 4.2. The concentration of the tungsten precursor was varied over a wide range to observe the growth behavior of WS_x on the carbon surfaces. The W, S, and C contents in the samples were estimated by quantitative EDS analysis, which indicated that controlled amounts of WS_x (1.1 wt.% to 12.0 wt.%) were generated on mesoporous carbon, allowing the investigation of WS_x loading-dependent growth behaviour (**Table 4.1**). The final WS_x@OMC nanostructures were denoted as X% WS_x@OMC (where X is nominal wt.% of WS_x). The small-angle X-ray diffraction (XRD) patterns of WS_x@OMCs (**Figure 4.2a**) exhibited distinct reflections below 2°, indicating the formation of a periodic mesostructure. Nitrogen adsorption-desorption analysis of WS_x@OMCs (**Figure 4.2b,c**) revealed the formation of uniform mesopores with Brunauer–Emmett–Teller (BET) surface areas as high as 1200 m^2 g^{-1} and large pore volumes (**Table 4.2**).

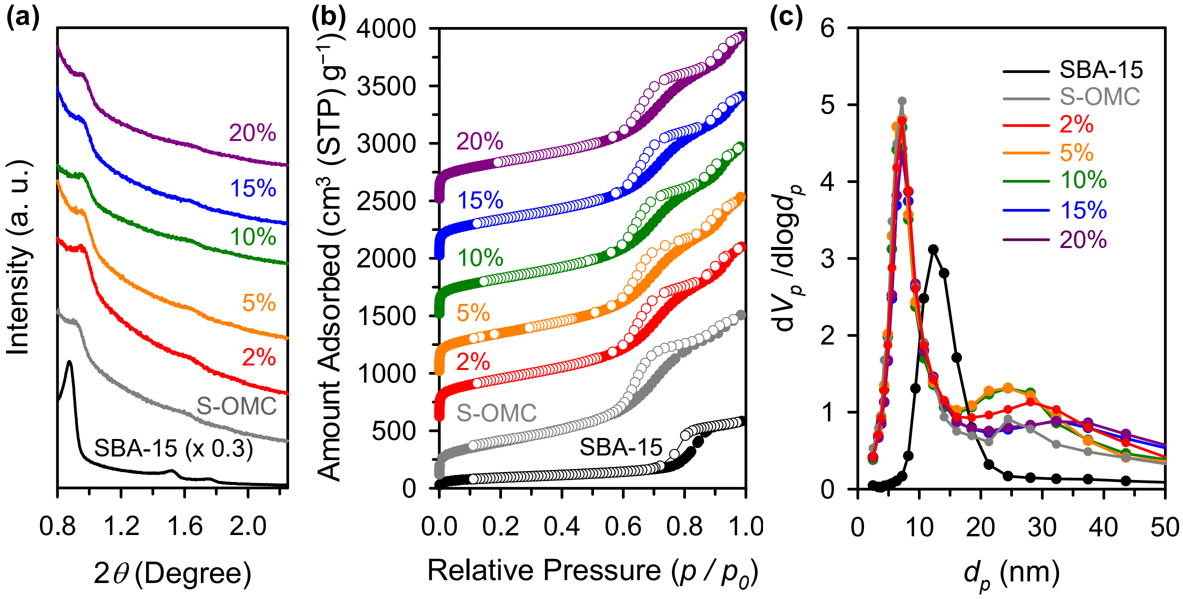

Figure 4.2. (a) Small-angle XRD patterns and (b) N_2 adsorption–desorption isotherms of SBA-15, S-OMC, and WS_x@OMCs. Filled circles and empty circles represent the adsorption and desorption branches, respectively. The isotherms of the S-OMC, 2 wt.%, 5 wt.%, 10 wt.%, 15 wt.%, and 20 wt.% WS_x@OMC were offset by 100, 600, 1000, 1500, 2000, and 2500 cm^3 g^{-1}, respectively, for clarity. (c) The BJH pore size distributions of SBA-15, S-OMC, and WS_x@OMCs obtained from the adsorption branches of their isotherms.

Table 4.2. BET surface areas, total pore volumes, and pore sizes obtained from nitrogen adsorption–desorption analysis.

Sample	BET surface area [a] (m^2 g^{-1})	Pore volume [b] (cm^3 g^{-1})	Pore size [c] (nm)
SBA-15	337	0.90	12.2
OMC@SBA-15	464	0.52	7.2–10.7
S-OMC	1112	2.18	7.2, 24.4
2% WS_x@OMC	1265	2.32	7.2, 28.1
2% WS_x@OMC_20 h	1243	2.28	7.2, 32.3
5% WS_x@OMC	1259	2.37	7.2, 24.4
10% WS_x@OMC	1172	2.28	7.2, 24.4
15% WS_x@OMC	1217	2.18	7.2, 32.3
20% WS_x@OMC	1210	2.21	7.2, 32.3

[a] BET surface area was obtained in the relative pressure range of 0.05–0.2.
[b] Pore volume was determined at the relative pressure of 0.98–0.99.
[c] Pore size was obtained by using BJH method from the adsorption branch.

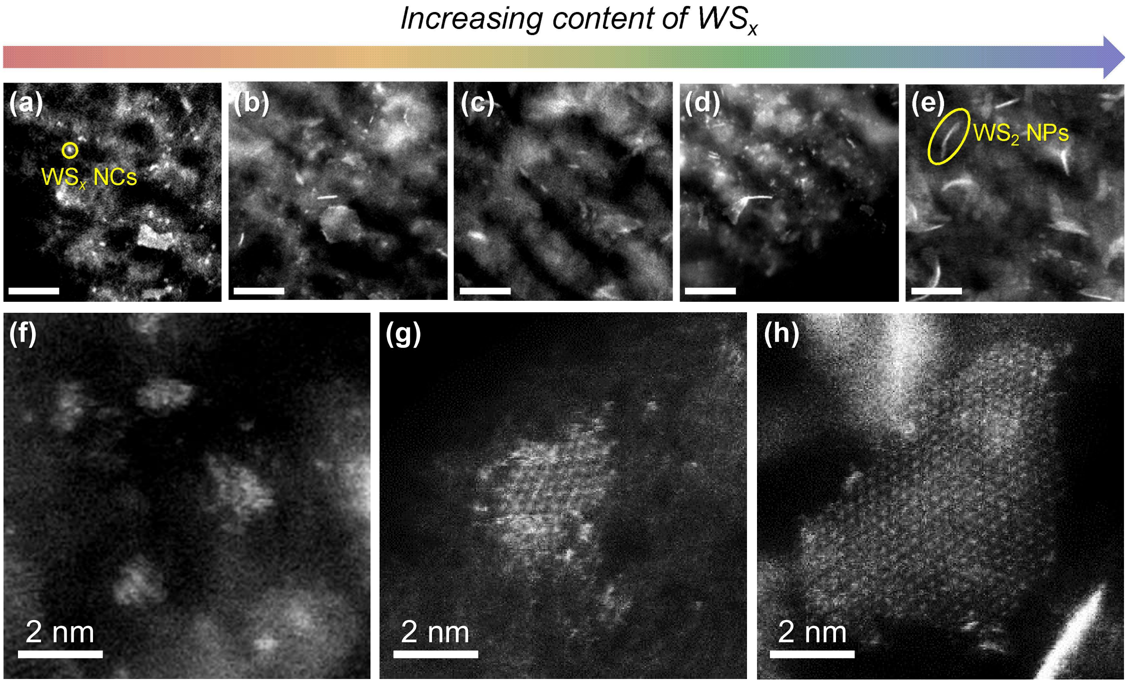

Figure 4.3. HAADF-STEM images of (b) 2% (c) 5% (d) 10% (e) 15%, and (f) 20% WS_x@OMCs (Scale bar: 10 nm). Atomic-resolution HAADF-STEM images for (g) WS_x NCs, (h) WS_x NCs + WS_2 NPs, and (i) WS_2 NPs. The brightness and contrast of the STEM images were modified to clarify the presence of NCs and NPs.

High-angle annular dark field scanning transmission electron microscopy (HAADF-STEM) images indicated that WS_x nanostructures were uniformly dispersed on the carbon nanorod arrays as subnanometer-sized nanoclusters and WS_2 nanoplates (**Figure 4.3a–e**). For the smallest WS_x loading (2% WS_x@OMC), most WS_x existed in the form of nanoclusters rather than WS_2 nanoplates (**Figure 4.3a**). As the WS_x loading was increased from 2 to 20 wt.%, mono- and few-layer nanoplates became dominant at the expense of the nanoclusters (**Figure 4.3a–e**). Atomic resolution HAADF-STEM images further confirmed the atomic arrangement of the ultrasmall WS_x nanoclusters and WS_2 nanoplates (**Figure 4.3f–h**). The average crystallite size of the basal planes in the WS_2 nanoplates were smaller than 5 nm, as determined by the TEM images. This indicates that mesopores of the OMC@SBA-15 composites effectively limit the growth of WS_2 nanoplates in the lateral directions, remaining the basal plane size into few nanometers. We also suggest that the micropores (< 2 nm) present within the frameworks of OMC structures could play an important role in forming the WS_x nanoclusters.

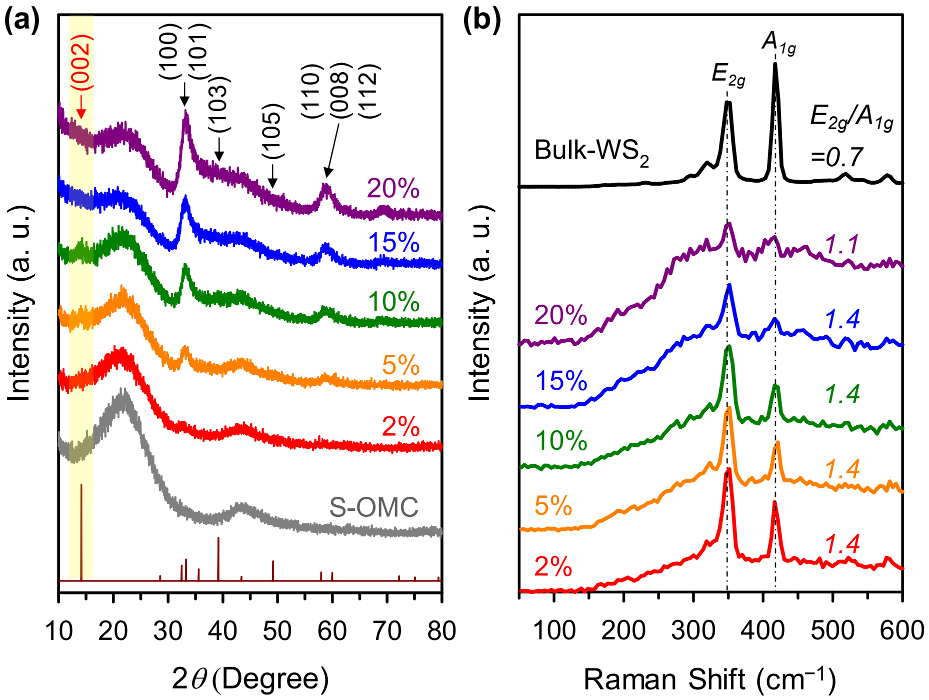

Figure 4.4. (a) High-angle XRD patterns of WS_x@OMCs and S-OMC. The vertical bars represent the WS_2 standard (JCPDS No. 71-4832). (b) Raman spectra for WS_x@OMCs and bulk-WS_2.

The XRD patterns of WS_x@OMCs were commensurate with that of the WS_2 standard (JCPDS No. 71-4832) (**Figure 4.4a**). Reflections for (002), (103) and (105) directions in the XRD patterns of WS_x@OMC were featureless, indicating the formation of mono- and few-layer WS_2 nanoplates, which is consistent with TEM observations. Accordingly, the highly overlapping peaks at 32.5° and

58.0° mainly originate from the reflections in (100) and (110) planes of the basal surface. With increased WS_x loadings, the intensity of the two XRD peaks increased while their full width at half maximum was almost invariant, indicating a similar basal plane size of WS_2 nanoplates, as confirmed by TEM analysis. Two peaks around 22° and 43° overlapped with the peaks from amorphous sulfur-doped OMC (S-OMC) (**Figure 4.4a**). Monolayer feature of the WS_2 nanoplates in WS_x@OMCs was further verified *via* Raman spectroscopy (**Figure 4.4b**). The two pronounced peaks at 350 and 417 cm^{-2} corresponded to the in-plane vibrational mode (E_{2g}) and out-of-plane vibrational mode (A_{1g}) in 2H-WS_2, respectively.[40,61] All WS_x@OMC samples showed the intensity ratio of E_{2g} to A_{1g} (E_{2g}/A_{1g}) greater than unity, which is a unique character of monolayer structure.[40,61] Moreover, the A_{1g} peaks were positioned at 417 cm^{-2} in all WS_x@OMC samples, which is in good agreement with the frequency reported for WS_2 monolayers.[40,61]

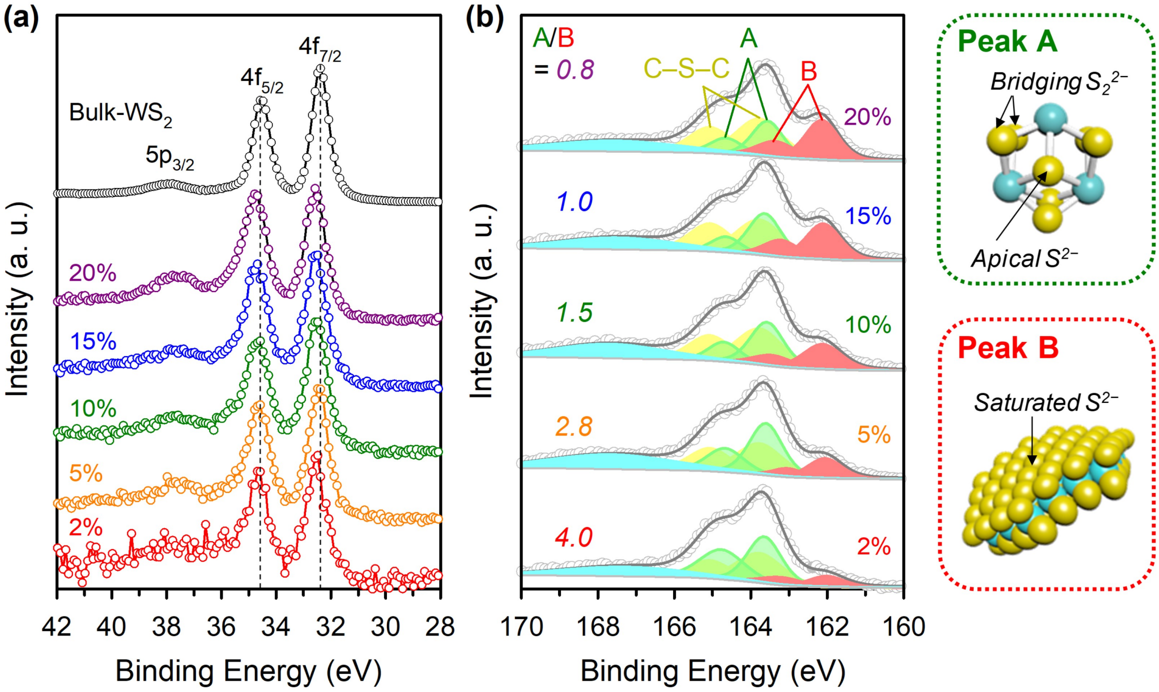

Figure 4.5. (a) W 4f XPS spectra for bulk-WS_2 and WS_x@OMCs. (b) S 2p XPS spectra for WS_x@OMCs. Peak A and B indicate bridging S_2^{2-}/apical S^{2-} and saturated S^{2-} ligands, respectively. The peak area ratio of peak A to B (A/B) increases with decrease in WS_x content.

The chemical state of WS_x within the composite was assessed by XPS. All WS_x@OMCs showed similar W 4f XPS spectra to that of bulk WS_2, with two major peaks at 32.6 eV (W $4f_{7/2}$) and 34.8 eV (W $4f_{5/2}$) (**Figure 4.5a**), which matched the W^{4+} state in WS_2.[44] Slight peak shifts toward higher binding energies in WS_x@OMCs compared to bulk WS_2 suggested surface oxidation of W caused by exposure to air during manipulation. In the deconvoluted S 2p XPS spectra (**Figure 4.5b**),

WS_x@OMCs showed doublet peaks at 162.3 eV (S $2p_{3/2}$) and 163.5 eV (S $2p_{1/2}$) (area in pink, denoted as ‘B’), which corresponded to S^{2-} ligands in WS_2.[44,62] The other doublet peaks appearing at 164.1 eV (S $2p_{3/2}$) and 165.1 eV (S $2p_{1/2}$) (area in green, denoted as ‘A’) are attributed to bridging S_2^{2-} and/or apical S^{2-}, consisting of WS_x nanoclusters.[62] The changes in deconvoluted peak areas for a series of WS_x@OMCs suggest that the peaks for S^{2-} ligand gradually evolved as the WS_x loading increased at the expense of the peaks for bridging S_2^{2-} and/or apical S^{2-} (**Figure 4.5b**). Thus, the decreasing peak area ratio of peak A to B (A/B) implies a decreasing fraction of the WS_x nanoclusters, which were consumed in the formation of WS_2 nanoplates. The doublet colored yellow at 163.8 eV and 165.1 eV originated from sulfur-doped carbon species (C–S–C).[63,64] The broad peak centered around 167.3–168.7 eV was attributed to sulfate groups, which could result from the oxidation of the catalyst upon exposure to air. The HAADF-STEM, XRD, Raman, and XPS results suggested a coherent growth picture that WS_x subnanometer clusters grow in a horizontal direction along the carbon surface with increased WS_x loading, yielding monolayer WS_2 nanoplates at the expense of WS_x nanoclusters.

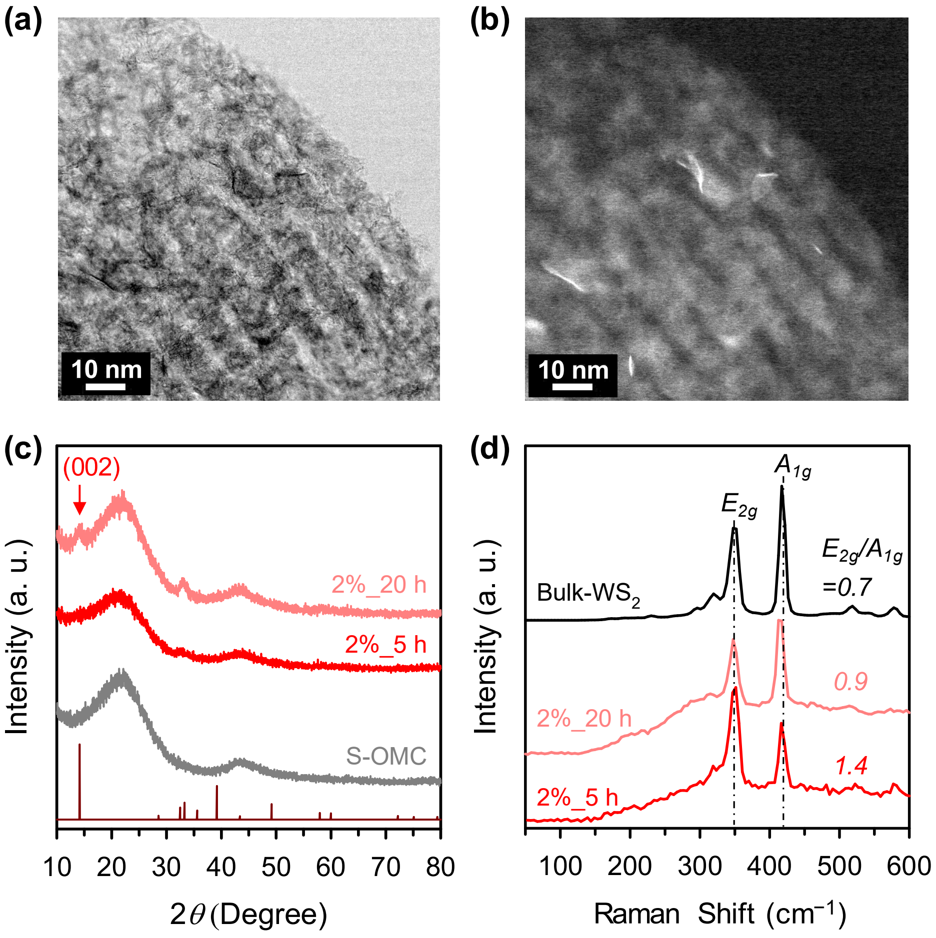

Figure 4.6. (a) BF-STEM and (b) HAADF-STEM images, (c) XRD patterns, and (d) Raman spectra of 2% WS_x@OMCs prepared with different sulfidation times of 5 h and 20 h.

The growth mechanism of WS_x was further verified with a time-dependent growth experiment using the 2% WS_x@OMC sample. When the sulfidation time was increased from 5 h to 20 h, most of the nanoclusters disappeared and the WS_2 nanoplates became the dominant species as confirmed by bright-field scanning TEM (BF-STEM), HAADF-STEM, and XRD analyses (**Figure 4.6a–c**). Moreover, Raman spectra revealed decreased E_{2g}/A_{1g} ratio with increasing reaction time, indicating the emergence of few-layer WS_2 nanoplates (**Figure 4.6d**). Scanning electron microscopy (SEM) image, nitrogen adsorption-desorption analysis, and small-angle XRD patterns showed that the mesoporous structures were maintained, even with the prolonged sulfidation time (**Figure 4.7 and Table 4.2**).

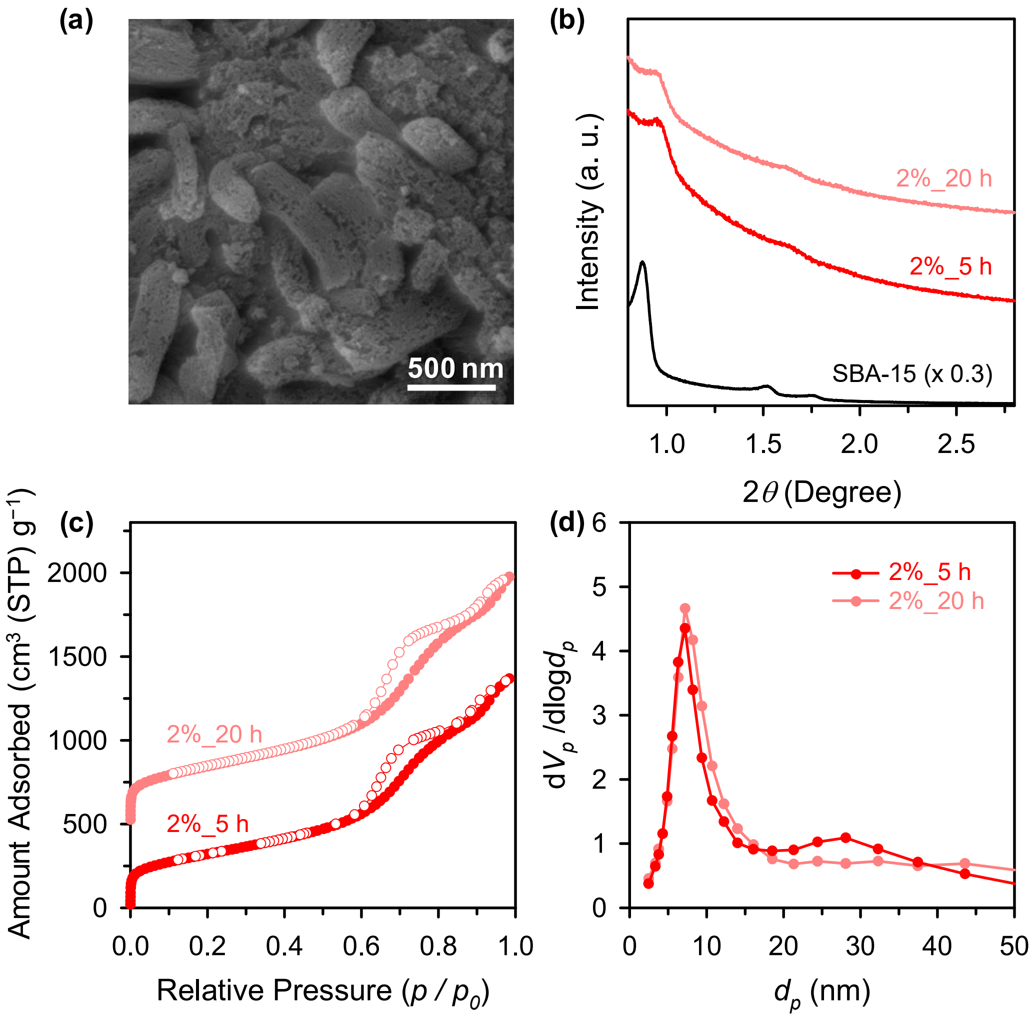

Figure 4.7. (a) SEM image, (b) small-angle XRD patterns for 2% WS_x@OMCs prepared with different sulfidation times of 5 h and 20 h. (c) Nitrogen adsorption–desorption isotherms of the samples. Filled circles and empty circles represent the adsorption and desorption branches, respectively. The isotherms of the 20 h sample was offset by 500 cm^3 g^{-1}, for clarity. (d) The BJH pore size distributions obtained from the adsorption branches of their isotherms.

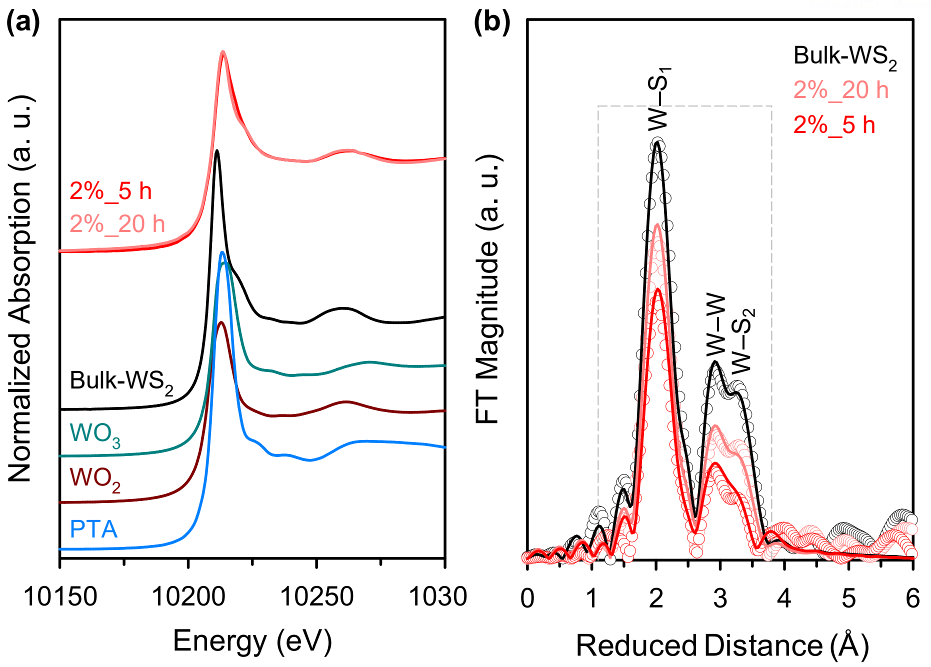

Figure 4.8. (a) W L_3-edge XANES spectra and (b) fitted RDF of 2% WS_x@OMCs prepared with different sulfidation times of 5 h and 20 h, displayed with reference samples. The empty circles and solid lines represent raw data and fitted results, respectively.

Table 4.3. Structural parameters derived from the fitted EXAFS for Bulk-WS_2 and 2% WS_x@OMCs prepared with different sulfidation times of 5 h and 20 h.

Sample	Shell [b]	CN	R (Å)	ΔE_0	σ^2 [a] ($\times 10^{-3}$ Å^{-2})	R factor (%)
Bulk-WS_2	W–S_1	6	2.394 (8)	6.0	1.9 (9)	0.96
	W–W	6	3.161 (16)	6.4	2.4 (9)	
	W–S_2	6	3.949 (25)	6.0	4.4 (30)	
2%_20 h	W–S_1	4.8 ± 0.5	2.399 (5)	7.1	1.9	1.31
	W–W	3.8 ± 0.6	3.151 (12)	5.3	2.4	
	W–S_2	3.8 ± 0.6	3.952 (22)	7.1	4.4	
2%_5 h	W-S_1	3.8 ± 0.4	2.408 (8)	8.7	1.9	3.13
	W–W	2.6 ± 0.6	3.129 (23)	2.6	2.4	
	W–S_2	2.6 ± 0.6	3.996 (44)	8.7	4.4	

[a] Debye-Waller parameter (σ^2) was fixed to the same value in the same type of bond.
[b] Bonds of W–W and W–S_2 were set to have the same CN.

Detailed atomic structure of WS_x species in these samples was investigated by XAS analysis (**Figure 4.8**). In the W L_3-edge X-ray absorption near-edge spectroscopy (XANES) spectra, the edge lines of the spectra for the two 2% WS_x@OMCs overlapped, indicating that the oxidation states of W were the same regardless of the sulfidation time (**Figure 4.8a**). The radial distribution function (RDF) of the Fourier transforms of k^3-weighted W L_3-edge Extended X-ray Absorption Fine Structure (EXAFS) spectra exhibited three major peaks, which were assigned as sulfur shells (2.03 Å and 3.28 Å) and a tungsten shell (2.92 Å) (**Figure 4.8b**).[65,66] To scrutinize the structural parameters, EXAFS spectra were fitted with a model, 2H-WS_2.[57] The fitted parameters for bulk-WS_2 were in good agreement with the literature values for 2H-WS_2 (**Table 4.3**).[65,66] For the sulfidation-time controlled samples, the refined CNs for the three bonds increased with increasing sulfidation time. As WS_2 nanoplates have higher coordination numbers in W–S and W–W bonds compared to WS_x nanoclusters (see dotted box in **Figure 4.1**), this result corroborated the formation of WS_2 nanoplates at the expense of WS_x nanoclusters. This control experiment further demonstrated the role of WS_x nanoclusters as seeds to form WS_2 nanoplates, which was consistent with the results obtained from loading-dependent experiment. Interestingly, the growth behavior of WS_x was different from that of MoS_2. As reported previously, MoS_2 grows in a layer-by-layer manner to yield nanoplates, whose layer numbers increase with MoS_2 loading (**Figure 3.1** in chapter 3).[10]

Table 4.4. Unit potential energies (eV, $\mu^{n}_{\mathrm{MS_2}}$) and stacking energies ($\Delta E_{stacking}$) of MS_2 cluster models (M = W, Mo).

		$(MS_2)_3$	**$(MS_2)_{12}$**	**$(MS_2)_{27}$**	**$(MS_2)_{bulk}$**
WS_2	Free-standing (1L) [a]	−5.56	−7.17	−7.94	−9.62
	On-top (2L) [b]	−5.89	−7.48	−8.21	−9.92
	Stacking energy ($\Delta E_{stacking}$)	−0.33	−0.31	−0.27	−0.30
MoS_2	Free-standing (1L) [a]	−4.37	−5.96	−6.70	−8.26
	On-top (2L) [b]	−4.73	−6.32	−7.07	−8.59
	Stacking energy ($\Delta E_{stacking}$)	−0.36	−0.36	−0.37	−0.33

[a] Free-standing (1L) denotes the $\mu^{n}_{\mathrm{MS_2}}$ of free-standing single layer MS_2 cluster model.

[b] On-top (2L) denotes the $\mu^{n}_{\mathrm{MS_2}}$ of on-top double layer MS_2 cluster model.

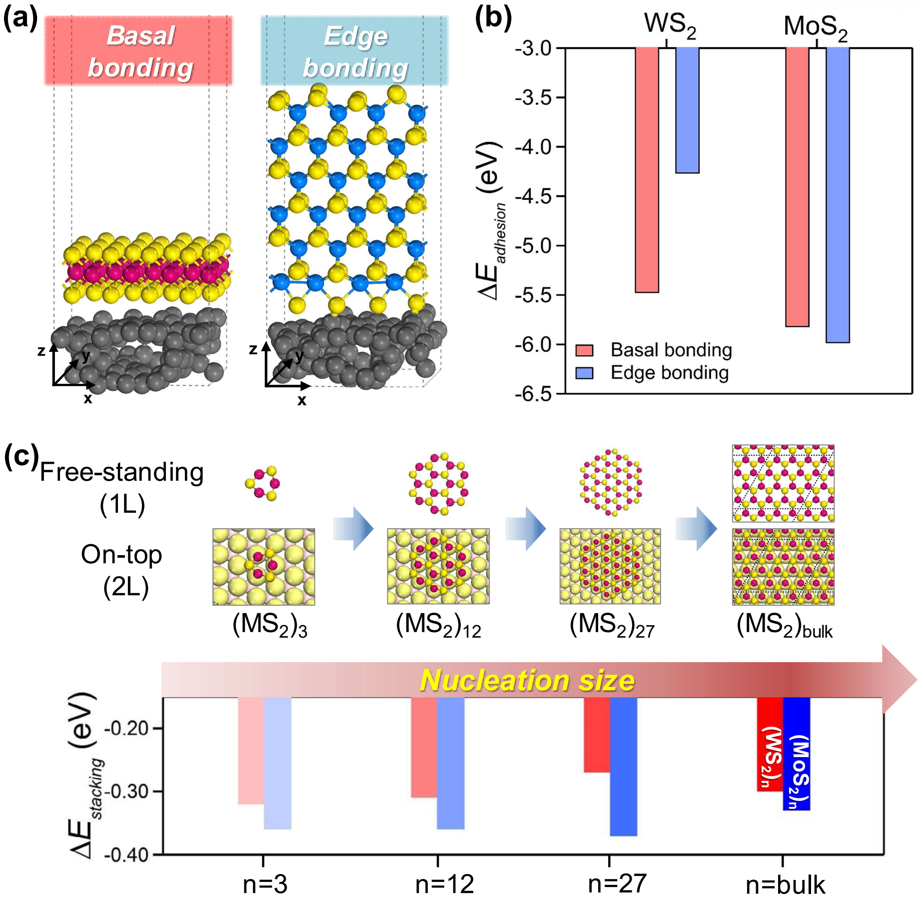

Figure 4.9. (a) Interface model systems used to calculate $\Delta E_{adhesion}$ of MS_2 sheets on a carbon support. Side views of basal and edge-on bonded MS_2 (M = W or Mo) sheets on a carbon support. (b) Vertical bar graph presenting the $\Delta E_{adhesion}$ values of MS_2 sheets on a carbon support in basal and edge-on bonding modes. (c) Top views of $(MS_2)_n$ cluster and bulk models for unit potential energy calculation, where n = 3, 12, 27, and bulk state, respectively. Vertical bar graph presenting stacking energy, i.e., the difference in the unit potential energies ($\mu^{n}_{\mathrm{MS}_2}$) in 1L and 2L $(MS_2)_n$ cluster and bulk models.

To understand the contrasting growth behavior of the two MS_2 (M = W and Mo) species, the adhesion energy ($\Delta E_{adhesion}$) on amorphous carbon was calculated using DFT calculations (see section 4.3.2 for computational details). Since the OMC support is constructed with amorphous carbon, this computational model may well mimic the experimental conditions. As shown in **Figure 4.9a**, two bonding models were considered: ‘basal bonding’ where the basal planes of MS_2 were parallel to the surface of the carbon support, and ‘edge bonding’ where the edge planes of MS_2 are attached to the carbon surface. A more negative adhesion energy was observed in the basal bonding as compared to the edge bonding for the WS_2 model, whereas the opposite results were obtained for MoS_2 (**Figure 4.9b**). The adhesion energy calculations suggested that WS_2 and MoS_2 favored basal plane and edge plane bonding modes with the carbon support, respectively.

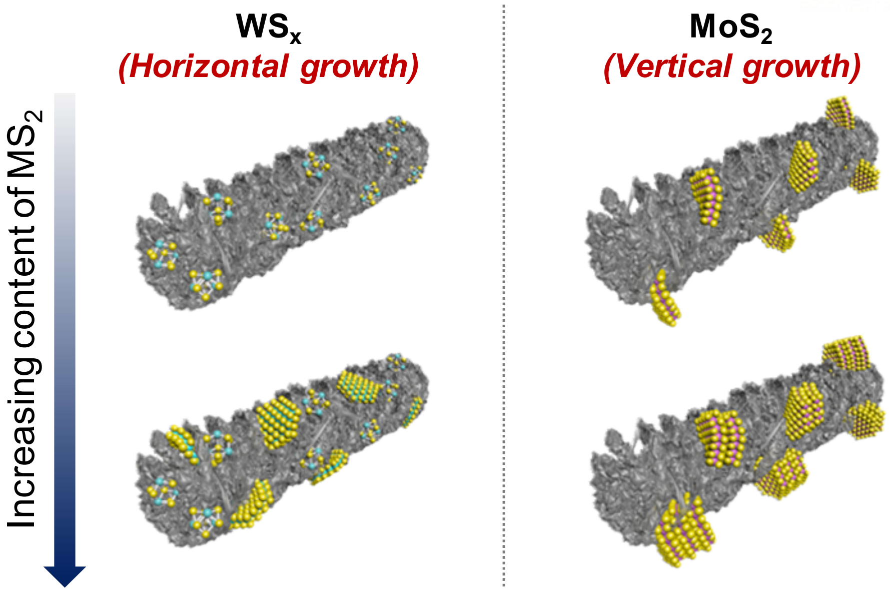

Figure 4.10. Growth orientation of MS_x (M = W or Mo).

Next, we compared the stacking energies of WS_2 and MoS_2 to investigate their growth tendencies. The stacking energy ($\Delta E_{stacking}$) describes the interaction between interlayers, and is calculated from the difference of unit potential energies ($\mu^n_{MS_2}$) in one-layer (1L) and two-layer (2L) $(MS_2)_n$ clusters (see section 4.3.3 for computational details). The calculated unit potential energies and stacking energy values (**Figure 4.9c and Table 4.4**) revealed that WS_2 sheets were more stable as single layers than MoS_2, regardless of the size of the clusters. Further, **Figure 4.9c** clearly shows that the stacking energies of MoS_2 are larger than those of WS_2 for all nucleation sizes, indicating that MoS_2 clusters prefer to stack in a multilayer mode. As a result, the favored intrinsic growth modes of TMD species are horizontal and vertical stacking for WS_2 and MoS_2, respectively.

The DFT calculations suggested that WS_2 preferentially adheres to the carbon surface by basal bonding and subsequent growth occurs in the thermodynamically favorable basal plane direction, which was in good agreement with the experimental results. In contrast, MoS_2 adheres to the carbon surface in an edge-on bonding mode, and growth preferentially occurs in the edge plane direction in a layer-by-layer manner.[13] **Figure 4.10** depicts the growth behavior of these TMDs on the surface of the carbon support.

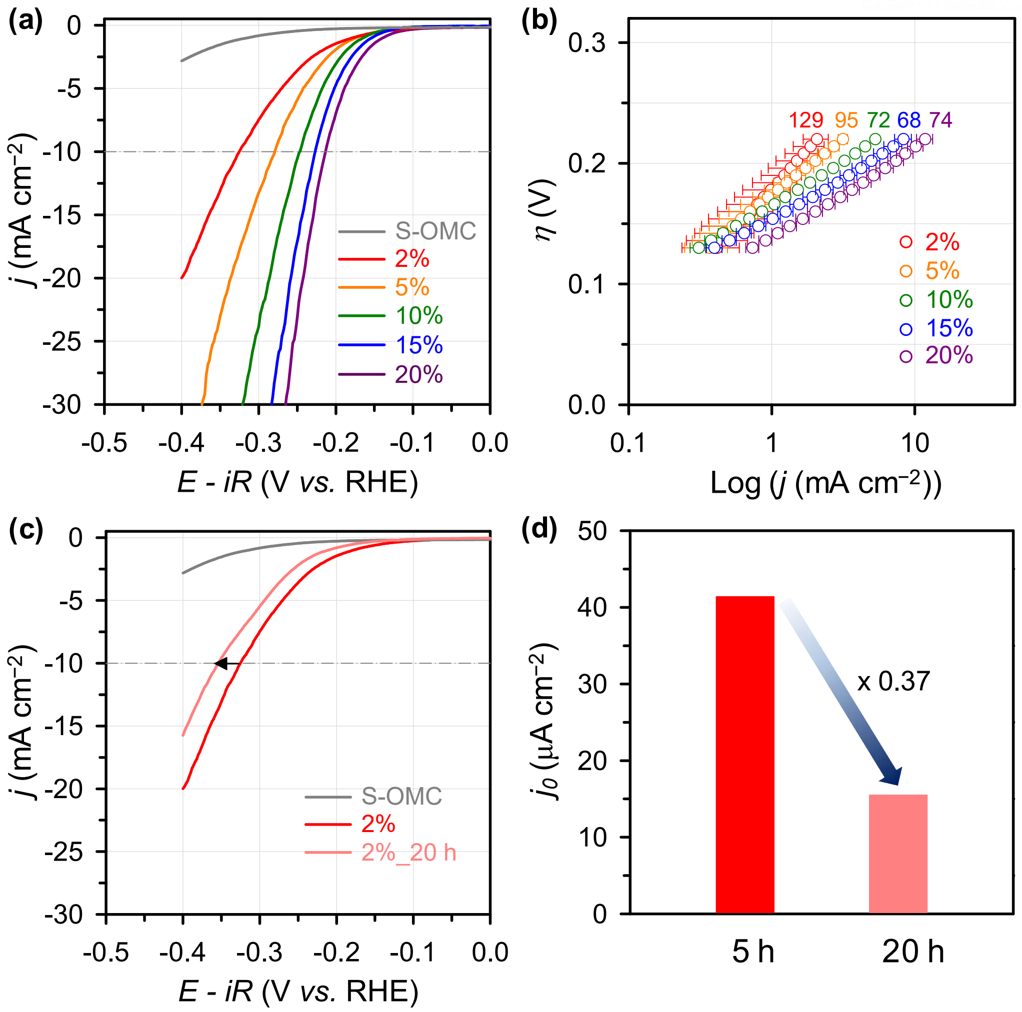

Figure 4.11. (a) LSV curves and (b) Tafel plots for WS_x@OMCs. (c) LSV curves and (d) exchange current densities (j_0) for 2% WS_x@OMCs prepared with different sulfidation times of 5 h and 20 h.

We next investigated the electrocatalytic activities of the monolayer WS_x@OMC catalysts for the HER using a three-electrode setup in 0.5 M H_2SO_4 (see section 2.2 for the details). For comparison, the HER activity of S-OMC was also measured. For all samples, linear sweep voltammetry (LSV) curves were measured three times and the average data were used. The LSV data were presented after *iR* correction, for which series resistance was measured using the electrochemical impedance spectroscopy (EIS) measurements. The LSV curves (**Figure 4.11a**) revealed that S-OMC exhibited negligible HER activity as evidenced from the large overpotential (> 400 mV) required to drive the current density of −10 mA cm^{-2}. In contrast, the WS_x@OMC catalysts showed good HER performance, driving −10 mA cm^{-2} in the overpotential range of 213–325 mV (**Table 4.5**). The Tafel slopes of the catalysts (**Figure 4.11b and Table 4.5**) were approximately 68–129 mV dec^{-1}. We point out that a variety of factors, such as catalyst ink composition and catalyst loading, contribute concomitantly to these device-oriented activity metrics.[67]

Table 4.5. HER activities of WS_x@OMCs expressed as overpotential at −10 mA cm^{-2}, Tafel slope, and exchange current density.

Sample	**Overpotential at 10 mA cm^{-2} (V)**	**Tafel slope [a] (mV dec^{-1})**	**Exchange current density [b] (A cm^{-2})**
2% WS_x@OMC	325	129	4.14×10^{-5}
2% WS_x@OMC_20 h	354	117	1.55×10^{-5}
5% WS_x@OMC	279	95	1.50×10^{-5}
10% WS_x@OMC	247	72	5.02×10^{-6}
15% WS_x@OMC	226	68	5.30×10^{-6}
20% WS_x@OMC	213	74	1.34×10^{-5}

[a,b] The Tafel slopes and exchange current densities were derived from the linear portion of the corresponding Tafel plots.

In order to extract only the structural effect while excluding the WS_x loading effect, the HER activities of 2% WS_x@OMC samples with different sulfidation times (5 h and 20 h) were compared. As characterized earlier with TEM, XRD, Raman, and XAS, the 5 h and 20 h samples were mainly comprised of ultrasmall nanoclusters and nanoplates, respectively. **Figure 4.11c** shows that the 5 h and 20 h samples required overpotential of 325 and 352 mV to drive the current density of −10 mA cm^{-2}, respectively, (**Table 4.5**). They achieved good HER performance even with a very small geometric loading of WS_x (as low as 4.6 μg cm^{-2}). In all potential region, the 5 h sample showed higher current densities than the 20 h sample. To gain further insight into their intrinsic activities, exchange current densities (j_0) were investigated by obtaining the x-intercept values of their Tafel plots (**Table 4.5**). An approximately 3-fold increase in j_0 was achieved in the 5 h sample, indicating an intrinsically faster electron-transfer rate for the HER than the 20 h sample (**Figure 4.11d and Table 4.5**).[68] The higher HER activity of the 5 h sample originated from the maximized active sulfur site densities in the clusters. WS_2 nanoplates contain a relatively low density of active sulfur sites, leaving the high density of the basal surface catalytically inert.

XPS and electrochemical analyses suggested that bridging S_2^{2-} species abundant in WS_x nanoclusters were more relevant to the catalytically active centers for initial hydrogen adsorption in the HER than the S^{2-} ligands, which are dominant in WS_2 nanoplates. Active sulfur sites for the adsorption of hydrogen atoms have been rarely explored in WS_x-based catalysts in the HER. Even for widely investigated MoS_x-based catalysts, the active sulfur site has not yet been unambiguously established due to the diverse chemical states of sulfur species, namely bridging S_2^{2-}, terminal S_2^{2-}, unsaturated S^{2-}, or apical S^{2-}.[69–74] A promising approach is to design a molecular mimic cluster compounds that are comprised of specific sulfur sites. For instance, Wu and coworkers reported $[Mo_2S_{12}]^{2-}$ clusters as a dimeric molecular analogue for MoS_2 edge sites, only possessing terminal and bridging S_2^{2-} ligands. They suggested that bridging S_2^{2-} sites were the preferred hydrogen adsorption site with a free energy near zero (−0.05 eV).[49] Yeo and co-workers revealed a linear correlation between turnover frequencies and the percentage of S species with higher binding energies in XPS spectra.[71] This suggested bridging S_2^{2-} species as the potential catalytic active sites, and apical S^{2-} was excluded through density functional simulations. However, some resent works proposed that the bridging S_2^{2-} sites diminishes during HER,[69–73] and they are transformed into unsaturated S^{2-} species.[73] Similar to the findings for MoS_x catalysts, we propose that the active sulfur sites in WS_x could initiate from the bridging disulfide ligands (S_2^{2-}), which are subsequently converted to reactive undercoordinated sulfur sites. Advanced *in situ* spectroelectrochemical studies of WS_x-based catalysts could reveal the active sulfur species by elucidating structural changes during the electrochemical reactions.

4.5. CONCLUSION

In summary, we have presented a combined experimental and computational study that demonstrates the preferential horizontal growth of WS_x nanoclusters to form monolayer WS_2 nanoplates on a carbon support, and their structure–activity correlation in the HER. The horizontal growth of WS_x is in stark contrast to that for MoS_2 nanoplates, which adhere to carbon surfaces in a vertical, edge-on bonding mode, promoting subsequent layer stacking. A sulfidation time-dependent control experiment further corroborated the formation of WS_2 nanoplates with consumption of WS_x nanoclusters. Notably, the sample prepared with a short sulfidation time, mainly comprised of WS_x nanoclusters, showed higher HER activity than the sample prepared with a long sulfidation time, which contained WS_2 nanoplates, indicating that bridging S_2^{2-} species abundant in nanoclusters are the more likely catalytic sites. We believe that these findings will serve as design guidelines for layered TMDs-carbon hybrid catalysts, which is valuable for both fundamental studies and a wide range of applications.

4.6. REFERENCES

1. Li, H.; Wu, J.; Yin, Z.; Zhang, H. *Acc. Chem. Res.* **2014**, *47*, 1067−1075.
2. Wang, H.; Yuan, H.; Hong, S. S.; Li, Y.; Cui, Y. *Chem. Soc. Rev.* **2015**, *44*, 2664−2680.
3. Jung, Y.; Shen, J.; Liu, Y.; Woods, J. M.; Sun, Y.; Cha, J. J. *Nano Lett.* **2014**, *14*, 6842−6849.
4. Backes, C.; Smith, R. J.; McEvoy, N.; Berner, N. C.; McCloskey, D.; Nerl, H. C.; O'Neill, A.; King, P. J.; Higgins, T.; Hanlon, D.; Scheuschner, N.; Maultzsch, J.; Houben, L.; Duesberg, G. S.; Donegan, J. F.; Nicolosi, V.; Coleman, J. N. *Nat. Commun.* **2014**, *5*, 4576.
5. Jin, H.; Ahn, M.; Jeong, S.; Han, J. H.; Yoo, D.; Son, D. H.; Cheon, J. *J. Am. Chem. Soc.* **2016**, *138*, 13253−13259.
6. Splendiani, A.; Sun, L.; Zhang, Y.; Li, T.; Kim, J.; Chim, C.-Y.; Galli, G.; Wang, F. *Nano Lett.* **2010**, *10*, 1271−1275.
7. Gutiérrez, H. R.; Perea-López, N.; Elías, A. L.; Berkdemir, A.; Wang, B.; Lv, R.; López-Urías, F.; Crespi, V. H.; Terrones, H.; Terrones, M. *Nano Lett.* **2013**, *13*, 3447−3454.
8. Scrace, T.; Tsai, Y.; Barman, B.; Schweidenback, L.; Petrou, A.; Kioseoglou, G.; Ozfidan, I.; Korkusinski, M.; Hawrylak, P. *Nat. Nanotech.* **2015**, *10*, 603−607.
9. Yu, Y.; Huang, S.-Y.; Li, Y.; Steinmann, S. N.; Yang, W.; Cao, L. *Nano Lett.* **2014**, *14*, 553−558.
10. Seo, B.; Jung, G. Y.; Sa, Y. J.; Jeong, H. Y.; Cheon, J. Y.; Lee, J. H.; Kim, H. Y.; Kim, J. C.; Shin, H. S.; Kwak, S. K.; Joo, S. H. *ACS Nano*, **2015**, *9*, 3728−3739.
11. An, Y.-R.; Fan, X.-L.; Luo, Z.-F.; Lau, W.-M. *Nano Lett.* **2017**, *17*, 368−376.
12. Novoselov, K. S.; Jiang, D.; Schedin, F.; Booth, T. J.; Khotkevich, V. V.; Morozov, S. V.; Geim, A. K. *Proc. Natl. Acad. Sci.* **2005**, *102*, 10451−10453.
13. Coleman, J. N.; Lotya, M.; O'Neill, A.; Bergin, S. D.; King, P. J.; Khan, U.; Young, K.; Gaucher, A.; De, S.; Smith, R. J.; Shvets, I. V.; Arora, S. K.; Stanton, G.; Kim, H.-Y.; Lee, K.; Kim, G. T.; Duesberg, G. S.; Hallam, T.; Boland, J. J.; Wang, J. J.; Donegan, J. F.; Grunlan, J. C.; Moriarty, G.; Shmeliov, A.; Nicholls, R. J.; Perkins, J. M.; Grieveson, E. M.; Theuwissen, K.; McComb, D. W.; Nellist, P. D.; Nicolosi, V. *Science* **2011**, *331*, 568−571.
14. Ji, Q.; Zhang, Y.; Zhang, Y.; Liu, Z. *Chem. Soc. Rev.* **2015**, *44*, 2587−2602.
15. Zhu, C.; Mu, X.; van Aken, P. A.; Yu, Y.; Maier, J. *Angew. Chem. Int. Ed.* **2014**, *53*, 2152−2156.
16. Zheng, X.; Xu, J.; Yan, K.; Wang, H.; Wang, Z.; Yang, S. *Chem. Mater.* **2014**, *26*, 2344−2353.
17. Duan, J.; Chen, S.; Chambers, B. A.; Andersson, G. G.; Qiao, S. Z. *Adv. Mater.* **2015**, *27*, 4234−4241.
18. Ouyang, Y.; Ling, C.; Chen, Q.; Wang, Z.; Shi, L.; Wang, J. *Chem. Mater.* **2016**, *28*, 4390−4396.
19. Li, H.; Tsai, C.; Koh, A. L.; Cai, L.; Contryman, A. W.; Fragapane, A. H.; Zhao, J.; Han, H. S.; Manoharan, H. C.; Abild-Pedersen, F.; Nørskov, J. K.; Zheng, X. *Nat. Mater.* **2016**, *15*, 48−53.
20. Merki, D.; Hu, X. *Energy Environ. Sci.* **2011**, *4*, 3878−3888.

21. Benck, J. D.; Hellstern, T. R.; Kibsgaard, J.; Chakthranont, P.; Jaramillo, T. F. *ACS Catal.* **2014**, *4*, 3957−3971.
22. Yang, J.; Shin, H. S. *J. Mater. Chem. A* **2014**, *2*, 5979−5985.
23. Yan, Y.; Xia, B.; Xu, Z.; Wang, X. *ACS Catal.* **2014**, *4*, 1693−1705.
24. Voiry, D.; Yang, J.; Chhowalla, M. *Adv. Mater.* **2016**, *28*, 6197−6206.
25. Jaramillo, T. F.; Jørgensen, K. P.; Bonde, J.; Nielsen, J. H.; Horch, S.; Chorkendorff, I. *Science* **2007**, *317*, 100−102.
26. Jaramillo, T. F.; Bonde, J.; Zhang, J.; Ooi, B.-L.; Andersson, K.; Ulstrup, J.; Chorkendorff, I. *J. Phys. Chem. C* **2008**, *112*, 17492−17498.
27. Chen, Z.; Cummins, D.; Reinecke, B. N.; Clark, E.; Sunkara, M. K.; Jaramillo, T. F. *Nano Lett.* **2011**, *11*, 4168−4175.
28. Kibsgaard, J.; Chen, Z.; Reinecke, B. N.; Jaramillo, T. F. *Nat. Mater.* **2012**, *11*, 963−969.
29. Kibsgaard, J.; Jaramillo, T. F.; Besenbacher, F. *Nat. Chem.* **2014**, *6*, 248−253.
30. Wang, H.; Lu, Z.; Xu, S.; Kong, D.; Cha, J. J.; Zheng, G.; Hsu, P.-C.; Yan, K.; Bradshaw, D.; Prinz, F. B.; Cui, Y. *Proc. Natl. Acad. Sci.* **2013**, *110*, 19701−19706.
31. Xie, J.; Zhang, J.; Li, S.; Grote, F.; Zhang, X.; Zhang, H.; Wang, R.; Lei, Y.; Pan, B.; Xie, Y. *J. Am. Chem. Soc.* **2013**, *135*, 17881−17888.
32. Lukowski, M. A.; Daniel, A. S.; Meng, F.; Forticaux, A.; Li, L.; Jin, S. *J. Am. Chem. Soc.* **2013**, *135*, 10274−10277.
33. Li, Y.; Wang, H.; Xie, L.; Liang, Y.; Hong, G.; Dai, H. *J. Am. Chem. Soc.* **2011**, *133*, 7296–7299.
34. Liao, L.; Zhu, J.; Bian, X.; Zhu, L.; Scanlon, M. D.; Girault, H. H.; Liu, B. *Adv. Funct. Mater.* **2013**, *23*, 5326−5333.
35. Li, D. J.; Maiti, U. N.; Lim, J.; Choi, D. S.; Lee, W. J.; Oh, Y.; Lee, G. Y.; Kim, S. O. *Nano Lett.* **2014**, *14*, 1228−1233.
36. Wu, Z.; Fang, B.; Bonakdarpour, A.; Sun, A.; Wilkinson, D. P.; Wang, D. *Appl. Catal. B* **2012**, *125*, 59−66.
37. Voiry, D.; Yamaguchi, H.; Li, J.; Silva, R.; Alves, D. C. B.; Fujita, T.; Chen, M.; Asefa, T.; Shenoy, V. B.; Eda G.; Chhowalla, M. *Nat. Mater.* **2013**, *12*, 850−855.
38. Tran, P. D.; Chiam, S. Y.; Boix, P. P.; Ren, Y.; Pramana, S. S.; Fize, J.; Artero, V.; Barber, J. Novel *Energy Environ. Sci.* **2013**, *6*, 2452−2459.
39. Yang, J.; Yoiry, D.; Ahn, S. J.; Kang, D.; Kim, A. Y.; Chhowalla, M.; Shin, H. S. *Angew. Chem. Int. Ed.* **2013**, *52*, 13751−13754.
40. Cheng, L.; Huang, W.; Gong, Q.; Liu, C.; Liu, Z.; Li, Y.; Dai, H. *Angew. Chem. Int. Ed.* **2014**, *53*, 7860−7863.
41. Lin, J.; Peng, Z.; Wang, G.; Zakhidov, D.; Larios, E.; Yacaman, M. J.; Tour, J. M. *Adv. Energy Mater.* **2014**, *4*, 1301875.

42. Lukowski, M. A.; Daniel, A. S.; English, C. R.; Meng, F.; Forticaux, A.; Hamers, R. J.; Jin, S. *Energy Environ. Sci.* **2014**, *7*, 2608−2613.
43. Seo, B.; Jeong, H. Y.; Hong, S. Y.; Zak, A.; Joo, S. H. *Chem. Commun.* **2015**, *51*, 8334−8337.
44. Zhang, J.; Wang, Q.; Wang, L.; Li, X.; Huang, W. *Nanoscale* **2015**, *7*, 10391−10397.
45. Zhao, X.; Ma, X.; Sun, J.; Li, D.; Yang, X. *ACS Nano* **2016**, *10*, 2159−2166.
46. Faber, M. S.; Lukowski, M. A.; Ding, Q.; Kaiser, N. S.; Jin, S. *J. Phys. Chem. C* **2014**, *118*, 21347−21356.
47. Wang, D.-Y.; Gong, M.; Chou, H.-L.; Pan, C.-J.; Chen, H.-A.; Wu, Y.; Lin, M.-C.; Guan, M.; Yang, J.; Chen, C.-W.; Wang, Y.-L.; Hwang, B.-J.; Chen, C.-C.; Dai, H. *J. Am. Chem. Soc.* **2015**, *137*, 1587−1592.
48. Yoon, D.; Seo, B.; Lee, J.; Nam, K. S.; Kim, B.; Park, S.; Baik, H.; Joo, S. H.; Lee, K. *Energy Environ. Sci.* **2016**, *9*, 850−856.
49. Huang, Z.; Luo, W.; Ma, L.; Yu, M.; Ren, X.; He, M.; Polen, S.; Click, K.; Garrett, B.; Lu, J.; Amine, K.; Hadad, C.; Chen, W.; Asthagiri, A.; Wu, Y. *Angew. Chem. Int. Ed.* **2015**, *54*, 15181−15185.
50. Zhao, D; Feng, J.; Huo, Q.; Melosh, N.; Fredrickson, G. H.; Chmelka, B. F.; Stucky, G. D. *Science* **1998**, *279*, 548−552.
51. Delley, B. *J. Chem. Phys.* **1990**, *92*, 508−517.
52. Delley, B. *J. Chem. Phys.* **2000**, *113*, 7756−7764.
53. *Materials Studio 2016*, BIOVIA Inc.: San Diego, CA, **2016**.
54. Perdew, J. P.; Burke, K.; Ernzerhof, M. *Phys. Rev. Lett.* **1996***, 77*, 3865−3868.
55. Tkatchenko, A.; Scheffler, M. *Phys. Rev. Lett.* **2009**, *102*, 073005.
56. Monkhorst, H. J.; Pack, J. D. *Phys. Rev. B* **1976**, *13*, 5188.
57. Sun, M.; Nelson, A. E.; Adjaye, J. *J. Catal.* **2004**, *226*, 41−53.
58. Hansen, L. P.; Johnson, E.; Brorson, M.; Helveg, S. *J. Phys. Chem. C* **2014**, *118*, 22768−22773.
59. Zhang, W.; Wu, P.; Li, Z,; Yang, J. *J. Phys. Chem. C* **2011**, *115*, 17782−17787.
60. Raybaud, P.; Hafner, J.; Kresse, G.; Kasztelan, S.; Toulhoat, H. *J. Catal.* **2000**, *189*, 129−146.
61. Berkdemir, A.; Gutiérrez, H. R.; Botello-Méndez, A. R.; Perea-López, N.; Elías, A. L.; Chia, C.-I.; Wang, B.; Crespi, V. H.; López-Urías, F.; Charlier, J.-C.; Terrones, H.; Terrones, M. *Sci. Rep.* **2013**, *3*, 1755.
62. Tan, S. M.; Pumera, M. *ACS Appl. Mater. Interfaces* **2016**, *8*, 3948−3957.
63. Qie, L.; Chen, W.; Xiong, X.; Hu, C. Zou, F.; Hu, P.; Huang, Y. *Adv. Sci.* **2015**, *2*, 1500195.
64. Li, W.; Zhou, M.; Li, H.; Wang, K.; Cheng, S.; Jiang, K. A *Energy Environ. Sci.* **2015**, *8*, 2916−2921.
65. Schutte, W. J.; de Boer, J. L.; Jellinek, F. *J. Solid State Chem.* **1987**, *70*, 207−209.
66. Walton, R. I.; Hibble, S. J. *J. Mater. Chem.* **1999**, *9*, 1347−1355.

67. Chakthranont, P.; Kibsgaard, J.; Gallo, A.; Park, J.; Mitani, M.; Sokaras, D.; Kroll, T.; Sinclair, R.; Mogensen, M. B.; Jaramillo, T. F. *ACS Catal.* **2017**, *7*, 5399−5409.
68. Ding, Q.; Song, B.; Xu, P.; Jin, S. *Chem* **2016**, *1*, 699−726.
69. Casalongue, H. G. S.; Benck, J. D.; Tsai, C.; Karlsson, R. K. B.; Kaya, S.; Ng, M. L.; Pettersson, L. G. M.; Abild-Pedersen, F.; Nøskorv, J. K.; Ogasawara, H.; Jaramillo, T. F.; Nilsson, A. *J. Phys. Chem. C* **2014**, *118*, 29252−29259.
70. Lassalle-Kaiser, B.; Merki, D.; Vrubel, H.; Gul, S.; Yachandra, V. K.; Hu, X.; Yano, J. *J. Am. Chem. Soc.* **2015**, *137*, 314−321.
71. Ting, L. R. L.; Deng, Y.; Ma, L.; Zhang, Y.-J.; Peterson, A. A.; Yeo, B. S. *ACS Catal.* **2016**, *6*, 861−867.
72. Tran, P. D.; Tran, T. V.; Orio, M.; Torelli, S.; Truong, Q. D.; Nayuki, K.; Sasaki, Y.; Chiam, S. Y.; Yi, R.; Honma, I.; Barber, J.; Artero, V. *Nat. Mater.* **2016**, *15*, 640−646.
73. Deng, Y.; Ting, L. R. L.; Neo, P. H. L.; Zhang, Y.-J.; Peterson, A. A.; Yeo, B. S. *ACS Catal.* **2016**, *6*, 7790−7798.
74. Seo, B.; Joo, S. H. *Nano Convergence* **2017**, *4*, 19.

5

IMPACT OF OXIDE IN TUNGSTEN SULFIDE CATALYSTS ON THE HYDROGEN EVOLUTION REACTION

This chapter includes the published content: Seo, B.; Jeong, H. Y.; Hong, S. Y.; Zak, A.; Joo, S. H. *Chem. Commun.* **2015**, *51*, 8334−8337. Reproduced with permission. Copyright 2015 The Royal Society of Chemistry.

5.1. INTRODUCTION

Tungsten disulfides (WS$_2$), which have structural and electronic similarities with MoS$_2$, have been widely investigated as electrocatalysts for the hydrogen evolution reaction (HER).[1–10] The majority of WS$_2$-based HER electrocatalysts have been developed with a focus on the preparation of WS$_2$ nanostructures with controlled morphology, such as nanoflakes,[2,3] nanoribbons,[4] and vertically aligned nanosheets,[5,6] to preferentially expose active edge sites. In addition, the formation of 1T phase WS$_2$[7] and hybridization with graphene oxide[8] have been suggested as alternative routes to advanced WS$_2$-based HER electrocatalysts by increasing electrical conductivity. While these morphological and structural controls enabled the enhancement of HER activity, the modification of the oxidation state in catalytic materials also represents an important means for potentially enhancing the catalytic activity. However, the impact of the oxidation state on WS$_2$-based HER electrocatalysts has been unexplored before.

In this study, we demonstrated that the formation of WS$_2$ nanostructures hybridized with tungsten oxide can boost their electrocatalytic activity for the HER. The core–shell structured tungsten oxide–tungsten sulfide nanorods (W$_{18}$O$_{49}$@WS$_2$ NRs) showed higher HER performance compared to the WS$_2$ nanotubes (NTs). The oxide core facilitates electron transfer at the catalyst–electrode interface without the aid of additional conducting supports such as carbon nanomaterials. We also showed that the HER activities of W$_{18}$O$_{49}$@WS$_2$ NRs and WS$_2$ NTs, which underwent electrochemical oxidative pre-treatment; cyclic voltammetry (CV) cycles in 0.05 – 1.2 V (*vs.* reversible hydrogen electrode, RHE), are superior to those of the catalysts treated with reductive CV cycles under −0.3 – 0.6 V (*vs.* RHE). The result demonstrates that the electrochemically induced surface oxidation of WS$_2$-based nanostructures can also preferentially impact on their HER activity.

5.2. SYNTHESIS OF CATALYSTS

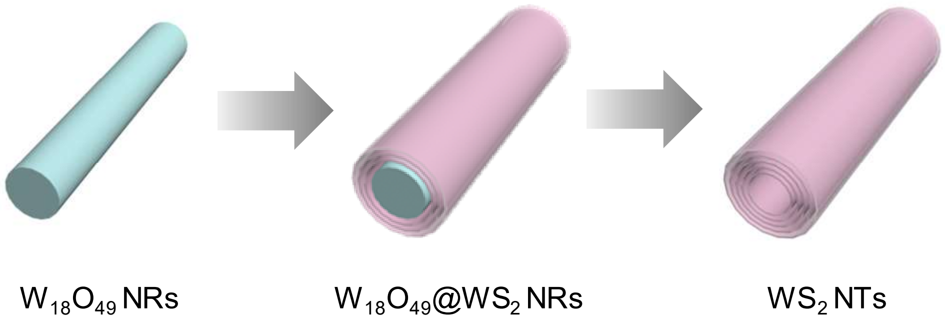

Figure 5.1. Schematic illustration for the formation of $W_{18}O_{49}$@WS_2 NRs and WS_2 NTs from sulfidation of $W_{18}O_{49}$ NRs.

Inorganic WS_2 NTs were synthesized *via* the combined reduction-sulfidation process[11] from tungsten oxide (WO_x) by the solid-gas reaction with hydrogen (H_2) and hydrogen sulfide (H_2S) at elevated temperatures of 840 °C over 6 h. The quartz reactor used in this synthesis was designed specifically for this process. The detailed growth mechanism of the NTs in this reaction has been recently elucidated.[12] The reaction mechanisms consists of two steps, namely growth of the oxide NRs, and subsequent sulfidation, under the flow of H_2S/H_2. In the first step of the mechanism, the spherical nanoparticle precursors of tungsten oxide (WO_x) grow into oxide NRs of approximately 5–50 μm length and 20–120 nm diameter. The oxide NRs subsequently undergo sulfidation in the second step, resulting in formation of WS_2 NTs. These oxide NRs grow as a result of partial reduction of the oxide precursor and formation of a volatile suboxide phase, which serves as a building material for one-dimensional crystal synthesis. The growth of the NRs results in the formation of a stable $W_{18}O_{49}$ ($WO_{2.72}$) phase, and followed by sulfidation. A fast reaction of H_2S with the oxide NRs leads to the quick formation of a number of cylindrical closed WS_2 layers encapsulating the oxide core. A slow diffusion-controlled reaction then leads to full replacement of the oxygen atoms with sulfur atoms, and subsequently to the synthesis of the hollow WS_2 NTs. In this study, partially sulfided sample in which few WS_2 layers encase the oxide NRs ($W_{18}O_{49}$@WS_2 NRs), was also prepared. To obtain this, the sulfidation was stopped in the early stage.

5.3. RESULTS AND DISCUSSION

$W_{18}O_{49}$@WS_2 NRs and WS_2 NTs were prepared *via* a controlled sulfidation reaction of $W_{18}O_{49}$ NRs, following previously reported methods (**Figure 5.1**).[11,12] The $W_{18}O_{49}$ NRs were sulfidized by a solid-gas reaction with hydrogen sulfide (H_2S), where the sulfidation process initiates from the surface and progresses inwards layer by layer. The reaction was stopped in the early stages to achieve partially sulfided NRs remaining the oxide core, yielding core–shell structured $W_{18}O_{49}$@WS_2 NRs. Prolonged sulfidation (6 h) led to the formation of WS_2 NTs with a hollow core, by full conversion of the oxide core into closed WS_2 layers. Detailed synthetic procedures are described in section 5.2.

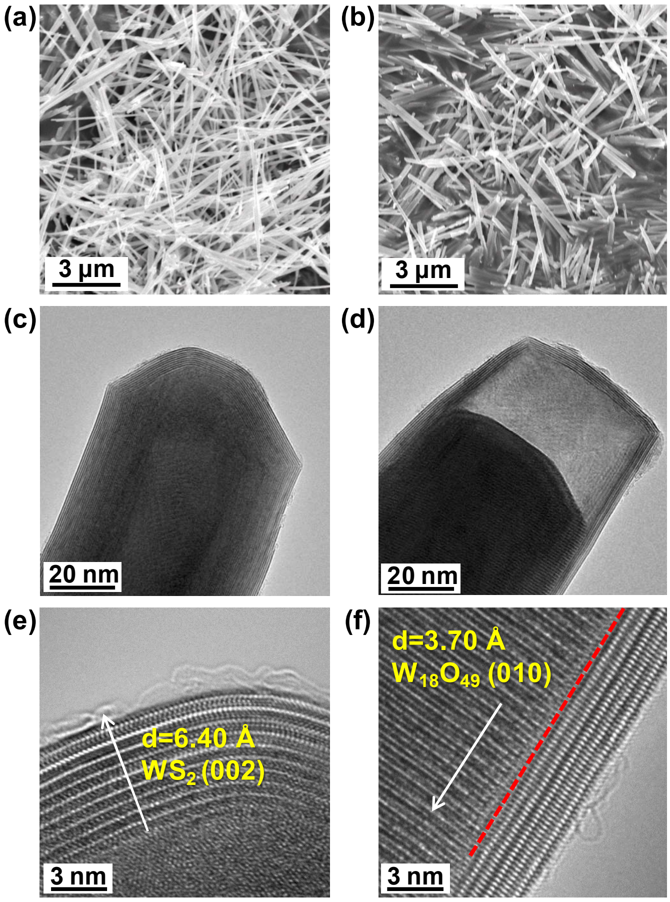

Figure 5.2. SEM images for (a) WS_2 NTs and (b) $W_{18}O_{49}$@WS_2 NRs. TEM images for (c,e) WS_2 NTs and (d,f) $W_{18}O_{49}$@WS_2 NRs.

The scanning electron microscopy (SEM) (**Figures 5.2a,b**) and transmission electron microscopy (TEM) (**Figures 5.2c,d**) images revealed that both the WS_2 NTs and $W_{18}O_{49}$@WS_2 NRs were approximately 60–70 nm in diameter. A high resolution TEM (HRTEM) image of WS_2 NTs (**Figure 5.2e**) indicates that WS_2 NTs are composed of multiwalled, crystalline WS_2 layers with a hollow core. The interlayer spacing between adjacent WS_2 layers (6.40 Å) was enlarged compared to that of the (002) planes of the 2H-WS_2 single crystal (6.16 Å),[13] which may be due to the curvatures and distortions of edge planes in the NTs. In the case of $W_{18}O_{49}$@WS_2 NRs (**Figure 5.2f**), it was observed that the external sulfide layers are cylindrical and closed, while oxide rods fill the core regions. In this core region, the crystalline spacing is 3.7 Å, which corresponds to the (010) planes of $W_{18}O_{49}$ ($WO_{2.72}$).[14]

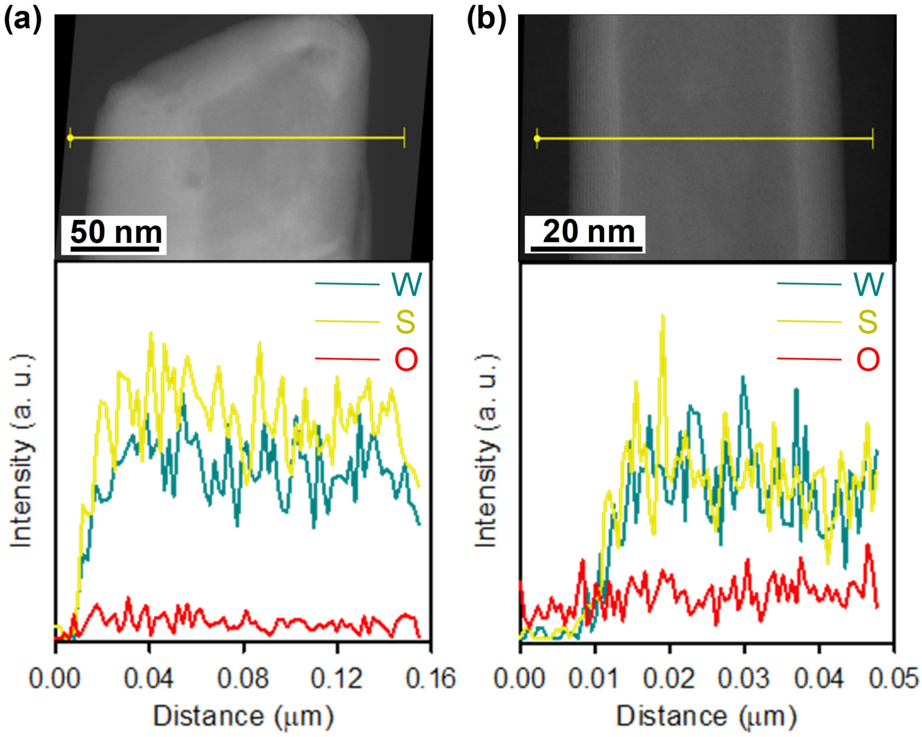

Figure 5.3. EDS element line profile images of (a) WS_2 NTs and (b) $W_{18}O_{49}$@WS_2 NRs.

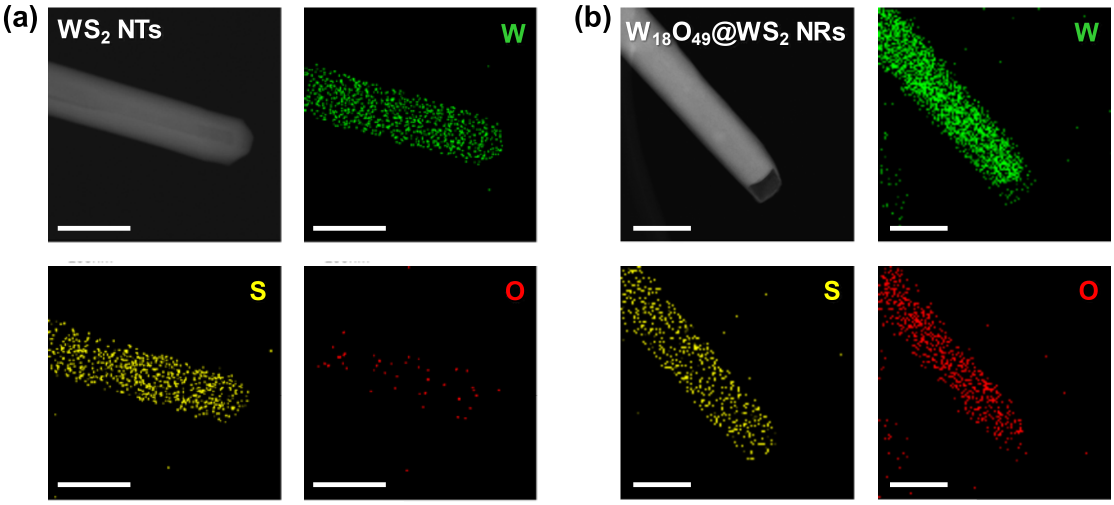

Figure 5.4. EDS elemental mapping images of (a) WS_2 NTs and (b) $W_{18}O_{49}$@WS_2 NRs. Scale bar: 100 nm.

The existence of an oxide–sulfide core–shell structure in $W_{18}O_{49}$@WS_2 NRs was also observed by energy-dispersive X-ray spectroscopy (EDS) line profile images (**Figure 5.3**). Compared to the WS_2 NTs, the relative intensity ratio of oxygen to sulfur or tungsten was higher in the core of $W_{18}O_{49}$@WS_2 NRs. EDS elemental mapping images (**Figure 5.4**) revealed that the tungsten and sulfur elements were uniformly distributed throughout the NTs and NRs, and allowed clear distinction of the oxygen content in the core regions of WS_2 NTs and $W_{18}O_{49}$@WS_2 NRs.

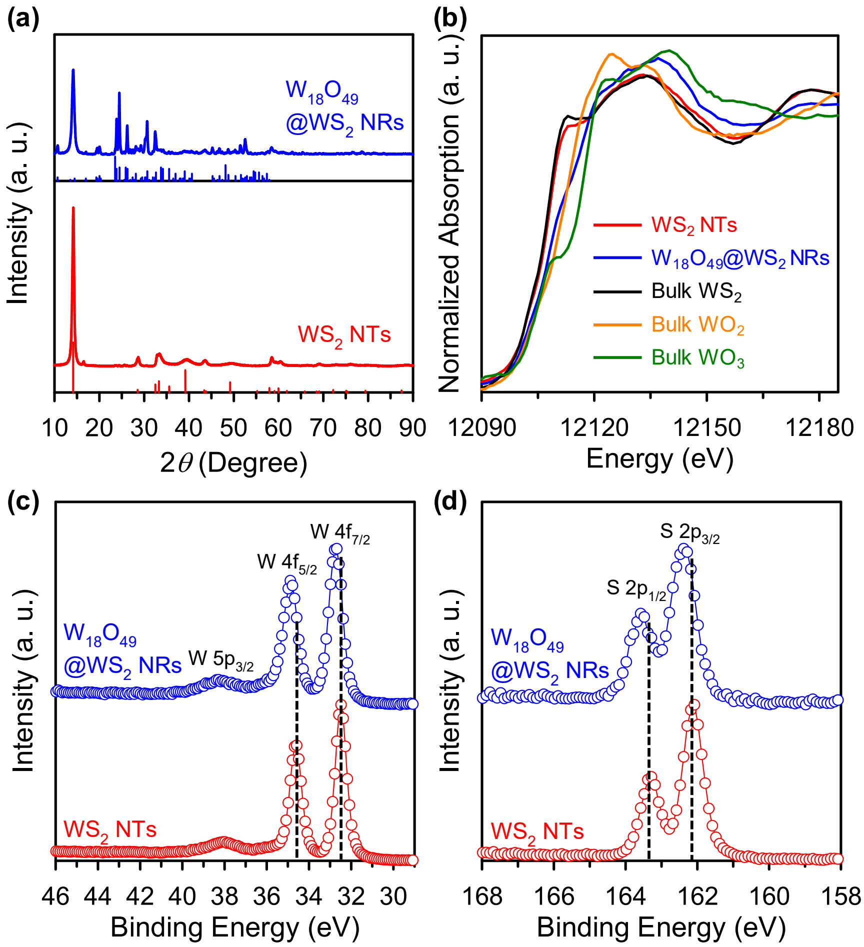

Figure 5.5. (a) Wide-angle XRD patterns of WS_2 NTs and $W_{18}O_{49}$@WS_2 NRs. Vertical bars in blue and red colors represent $W_{18}O_{49}$ standard (JCPDS No. 5-0392) and 2H-WS_2 standard (JCPDS No. 71-4832), respectively. (b) W L_1-edge XANES spectra of the samples. (c) W 4f and (d) S 2p XPS spectra of WS_2 NTs and $W_{18}O_{49}$@WS_2 NRs.

Structural information was further elucidated by examination of the X-ray diffraction (XRD) patterns, as shown in **Figure 5.5a**. The XRD pattern indicates that the structure of the WS_2 NTs is commensurate with that of the 2H-WS_2 standard (JCPDS No. 71-4832), whereas the $W_{18}O_{49}$@WS_2 NRs is composed of a mixture of $W_{18}O_{49}$ phase (JCPDS No. 5-0392) and 2H-WS_2. Tungsten L_1-edge

X-ray absorption near edge spectroscopy (XANES) provides further evidence for distinction of the oxidation states of tungsten in WS_2 NTs and $W_{18}O_{40}$@WS_2 NRs. For reference, the XANES spectra of bulk WS_2, WO_2, and WO_3 were also measured. The edges of WO_3 (W^{+6}) appeared to be at higher energy than those of WS_2 (W^{+4}) and WO_2 (W^{+4}), indicating the higher oxidation state of the former (**Figure 5.5b**).[15] While the XANES spectrum of the WS_2 NTs has a high degree of similarity to that of bulk WS_2, $W_{18}O_{49}$@WS_2 clearly exhibited a different XANES spectrum compared to the reference compounds, WO_2, WS_2 and WO_3.[16] A closer look at the spectra revealed that the absorption edge of the $W_{18}O_{49}$@WS_2 NRs is closer to that of WO_2 (W^{+4}) than WO_3 (W^{+6}), which correlates with the fact that $W_{18}O_{49}$@WS_2 NRs are composed of $W_{18}O_{49}$ ($WO_{2.72}$) and WS_2. The tungsten L_3-edge XANES spectra of the samples were also measured (**Figure 5.6**), with the data indicating similar trends to the tungsten L_1-edge spectra, *i.e.* the adsorption edge shape of the $W_{18}O_{49}$@WS_2 NRs is closer to the edge shape of WO_2 than that of WO_3.

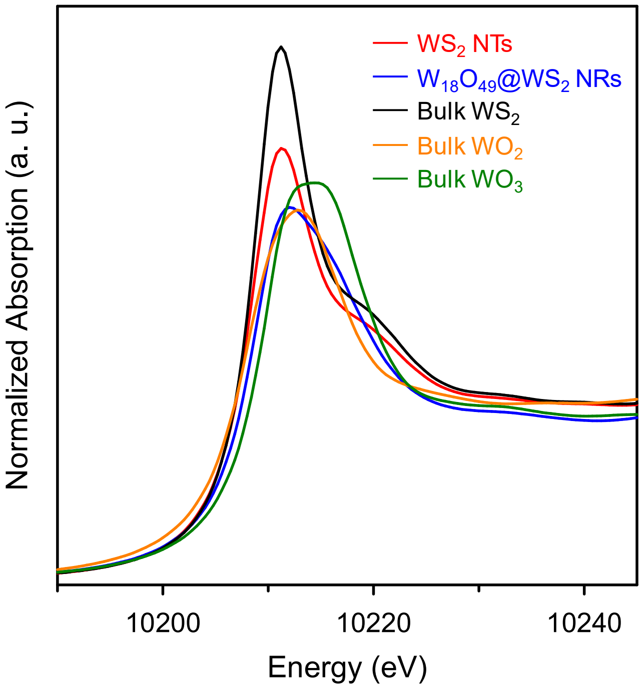

Figure 5.6. W L_3-edge XANES spectra of WS_2 NTs, $W_{18}O_{49}$@WS_2 NRs, Bulk WS_2, Bulk WO_2, and Bulk WO_3.

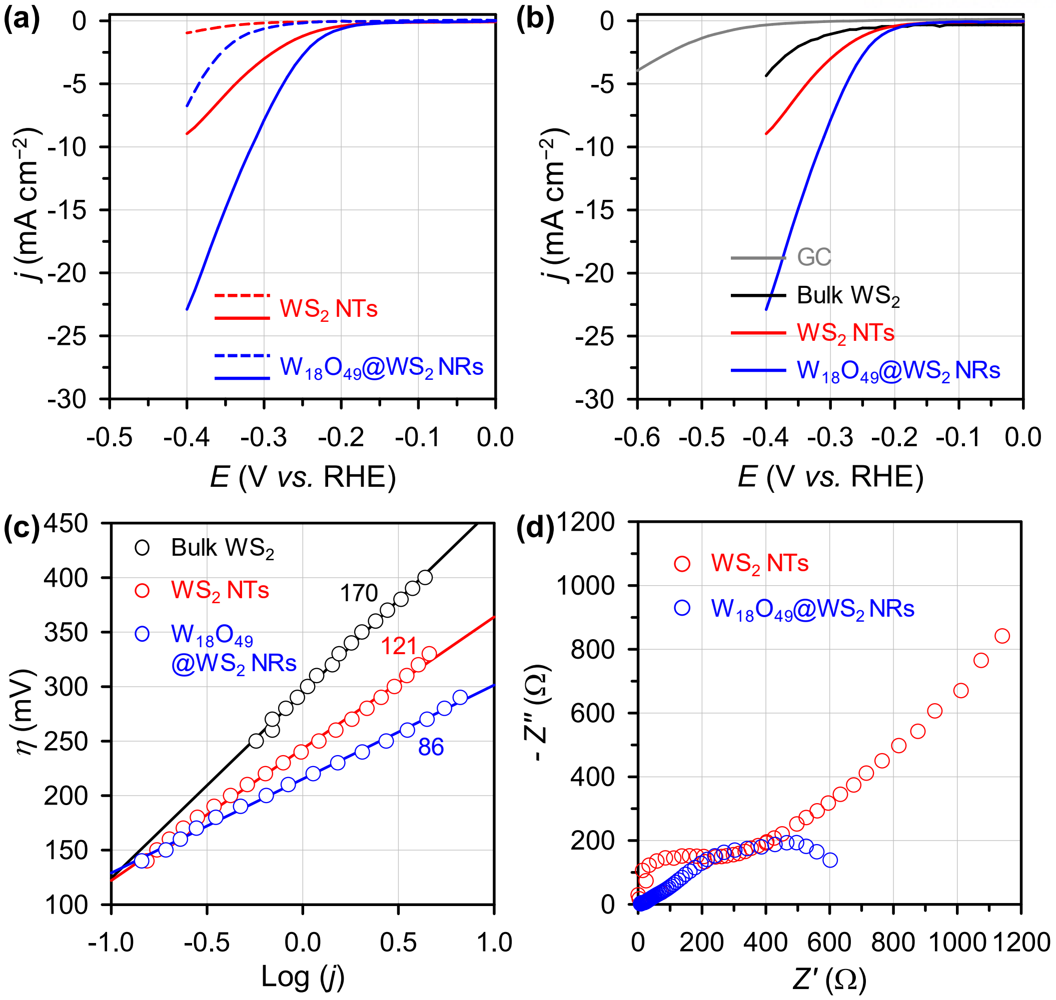

Figure 5.7. (a) LSV curves showing cycling potential effect on HER activities of WS_2 NTs and $W_{18}O_{49}$@WS_2 NRs. Dashed and solid lines represent LSV curves measured after reductive potential (−0.3–0.6 V *vs.* RHE) and oxidative potential (0.05–1.2 V *vs.* RHE) cycles, respectively. (b) LSV curves and (c) corresponding Tafel plots of the samples. (d) Nyquist plots measured at −100 mV (*vs.* RHE) from 100 kHz to 0.01 Hz.

The electrochemical catalytic activities of the WS_2 NTs and $W_{18}O_{49}$@WS_2 NRs were investigated using a three-electrode setup with a Ag/AgCl and a graphite rod as the reference and counter electrode, respectively. Details of electrochemical measurements are described in section 2.2. The linear sweep voltammetry (LSV) curve for each sample was obtained by taking the potential from 0.1 V to −0.4 V (*vs.* RHE) (for glassy carbon (GC), from 0.1 V to −0.6 V) in a 0.5 M H_2SO_4 solution, with a scan rate of 2 mV s^{-1}, and a rotation speed of 1500 rpm. During the measurements, hydrogen gas was continuously bubbled to maintain a constant RHE potential. For comparison, the HER activities of GC and bulk WS_2 were also measured. In addition, before each electrochemical measurement was carried out, the working electrode was electrochemically activated by conducting CV at a selected potential range 20 times, with a scan rate of 100 mV s^{-1}.

Interestingly, we found that the choice of the potential range for the electrochemical activation procedure has a considerable impact on the HER activities of the samples. As shown in **Figure 5.7a**, both WS_2 NTs and $W_{18}O_{49}$@WS_2 NRs that underwent electrochemical pre-treatment with an oxidative potential range (0.05–1.2 V *vs.* RHE) showed lower overpotentials (η) and higher current density (j) than those of the samples treated under a reductive potential range (−0.3−0.6 V *vs.* RHE). These results indicate that electrochemically induced surface oxidation and/or defect formation in WS_2 may improve the HER activity. Recently, similar electrochemical pre-treatment has been reported to play noticeable role in the HER,[17,18] with Qiao and co-workers reporting that 750 times potential cycling dramatically boost the HER activity of the hybrid film of porous C_3N_4 nanolayers with N-doped graphene sheets.[18]

Based on the above results, the LSV curves of the samples (**Figure 5.7b**) were obtained using the oxidative electrochemical activation protocol. The initial cathodic currents by hydrogen evolution on $W_{18}O_{49}$@WS_2 NRs and WS_2 NTs were driven at a similar onset overpotential of approximately 170 mV. In order to reach a current density of −10 mA cm^{-2}, $W_{18}O_{49}$@WS_2 NRs containing an oxide core required an overpotential of 310 mV, whereas WS_2 NTs showed an overpotential larger than 400 mV to drive the same current density. The enhanced HER activity of $W_{18}O_{49}$@WS_2 NRs can be attributed to the presence of conductive oxide cores, which can promote electron transfer between the electrode and the catalyst without using additional conducting supports such as carbon. To gain further insight into the catalytic activity, Tafel slopes were extracted from linear portion of Tafel plots, derived from LSV curves (**Figure 5.7c**). The Tafel slopes of bulk WS_2, WS_2 NTs and $W_{18}O_{49}$@WS_2 NRs were approximately 170, 121 and 86 mV dec^{-1}, respectively. The relatively smaller Tafel slope of $W_{18}O_{49}$@WS_2 NRs indicated faster kinetics during the HER. The HER reaction kinetics were also assessed using electrochemical impedance spectroscopy (EIS), which indicated a dramatically low charge transfer resistance in $W_{18}O_{49}$@WS_2 NRs compared to WS_2 NTs (**Figure 5.7d**).

Previously, WS_2 NT-based nanostructures have been investigated as electrocatalysts for the HER. Dai and co-workers prepared WS_2 nanoflakes by breaking the interlayer and intralayer bonds of WS_2 NTs through sonochemical exfoliation.[2] The resulting WS_2 nanoflakes showed higher HER activity compared to the WS_2 NTs due to an increased density of catalytically active edge sites. Interestingly, despite the increased exposure of the active sites, the overpotential at 10 mA cm^{-2} for the WS_2 nanoflakes (0.35 V) is larger than that for the $W_{18}O_{49}$@WS_2 NRs (0.31 V). This demonstrates that besides morphological control, the oxidation state and composition also have a considerable effect on HER activity. In a similar context to our results, MoO_3-MoS_2 core-shell structures were also reported to be advantageous in regards to enhancement of HER activity, as the oxide core facilitates electron transfer during the HER.[19] In addition, component-controllable $WS_{2(1-x)}Se_{2x}$ NTs on flexible carbon fibres using WO_3 NTs as a conversion template, were recently reported.[10] This work showed that ternary $WS_{2(1-x)}Se_{2x}$ NTs exhibited higher HER activity than those composed of binary components (WS_2-, WSe_2-, and WO_3 NTs).

5.4. CONCLUSION

In summary, we have demonstrated the positive impact of oxides in WS_2-based nanostructures on the enhancement of HER performance. The core–shell structured tungsten oxide–tungsten sulfide NRs, prepared with partial sulfidation of $W_{18}O_{49}$ NRs, showed superior HER activity compared to the fully sulfided WS_2 NTs. The higher HER activities of $W_{18}O_{49}$@WS_2 NRs could be attributed to the existence of the oxide core, facilitating electron transfer during the HER process. Furthermore, we confirmed that the samples underwent oxidative pre-treatment showed higher HER activity than those underwent reductive pre-treatment. The enhanced HER performance of $W_{18}O_{49}$@WS_2 NRs was yet still lower than those of highly active HER catalysts due to their nested structures, impeding the maximum usage of active edge plane. Such a structural disadvantage can be counterbalanced by exploiting transition metal promotion to modulate the free energy of hydrogen adsorption, by exfoliating the multilayer $W_{18}O_{49}$@WS_2 NRs, and by employing conductive additives such as carbon nanomaterials. Furthermore, in order to better understand the influence of the oxide core on HER, the relationship between the sulfidation level and the HER activity could be investigated with preparation of the core–shell NRs with different amount of the sulfide layers or different diameter of the oxide core. Finally, we envisage that this approach can be extended to other transition metal sulfides and is applicable to a range of catalytic reactions.

5.5. REFERENCES

1. Sobczynski, A.; Yildiz, A.; Bard, A. J.; Campion, A.; Fox, M. A.; Mallouk, T.; Webber, S. E.; White, J. M. *J. Phys. Chem.* **1988**, *92*, 2311–2315.
2. Choi, C. L.; Feng, J.; Li, Y.; Wu, J.; Zak, A.; Tenne, R.; Dai, H. *Nano Res.* **2013**, *6*, 921–928.
3. Cheng, L.; Huang, W.; Gong, Q.; Liu, C.; Liu, Z.; Li, Y.; Dai, H. *Angew. Chem. Int. Ed.* **2014**, *53*, 7860–7863.
4. Lin, J.; Peng, Z.; Wang, G.; Zakhidov, D.; Larios, E.; Yacaman, M. J.; Tour, J. M. *Adv. Energy Mater.* **2014**, *4*, 1301875.
5. Wu, Z.; Fang, B.; Bonakdarpour, A.; Sun, A.; Wilkinson, D. P.; Wang, D. *Appl. Catal., B* **2012**, *125*, 59–66.
6. Lukowski, M. A.; Daniel, A. S.; English, C. R.; Meng, F.; Forticaux, A.; Hamers, R. J.; Jin, S. *Energy Environ. Sci.* **2014**, *7*, 2608–2613.
7. Voiry, D.; Yamaguchi, H.; Li, J.; Silva, R.; Alves, D. C. B.; Fujita, T.; Chen, M.; Asefa, T.; Shenoy, V. B.; Eda, G.; Chhowalla, M. *Nat. Mater.* **2013**, *12*, 850–855.
8. Yang, J.; Voiry, D.; Ahn, S. J.; Kang, D.; Kim, A. Y.; Chhowalla, M.; Shin, H. S. *Angew. Chem. Int. Ed.* **2014**, *52*, 13751–13754.
9. Tran, P. D.; Chiam, S. Y.; Boix, P. P.; Ren, Y.; Pramana, S. S.; Fize, J.; Artero, V.; Barber, J. *Energy Environ. Sci.* **2013**, *6*, 2452–2459.
10. Xu, K.; Wang, F.; Wang, Z.; Zhan, X.; Wang, Q.; Cheng, Z.; Safdar, M.; He, J. *ACS Nano* **2014**, *8*, 8468–8476.
11. Rothschild, A.; Sloan, J.; Tenne, R. *J. Am. Chem. Soc.* **2000**, *122*, 5169–5179.
12. Zak, A.; Sallacan-Ecker, L.; Margolin, A.; Feldman, Y.; Popovitz-Biro, R.; Albu-Yaron, A.; Genut, M.; Tenne, R. *Fuller. Nanotube. Car. N.* **2011**, *19*, 18–26.
13. Krause, M.; Mucklich, A.; Zak, A.; Seifert, G.; Gemming, S. *Phys. Status Solidi B* **2011**, *248*, 2716–2719.
14. Li, Y.; Bando, Y.; Golberg, D. *Adv. Mater.* **2003**, *15*, 1294–1296.
15. Bilbrig, F.; Göbel, H. E.; Knözinger, H.; Schmelz, H.; Leneler, B. *J. Phys. Chem.* **1991**, *95*, 6973–6978.
16. Logie, V.; Maire, G.; Michel, D.; Vignes, J.-L. *J. Catal.* **1999**, *188*, 90–101.
17. Cui, W.; Liu, Q.; Cheng, N.; Asiri, A. M.; Sun, X. *Chem. Commun.* **2014**, *50*, 9340–9342.
18. Duan, J.; Chen, S.; Jaroniec, M.; Qiao, S. Z. *ACS Nano* **2015**, *9*, 931–940.
19. Chen, Z.; Cummins, D.; Reinecke, B. N.; Clark, E.; Sunkara, M. K.; Jaramillo, T. F. *Nano Lett.* **2011**, *11*, 4168–4175.

6

HIGHLY ACTIVE AND ROBUST HOLLOW RHODIUM SULFIDE CATALYSTS FOR THE HYDROGEN EVOLUTION REACTION

This chapter includes the published content: Yoon, D.;† Seo, B.;† Lee, J.;† Nam, K. S.; Kim, B.; Park, S.; Baik, H.; Joo, S. H. *Energy Environ. Sci.* **2016**, *9*, 850–856. Reproduced with permission. Copyright 2015 The Royal Society of Chemistry. These authors equally contributed to this work.

6.1. INTRODUCTION

An essential prerequisite for efficient water electrolysis is the development of highly active catalysts with structural and compositional robustness in the given electrolyte. Among various catalytic systems, metal sulfides have shown superb catalytic activities and stabilities in acidic media toward hydrogen evolution reaction (HER).[1–21] Hence, as mentioned in previous chapters, significant efforts have been devoted to controlling the morphology of metal sulfide electrocatalysts to preferentially expose catalytically active sites, as well as to guarantee structural durability.

In this regard, nanoparticle (NP)-based catalysis has witnessed a great advance in recent years. The control of size, shape, and composition of colloidal NPs has enabled the systematic investigation of critical factors responsible for activity, selectivity and stability of many important catalytic transformations.[22–24] Furthermore, advances in NP synthesis allowed for the preparation of NPs with previously unprecedented, complex morphologies, including nanoscale hollow and framework structures.[25–32] These NPs can exhibit higher surface area and larger proportion of reactive surface sites, as compared to conventional NPs, thus affording enhanced catalytic activity. The hollow or skeletal NPs have been prepared by exploiting the nanoscale Kirkendall effect,[33–35] Galvanic replacement reaction,[36–38] cation exchange reaction,[39–41] etc. While hollow NPs of metals and metal oxides with a variety of composition have been intensively investigated,[42–44] the studies on metal sulfide NPs with a hollow shape have been very limited.[45–47] Furthermore, hollow metal sulfide NPs with well-defined shape and facets have been rarely reported, and little is known for the facet-stabilization mechanism and growth kinetics of them.

In this work, hollow rhodium sulfide NPs with well-defined crystalline facets were applied as very high active and durable electrocatalysts toward HER. They were prepared *via* one-step formation of core-shell NPs followed by selective etching of the core. This method provides a convenient access to hollow, crystalline NPs, which is distinguishable from previously reported routes including the Kirkendall effect-driven, Galvanic replacement, and cation exchange reactions.[33–41] As illustrated in **Figure 6.1**, the co-decomposition of Cu and Rh precursors gave rise to size- and facet-controlled, core-shell structured $Cu_{1.94}S@Rh_2S_3$ NPs, which are generated by the fast formation of $Cu_{1.94}S$ nanoprisms, [48] followed by the growth of Rh_2S_3 phase. Subsequent removal of $Cu_{1.94}S$ phase by a strong acid selectively yielded hollow Rh_2S_3 hexagonal nanoprisms with well-defined facets. The hollow Rh_2S_3 nanoprisms show excellent activity for the HER, evidenced by overpotential as low as 122 mV to drive a current density of −10 mA cm^{-2}. Furthermore, they exhibited very high stability with increased activity after 10,000 cycling of long-term durability tests, suggesting excellent structural integrity under strongly acidic conditions.

6.2. SYNTHESIS OF CATALYSTS

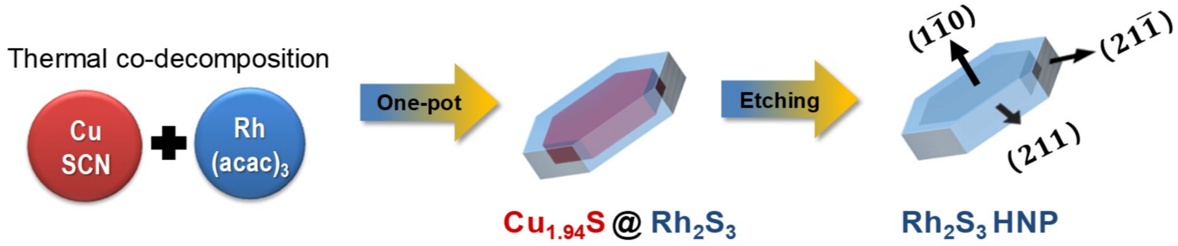

Figure 6.1. Schematic illustration for the formation of facet-controlled hollow rhodium sulfide nanoprisms.

In a typical synthesis of hollow Rh_2S_3 nanoprisms, a slurry of CuSCN and $Rh(acac)_3$ in oleylamine was prepared in a 100 mL Schlenk tube. After being placed under vacuum at 100 °C for 10 min, the reaction mixture was charged with 1 atm Ar gas. Then, the Schlenk tube was placed in a hot oil bath, which was preheated to 240 °C. After heating at the same temperature for 30 min, the reaction mixture was cooled down to room temperature, washed several times with toluene and methanol, followed by centrifugal separation to give $Cu_{1.94}S@Rh_2S_3$ nanoprism. The nanoprisms were then etched in a solution containing 1 mL HCl, 3 mL ethanol, and 3 mL toluene for 3 hours with a magnetic stirring to give hollow Rh_2S_3 nanoprisms. For the electrocatalytic measurement, carbon black Vulcan XC-72R powder was put into a 70 mL vial with 20 mL hexane, and stirred for 10 minutes under sonication. The synthesized NPs were put into a 50 mL conical tube with 10 mL hexane, and were sonicated for 10 minutes. After 10 minutes, the slurry with NPs was poured into the 70 mL vial containing carbon black, and the combined slurry was sonicated for additional 3 minutes.

The resultant slurry with NPs loaded on carbon black was transferred to a 50 mL conical tube, and 20 mL of hexane was added to the slurry. After this procedure, the NPs loaded on carbon black were separated by centrifugation and then dried in oven for 24 hours.

6.3. RESULTS AND DISCUSSION

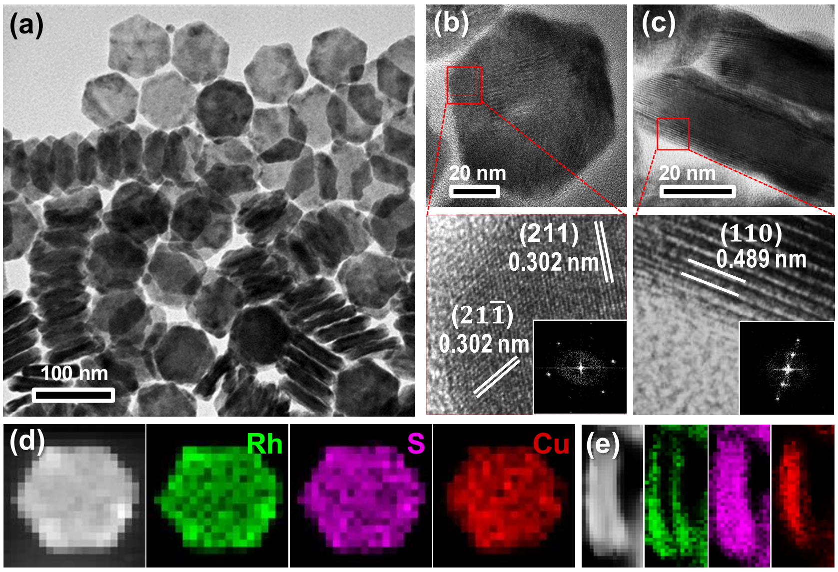

Figure 6.2. (a–c) TEM and HRTEM images with FFT analyses, and (d–e) STEM and elemental mapping images of Cu$_{1.94}$S@Rh$_2$S$_3$ nanocrystal.

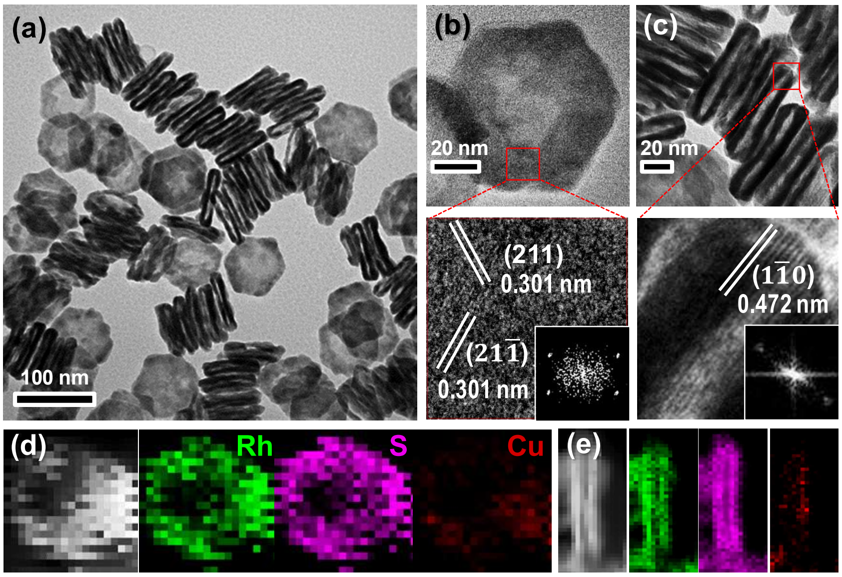

Figure 6.3. (a–c) TEM and HRTEM images with FFT analyses, and (d–e) STEM and elemental mapping images of hollow Rh$_2$S$_3$ nanoprisms.

Representative transmission electron microscopy (TEM) and high resolution TEM (HRTEM) images with fast Fourier transformation (FFT) patterns of $Cu_{1.94}S@Rh_2S_3$ and Rh_2S_3 nanoprisms are shown in **Figures 6.2 and 6.3**. The monodisperse size distribution and the hexagonal plate shape are clearly observed for both $Cu_{1.94}S@Rh_2S_3$ and hollow Rh_2S_3 nanoprisms. The size of hollow Rh_2S_3 nanoprisms are slightly reduced from that of $Cu_{1.94}S@Rh_2S_3$ after the core etching; the average sizes of hexagonal $Cu_{1.94}S@Rh_2S_3$ nanoprisms and hollow Rh_2S_3 nanoprisms are 88.0 ± 4.1 nm and 84.1 ± 4.0 nm, respectively, which are measured from diagonal point to point. The average thickness of 19.3 ± 1.5 nm for $Cu_{1.94}S@Rh_2S_3$ is also decreased to 17.0 ± 2.2 nm for Rh_2S_3. The hexagonal faces of orthorhombic Rh_2S_3 nanoprisms are enclosed with $(1\bar{1}0)$ facets. The six sides of hexagonal nanoprisms are found to be (211) and $(2\bar{1}1)$ planes as verified by HRTEM image and FFT pattern. The elemental mapping images by energy-dispersive X-ray spectroscopy (EDS) shown in **Figures 6.2d,e and Figures 6.3d,e** provide information about the elemental compositions of core@shell and hollow nanoprisms. Copper atoms (red color) located in inner part of the $Cu_{1.94}S@Rh_2S_3$ nanocrystal are rarely seen in the inner wall of the hollow Rh_2S_3 nanocrystal. The overall position of rhodium atoms (green color) is not altered by the etching process.

The size and thickness of the nanocrystals were controlled to investigate the relationship between the morphology and catalytic activity. The void volume and thickness of the hollow nanocatalyst have been considered as crucial factors in catalytic activity.[49–53] Three hollow nanoprisms, namely, Rh_2S_3_ThinHNP, Rh_2S_3_MedHNP, and Rh_2S_3_ThickHNP, were prepared by using 8:1, 8:2, 8:4 ratio of CuSCN:Rh(acac)$_3$, respectively, and their TEM images with corresponding FFT patterns and size analyses are shown in **Figure 6.4** At a constant CuSCN concentration, lower Rh(acac)$_3$ concentration yielded thinner nanoprisms with higher aspect ratio and smaller void volume; the aspect ratios of the three samples are 10.7, 7.9, and 4.9, respectively. Interestingly, the cavity size was found to correlate with the shell thickness of the Rh_2S_3 nanocrystal, which were obtained by varying the ratio of CuSCN and Rh(acac)$_3$ precursors. The average thicknesses of cavity were found to be 0.79 nm, 2.2 nm, and 3.7 nm for Rh_2S_3_ThinHNP, Rh_2S_3_MedHNP, and Rh_2S_3_ThickHNP, respectively.

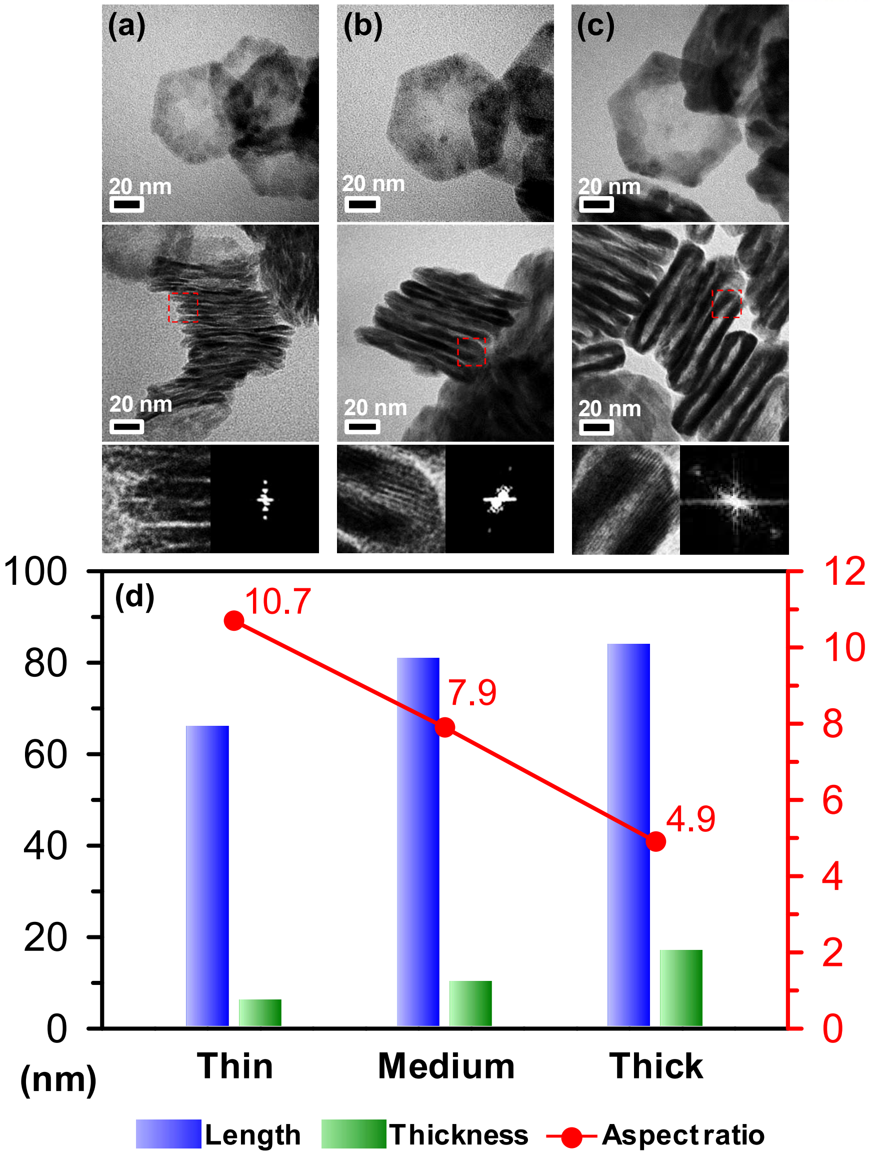

Figure 6.4. TEM and HRTEM images with FFT patterns of morphology controlled hollow Rh_2S_3 nanoprisms. (a) ThinHNP, (b) MedHNP, and (c) ThickHNP. (d) Change of length, thickness, and aspect ratio in the three hollow Rh_2S_3 nanoprisms.

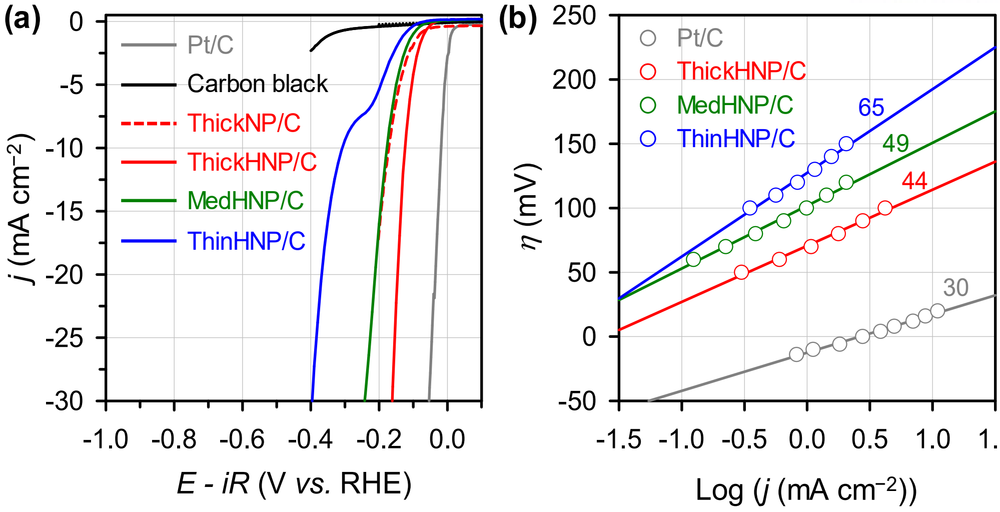

Figure 6.5. (a) LSV curves for Rh_2S_3_HNP/C, $Cu_{1.94}S@Rh_2S_3$_NP/C, Carbon black and 20 wt.% Pt/C. (b) Corresponding Tafel plots for Rh_2S_3/C_HNP/C and 20 wt.% Pt/C.

Next, we investigated the electrocatalytic activities of size- and thickness-controlled hollow Rh_2S_3 nanoprisms for the HER. For this purpose, they were supported on carbon black (Vulcan carbon). Nominal content of Rh_2S_3 HNP in the composite was 13 wt.%. For comparison, the electrocatalytic activities for $C_{1.94}S@Rh_2S_3$_ThickNP/C, carbon black, and 20 wt.% Pt/C were also investigated. The electrocatalytic activities were measured using a three-electrode electrochemical cell with an Ag/AgCl and a graphite rod as the reference and counter electrode, respectively. All linear sweep voltammetry (LSV) curves were presented after the correction for Ohmic potential drop (*iR*) loss arising from solution resistance and normalization of the current with the geometric surface area of the electrode (0.126 cm^{-2}). As shown in the LSV curves (**Figure 6.5a**), the Rh_2S_3_ThickHNP/C catalyst showed the best HER activity among the compared samples. To drive a current density of −10 mA cm^{-2}, the Rh_2S_3_ThickHNP/C required an overpotential of 122 mV, whereas the $C_{1.94}S@Rh_2S_3$_ThickNP/C, Rh_2S_3_MedHNP/C and Rh_2S_3_ThinHNP/C needs larger overpotentials of 175 mV, 175 mV, and 300 mV, respectively. The importance of hollow morphology was further proved by the superior HER performance of Rh_2S_3-ThickHNP/C compared to that of $Cu_{1.94}S@Rh_2S_3$_ThickNP/C (**Figure 6.5a**). The considerably high HER activity for the non-etched samples ($Cu_{1.94}S@Rh_2S_3$_ThickNP/C), which is similar to that of Rh_2S_3_MedHNP/C, and even higher than that of Rh_2S_3_ThinHNP/C samples indicates the active surface sites in the hollow Rh_2S_3 nanostructures originate from not only inside but also the outside the hollow structure. In addition, the unusual shape of LSV curve for Rh_2S_3_ThinHNP/C could be attributed to the limited mass transport due to the relatively smaller void volume of Rh_2S_3_ThinHNP compared to other two hollow Rh_2S_3 nanoprisms. The results emphasize the importance of a relatively wide cavity for facilitating mass transport along with the increased catalytic active sites. To investigate the reaction kinetics during the HER, Tafel slopes were extracted from linear portion of Tafel plots, derived from LSV curves (**Figure 6.5b**). The Tafel slope of 20 wt.% Pt/C was 30 mV s^{-1}, indicating Volmer–Tafel mechanism.[12] The Tafel slopes of Rh_2S_3_ThickHNP/C, Rh_2S_3_MedHNP/C, and Rh_2S_3_ThinHNP/C were approximately 44, 49 and 65 mV dec^{-1}, respectively. The relatively smaller Tafel slope of Rh_2S_3_ThickHNP/C indicated faster kinetics during the HER. All Tafel slope of 44–65 mV dec^{-1} for Rh_2S_3/C may suggest Volmer–Heyrovsky HER mechanism.[54] The Tafel slope of 44 mV dec^{-1} for Rh_2S_3/C_ThickHNP is smaller than those of most metal sulfide-based HER catalysts.

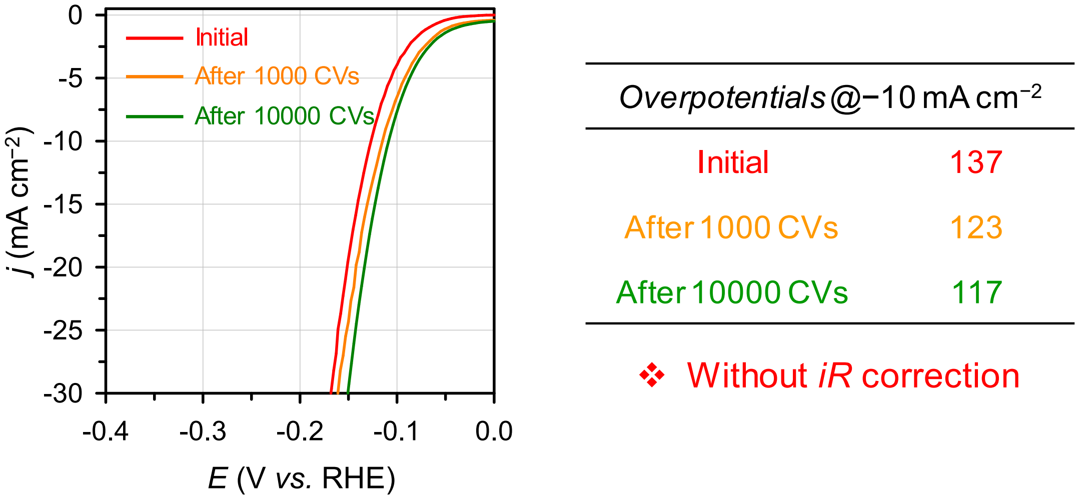

Overpotentials @−10 mA cm^{-2}	
Initial	137
After 1000 CVs	123
After 10000 CVs	117

❖ Without *iR* correction

Figure 6.6. LSV curves of Rh_2S_3_ThickHNP/C recorded before and after 1000 and 10000 CVs between 0.01 V and 1.2 V (*vs.* RHE) at a scan rate of 50 mV s^{-1}.

We next examined the long-term stability of Rh_2S_3_ThickHNP/C by conducting consecutive potential cycles between 0.1 and −0.3 V (*vs.* RHE) at a sweep rate of 50 mV s^{-1}. **Figure 6.6** shows LSV curves recorded before and after 1000 and 10000 potential cycles. Interestingly, after 10000 CV cycles, the overpotential to reach a current density of −10 mA cm^{-2} was considerably reduced from 137 mV to 117 mV (data were presented without *iR* compensation). To the best of our knowledge, such enhancement of catalytic activity after cycling test has not been reported in previous sulfide-based HER catalysts. The potential cycles further removed the inactive Cu impurities from the hollow Rh_2S_3 nanoprisms, which would increase the number of active Rh-based catalytic sites. The Cu leaching was confirmed by measuring the content of Cu in the electrolyte before and after 10000 potential cycles using inductively coupled plasma optical emission spectrometry (ICP-OES) (**Table 6.1**). TEM images after potential cycles revealed that the hollow structure of Rh_2S_3 nanoprisms is well preserved and the nanoprisms are uniformly distributed on the carbon support without agglomeration (**Figure 6.7**)

Table 6.1. Content of Cu in 0.5 M H_2SO_4 electrolyte before and after cycling test, determined by ICP-OES anlaysis.

Before cycling test	0.000 mg/L
After cycling test	0.003 mg/L

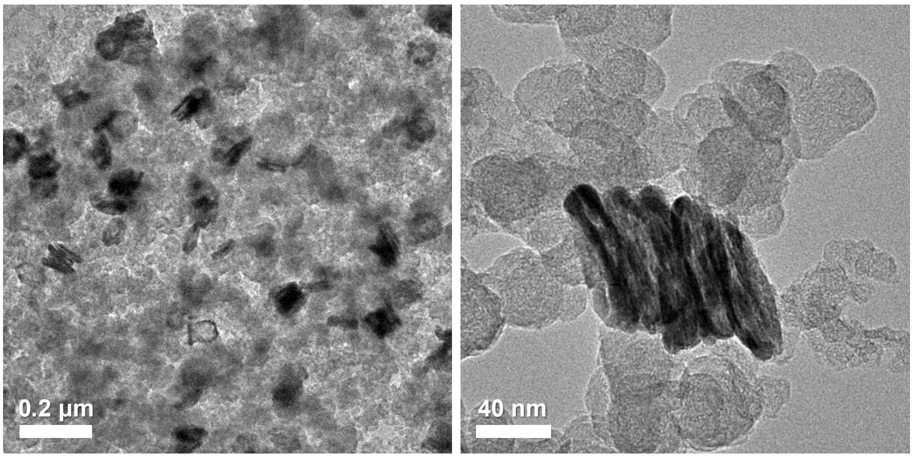

Figure 6.7. TEM images of Rh_2S_3_ThickHNP/C after potential cycles.

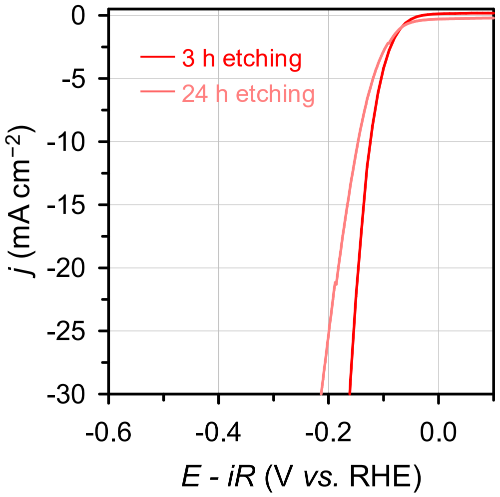

Figure 6.8. LSV curves for Rh_2S_3_ThickHNP/C with different etching times of 3 h and 24 h.

Inspired by the finding that residual Cu impurities could block the catalytic active sites, we increased Cu core-etching time from 3 h to 24 h when preparing the Rh_2S_3_ThickHNP/C. Even though the amount of Cu was reduced to one third (from 1.5 wt.% to 0.53 wt.%, determined *via* ICP-OES), the HER activity was rather decreased with increased etching time (**Figure 6.8**). The excessive acid etching could destroy the hollow morphology, deteriorating the HER performance. Thus, we conclude that the relatively mild electrochemical leaching of remnant Cu was more advantageous for preserving the hollow morphology, which appears to be a decisive factor determining the HER performance.

In addition, we explored the catalyst loading effect toward HER. The HER performance was enhanced with increasing catalyst loading (**Figure 6.9**). Rh_2S_3_ThickHNP/C with a catalyst loading of 918 µg cm^{-2} reached geometric current density of −10 mA cm^{-2} at overpotential of only 88 mV, which is the highest performance among the sulfide-based HER catalysts. We extensively compared the HER activity and kinetics of Rh_2S_3_ThickHNP/C catalyst with previously reported metal sulfide-based HER catalysts. **Figure 6.10** present the overpotentials required to drive −10 mA cm^{-2} and Tafel slopes for the HER of representative metal sulfide catalysts. It is clear that the HER performance of Rh_2S_3_ThickHNP/C catalyst is one of the best among the compared HER catalysts in terms of overpotential and Tafel slope.

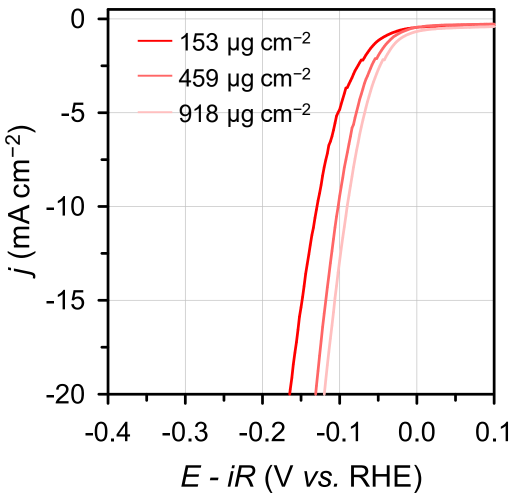

Figure 6.9. LSV curves for Rh_2S_3_ThickHNP/C with different catalyst loadings of 153 µg cm^{-2}, 459 µg cm^{-2} and 918 µg cm^{-2}.

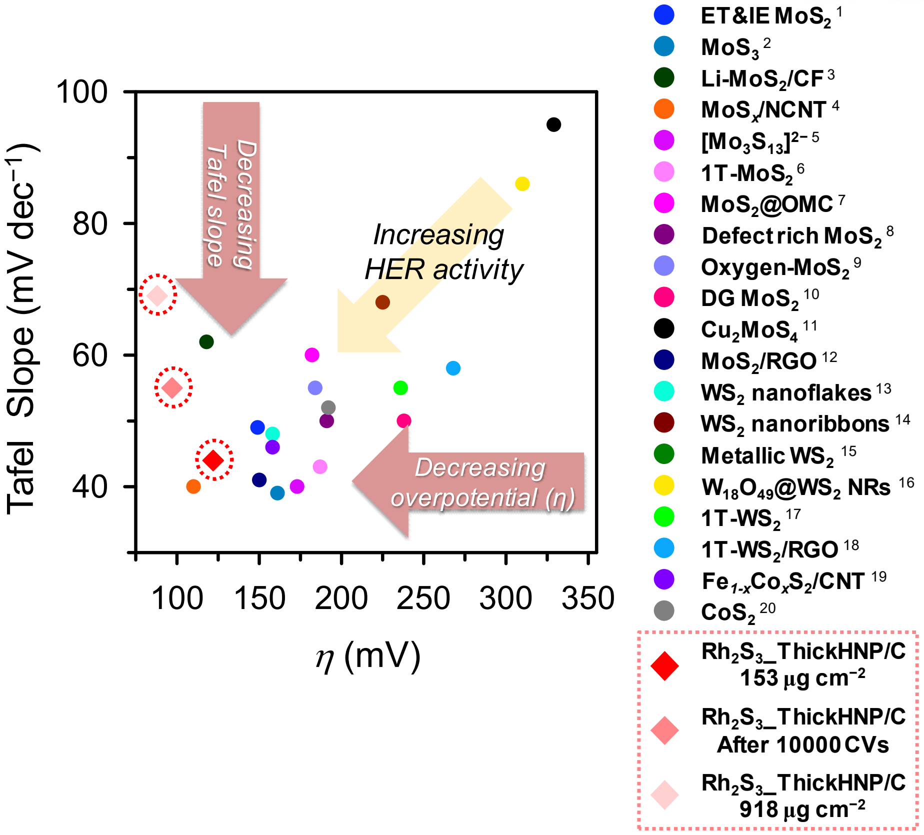

Figure 6.10. HER activity comparison graph showing Tafel slopes (mV dec^{-1}) and overpotentials (mV) to reach a current density of −10 mA cm^{-2}.

6.4. CONCLUSION

In conclusion, we have developed a highly active and robust Rh_2S_3-based electrocatalyst toward HER under strongly acidic operation conditions. The facet-controlled hollow nanostructure of Rh_2S_3 could be conveniently synthesized by thermal co-decomposition of $Rh(acac)_3$ and CuSCN, and subsequent removal of the $Cu_{1.94}S$ core from the core-shell $Cu_{1.94}@Rh_2S_3$ hexagonal nanoprism by acid etching. The hollow Rh_2S_3 nanoprisms with catalytically highly active sites exhibit excellent catalytic activity and structural robustness for the HER. We believe that the synthetic strategy used in this study can be applied to prepare other catalytically useful hollow nanostructures.

6.5. REFERENCES

1. Gao, M.-R.; Chan, M. K. Y.; Sun, Y. *Nat. Commun.* **2015**, *6*, 7493.
2. Li, Y.; Yu, Y.; Huang, Y.; Nielsen, R. A.; Goddard, W. A.; Li, Y.; Cao, L. *ACS Catal.* **2015**, *5*, 448–455.
3. Wang, H.; Lu, Z.; Kong, D.; Sun, J.; Hymel, T. M.; Cui, Y. *ACS Nano* **2014**, *8*, 4940–4947.
4. Li, D. J.; Maiti, U. N.; Lim, J.; Choi, D. S.; Lee, W. J.; Oh, Y.; Lee, G. Y.; Kim, S. O. *Nano Lett.* **2014**, *14*, 1228–1233.
5. Kibsgaard, J.; Jaramillo, T. F.; Besenbacher, F. *Nat. Chem.* **2014**, *6*, 248–253.
6. Lukowski, M. A.; Daniel, A. S.; Meng, F.; Forticaux, A.; Li, L.; Jin, S. *J. Am. Chem. Soc.* **2013**, *135*, 10274–10277.
7. Seo, B.; Jung, G. Y.; Sa, Y. J.; Jeong, H. Y.; Cheon, J. Y.; Lee, J. H.; Kim, H. Y.; Kim, J. C.; Shin, H. S.; Kwak, S. K.; Joo, S. H. *ACS Nano* **2015**, *9*, 3728–3739.
8. Xie, J.; Zhang, H.; Li, S.; Wang, R.; Sun, X.; Zhou, M.; Zhou, J.; Lou, X. W.; Xie, Y. *Adv. Mater.* **2013**, *25*, 5807–5813.
9. Xie, J.; Zhang, J.; Li, S.; Grote, F.; Zhang, X.; Zhang, H.; Wang, R.; Lei, Y.; Pan, B.; Xie, Y. *J. Am. Chem. Soc.* **2013**, *135*, 17881–17888.
10. Kibsgaard, J.; Chen, Z.; Reinecke, B. N.; Jaramillo, T. F. *Nat. Mater.* **2012**, *11*, 963–969.
11. Tran, P. D.; Nguyen, M.; Pramana, S. S.; Bhattacharjee, A.; Chiam, S. Y.; Fize, J.; Field, M. J.; Artero, V.; Wong, L. H.; Loo, J.; Barber, J. *Energy Environ. Sci.* **2012**, *5*, 8912–8916.
12. Li, Y.; Wang, H.; Xie, L.; Liang, Y.; Hong, G.; Dai, H. *J. Am. Chem. Soc.* **2011**, *133*, 7296–7299.
13. Cheng, L.; Huang, W.; Gong, Q.; Liu, C.; Liu, Z.; Li, Y.; Dai, H. *Angew. Chem. Int. Ed.* **2014**, *53*, 7860–7863.
14. Lin, J.; Peng, Z.; Wang, G.; Zakhidov, D.; Larios, E.; Yacaman, M. J.; Tour, J. M. *Adv. Energy Mater.* **2014**, *4*, 1301875.
15. Lukowski, M. A.; Daniel, A. S.; English, C. R.; Meng, F.; Forticaux, A.; Hamers, R. J.; Jin, S. *Energy Environ. Sci.* **2014**, *7*, 2608–2613.
16. Seo, B.; Jeong, H. Y.; Hong, S. Y.; Zak, A.; Joo, S. H. *Chem. Commun.* **2015**, *51*, 8334–8337.
17. Voiry, D.; Yamaguchi, H.; Li, J.; Silva, R.; Alves, D. C. B.; Fujita, T.; Chen, M.; Asefa, T.; Shenoy, V. B.; Eda, G.; Chhowalla, M. *Nat. Mater.* **2013**, *12*, 850–855.
18. Yang, J.; Voiry, D.; Ahn, S. J.; Kang, D.; Kim, A. Y.; Chhowalla, M.; Shin, H. S. *Angew. Chem. Int. Ed.* **2013**, *52*, 13751–13754.
19. Wang, D.-Y.; Gong, M.; Chou, H.-L.; Pan, C.-J.; Chen, H.-A.; Wu, Y.; Lin, M.-C.; Guan, M.; Yang, J.; Chen, C.-W.; Wang, Y.-L.; Hwang, B.-J.; Chen, C.-C.; Dai, H. *J. Am. Chem. Soc.* **2015**, *137*, 1587–1592.
20. Faber, M. S.; Lukowski, M. A.; Ding, Q.; Kaiser, N. S.; Jin, S. *J. Phys. Chem. C* **2014**, *118*, 21347–21356.

21. Tang, Y.-J.; Gao, M.-R.; Liu, C.-H.; Li, S.-L.; Jiang, H.-L.; Lan, Y.-Q.; Han, M.; Yu, S.-H. *Angew. Chem. Int. Ed.* **2015**, *54*, 12928–12932.
22. Wang, Q.; Cui, X.; Guan, W.; Zhang, L.; Fan, X.; Shi, Z.; Zheng, W. *J. Power Sources* **2014**, *269*, 152–157.
23. Hong, J. W.; Kang, S. W.; Choi, B.-S.; Kim, D.; Lee, S. B.; Han, S. W. *ACS Nano* **2012**, *6*, 2410–2419.
24. Zhang, Q.; Wang, H. *ACS Catal.* **2014**, *4*, 4027–4033.
25. Bang, S.; Yoon, D.; Kim, J.; Baik, H.; Yang, H.; Lee, K. *CrystEngComm* **2015**, *17*, 4084–4088.
26. Yoon, D.; Park, S.; Park, J.; Kim, J.; Baik, H.; Yang, H.; Lee, K. *Nanoscale* **2014**, *6*, 12397–12402.
27. Zhang, Z.-P.; Zhu, W.; Yana, C.-H.; Zhang, Y.-W. *Chem. Commun.* **2015**, *51*, 3997–4000.
28. González, E.; Arbiol, J.; Puntes, V. F. *Science* **2011**, *334*, 1377–1380.
29. Hong, X.; Wang, D.; Cai, S.; Rong, H.; Li, Y. *J. Am. Chem. Soc.* **2012**, *134*, 18165–18168.
30. Moghimi, N.; Abdellah, M.; Thomas, J. P.; Mohapatra, M.; Leung, K. T. *J. Am. Chem. Soc.* **2013**, *135*, 10958–10961.
31. Xie, S.; Lu, N.; Xie, Z.; Wang, J.; Kim, M. J.; Xia, Y. *Angew. Chem. Int. Ed.* **2012**, *51*, 10266–10270.
32. Lu, X.; Au, L.; McLellan, J.; Li, Z.-Y.; Marquez, M.; Xia, Y. *Nano Lett.* **2007**, *7*, 1764–1769.
33. Yin, Y.; Rioux, R. M.; Erdonmez, C. K.; Hughes, S.; Somorjai, G. A.; Alivisatos, A. P. *Science* **2004**, *304*, 711–714.
34. Wang, W.; Dahl, M.; Yin, Y. *Chem. Mater.* **2013**, *25*, 1179–1189.
35. Hung, L.-I.; Tsung, C.-K.; Huang, W.; Yang, P. *Adv. Mater.* **2010**, *22*, 1910–1914.
36. Zhang, H.; Jin, M.; Liu, H.; Wang, J.; Kim, M. J.; Yang, D.; Xie, Z.; Liu, J.; Xia, Y. *ACS Nano* **2011**, *5*, 8212–8222.
37. Zhang, H.; Jin, M.; Wang, J.; Li, W.; Camargo, P. H. C.; Kim, M. J.; Yang, D.; Xie, Z.; Xia, Y. *J. Am. Chem. Soc.* **2011**, *133*, 6078–6089.
38. Yu, Y.; Zhang, Q.; Xie, J.; Lee, J. Y. *Nat. Commun.* **2013**, *4*, 1454.
39. Zhang, D.; Wong, A. B.; Yu, Y.; Brittman, S.; Sun, J.; Fu, A.; Beberwyck, B.; Alivisatos, A. P.; Yang, P. *J. Am. Chem. Soc.* **2014**, *136*, 17430–17433.
40. Justo, Y.; Sagar, L. K.; Flamee, S.; Zhao, Q.; Vantomme, A.; Hens, Z. *ACS Nano* **2014**, *8*, 7948–7957.
41. Trizio, L. D.; Prato, M.; Genovese, A.; Casu, A.; Povia, M.; Simonutti, R.; Alcocer, M. J. P.; D'Andrea, C.; Tassone, F.; Manna, L. *Chem. Mater.* **2012**, *24*, 2400–2406.
42. Wang, Z.; Zhou, L.; Lou, X. W. *Adv. Mater.* **2012**, *24*, 1903–1911.
43. Oh, M. H.; Yu, T.; Yu, S.-H.; Lim, B.; Ko, K.-T.; Willinger, M.-G.; Seo, D.-H.; Kim, B. H.; Cho, M. G.; Park, J.-H.; Kang, K.; Sung, Y.-E.; Pinna, N.; Hyeon, T. *Science* **2013**, *340*, 964–968.

44. Phan, V. N.; Lim, E.-K.; Kim, T.; Kim, M.; Choi, Y.; Kim, B.; Lee, M.; Oh, A.; Jin, J.; Chae, Y.; Baik, H.; Suh, J.-S.; Haam, S.; Huh, Y.-M.; Lee, K. *Adv. Mater.* **2013**, *25*, 3202–3208.
45. Shen, L.; Yu, L.; Wu, H. B.; Yu, X.-Y.; Zhang, X.; Lou, X. W. *Nat. Commun.* **2015**, *6*, 6694.
46. Macdonald, J. E.; Sadan, M. B.; Houben, L.; Popov, I.; Banin, U. *Nat. Mater.* **2010**, *9*, 810–815.
47. Pu, J.; Cui, F.; Chu, S.; Wang, T.; Sheng, E.; Wang, Z. *ACS Sustainable Chem. Eng.* **2014**, *2*, 809–815.
48. Yoon, D.; Jin, H.; Ryu, S.; Park, S.; Baik, H.; Oh, S. J.; Haam, S.; Joo, C.; Lee, K. *CrystEngComm* **2015**, *17*, 4627–4631.
49. Hu, J.; Chen, M.; Fang, X.; Wu, L. *Chem. Soc. Rev.* **2011**, *40*, 5472–5491.
50. Mahmoud, M. A.; Saira, F.; El-Sayed, M. A. *Nano Lett.* **2010**, *10*, 3764–3769.
51. Yen, C. W.; Mahmoud, M. A.; El-Sayed, M. A. *J. Phys. Chem. A* **2009**, *113*, 4340–4345.
52. Peng, Z.; You, H.; Wu, J.; Yang, H. *Nano Lett.* **2010**, *10*, 1492–1496.
53. Zeng, J.; Zhang, Q.; Chen, J.; Xia, Y. *Nano Lett.* **2010**, *10*, 30–35.
54. Merki, D.; Vrubel, H.; Rovelli, L.; Fierro, S.; Hu, X. *Chem. Sci.* **2012**, *3*, 2515–2525.

7

SHAPE EFFECTS OF NICKEL PHOSPHIDE CATALYSTS ON THE HYDROGEN EVOLUTION REACTION

This chapter includes the published content: Seo, B.; Baek, D. S.; Sa, Y. J.; Joo, S. H. *CrystEngComm.* **2016**, *18*, 6083–6089. Reproduced with permission. Copyright 2016 The Royal Society of Chemistry.

7.1. INTRODUCTION

Nanoparticles (NPs) have great potential in a wide range of areas, such as catalysis, biological labelling, optoelectronics, and magnetic storage, because of their attractive material properties that distinguish them from their bulk counterparts.[1–4] Recent advances in synthetic colloidal chemistry have enabled the regulation of the properties of NP with excellent control of their size and shape. In catalysis, the size- and shape-controlled NPs can be utilized as excellent model systems for the systematic investigation of structure-catalytic property relationships.[5–8] Particularly, shape-controlled NPs can selectively expose desired crystallographic surfaces, thereby enhancing activity and/or selectivity in the given catalytic reactions. In addition, such model studies using shape-controlled NPs can bridge the gap between the fundamental knowledge and practical catalysis used in industry. This possibility was initially realised by El-Sayed and Somorjai, who used shape-controlled Pt NPs for selective catalytic transformations in the liquid and gas phases, respectively.[9,10] Recently, as an example of electrocatalytic applications, shape-controlled octahedral PtNi NPs with dominant (111) surfaces demonstrated very high oxygen reduction reaction activity,[11] which was consistent with single crystal-based model catalyst studies.[12] Up to now, shape-controlled syntheses of catalytic NPs have been well established for metals, metal oxides, and metal chalcogenides, yet metal phosphide NPs have received less attention.

Metal phosphides constitute an important class of catalysts for hydrogen-involving reactions. In particular, metal phosphides have attracted considerable attention in recent years as efficient, noble metal-free catalysts for the hydrogen evolution reaction (HER).[13–43] The HER produces hydrogen as a clean energy carrier from a sustainable source, as cathodic half reaction of water electrolysis. While Pt-based materials are the most active catalysts for the HER, their high cost and scarcity hampered widespread application. In this context, non-noble metal-based materials, including metal phosphides, are of great interest as viable substitutes for Pt-based catalysts.[13–53] Of the various compositions of metal phosphides, nickel phosphide catalysts, in particular, have exhibited very high HER activity.[15–31] Rodriguez and co-workers employed density functional theory (DFT) calculations to investigate the HER activity over a series of HER catalysts including [NiFe] hydrogenase, analogue metal complexes, and Pt(111), Ni(111), and $Ni_2P(001)$ single crystal surfaces. The hollow sites of $Ni_2P(001)$ surface poisoned with H showed superior HER activity to the Pt(111) surface, and even displayed a comparable HER activity to [NiFe] hydrogenase, which had the highest HER activity among the compared catalysts. Recently, Schaak and co-workers demonstrated the translation of theoretical prediction to nanoscale catalysts by preparing Ni_2P NPs containing a high density of $Ni_2P(001)$ surfaces, which showed excellent HER activity. Thanks to these pioneering studies, nickel phosphide NPs have become a recent focus of attention as advanced HER catalysts. However, despite numerous ongoing studies, the shape effects of nickel phosphide NPs on HER activity have not yet been clarified, due to the complex synthetic chemistry required for shape control in metal phosphide NPs.

Herein, the shape-dependent electrocatalytic activity of Ni_2P NPs for the HER was investigated. Ni_2P NPs with different shapes, namely nanospheres (NSs) and nanorods (NRs), were prepared through a colloidal synthesis approach, and were used as well-defined model catalytic systems.[54–57] Transmission electron microscopy (TEM) analysis and electrochemical measurements revealed that Ni_2P NSs predominantly expose $Ni_2P(001)$ surfaces and show higher HER activity than Ni_2P NRs mainly exposing (210) surface. Ni_2P NSs required an overpotential of 135 mV to drive a current density of -10 mA cm^{-2}, whereas Ni_2P NRs needed a larger overpotential of 270 mV to produce the same current density. Furthermore, the turnover frequency (TOF) of Ni_2P NSs was around thirteen times higher than that of Ni_2P NRs. The results suggest that the crystallographic facets of Ni_2P NPs play an important role in dictating HER activities. The catalytic activity of Ni_2P NSs in the HER could be further enhanced by increasing the catalyst loading. Ni_2P NSs with an increased catalyst loading of 3 mg cm^{-2} produced a current density of -10 mA cm^{-2} at an overpotential of only 120 mV, and a Tafel slope of 55 mV dec^{-1}, which puts them among the most active nickel phosphide-based HER catalysts.[15–31]

7.2. SYNTHESIS OF CATALYSTS

7.2.1. Synthesis of Ni_2P NSs

Ni_2P NSs were synthesised using a previously reported one-pot heat-up method with some modifications.[54,55] First, 0.513 g of $Ni(acac)_2$ (2 mmol), 10 mL of n-octylether (95+%, TCI), and 3.75 mL of oleyl amine (70+%, Sigma-Aldrich, 6 mmol) were mixed in a 100 mL three-neck round-bottom flask (RBF) equipped with a reflux condenser vented by an oil bubbler, heating mantle, thermometer, and magnetic stirrer. The mixture was stirred and heated to 100 °C, and the flask was degassed to remove water and other low-boiling impurities before purging with N_2 gas to provide an inert atmosphere. Then, 3 mL of tri-n-octylphosphine (TOP, Sigma-Aldrich, 7.5 mmol) was injected into the flask and the temperature was raised to 230 °C at a rate of 5 °C min^{-1}. The solution was maintained at this temperature for 1.5 h to form the nuclei. Next, the temperature was rapidly increased to 310 °C over 3 min and maintained for 3 h to allow crystallisation of the Ni_2P NSs. The resulting products were isolated by precipitation using excess absolute ethanol (EtOH). The isolated NSs were dispersed in 5 mL of chloroform with sonication and reprecipitated using 40 mL of EtOH. The washing procedure was carried out three times, and the resultant product was dried in a 60 °C drying oven.

7.2.2. Synthesis of Ni_2P NRs–S

Ni_2P Short NRs (Ni_2P NRs–S) were prepared using a continuous injection method with a syringe pump, reported by Hyeon *et al*. with some modifications.[52,53] Prior to synthesis, vacuum degassing and N_2 purging processes were performed for 20 min, respectively. All reactions were carried out under N_2 atmosphere using a Schlenk line, adopting continuous delivery of a pre-made Ni–TOP complex stock solution (prepared by adding 0.19 g of $Ni(acac)_2$ (0.72 mmol) into 10 mL of TOP at 60 °C.) into 5 g of tri-n-octyl phosphine oxide (TOPO, 90%, Sigma-Aldrich) in a three-neck RBF. The reaction mixture was heated 330 °C at a rate of 5 °C min^{-1}. The stock solution was continuously injected at 10 mL h^{-1} by a syringe pump at 330 °C. The products were isolated by precipitation with excess absolute EtOH. The isolated precipitates were dispersed in 5 mL of chloroform with sonication, and reprecipitated with 40 mL of absolute EtOH. The washing procedure was carried out three times, and the resultant products were dried in a 60 °C oven.

7.2.3. Synthesis of Ni_2P NRs–L

The typical synthetic procedure for Ni_2P Long NRs (Ni_2P NRs–L) was the same as for Ni_2P NRs–S, except for the injection rate of Ni–TOP complex stock solution, which was adjusted to 5 mL h^{-1}.

7.2.4. Preparation of Electrodes

Catalyst inks were prepared by mixing 10 mg of the catalyst with 20 μL of Nafion (5 wt%, Sigma-Aldrich) in a solution of 375 μL deionized (DI) water and 125 μL of EtOH (99.9%). The mixed solution was sonicated for 30 min to produce a homogeneous slurry. Afterwards, 52 μL of the catalyst ink was dropped onto 1 cm^2 pieces of carbon paper (CP), and dried at room temperature. The catalyst loading on CP was 1 mg cm^{-2}. To remove residual surfactants, the resulting Ni_2P-deposited CP was annealed at 450 °C under 10% H_2/N_2 for 30 min.[16]

7.3. TOF CALCULATION

The TOF (s^{-1}) defined as the HER rate per active site and per time, was derived from the following equation.

$$\mathrm{TOF(s^{-1})} = \left(i \times \frac{1\mathrm{H_2}}{2\mathrm{e^-}} \times \frac{1\mathrm{e^-}}{q_\mathrm{e}} \right) \div N_{active}$$

Here, the current (i) was experimentally determined from electrochemical measurement, and q_e is the electron charge of 1.602 × 10^{-19} C. In this work, the current at −200 mV (*vs.* RHE) was used for TOF calculation. N_{active} is the number of active surface atoms. For determining N_{active}, the method proposed by previous works was employed.[16,24] The approach use average of the atoms in the molar volume to a surface, providing a crude upper bound for TOF values. The hexagonal unit cell for Ni_2P has a molar volume of:

$$V_\mathrm{m} = \frac{F_\mathrm{w}}{\rho} = \frac{148.36\ \mathrm{g\ mol^{-1}}}{7.35\ \mathrm{g\ cm^{-3}}} = \frac{20.1850\ \mathrm{cm^3}}{1\ \mathrm{mol_{Ni_2P}}}$$

The average surface occupancy is:

$$\left(\frac{1\ \mathrm{mol_{Ni_2P}}}{20.1850\ \mathrm{cm^3}} \times \frac{3 \times 6.022 \times 10^{23}\ \mathrm{atoms}}{1\ \mathrm{mol_{Ni_2P}}} \right)^{\frac{2}{3}} = 2.00 \times 10^{15}\ \frac{\mathrm{atoms}}{\mathrm{cm^2}}$$

The N_{active} was determined using the ECSA, which was derived from double layer capacitance measurement (See section 2.2.4 for details),[58] as described in the following equation:

$$N_{active} = \mathrm{ECSA(cm^2)} \times 2.00 \times 10^{15}\ \frac{\mathrm{atoms}}{\mathrm{cm^2}}$$

7.4. RESULTS AND DISCUSSION

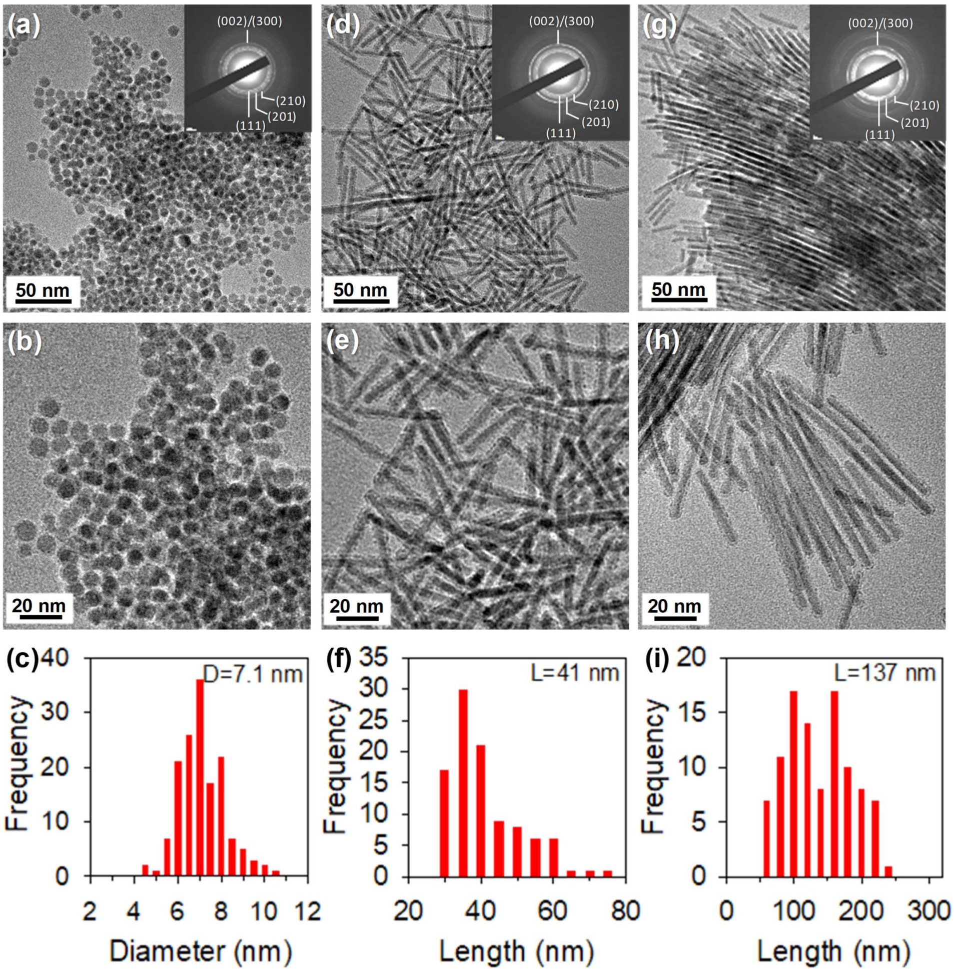

Figure 7.1. TEM images and particle diameter distributions for (a–c) Ni_2P NSs, (d–f) Ni_2P NRs–S, and (g–i) Ni_2P NRs–L. Insets in (a,d,g) show electron diffraction patterns.

Shape-controlled Ni_2P NPs were synthesised following previously reported colloidal synthetic methods with some modifications.[54-57] $Ni(acac)_2$ and TOP were used as nickel and phosphorous sources, respectively. Synthetic procedures are described in section 6.2. The size and shape of the NPs were significantly influenced by synthetic conditions.[54-57] Spherical NPs could be produced *via* a heat-up method,[54,55] whereas a continuous delivery of precursor yielded rod-shaped NPs.[52] The formation of NRs can be explained by a combination of several factors: control of nuclei concentration by continuous delivery of precursor, different binding affinities of the two organic surfactants (TOP and TOPO), and intrinsically anisotropic crystal growth of the phosphide NPs with a hexagonal Fe_2P structure.[16,56] However, the synthetic factors that influence the growth mechanism in different synthetic approaches are not yet fully understood. TEM images show that the resulting nickel phosphide NPs have three well-defined morphologies: NSs, short NRs, and long NRs (**Figure 7.1**), which are denoted as Ni_2P NSs, Ni_2P NRs–S, and Ni_2P NRs–L, respectively. The average particle sizes were determined by the TEM images (**Figures 7.1c,f,i and Table 7.1**). Ni_2P NSs have an average diameter of 7.1 ± 1.0 nm. Ni_2P NRs–S and Ni_2P NRs–L samples have average diameters of 5.3 ± 1.1 nm and 4.0 ± 0.4 nm, and lengths of 41 ± 10 nm and 137 ± 47 nm, respectively. The aspect ratio of Ni_2P NRs samples was dependent on the injection rate of the precursor solution. The relatively slow infusion rate (5 mL h^{-1}) produced Ni_2P NRs–L sample with a longer aspect ratio compared to the prepared Ni_2P NRs–S sample using a faster infusion rate (10 mL h^{-1}). Based on previous suggestions,[56] we propose the following growth mechanism for Ni_2P NRs. At the initial stage of nucleation, spherical NPs are formed. Continuously delivered Ni–TOP complexes decompose at the surface of NPs. The octyl groups produced by the decomposition of Ni-TOP complexes are preferentially adhered to the (210) surface, parallel to the growth direction of NRs. Slow injection of Ni–TOP complexes can lead to growth toward [001] direction by more effectively blocking the (210) surface with sufficient capping agents.

Table 7.1. The average length and diameter of Ni_2P NRs–S and NRs–L, and the diameter of Ni_2P NSs, determined by TEM images.

Sample	Diameter (nm) [a]	Length (nm) [a]
Ni_2P NSs	7.1 ± 1.0	
Ni_2P NRs–S	5.3 ± 1.1	41 ± 10
Ni_2P NRs–L	4.0 ± 0.4	137 ± 47

[a] Crystallite sizes (diameter and length) were measured on the particles in TEM images. The values were obtained by averaging the measured sizes over one hundred of particles.

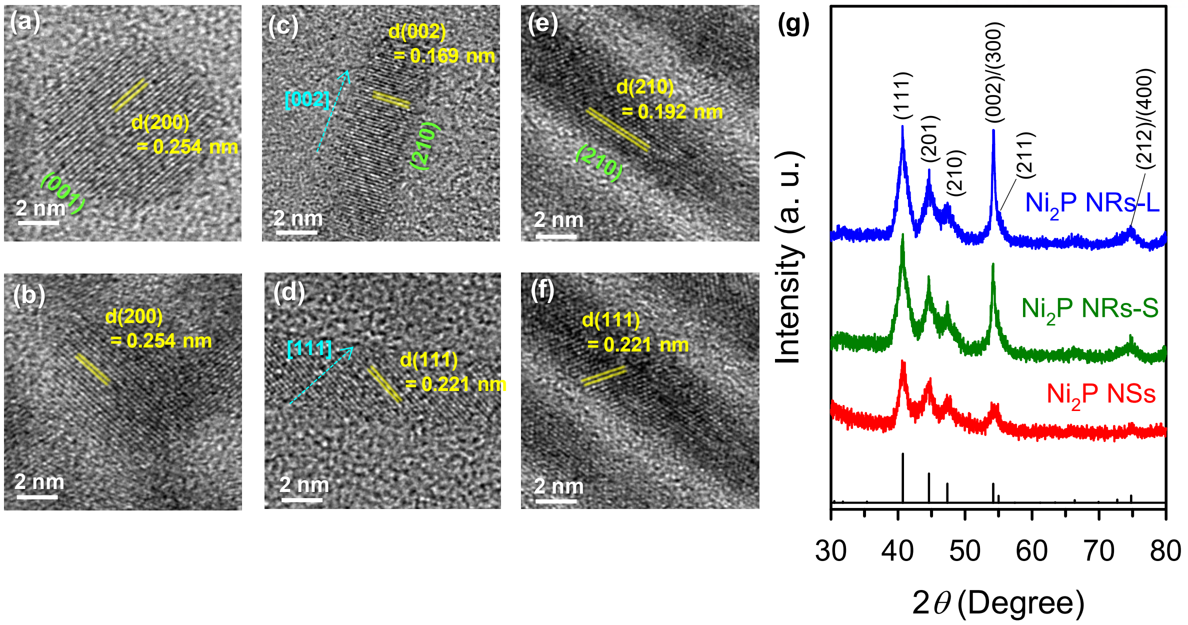

Figure 7.2. HRTEM images for (a,b) Ni$_2$P NSs, (c,d) Ni$_2$P NRs–S, and (e,f) Ni$_2$P NRs–L. (g) XRD patterns of Ni$_2$P NPs. Vertical bars represent the XRD pattern for Ni$_2$P standard (JCPDS No. 89-2742).

The microstructures of Ni$_2$P NPs were observed with high resolution TEM (HRTEM) images (**Figure 7.2**). In the HRTEM images of Ni$_2$P NSs (**Figures 7.2a,b**), a lattice spacing of 0.254 nm was observed, which can be matched to the inter-planar distance for the Ni$_2$P(200) plane, perpendicular to the (001) plane.[16] HRTEM images for two Ni$_2$P NRs (**Figures 7.2c–f**) revealed lattice spacings of 0.169 nm and 0.192 nm, corresponding to the inter-planar distances of the (002) and (210) planes of Ni$_2$P NPs, respectively, which are perpendicular and parallel to the growth direction of [001], resepctively.[57] Hence, these HRTEM analyses suggested that Ni$_2$P NSs mainly exposed Ni$_2$P(001) surfaces[16], whereas Ni$_2$P NRs predominantly exposed Ni$_2$P(210) surfaces. The structures of Ni$_2$P NPs were further analyzed by X-ray diffraction (XRD) patterns (**Figure 7.2g**). The three Ni$_2$P NPs have good crystallinity, in accordance with HRTEM analysis. The positions of all XRD peaks were consistent with those of the Ni$_2$P standard (JCPDS No. 89-2742), and no impurity phases were found. The (002)/(300) diffraction peak at 2θ = 54.2° became sharper in the order of NRs–L > NRs–S > NSs due to the increase in crystallite length toward [001] direction. The XRD analysis well match the HRTEM analysis. From the close examination of HRTEM images and XRD patterns, it is clear that the crystal growth of NRs occurs mainly along the [001] directions, exposing the Ni$_2$P(210) surfaces.

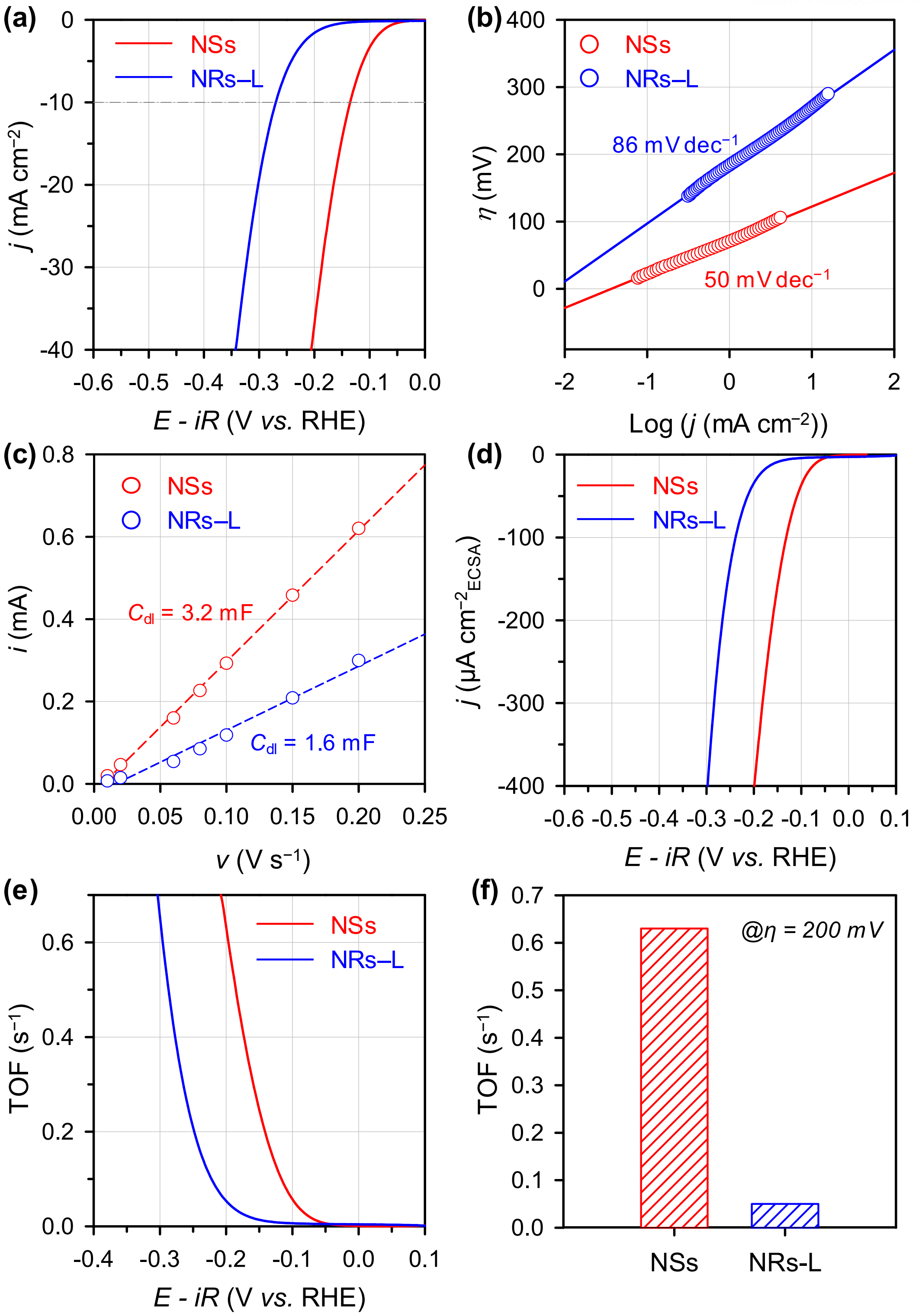

Figure 7.3. (a) LSV curves of Ni_2P NSs and Ni_2P NRs–L catalysts and (b) corresponding Tafel plots for the HER. (c) Double layer capacitance measurements for determining the ECSAs. (d) LSV curves normalized by the ECSA. (e) TOFs with respect to potentials. (f) Comparison of TOFs for Ni_2P NSs and Ni_2P NRs–L catalysts at −200 mV (*vs*. RHE).

The above prepared Ni_2P NPs with distinctively different surfaces served as well-defined model catalysts for investigating their shape-dependent HER activity. The HER activities of Ni_2P NPs were examined using a three-electrode system in 0.5 M H_2SO_4. Prior to electrochemical measurements, the Ni_2P NPs were drop-cast onto a 1 cm^2 CP substrate at a mass loading of 1 mg cm^{-2}. The resulting Ni_2P/CP catalysts were annealed at 450 °C in 10% H_2/N_2 to remove residual organic surfactants surrounding the NPs.[16] Electrode preparation is described in detail in section 7.2.4. Linear sweep voltammetry (LSV) curves were displayed after *iR* correction for Ohmic drops (**Figure 7.3a**). Notably, Ni_2P NSs/CP showed significantly higher HER activity than Ni_2P NRs–L/CP samples in terms of overpotential and Tafel slope (**Table 7.2**). Ni_2P NSs/CP required 135 mV of overpotential to produce a cathodic current density of −10 mA cm^{-2}, whereas Ni_2P NRs–L/CP required larger overpotential of 270 mV. In combination with XRD and TEM analyses, we suggest that the predominantly exposed $Ni_2P(001)$ surface of Ni_2P NSs provided active sites, in agreement with previous work.[16]

The HER process proceeds with three reaction steps in acidic media. The first step is the Volmer step (discharge step):

$$\text{Volmer step: } H_3O^+ + e^- + S \rightarrow SH_{ads} + H_2O$$

In the Volmer step, electrons transferred to the cathode are combined with protons adsorbed on empty catalytic active sites (S). The Volmer step is followed either by a Heyrovsky step (electrochemical desorption) or Tafel step (chemical desorption) to complete HER:

$$\text{Heyrovsky step: } SH_{ads} + e^- + H^+ \rightarrow S + H_2$$

$$\text{Tafel step: } 2SH_{ads} \rightarrow 2S + H_2$$

In the Heyrovsky step, an electron and proton are delivered to the adsorbed hydrogen atom to generate a hydrogen molecule, whereas in the Tafel step, two adsorbed hydrogen atoms are combined to form molecular hydrogen. Hence, to complete the HER, Volmer-Heyrovsky or Volmer-Tafel mechanisms must be involved. To estimate the reaction mechanism of HER, Tafel slope is used as an indicator. These slopes were extracted from the linear portion of Tafel plots, which were derived from the LSV curves. The Tafel slopes for Ni_2P NSs/CP, and Ni_2P NRs–L/CP were 50 and 86 mV dec^{-1}, respectively (**Figure 7.3b**). The Tafel slope range of 50−100 mV dec^{-1} for Ni_2P NPs/CP samples demonstrate that the rate-determining step of this HER is the Volmer step.[26] The relatively smaller Tafel slope indicates faster kinetics for Ni_2P NSs/CP than Ni_2P NRs–L/CP during HER, indicating that hydrogen adsorption was more favourable on the $Ni_2P(001)$ surface. In terms of overpotential at −10 mA cm^{-2} and Tafel slopes, the HER performance of Ni_2P NSs/CP (135 mV, 50 mV dec^{-1}) was comparable to those of other nickel phosphide HER catalysts, such as Ni_2P NPs on Ti foil (130 mV, 50 mV dec^{-1}),[16] Ni_2P on carbon nanotubes (124 mV, 53 mV dec^{-1}),[23] and Ni_5P_4-Ni_2P nanosheet array on Ni foam (120 mV, 79.1 mV dec^{-1}).[25]

While overpotentials and Tafel slopes can be useful for comparing device-level performance of HER catalysts, TOF can provide activity data of more fundamental relevance. To calculate the TOF of the two catalysts, we first estimated the electrochemically active surface area (ECSAs) by measuring C_{dl} from cyclic voltammograms (CVs) with multiple scan rates (see section 2.2.4 for details).[58,59] Plotting the cathodic currents as a function of scan rate yielded a slope equal to the C_{dl} (**Figure 7.3c**). The C_{dl}-derived ECSAs for Ni_2P NSs/CP and Ni_2P NRs/CP were 91 and 46 cm^2, respectively, indicating that more surface sites were available for electrochemical reactions in the Ni_2P NSs/CP. **Figure 7.3d** shows the LSV curves normalized by ECSA. Based on the ECSA values and the assumption of a cubic unit cell, we calculated TOF values for the shape-controlled NP catalysts (**Figure 7.3e,f**).[16,24] The TOF values determined at −200 mV (*vs.* reversible hydrogen electrode, RHE) were around 13-fold higher for Ni_2P NSs/CP (0.63) than for Ni_2P NRs–L/CP (0.05), providing clear evidence that Ni_2P(001) was a more catalytically active surface than Ni_2P(210). Overall HER activity parameters are summarized in **Tables 7.2 and 7.3**.

Table 7.2. HER activities of Ni_2P NPs, expressed in terms of overpotential at −10 mA cm^{-2}, Tafel slope, and exchange current density.

Sample	Overpotential at 10 mA cm^{-2} (V)	Tafel slope [a] (mV dec^{-1})	Exchange current density [b] (A cm^{-2})
Ni_2P NSs/CP	0.135	50	3.68×10^{-5}
Ni_2P NRs–L/CP	0.270	86	7.45×10^{-6}

[a,b] The Tafel slopes and exchange current densities were derived from the linear portion of the corresponding Tafel plots.

Table 7.3. Double layer capacitance, ECSA, and TOF values of the Ni_2P NPs.

Sample	Double layer capacitance [a] (C_{dl}, mF)	ECSA [b] (cm^2)	TOF [c] (s^{-1})
Ni_2P NSs/CP	0.135	50	3.68×10^{-5}
Ni_2P NRs–L/CP	0.270	86	7.45×10^{-6}

[a,b] Double layer capacitance and ECSA were determined *via* previous method.[58,59]
[c] TOF was determined by previous method (see Experimental section in manuscript).[60,61]

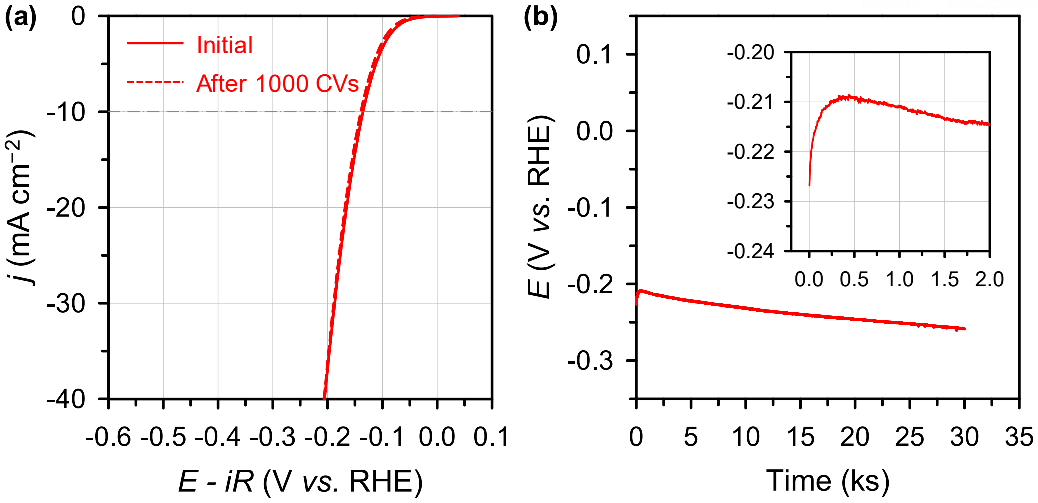

Figure 7.4. (a) LSV curves of Ni_2P NSs/CP recorded before and after 1,000 CVs between −0.3 V and 0.1 V (*vs.* RHE) at a scan rate of 50 mV s^{-1} in 0.5 M H_2SO_4. (b) Chronopotentiometry measured at a static current of −10 mA.

In addition to the catalytic activity, practical applications are highly dependent on the long-term durability of the catalysts. The durability of the Ni_2P NSs/CP catalyst with better activity was assessed through 1000 CV repetitions between −0.3 V and 0.1 V (*vs.* RHE) at a scan rate of 50 mV s^{-1} in 0.5 M H_2SO_4 (**Figure 7.4a**). The LSV curves before and after potential cycles nearly overlapped. In addition, chronopotentiometry was carried out by applying a static current of −10 mA for 30,000 s (**Figure 7.4b**). During the initial 500 s of electrolysis, the HER performance continuously increased, as evidenced by the overpotential decreasing from 227 mV to 209 mV (**Figure 7.4b, inset**). This initial “activation” phenomenon could arise from the removal of residual inactive impurities from the Ni_2P NSs, exposing more catalytically active sites. After 500 s, the HER activity gradually decreased.

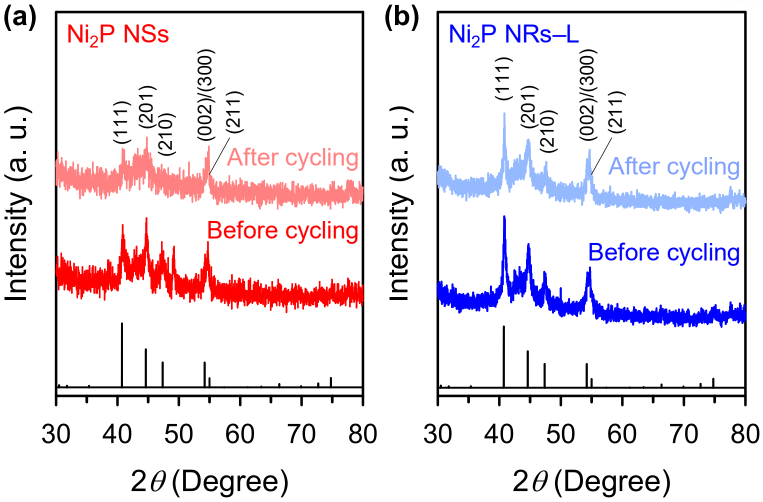

Figure 7.5. XRD patterns of (a) Ni_2P NSs/CP and (b) Ni_2P NRs–L/CP recorded before and after 1,000 CVs. Vertical bars represent the XRD pattern for Ni_2P standard (JCPDS No. 89-2742).

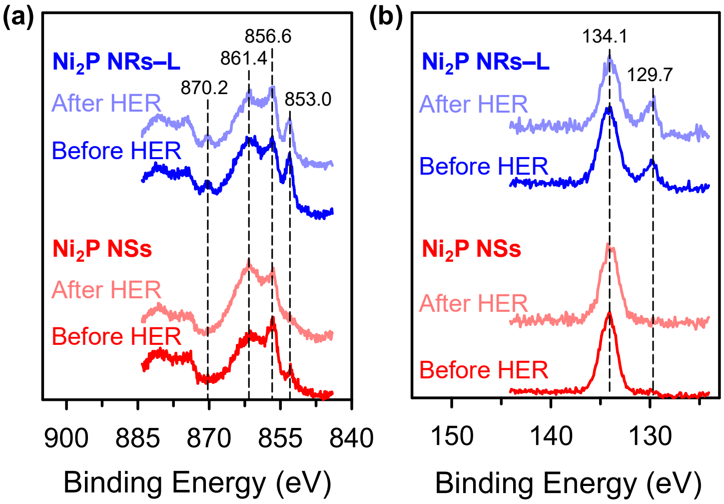

Figure 7.6. (a) Ni 2p and (b) P 2p XPS spectra for Ni_2P NPs/CP before and after 1,000 CVs.

XRD and X-ray photoelectron spectroscopy (XPS) analyses confirmed that the physical and chemical states of Ni_2P NPs were nearly preserved after 1,000 CV cycles between 0.1 V and −0.3 V (*vs.* RHE) at a sweep rate of 50 mV s^{-1} in 0.5 M H_2SO_4 (**Figures 7.5 and 7.6**). The high stability of Ni_2P NSs can be explained by the passivation layer on the surface of Ni_2P NSs with nickel phosphate phase, as evidenced by the XPS analysis (**Figure 7.6**). The durability tests revealed that Ni_2P NSs were highly durable electrocatalysts in acidic media.

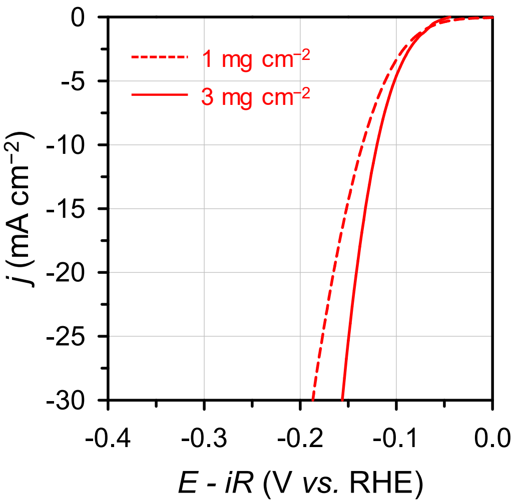

Figure 7.7. LSV curves of Ni_2P NSs/CP for the HER with different catalyst loadings of 1 mg cm^{-2} and 3 mg cm^{-2}.

Finally, to further improve the catalytic performance of Ni_2P NSs for HER, the catalyst was fabricated with a higher loading. **Figure 7.7** shows the LSV curves for Ni_2P NSs/CP with catalyst loadings of 1 mg cm^{-2} and 3 mg cm^{-2}. Ni_2P NSs/CP with a loading of 3 mg cm^{-2} achieved a cathodic current density of -10 mA cm^{-2} at an overpotential of only 120 mV in 0.5 M H_2SO_4 with a Tafel slope of 55 mV dec^{-1}, which is one of the best performances among Ni_2P-based HER catalysts.[15–31]

7.5. CONCLUSION

In conclusion, the shape-dependent catalytic activities of Ni_2P NPs were investigated toward the HER. In combination with TEM and XRD analyses revealed that the mainly exposed crystal surfaces in Ni_2P NSs and NRs are (001) and (210), respectively. Electrochemical measurements showed that the overall HER activity of Ni_2P NSs was superior to that of Ni_2P NRs–L in terms of overpotential, Tafel slope, and TOF. The results clearly show that the Ni_2P(001) surface was more likely to be active than the Ni_2P(210) surface. Furthermore, Ni_2P NSs reported herein exhibited excellent HER performance and stability. Overall, this study suggests that the rational control of catalyst morphology is important for enhancing HER performance.

7.6. REFERENCES

1. Alivisatos, P. *Science* **1996**, *271*, 933–937.
2. Burda, C.; Chen, X.; Narayanan, R.; El-Sayed, M. A. *Chem. Rev.* **2005**, *105*, 1025–1102.
3. Park, J.; Joo, J.; Kwon, S. G.; Jang, Y.; Hyeon, T. *Angew. Chem. Int. Ed.* **2007**, *46*, 4630–4660.
4. Xia, Y.; Xiong, Y.; Lim, B.; Skrabalak, S. E. *Angew. Chem. Int. Ed.* **2009**, *48*, 60–103.
5. Lee, K.; Kim, M.; Kim, H. *J. Mater. Chem.* **2010**, *20*, 3791–3798.
6. Jia, C.-J.; Schüth, F. *Phys. Chem. Chem. Phys.* **2011**, *13*, 2457–2487.
7. An, K.; Somorjai, G. A. *ChemCatChem* **2012**, *4*, 1512–1524.
8. Cargnello, M.; Fornasiero, P.; Gorte, R. J. *ChemPhysChem* **2013**, *14*, 3869–3877.
9. Narayanan, R.; El-Sayed, M. A. *J. Phys. Chem. B* **2005**, *109*, 12663–12676.
10. Bratlie, K. M.; Lee, H.; Komvopoulos, K.; Yang, P.; Somorjai, G. A. *Nano Lett.* **2007**, *7*, 3097–3101.
11. Huang, X.; Zhao, Z.; Cao, L.; Chen, Y.; Zhu, E.; Lin, Z.; Li, M.; Yan, A.; Zettl, A.; Wang, Y. M.; Duan, X.; Mueller, T.; Huang, Y. *Science* **2015**, *348*, 1230–1234.
12. Stamenkovic, V. R.; Fowler, B.; Mun, B. S.; Wang, G.; Ross, P. N.; Lucas, C. A.; Markovic, N. M. *Science*, **2007**, *315*, 493–497.
13. Xiao, P.; Chen, W.; Wang, X. *Adv. Energy Mater.* **2015**, *5*, 1500985.
14. Kibsgaard, J.; Tsai, C.; Chan, K.; Benck, J. D.; Nøskov, J. K.; Abild-Pedersen, F.; Jaramillo, T. F. *Energy Environ. Sci.* **2015**, *8*, 3022–3029.
15. Liu, P.; Rodriguez, J. A. *J. Am. Chem. Soc.* **2005**, *127*, 14871–14878.
16. Popczun, E. J.; McKone, J. R.; Read, C. G.; Biacchi, A. J.; Wiltrout, A. M.; Lewis, N. S.; Schaak, R. E. *J. Am. Chem. Soc.* **2013**, *135*, 9267–9270.
17. Feng, L.; Vrubel, H.; Bensimon, M.; Hu, X. *Phys. Chem. Chem. Phys* **2014**, *16*, 5917–5921.
18. Kucernak, A. R. J.; Sundaram, V. N. N. *J. Mater. Chem. A* **2014**, *2*, 17435–17445.
19. Pu, Z.; Liu, Q.; Tang, C.; Asiri, A. M.; Sun, X. *Nanoscale*, **2014**, *6*, 11031–11034.
20. Jin, Z.; Li, P.; Huang, X.; Zeng, G.; Jin, Y.; Zheng, B.; Xiao, D. *J. Mater. Chem. A.* **2014**, *2*, 18593–18599.
21. Huang, Z.; Chen, Z.; Chen, Z.; Lv, C.; Meng, H.; Zhang, C. *ACS Nano* **2014**, *8*, 8121–8129.
22. Pan, Y.; Liu, Y.; Zhao, J.; Yang, K.; Liang, J.; Liu, D.; Hu, W.; Liu, D.; Liu, Y.; Liu, C. *J. Mater. Chem. A* **2015**, *3*, 1656–1665.
23. Pan, Y.; Hu, W.; Liu, D.; Liu, Y.; Liu, C. *J. Mater. Chem. A* **2015**, *3*, 13087–13094.
24. Laursen, A. B.; Patraju, K. R.; Whitaker, M. J.; Retuerto, M.; Sarkar, T.; Yao, N.; Ramanujachary, K. V.; Greenblatt, M.; Dismukes, G. C. *Energy Environ. Sci.* **2015**, *8*, 1027–1034.
25. Wang, X.; Kolen'ko, Y. V.; Bao, X.-Q.; Kovnir, K.; Liu, L. *Angew. Chem. Int. Ed.* **2015**, *54*, 8188–8192.
26. Moon, J.-S.; Jang, J.-H.; Kim, E.-G.; Chung, Y.-H.; Yoo, S. J.; Lee, Y.-K. *Journal of Catalysis*

2015, *326*, 92–99.

27. Han, A.; Jin, S.; Chen, H.; Ji, H.; Sun, Z.; Du, P. *J. mater. Chem. A* **2015**, *3*, 1941–1946.
28. Stern, L.-A.; Feng, L.; Song, F.; Hu, X. *Energy Environ. Sci.* **2015**, *8*, 2347–2351.
29. Zhuo, J.; Cabán-Acevedo, M.; Liang, H.; Samad, L.; Ding, Q.; Fu, Y.; Li, M.; Jin, S. *ACS Catal.* **2015**, *5*, 6355–6361.
30. Tian, T.; Ai, L.; Jiang, J. *RSC Adv.* **2015**, *5*, 10290–10295.
31. Wang, C.; Ding, T.; Sun, Y.; Zhou, X.; Liu, Y.; Yang, Q. *Nanoscale* **2015**, *7*, 19241–19249.
32. Jiang, P.; Liu, Q.; Liang, Y.; Tian, J.; Asiri, A. M.; Sun, X. *Angew. Chem. Int. Ed.* **2014**, *53*, 12855–12859.
33. Tian, J.; Liu, Q.; Asiri, A. M.; Sun, X. *J. Am. Chem. Soc.* **2014**, *136*, 7587–7590.
34. Liang, Y.; Liu, Q.; Asiri, A. M.; Sun, X.; Luo, Y. *ACS Catal.* **2014**, *4*, 4065–4069.
35. Callejas, J. F.; McEnaney, J. M.; Read, C. G.; Crompton, J. C.; Biacchi, A. J.; Popczun, E. J.; Gordon, T. R.; Lewis, N. S.; Schaak, R. E. *ACS Nano* **2014**, *8*, 11101–11107.
36. McEnaney, J. M.; Crompton, J. C.; Callejas, J. F.; Popczun, E. J.; Biacchi, A. J.; Lewis, N. S.; Schaak, R. E. *Chem. Mater.* **2014**, *26*, 4826–4831.
37. Ryu, J.; Jung, N.; Jang, J. H.; Kim, H.-J.; Yoo, S. J. *ACS Catal.* **2015**, *5*, 4066–4074.
38. Callejas, J. F.; Read, C. G.; Popczun, E. J.; McEnaney, J. M.; Schaak, R. E. *Chem. Mater.* **2015**, *27*, 3769–3774.
39. Son, C. Y.; Kwak, I. H.; Kim, Y. R.; Park, J. *Chem. Commun.* **2016**, *52*, 2819–2822.
40. Pan, Y.; Liu, Y.; Liu, C. *J. Power Sources* **2015**, *285*, 169–177.
41. Pan, Y.; Yang, N.; Chen, Y.; Lin, Y.; Li, Y.; Liu, Y.; Liu, C. *J. Power Sources*, **2015**, *297*, 45–52.
42. Pan, Y.; Lin, Y.; Chen, Y.; Liu, Y.; Liu, C. *J. Mater. Chem. A* **2016**, *4*, 4745–4754.
43. Pan, Y.; Lin, Y.; Liu, Y.; Liu, C. *Catal. Sci. Technol.* **2016**, *6*, 1611–1615.
44. Zou, X.; Zhang, Y. *Chem. Soc. Rev.* **2015**, *44*, 5148–5180.
45. Jaramillo, T. F.; Jørgensen, K. P.; Bonde, J.; Nielsen, J. H.; Horch, S.; Chorkendorff, I. *Science* **2007**, *317*, 100–102.
46. Li, Y.; Wang, H.; Xie, L.; Liang, Y.; Hong, G.; Dai, H. *J. Am. Chem. Soc.* **2011**, *133*, 7296–7299.
47. Wang, H.; Lu, Z.; Xu, S.; Kong, D.; Cha, J. J.; Zheng, G.; Hsu, P.-C.; Yan, K.; Bradshaw, D.; Prinz, F. B.; Cui, Y. *Proc. Natl. Acad. Sci.* **2013**, *110*, 19701–19706.
48. Seo, B.; Jung, G. Y.; Sa, Y. J.; Jeong, H. Y.; Cheon, J. Y.; Lee, J. H.; Kim, H. Y.; Kim, J. C.; Shin, H. S.; Kwak, S. K.; S. H. Joo, *ACS Nano* **2015**, *9*, 3728–3739.
49. Seo, B.; Jeong, H. Y.; Hong, S. Y.; Zak, A.; Joo, S. H. *Chem. Commun.*, **2015**, *51*, 8334–8337.
50. Yoon, D.; Seo, B.; Lee, J.; Nam, K. S.; Kim, B.; Park, S.; Baik, H.; Joo, S. H.; Lee, K. *Energy Environ. Sci.* **2016**, *9*, 850–856.
51. Kibsgaard, J.; Jaramillo, T. F. *Angew. Chem. In. Ed.* **2014**, *53*, 14433–14437.
52. Cabán-Acevedo, M.; Stone, M. L.; Schmidt, J. R.; Thomas, J. G.; Ding, Q.; Chang, H.-C.; Tsai,

M.-L.; He, J.-H.; Jin, S. *Nat. Mater.* **2015**, *14*, 1245–1251.

53. Chen, W.-f.; Wang, C.-H.; Sasaki, K.; Marinkovic, N.; Xu, W.; Muckerman, J. T.; Zhu, Y.; Adzic, R. R. *Energy Environ. Sci.* **2013**, *6*, 943–951.
54. Liyanage, D. R.; Danforth, S. J.; Liu, Y.; Bussel, M. E.; Brock, S. L. *Chem. Mater.* **2015**, *27*, 4349–4357.
55. Muthuswamy, E.; Savithra, G. H. L.; Brock, S. L. *ACS Nano* **2011**, *5*, 2402–2411.
56. Park, J.; Koo, B.; Yoon, K. Y.; Hwang, Y.; Kang, M.; Park, J.-G.; Hyeon, T. *J. Am. Chem. Soc.* **2005**, *127*, 8433–8440.
57. Chen, Y.; She, H.; Luo, X.; Yue, G.-H.; Peng, D.-L. *Journal of Crystal Growth* **2009**, *311*, 1229–1233.
58. McCrory, C. C. L.; Jung, S.; Peters, J. C.; Jaramillo, T. F. *J. Am. Chem. Soc.* **2013**, *135*, 16977–16987.
59. McCrory, C. C. L.; Jung, S.; Ferrer, I. M.; Chatman, S. M.; Peters, J. C.; Jaramillo, T. F. *J. Am. Chem. Soc.* **2015**, *137*, 4347–4357.
60. Popczun, E. J.; McKone, J. R.; Read, C. G.; Biacchi, A. J.; Wiltrout, A. M.; Lewis, N. S.; Schaak, R. E. *J. Am. Chem. Soc*. **2013**, *135*, 9267–9270.
61. Laursen, A. B.; Patraju, K. R.; Whitaker, M. J.; Retuerto, M.; Sarkar, T.; Yao, N.; Ramanujachary, K. V.; Greenblatt, M.; Dismukes, G. C. *Energy Environ. Sci.* **2015**, *8*, 1027–1034.

8

MONOMERIC MoS_4^{2-} ADHERED ON GOLD NANOCRYSTALS FOR EFFICIENT HYDROGEN EVOLUTION REACTION

8.1. INTRODUCTION

As a representative non-precious hydrogen evolution reaction (HER) catalyst, molybdenum sulfides have received significant attention, and have demonstrated high activity and stability in acidic media.[1–7] Since MoS_2 edge sites were suggested as major active species by theoretical and experimental studies,[8–10] significant efforts have been geared to maximize the active edge site densities.[11–22] In this context, several strategies have been developed, including space-confined growth,[11–14] vertical alignment,[15–17] and the design of biomimetic molecular catalysts,[18–22] which could significantly enhance the HER performance. In particular, the molecular mimic approach is highly intriguing, as such a design allows for exposing active edge configurations to maximum extent. A number of molecular analogues to MoS_2 edge have been explored as the electrocatalysts for the HER.[18–22] Representative examples include trimeric cluster compounds based on $[Mo_3S_4]^{4+}$,[18] and $[Mo_3S_{13}]^{2-}$,[20,22] a dimeric $[Mo_2S_{12}]^{2-}$ cluster,[21] and an exquisitely designed molybdenum complex, $[(PY5Me_2)MoS_2]^{2+}$ ($PY5Me_2$ = 2,6-bis(1,1-bis(2-pyridyl)ethyl)pyridine).[19] The cluster-based MoS_2 molecular mimics have demonstrated excellent electrocatalytic performances for the HER. Furthermore, as well-defined molecular catalysts selectively contain desirable sulfur sites, they can serve as appropriate model catalysts for elucidating genuine active sulfur sites for hydrogen adsorption.

In MoS_x-based HER catalysts, understanding of the active sulfur sites is of crucial importance because sulfur sites have been widely accepted as proton reduction centers in the HER.[23,24] However, diverse chemical states of the sulfur species, i.e., bridging S_2^{2-}, terminal S_2^{2-}, apical S^{2-}, and unsaturated S^{2-}, have rendered the identification of genuine active sulfur sites difficult.[22,25–27] In this regard, exploiting molecular cluster compounds possessing specific sulfur sites can provide important clues for identifying active sulfur species. For instance, $[Mo_2S_{12}]^{2-}$ clusters with only bridging and terminal S_2^{2-} sites showed higher HER performance than trimeric $[Mo_3S_{13}]^{2-}$ clusters containing apical S^{2-} sites together with the bridging and terminal S_2^{2-} sites. The results suggest that apical S^{2-} species is catalytically inactive or less active for the HER compared to the bridging or terminal S_2^{2-} sites.[21] Recent *in situ* Raman study of MoS_x catalysts suggested that the bridging S_2^{2-} sites are transformed into unsaturated S^{2-} species under the HER potential.[24]

Herein, inspired by the previous findings, we demonstrate that even a monomeric thiomolybdate, MoS_4^{2-}, possessing only S^{2-} ligands and mimicking coordinatively unsaturated S^{2-} sites of MoS_2, can be exploited as an efficient HER catalyst.[28] The MoS_4^{2-} represents the smallest molecular mimic for MoS_2 active sites ever reported. MoS_4^{2-} could efficiently catalyze the HER in acidic media without any further treatment or structuring engineering. The activity and durability of MoS_4^{2-} could be further enhanced by immobilizing them onto the surfaces of Au nanocrystals (NCs). The resulting Au–MoS_4^{2-} structure exhibited very high intrinsic HER activity, with turnover frequency (TOF) of 0.30 s^{-1} at −150 mV (*vs.* reversible hydrogen electrode, RHE), which surpasses those for the state-of-the-art MoS_x-based HER catalysts.

8.2. SYNTHESIS OF CATALYSTS

8.2.1. Synthesis of Au NCs

The Au NCs were synthesized following a reported procedure with some modification.[29] At first, 0.5 mmol of borane tert-butylamine complex (TBAB) was dissolved in 1 mL of 1,2,3,4,-tetrahydronaphthalene(tetraline) and 1 mL of oleylamine (OAm) *via* sonication for 1 h. Using a 100 mL of three-neck flask, 0.2 g of gold(III)chloride trihydrate ($HAuCl_4$) was dissolved in 10 mL of tetralin and 10 mL of OAm at room temperature (RT) under N_2 flow and the solution was vigorously stirred for 10 min. Then, the TBAB solution was injected into the flask. The mixed solution was then stirred for 1 h at RT. The synthesized Au NCs were precipitated by addition of ethanol with a volume ratio of (mixture : ethanol = 1 : 2) and centrifugation at 7000 rpm for 5 min. The washing process was repeated three times for complete elimination of unreacted precursors and by-products. Finally, the obtained Au NCs were re-dispersed in 5 mL of hexane.

8.2.2. Synthesis of Au–MoS_4^{2-}

The Au–MoS_4^{2-} was synthesized *via* ligand exchange method following a previous report.[30] The ligand exchange process was typically carried out in a glovebox. For the exchange of organic ligands (oleyl amine) with MoS_4^{2-} inorganic ligands, 30 mg of the Au NCs in hexane (30 mg mL^{-1}) was added to a vial containing 80 mg of ammonium tetrathiomolybdate ($(NH_4)_2MoS_4$, 99.97%, Sigma-Aldrich) dissolved in N-methylformamide (NMF) (20 mg mL^{-1}). The immiscible phase mixture was stirred vigorously until the ligand transfer of NCs is completed. The phase transfer process can be monitored through the color change of hexane phase from orange to colorless. After ligand exchange, upper hexane phase was discarded by pipette, and the MoS_4^{2-}-capped NCs was then precipitated from the remained solution by addition of isopropanol with a volume ratio of (solution : ethanol = 1 : 3), and centrifugation at 7800 rpm for 6 min. This washing process was repeated three times to remove the unreacted MoS_4^{2-} completely, and MoS_4^{2-}-capped NCs were re-dispersed in 2 mL of NMF for further analysis.

8.2.3. Preparation of Electrodes

The Au NCs, MoS_4^{2-} and Au–MoS_4^{2-} solutions were drop-cast on carbon paper (CP) with an area of 1 cm^{-2}. For Au NCs, 33 μL of the Au NCs dispersed in hexane (30 mg mL^{-1}) was drop-cast on the CP and dried at RT for 2 min. For MoS_4^{2-}, a catalyst ink was prepared by mixing 590 μL of the $(NH_4)_2MoS_4$ in NMF (20 mg mL^{-1}) with 20 μL of Nafion (5 wt.% in isopropanol/DI water, Sigma-Aldrich), and sonicated for 30 min to produce a homogeneous slurry. Afterward, aliquots of the ink (3, 6, 18, 30, and 61 μL) were dropped onto the CP, and dried at 120 C for 10 min. For Au–MoS_4^{2-}, a catalyst ink was prepared by mixing the 260 μL of Au–MoS_4^{2-} in NMF (0.77 mg mL^{-1} for Mo and S, determined by inductively coupled plasma optical emission spectrometry (ICP-OES) (**Table 8.1**), with 20 μL of Nafion (5 wt.% in isopropanol/DI water, Sigma-Aldrich), and sonicated for 30 min to produce a homogeneous slurry. Afterward, aliquots of the ink (3.9, 7.5, 13, 26, and 30 μL) were dropped onto the CP, and dried at 120 C for 10 min. The catalyst-coated CPs are connected with copper wires using kapton tapes for electrochemical measurements.

Table 8.1. Contents of Au, Mo, and S in Au–MoS_4^{2-}, determined by ICP-OES analysis.

Element	**mg mL^{-1}**
Au	129
Mo	0.310
S	0.458

[a] 3.9, 7.5, 13, 26, and 39 μL of the Au–MoS_4^{2-} colloidal solution was drop-cast on the CP with an area of 1 cm^2. The corresponding catalyst loadings on the CP were 3, 5, 10, 20, and 30 μg_{Mo+S} cm^{-2}, respectively.

8.3. TOF CALCULATION

The TOF (s^{-1}) defined as the HER rate per active site and per time, was derived from the following equation **(1)**:

$$\text{TOF}\,(\text{s}^{-1}) = \left\{ j\,(\text{A cm}^{-2}) \times S\,(\text{cm}^{2}) \times \frac{1\text{H}_2}{1\text{e}^{-}} \times \frac{1\text{e}^{-1}}{q_\text{e}} \right\} \div N_{active} \quad \cdots\cdots \ \textbf{(1)}$$

where j is the current density, as calculated from the current generated during the HER, S is the geometric surface area of the working electrode (1 cm^2), and q_e is the elementary charge (1.602 × 10^{-19} C). N_{active} is the number of Mo atoms, which were assumed to be the active sites. We assumed all the Mo atoms are involved in the catalysis (lower bound limit). For example, for the MoS_4^{2-}, N_{active} was obtained from the following equation **(2)**:

$$\text{N}_{\text{active}} = \left\{ \frac{m \times S\,(\text{cm}^{2}) \times N_\text{A}}{MW \text{ of MoS}_4} \right\} \quad \cdots\cdots \ \textbf{(2)}$$

where, m is the catalyst loading on the electrode (10 μg_{Mo+S} cm^{-2}), and N_A is Avogadro's number (6.022 × 10^{23}). The catalyst loading was estimated by ICP-OES analysis, as summarized in **Table 8.1**. The calculated value of N_{active} was used in equation **(1)**, thus affording TOFs. Likewise, TOFs for other cluster catalysts, namely, $[Mo_3S_4]^{4+}$, $[Mo_3S_{12}]^{2-}$, and $[Mo_2S_{12}]^{2-}$, were calculated (**Figure 8.8a**).

8.4. RESULTS AND DISCUSSION

The MoS_4^{2-} is derived from commercially available inorganic precursor, $(NH_4)_2MoS_4$, in which each Mo center is coordinated to four S atoms (**Figure 8.1a**).[28] Au–MoS_4^{2-} was prepared *via* a ligand exchange of pre-synthesized, oleyl amine capped Au NCs, following previously reported procedure.[30] The experimental details are described in section 8.2. Transmission electron microscope (TEM) images show that the primary size and shape of the original Au NCs (**Figure 8.1b,d**) were well preserved after the ligand exchange (**Figure 8.1c,e**). The distance between the NCs were reduced in Au–MoS_4^{2-} compared to Au NCs due to a shorter length of MoS_4^{2-} ligand than oleyl amine (**Figure 8.1b,c**).[30] Energy dispersive X-ray spectroscopy (EDS) elemental mapping images confirmed the existence of Au, Mo, and S elements in the Au–MoS_4^{2-} (**Figure 8.2**). For physicochemical characterizations and electrochemical measurements, MoS_4^{2-} and Au–MoS_4^{2-} were drop-cast on a CP substrate. The loadings of each element of Au–MoS_4^{2-} on a CP were determined by ICP-OES analysis (**Table 8.1**). Raman spectra for MoS_4^{2-} and Au–MoS_4^{2-} and their deposited films on a CP substrate were nearly identical, indicating there was no significant changes in electronic structure of MoS_x in MoS_4^{2-} and Au–MoS_4^{2-} after the deposition on CP (**Figure 8.3**).

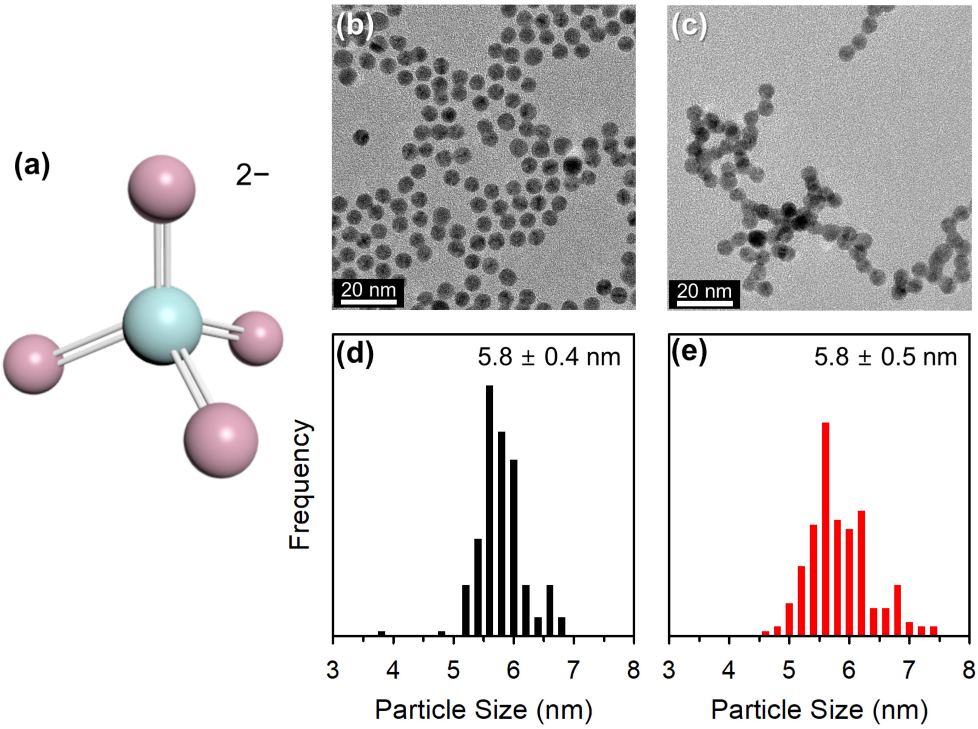

Figure 8.1. (a) Tetrahedral molecular structure of MoS_4^{2-} (cyan: Mo; pink: S). TEM images for (b) Au and (c) Au–MoS_4^{2-}. Particle size distributions for (d) Au and (e) Au–MoS_4^{2-}.

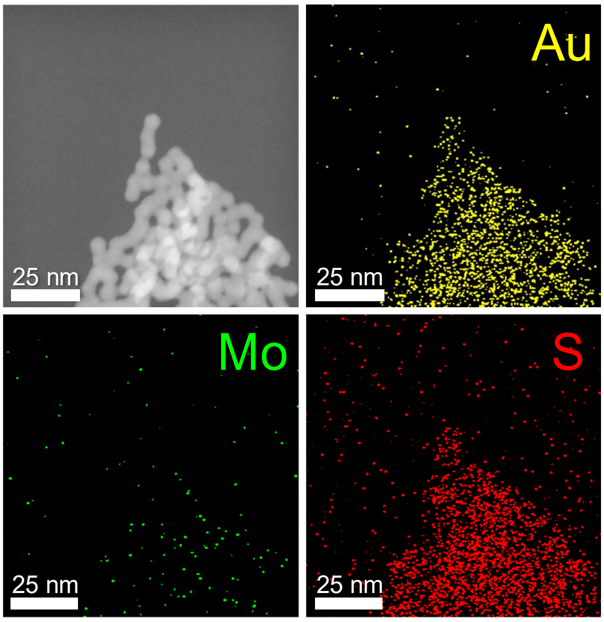

Figure 8.2. EDS elemental mapping images for Au–MoS_4^{2-}.

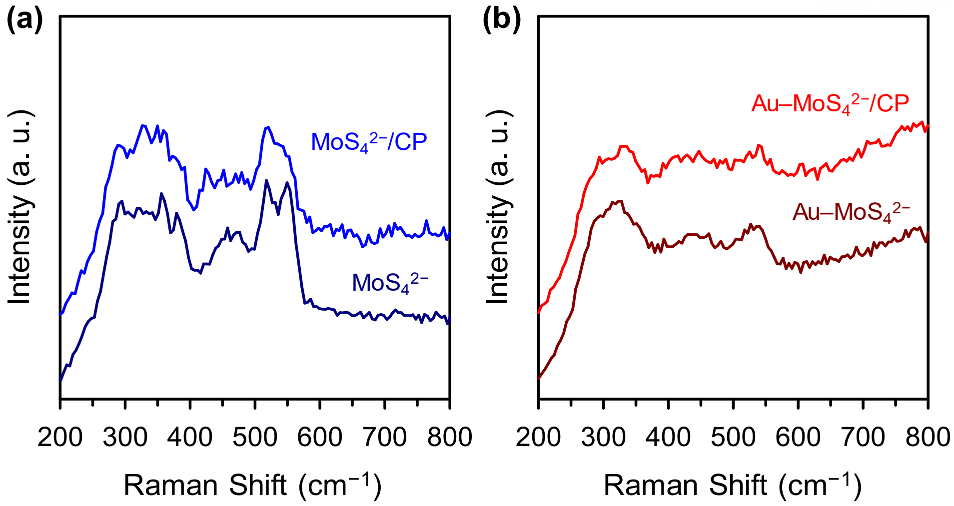

Figure 8.3. Raman spectra for (a) MoS_4^{2-} and (b) Au–MoS_4^{2-} before and after drop-casting on CP.

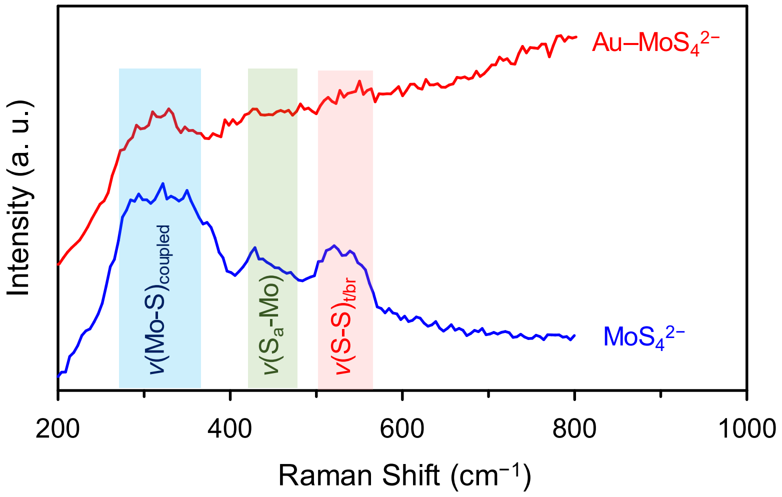

Figure 8.4. Comparison of Raman spectra for MoS_4^{2-} and Au–MoS_4^{2-} on CP.

The effect of Au NCs on the electronic properties of MoS_4^{2-} was investigated by Raman spectra (**Figure 8.4**). The MoS_4^{2-} shows Raman peaks centered around 328 cm^{-1}, 447 cm^{-1}, and 540 cm^{-1}, which correspond to the vibrations for $(Mo–S)_{coupled}$, S_{apical}–Mo, and $(S–S)_{terminal/bridging}$ species, respectively.[24] The dominance of the peak for $(Mo–S)_{coupled}$ compared to the other two peaks indicate that sulfur species exist mainly in the form of S^{2-} ligands rather than apical S^{2-} and terminal/bridging S_2^{2-} states. After the immobilization of MoS_4^{2-} on the Au NCs, the peak for $(Mo–S)_{coupled}$, was still dominant whereas the peaks for S_{apical}–Mo, and $(S–S)_{terminal/bridging}$ species almost vanished.

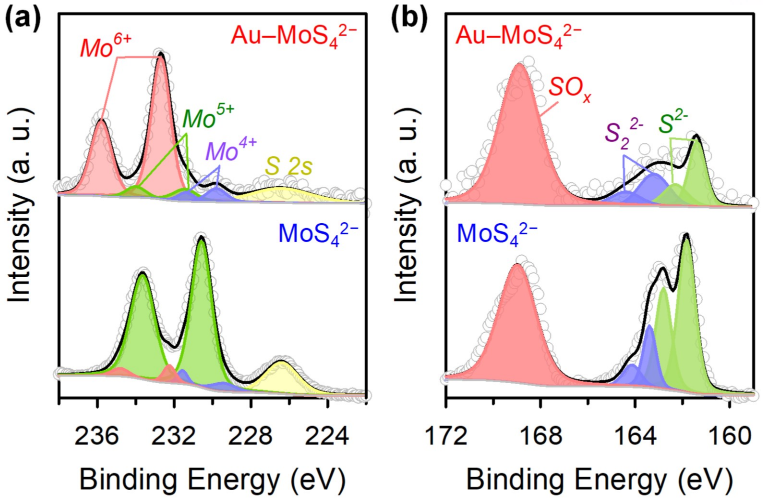

Figure 8.5. (a) Mo 3d and (b) S 2p XPS spectra for MoS_4^{2-} and Au–MoS_4^{2-}.

Table 8.2. XPS peak areas determined from the deconvoluted S 2p XPS spectra.

Species	**Peak position**		**Peak area** [a]	
	MoS_4^{2-}	**Au–MoS_4^{2-}**	**MoS_4^{2-}**	**Au–MoS_4^{2-}**
S^{2-} ($2p_{3/2}$)	161.8	161.4	1.00	0.41
S^{2-} ($2p_{1/2}$)	162.8	162.3	0.61	0.21
S_2^{2-} ($2p_{3/2}$)	163.4	163.2	0.31	0.32
S_2^{2-} ($2p_{1/2}$)	164.1	164.4	0.15	0.16
SO_x	169.0	168.9	1.69	2.12

[a] Relative peak area ratio for S^{2-}/S_2^{2-} are 3.5 and 1.3 for MoS_4^{2-} and Au–MoS_4^{2-}, respectively.

The surface chemical structures for MoS_4^{2-} and Au–MoS_4^{2-} were investigated with X-ray photoelectron spectroscopy (XPS). Deconvoluted Mo 3d XPS spectra (**Figure 8.5a**) show three doublets corresponding to (i) Mo(IV) species around 229.3–229.8 eV ($3d_{5/2}$) and 231.4–231.6 eV ($3d_{3/2}$), (ii) Mo(V) at 230.6–231.4 eV ($3d_{5/2}$) and 233.6–234.1 eV ($3d_{3/2}$), and (iii) Mo(VI) at 232.2–232.6 eV ($3d_{5/2}$) and 234.8–235.7 eV ($3d_{3/2}$).[14] The Mo 3d peaks for Au–MoS_4^{2-} were systematically shifted to higher binding energy, compared to those of MoS_4^{2-}. In addition, most dominant Mo species was changed from Mo(V) states for MoS_4^{2-} to Mo(VI) for Au–MoS_4^{2-}. These changes in binding energies and dominant species suggest that Mo species were oxidized after immobilization of MoS_4^{2-} on the Au NCs. Similarly, in S 2p XPS spectra (**Figure 8.5b**), a peak area for sulfate groups centered around 168.9 eV increased with the adhesion of MoS_4^{2-} to Au NCs. The numerical data for XPS peak area are summarized in **Table 8.2**. Another notable change in S 2p XPS spectra is that the relative peak area of S_2^{2-} species (around 163.1–163.4 eV ($2p_{3/2}$) and 164.1–164.4 eV ($2p_{1/2}$)) to that of S^{2-} species (around 161.4–161.8 eV ($2p_{3/2}$) and 162.3–162.8 eV ($2p_{1/2}$)) increased in Au–MoS_4^{2-} compared to MoS_4^{2-} (**Table 8.2**). It could be attributed to dimerization of adjacent S^{2-} species on Au NCs. The Raman and XPS studies indicate that the overall electronic and chemical properties of MoS_x were in general preserved even after the deposition onto the Au NCs, and only the surface oxidation states of Mo and S were altered, generating an oxide passive layer. We note that the oxide layer formed on the surface could facilitate electron transfer at the interface between the intrinsically less conductive MoS_x and the electrode, and could prevent dissolution of MoS_4^{2-} during electrolysis.[31]

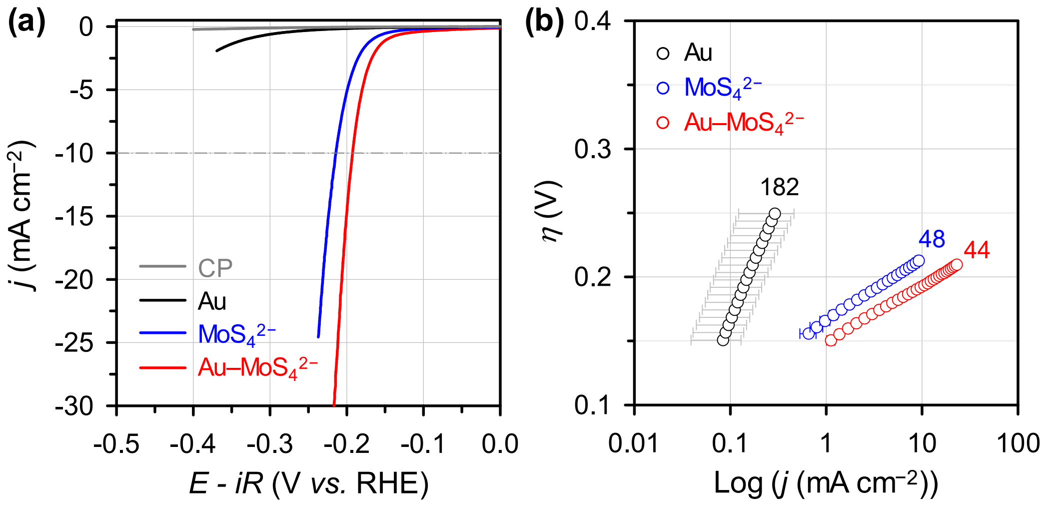

Figure 8.6. (a) LSV curves and (b) corresponding Tafel plots for Au, MoS_4^{2-} and Au–MoS_4^{2-}.

We examined the electrocatalytic activities of MoS_4^{2-} and Au–MoS_4^{2-} for the HER using a three-electrode setup in 0.5 M H_2SO_4. All linear sweep voltammetry (LSV) curves are presented after compensating Ohmic loss, which was determined by electrochemical impedance spectroscopy (EIS) analysis. The details for electrochemical measurements are described in sections 2.2 and 8.2.3. Au NCs exhibited negligible HER activity compared to MoS_4^{2-} and Au–MoS_4^{2-}. Notably, MoS_4^{2-} required overpotential of 214 mV to derive a current density of −10 mA cm^{-2} with a very low Tafel slope of 48 mV dec^{-1} (**Figure 8.6 and Table 8.3**). Given the preparation of MoS_x-based HER catalysts commonly requires structural engineering combined with high-temperature treatment under toxic H_2S gas, hydrothermal treatment to endow high activity, or electrodeposition, this result is intriguing that a simple molecular precursor itself shows unexpectedly high HER activity without any additional treatment. The HER activity of MoS_4^{2-} catalyst could be further enhanced by immobilizing them on Au NCs. As a result, Au–MoS_4^{2-} required an overpotential of 192 mV, which is shifted to positive potential by 22 mV compared to MoS_4^{2-}. We also note that the loaded amounts of Mo and S elements are 20 μg cm^{-2} for the Au–MoS_4^{2-}, which is five-fold lower amount in MoS_4^{2-} (100 μg cm^{-2}). Nyquist plots obtained from EIS measurements (**Figure 8.7**) revealed that Au–MoS_4^{2-} show the smallest semi-circle among the compared catalysts, indicating the smallest charge transfer resistance. The results are explained by the formation of conductive oxide layer with adhesion of MoS_4^{2-} on Au NCs, as revealed by XPS analysis.

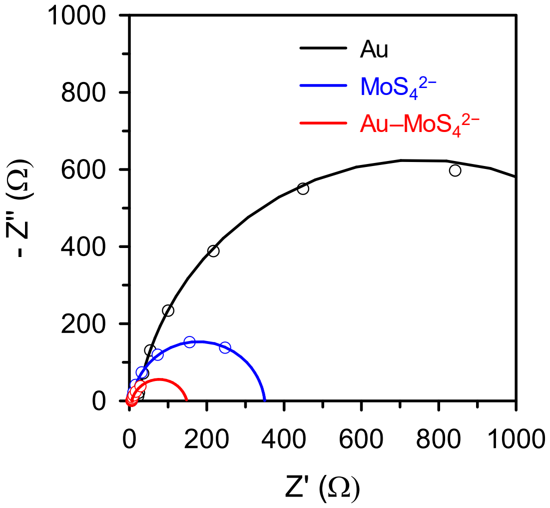

Figure 8.7. Nyquist plots for Au, MoS_4^{2-} and Au–MoS_4^{2-}. The scatters and solid lines indicate the raw data and fitted results, respectively.

Next, the intrinsic activity of catalysts was compared in terms of TOF. As the catalyst loading could influence on the HER performance,[20] we evaluated the TOFs by varying the catalyst loadings, and plotted as areas in **Figure 8.8**. The improvement of HER activity after the immobilization is more clearly evidenced by comparing TOF values of MoS_4^{2-} and Au–MoS_4^{2-}. In all potential regions, Au–MoS_4^{2-} showed higher TOF values than those for MoS_4^{2-}, regardless of loadings. When the TOFs for MoS_4^{2-} and Au–MoS_4^{2-} were compared with those for MoS_x clusters-based catalysts for the HER (**Figure 8.8a**), the TOF increases with the order of $[Mo_3S_4]^{4+}$ < MoS_4^{2-} < $[Mo_3S_{13}]^{2-}$ < $[Mo_2S_{12}]^{2-}$ < Au–MoS_4^{2-} (3 μg_{Mo+S}) at −150 mV (*vs*. RHE). From the TOF comparison, we found that the presence of Au NCs significantly enhanced the TOF of the monomeric MoS_4^{2-}. The use of Au support is advantageous in that (i) the highly electronegative Au can modify the oxidation states of catalyst surface, (ii) the strong physical adhesion between catalyst and support prevents dissolution of catalysts during electrolysis, and (iii) the intimate contact lowers the catalyst film resistance.[32–36] This kind of support effect was also observed in a previous work.[20] Trimeric $[Mo_3S_{13}]^{2-}$ loaded on a highly orientated pyrolytic graphite (HOPG) exhibited three orders of magnitude higher TOF compared to that of $[Mo_3S_{13}]^{2-}$ loaded on a graphite paper. The results suggest that the strong interaction between catalyst and substrate plays a key role in dictating HER performance of the given electrocatalyst. Additionally, we compared the TOFs of MoS_4^{2-} and Au–MoS_4^{2-} with the state of art non-molecular MoS_x-based HER catalysts (**Figure 8.8b**). From the comparison, we concluded that the monomeric MoS_4^{2-} on Au NCs is highly promising electrocatalysts for the HER.

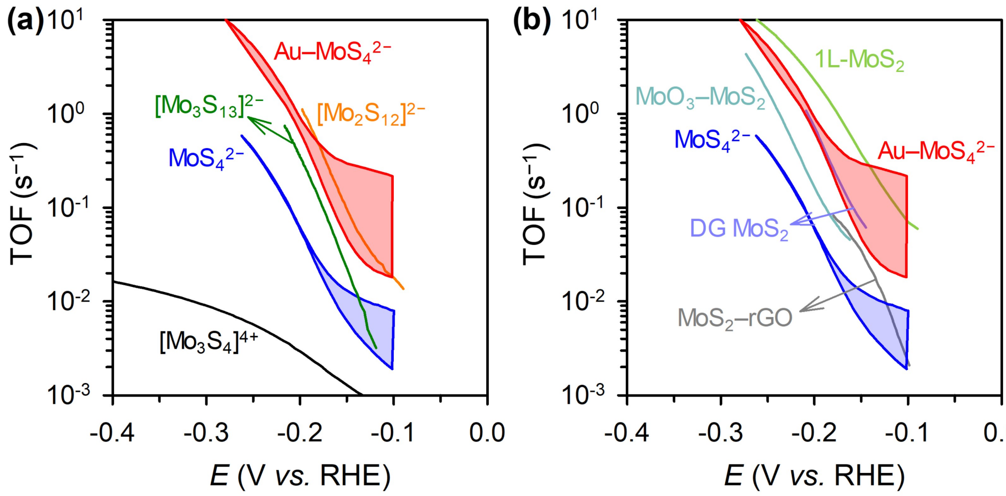

Figure 8.8. TOFs for (a) molecular and (b) non-molecular MoS_x-based HER catalysts with those for MoS_4^{2-} and Au–MoS_4^{2-}.

Table 8.3. HER activities of Au, MoS_4^{2-}, Au-MoS_4^{2-} catalysts expressed as overpotential at −10 mA cm^{-2}, Tafel slope, exchange current density, and TOF.

Sample	**Overpotential at 10 mA cm^{-2} (V)**	**Tafel slope ^{a} (mV dec^{-1})**	**Exchange current density ^{b} (A cm^{-2})**	**TOF ^{c} (s^{-1}) @−150 mV (*vs.* RHE)**
Au	> 400 mV	182	1.22×10^{-5}	-
MoS_4^{2-}	214 mV	48	3.44×10^{-7}	0.013
Au–MoS_4^{2-}	192 mV	44	3.81×10^{-7}	0.30

[a,b] The Tafel slopes and exchange current densities were derived from the linear portion of the corresponding Tafel plots.

[c] The TOFs were determined with catalyst loadings of 3 and 50 μg cm^{-2} for MoS_4^{2-} and Au–MoS_4^{2-}, respectively. The TOF was calculated per Mo atom, the details of which has been described in Section 1.5 of this Supporting Information.

This finding suggests that the coordinatively unsaturated S^{2-} sites in MoS_4^{2-} are highly correlated to the active sulfur sites for proton reduction as much as the bridging S_2^{2-} sites, which has been considered as the most plausible site for hydrogen adsorption.[21,27] In addition, the use of thiomolybdate molecule significantly simplifies the preparation of active MoS_x-based catalysts that commonly require complex thermochemical activation process. Therefore, we believe that this simple molecular catalyst can serve as a new class of MoS_x catalysts distinguished from the widely investigated crystalline and amorphous MoS_x catalysts.

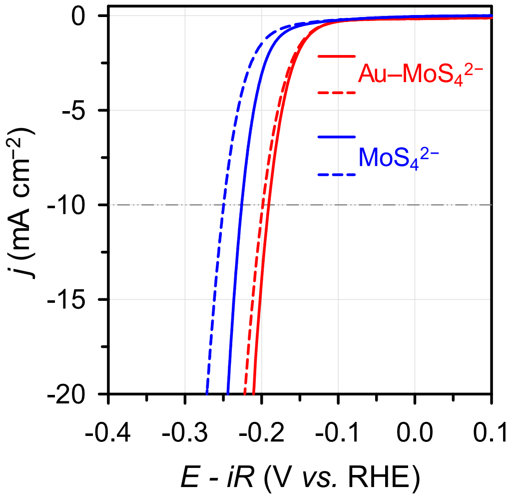

Figure 8.9. LSV curves of MoS_4^{2-} and Au–MoS_4^{2-} before and after 1000 CVs between −0.3 V and 0.1 V (*vs.* RHE) at a scan rate of 50 mV s^{-1}.

Table 8.4. Contents (μg) of Au, Mo and S dissolved from electrode during cycling test, determined by ICP-OES analysis.

Element	Blank	Au–MoS_4^{2-}	MoS_4^{2-}
Au	0.08	0.16	0.16
Mo	0.1	8.2	26.3

Another important issue for practical implementation is durability. **Figure 8.9** shows the LSV curves before and after 1000 times of cyclic voltammograms (CVs) in a potential range between −0.3 V and 0.1 V at a scan rate of 50 mV s^{-1}. After 1000 CVs, there was negligible activity decay in Au–MoS_4^{2-} catalysts. In contrast, about three-fold higher increase in overpotential (~30 mV) at −10 mA cm^{-2} was observed in MoS_4^{2-} catalysts. It indicates that monomeric MoS_4^{2-} became highly stable when the catalyst is stick to the electrode substrate well. It was further substantiated by measuring the content of Mo dissolved from the catalyst in electrolyte before and after 1000 CVs (**Table 8.4**). Around three-fold amount of Mo was dissolved from the MoS_4^{2-} catalysts compared to that from Au–MoS_4^{2-} catalysts. To investigate the structural changes during the long-term durability test, Raman analysis was conducted after the potential cycles (**Figure 8.10**). Similar Raman spectra before and after CVs indicate there was no significant change in electronic structure of MoS_4^{2-} with and without Au NCs. The stable nature of Au–MoS_4^{2-} originates from the strong physical adhesion between the catalyst and substrate.

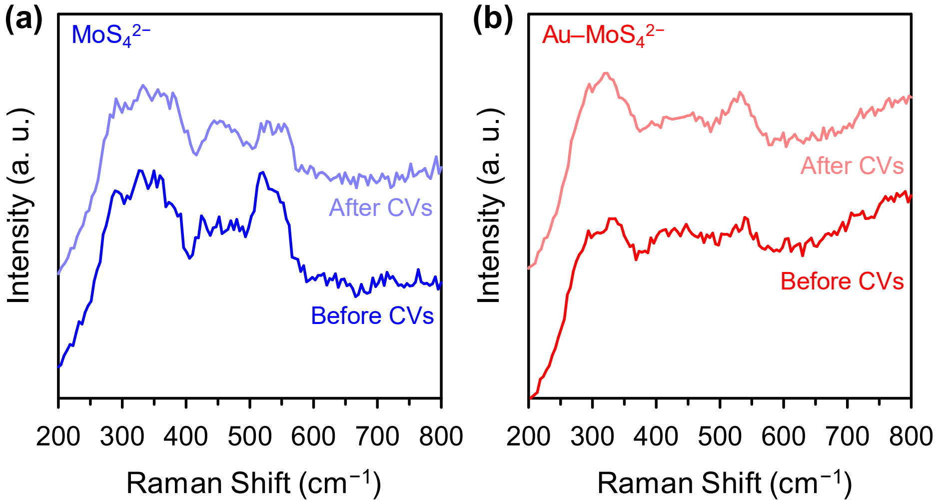

Figure 8.10. Raman spectra for (a) MoS_4^{2-} and (b) Au–MoS_4^{2-} before and after the cycling test.

8.5. CONCLUSION

In conclusion, we demonstrated that a simple inorganic molecule, monomeric thiomolybdate, which were previously used as a precursor for the preparation of MoS_x catalysts, itself can catalyze the HER with unexpectedly high efficiency. Furthermore, its activity and durability could be enhanced after the formation of hybrid with Au NCs. The Au–MoS_4^{2-} catalysts exhibited very high TOF of 0.30 s^{-1} at −150 mV (*vs*. RHE). The TOF value surpasses those for the state-of-the-art MoS_x-based HER catalysts. Long-term HER operation tests showed that the hybrid effectively prevent catalyst dissolution in strongly acidic environment. This work demonstrated possibility of the smallest molecular analogue, MoS_4^{2-} as highly active and durable HER electrocatalysts.

8.6. REFERENCES

1. Merki, D.; Hu, X. *Energy Environ. Sci.* **2011**, *4*, 3878–3888.
2. Benck, J. D.; Hellstern, T. R.; Kibsgaard, J.; Chakthranont, P.; Jaramillo, T. F. *ACS Catal.* **2014**, *4*, 3957–3971.
3. Yan, Y.; Xia, B.; Xu, Z.; Wang, X. *ACS Catal.* **2014**, *4*, 1693–1705.
4. Zheng, Y.; Jiao, Y.; Jaroniec, M.; Qiao, S. Z. *Angew. Chem. Int. Ed.* **2015**, *54*, 52–65.
5. Lv, R.; Robinson, J. A.; Schaak, R. E.; Sun, D.; Sun, Y.; Mallouk, T. E.; Terrones, M. *Acc. Chem. Res.* **2015**, *48*, 56–64.
6. Voiry, D.; Yang, J.; Chhowalla, M. *Adv. Mater.* **2016**, *28*, 6197–6206.
7. Ding, Q.; Song, B.; Xu, P.; Jin, S. *Chem* **2016**, *1*, 699–726.
8. Hinnemann, B.; Moses, P. G.; Bonde, J.; Jørgensen, K. P.; Nielsen, J. H.; Horch, S.; Chorkendorff, I.; Nørskov, J. K. *J. Am. Chem. Soc.* **2005**, *127*, 5308–5309.
9. Jaramillo, T. F.; Jørgensen, K. P.; Bonde, J.; Nielsen, J. H.; Horch, S.; Chorkendorff, I. *Science* **2007**, *317*, 100–102.
10. Seo, B.; Joo, S. H. *Nano Convergence* **2017**, *4*, 19.
11. Kibsgaard, J.; Chen, Z.; Reinecke, B. N.; Jaramillo, T. F. *Nat. Mater.* **2012**, *11*, 963–969.
12. Zhu, C.; Mu, X.; van Aken, P. A.; Yu, Y.; Maier, J. *Angew. Chem. Int. Ed.* **2014**, *53*, 2152–2156.
13. Zheng, X.; Xu, J.; Yan, K.; Wang, H.; Wang, Z.; Yang, S. *Chem. Mater.* **2014**, *26*, 2344–2353.
14. Seo, B.; Jung, G. Y.; Sa, Y. J.; Jeong, H. Y.; Cheon, J. Y.; Lee, J. H.; Kim, H. Y.; Kim, J. C.; Shin, H. S.; Kwak, S. K.; Joo, S. H. *ACS Nano* **2015**, *9*, 3728–3739.
15. Wang, H.; Lu, Z.; Xu, S.; Kong, D.; Cha, J. J.; Zheng, G.; Hsu, P.-C.; Yan, K.; Bradshaw, D.; Prinz, F. B.; Cui, Y. *Proc. Natl. Acad. Sci.* **2013**, *110*, 19701–19706.
16. Kong, D.; Wang, H.; Cha, J. J.; Pasta, M.; Koski, K. J.; Yao, J.; Cui, Y. *Nano Lett.* **2013**, *13*, 1341–1347.
17. Chatti, M.; Gengenbach, T.; King, R.; Spiccia, L.; Simonov, A. N. *Chem. Mater.* **2017**, *29*, 3092–3099.
18. Jaramillo, T. F.; Bonde, J.; Zhang, J.; Ooi, B.-L.; Andersson, K.; Ulstrup, J.; Chorkendorff, I. *J. Phys. Chem. C* **2008**, *112*, 17492–17498.
19. Karunadasa, H. I.; Montalvo, E.; Sun, Y.; Majda, M.; Long, J. R.; Chang, C. J. *Science* **2012**, *335*, 698–702.
20. Kibsgaard, J.; Jaramillo, T. F.; Besenbacher, F. *Nat. Chem.* **2014**, *6*, 248–253.
21. Huang, Z.; Luo, W.; Ma, L.; Yu, M.; Ren, X.; He, M.; Polen, S.; Click, K.; Garrett, B.; Lu, J.; Amine, K.; Hadad, C.; Chen, W.; Asthagiri, A.; Wu, Y. *Angew. Chem. Int. Ed.* **2015**, *54*, 15181–15185.
22. Tran, P. D.; Tran, T. V.; Orio, M.; Torelli, S.; Truong, Q. D.; Nayuki, K.; Sasaki, Y.; Chiam, S. Y.; Yi, R.; Honma, I.; Barber, J. Artero, V. *Nat. Mater.* **2016**, *15*, 640–646.

23. Raybaud, P.; Hafner, J.; Kresse, G.; Kasztelan, S.; Toulhoat, H. *J. Catal.* **2000**, *189*, 129–146.
24. Deng, Y.; Ting, L. R. L.; Neo, P. H. L.; Zhang, Y.-J.; Peterson, A. A.; Yeo, B. S. *ACS Catal.* **2016**, *6*, 7790–7798.
25. Vrubel, H.; Hu, X. *ACS Catal.* **2013**, *3*, 2002–2011.
26. Morales-Guio, C. G.; Hu, X. *Acc. Chem. Res.* **2014**, *47*, 2671–2681.
27. Ting, L. R. L.; Deng, Y.; Ma, L.; Zhang, Y.-J.; Peterson, A. A.; Yeo, B. S. *ACS Catal.* **2016**, *6*, 861–867.
28. Bernholc, J.; Stiefel, E. I. *Inorg. Chem.* **1985**, *24*, 1323–1330.
29. Zhu, W.; Michalsky, R.; Metin, O.; Lv, H.; Guo, S.; Wright, C. J.; Sun, X.; Peterson, A. A.; Sun, S. *J. Am. Chem. Soc.* **2013**, *135*, 16833–16836.
30. Ban, H. W.; Park, S.; Jeong, H.; Gu, D. H.; Jo, S.; Park, S. H.; Park, J.; Son, J. S. *J. Phys. Chem. Lett.* **2016**, *7*, 3627–3635.
31. Seo, B.; Jeong, H. Y.; Hong, S. Y.; Zak, A.; Joo, S. H. *Chem. Commun.* **2015**, *51*, 8334–8337.
32. Yeo, B. S.; Bell, A. T. *J. Am. Chem. Soc.* **2011**, *133*, 5587–5593.
33. Shi, Y.; Wang, J.; Wang, C.; Zhai, T.-T.; Bao, W.-J.; Xu, J.-J.; Xia, X.-H.; Chen, H.-Y. *J. Am. Chem. Soc.* **2015**, *137*, 7365–7370.
34. Joshi, U.; Lee, J.; Giordano, C.; Malkhandi, S.; Yeo, B. S. *Phys. Chem. Chem. Phys.* **2016**, *18*, 21548–21553.
35. Joshi, U.; Malkhandi, S.; Yeo, B. S. *Phys. Chem. Chem. Phys.* **2017**, *19*, 20861–20866.
36. Chakthranont, P.; Kibsgaard, J.; Gallo, A.; Park, J.; Mitani, M.; Sokaras, D.; Kroll, T.; Sinclair, R.; Mogensen, M. B.; Jaramillo, T. F. *ACS Catal.* **2017**, *7*, 5399–5409.

9

SUMMARY AND SUGGESTIONS FOR FUTURE WORKS

9.1. SUMMARY

This dissertation describes the development of non-precious electrocatalysts for the hydrogen evolution reaction (HER), focusing on the investigation of the structural factors responsible for catalytic performance. As non-precious alternatives to Pt catalysts, transition metal sulfides and phosphides were explored as HER catalysts and their structural features were controlled to establish the structure-activity relationship.[1–4] The major results are summarized as follows.

MoS_2 nanoplates with discrete layer numbers were successfully prepared *via* nanopore-confined synthesis, which enabled the investigation of layer number effects in the HER.[1] Combination of the results from electrochemical analyses and density functional theory (DFT) calculations revealed that the turnover frequencies (TOFs) of MoS_2@OMC for the HER clearly increased in a quasi-linear manner with a decrease in the layer number of MoS_2 nanoplates. The enhanced activity in reduced layer numbers was attributed to several factors, including the high ratio of edge sulfur sites, the tendency toward surface oxidation, the propensity toward 1T phase formation, and the lower activation energy required to overcome the transition state. Even though it was not considered in this work, electron hopping efficiency between layers has been suggested as being another important factor influencing the HER performance.[5] The HER activity trend was generalized with $CoMoS_2$@OMC nanostructures, increasing the HER performance through cobalt doping.

The nanopore-confined growth approach was also applied to the synthesis of WS_2 nanoplates. In contrast to MoS_2, WS_2 prefers lateral growth to form monolayer nanoplates on a carbon support. The different growth behavior was investigated by theoretical calculations. According to their adhesion energies on carbon surfaces, MoS_2 and WS_2 prefer basal plane and edge plane bondings with the carbon surface, respectively. This result well explains the growth tendency toward the lateral direction along the basal surface to form monolayers in WS_2, and the growth tendency toward the edge plane direction to form a stack of layers in MoS_2. A time-dependent control experiment further corroborated the preferential horizontal growth of WS_2 nanoplates. Notably, the sample prepared with a short sulfidation time, mainly comprising WS_x nanoclusters, showed higher HER activity compared to the sample prepared with a long sulfidation time, which mainly contained WS_2 nanoplates. The result indicates that the bridging S_2^{2-} species abundant in the nanoclusters are more relevant to catalytic active sites compared to the S^{2-} ligands predominant in nanoplates. In summary, the nanopore-confined synthesis strategy effectively controlled the transition metal dichalcogenides (TMDs) particle size at the nanoscale, providing catalysts that were suitable for revealing the structure–activity relationship. This strategy can be generalized to other layered TMDs. In addition, improvement of the synthetic procedure would yield TMD nanoplates with a narrower size distribution, which in turn can be used as a more reliable platform for investigating the nanoscale size effect.

The impact of oxides in WS_2-based nanostructures on the HER performance was investigated.[2] The core–shell structured $W_{18}O_{49}$@WS_2 nanorods (NRs) showed superior HER activity and lower charge transfer resistance compared to the WS_2 nanotubes (NTs). The oxide present in the core facilitates electron transfer at the interface between the catalyst and the electrode without the aid of additional conductive supports. Interestingly, it was also found that the samples that underwent oxidative potential cycles showed higher HER activity than those that underwent reductive potential cycles. The electrochemical oxidative pre-treatment could induce surface oxidation, further enhancing the HER activity of the WS_2. However, the enhanced HER performance of $W_{18}O_{49}$@WS_2 NRs was still lower than those of the state-of-the-art HER catalysts due to their nested structures, impeding the maximum usage of the active edge planes. Such a structural disadvantage can be counterbalanced by exploiting transition metal promotion and by exfoliating the WS_2 multilayers in $W_{18}O_{49}$@WS_2 NRs. Furthermore, the relationship between the sulfidation level and the HER activity could reveal the optimized oxidation level in the HER.

A highly active Rh_2S_3 hollow nanoparticles (HNPs) catalyst was developed, which is very robust in a strongly acidic electrolyte for the HER.[3] The Rh_2S_3 HNPs were conveniently prepared *via* one-step formation of core–shell $Cu_{1.94}S$@Rh_2S_3 nanoparticles (NPs), followed by selective removal of the oxide core. The importance of the hollow morphology was confirmed by the superior HER activity of Rh_2S_3 HNPs compared to that of non-etched $Cu_{1.94}S$@Rh_2S_3 NPs. Additionally, the shell thickness of HNP was controlled to exploit structure-dependent HER activity. Thicker-shell HNPs have larger void volume because of their better structural rigidity, retaining the hollow morphology better than thinner-shell HNPs. As a result, the HNPs with the thickest shell showed the best HER activity among the shell thickness-controlled HNPs. This result emphasizes the importance of a wide cavity for facilitating mass transport along with the enhanced catalytic active sites originating from both the inside and the outside the hollow structure. Notably, the Rh_2S_3 HNPs showed unprecedented activity enhancement after 10000 potential cycles. The electrolysis further removed the inactive Cu impurities remaining in the HNPs. The synthetic strategy in this study can be applied to prepare other catalytically useful hollow nanostructures.

The shape-dependent catalytic activities of Ni_2P NPs were investigated for the HER.[4] Sphere and rod-shaped Ni_2P NPs were successfully prepared *via* colloidal synthesis and they mainly expose crystal surfaces of $Ni_2P(001)$ and $Ni_2P(210)$, respectively. Electrochemical measurements showed that the overall HER activities of Ni_2P nanospheres (NSs) were higher than those of Ni_2P long nanorods (NRs-L) in terms of overpotential, Tafel slope, and TOF. The result implies that the $Ni_2P(001)$ surface would have preferential interactions with hydrogen atoms for the HER, and a lower activation barrier for the initial hydrogen adsorption, activating the overall HER. Furthermore, the Ni_2P NSs reported here exhibited excellent HER performance and stability. This study suggests that the crystallographic facets of Ni_2P NPs play a key role in dictating the HER performance.

A commercially available inorganic precursor, thiomolybdate (MoS_4^{2-}), which is commonly used for the preparation of MoS_x catalysts, catalyzed the HER with unexpectedly high efficiency. The high HER activity of MoS_4^{2-} could be attributed to the S^{2-} ligands, which have good resemblance to the coordinatively unsaturated S^{2-} sites in active MoS_2 edges. Furthermore, its activity and durability were enhanced by immobilizing MoS_4^{2-} on the surface of Au nanocrystals. The formation of a Au–MoS_4^{2-} hybrid significantly enhanced the TOF for the HER and effectively prevented dissolution of the MoS_4^{2-} in an acidic environment. This work demonstrated the potential of the smallest molecular analogue to MoS_2 edges as a highly active and durable HER electrocatalyst.

Overall, the dissertation suggests that the rational control of catalyst structure is important for enhancing the HER activity and stability. The discernments gleaned from this work can provide guidelines for designing advanced HER catalysts, which is valuable for both fundamental studies and a wide range of applications in the field of catalysis. Furthermore, the structural modifications introduced here can be applied to hydrotreating catalysis, which has a mechanistic analogy with the HER.[6]

9.2. SUGGESTIONS FOR FUTURE WORKS

Despite the numerous studies toward the development of non-precious metal-based HER catalysts, there remain several challenges to be solved for the design of advanced HER catalysts. Even with the most highly studied MoS_x-based HER catalysts, the active sulfur sites for hydrogen adsorption and the reaction mechanism were not clearly identified. In this regard, *in situ* techniques combined with elaborately made electrochemical cells could provide a good platform to interrogate the origin of HER activity for a given electrocatalyst.[7–9] The *in situ* characterizations are powerful tools to capture the active intermediates, which could be different from the as-made catalyst structures under the HER potentials. Specifically, an *in situ* Raman spectroscope combined with electrochemical quartz crystal microbalance (EQCM) can be used for chasing the electronic structural changes while simultaneously measuring the mass changes on the electrode (**Figure 9.1**). It allows reliable evaluation of the TOFs in entire potential regions. Abrupt change of TOF at a certain HER potential could indicate the emergence of active intermediates. The electronic structure of the catalyst appearing near the potential can be directly related to the catalytic active centers, and can be captured by the Raman spectroscope. Together with the advanced analytical techniques, DFT calculations can further narrow the gap between the fundamental studies in the laboratory and practical applications in industry.

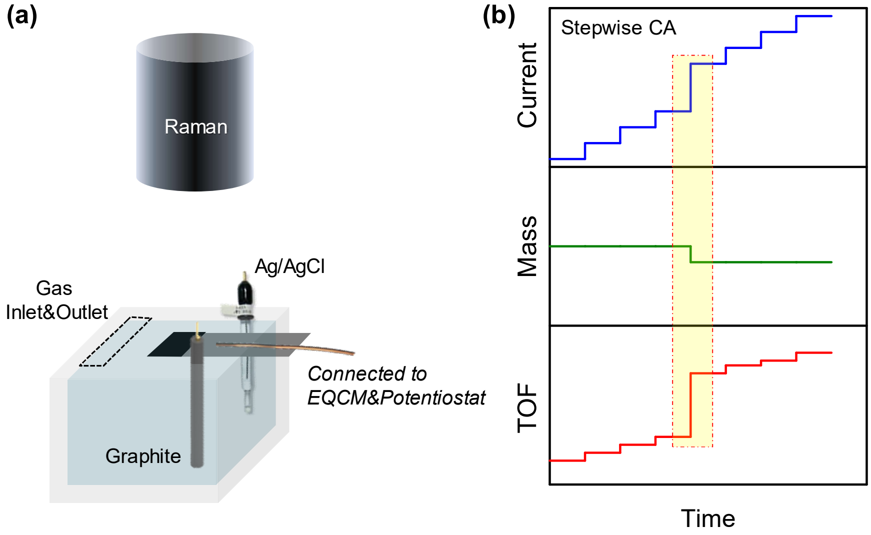

Figure 9.1. (a) Illustration for home-made spectroelectrochemical cell equipped with Raman spectroscope, EQCM and potentiostat. (b) Simple example of stepwise chronoamperometry (blue), mass change (green) and calculated TOFs (red) curves, which could be obtained from EQCM and potentiostat. *In situ* Raman spectra taken at the potentials where TOFs abruptly change, could provide important clues for the active intermediate structures.

In parallel to studying the origin of the HER activity, it is necessary to diversify the catalyst materials to balance the supply and demand of catalysts for practical viability. The actively studied non-precious HER catalysts, such as MoS_2, Mo_2C, and Ni_2P, have long been well-known catalysts for hydrotreating reactions, including hydrodesulfurization (HDS), hydrodenitrogenation (HDN), hydrodeoxygenation (HDO), and hydrodemetallization (HDM).[6] There are mechanistic analogies between the hydrotreating reactions and the HER. Both reactions require adsorption and desorption of hydrogen atoms on catalyst surface, and the binding strength of hydrogen significantly influence the overall catalytic efficiency. Similar to the HER, optimum hydrogen binding ability with Gibbs free energy close to zero could be a good candidate as the hydrotreating catalysts.[10,11] Therefore, new non-precious HER catalysts could be discovered by screening the various hydrotreating catalysts.

Another important issue for water electrolysis is the compatibility with photon energy for utilizing light as an input energy. The photo(electro)catalytic hydrogen production is indeed the most promising way for fully utilizing surplus solar energy, and producing high purity hydrogen fuels in an environmentally benign manner. There are few requirements for designing active photo(electro)catalysts for the HER, including a small enough bandgap for effective absorption of photons, and fast charge separation and transport to catalyst surface. Promising candidates are transition metal oxides,[12] TMDs,[13,14] and carbon nitride.[15] In order to increase their energy conversion efficiency, co-catalysts are commonly loaded on the photocatalysts (**Figure 9.2**).[16] Two-dimensional (2D) TMDs have been effective co-catalysts because of their tunable bandgap, suitable band positions and highly active proton reduction centers on chalcogenide atoms.[17] In this regard, photo-assisted activation of the semiconducting 2D TMDs has been the recent focus on modulation of their electronic structure, thereby activating the photo(electro)catalytic HER.[18–20]

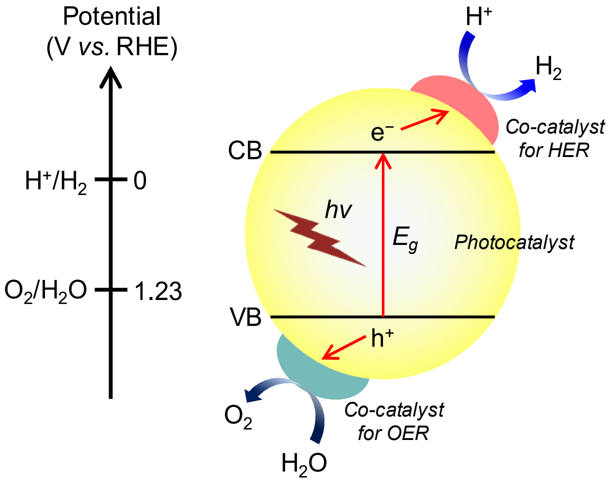

Figure 9.2. Schematic energy diagram of photocatalyst combined with co-catalysts for HER and oxygen evolution reaction (OER). CB: conduction band; VB: valence band; E_g: band gap.

Long-term durability is also important requirement for wide applicability of water electrolysis. It is particularly important issue for PEM electrolyzers as the strongly acidic environment reduces the durability of the electrode materials and increase operating cost. In this regard, development of a pH-universal catalytic system will expand the applicability of water electrolyzers in various fields. For example, it could be appealing in the ballast water treatment system, allowing direct utilization of sea water as the reactant and electrolyte without being affected by pH.[21]

9.3. REFERENCES

1. Seo, B.; Jung, G. Y.; Sa, Y. J.; Jeong, H. Y.; Chen, J. Y.; Lee, J. H.; Kim, H. Y.; Kim, J. C.; Shin, H. S.; Kwak, S. K.; Joo, S. H. *ACS Nano* **2015**, *9*, 3728–3739.
2. Seo, B.; Jeong, H. Y.; Hong, S. Y.; Zak, A.; Joo, S. H. *Chem. Commun.* **2015**, *51*, 8334–8337.
3. Yoon, D.; Seo, B.; Lee, J.; Nam, K. S.; Kim, B.; Park, S.; Baik, H.; Joo, S. H.; Lee, K. *Energy Environ. Sci.* **2016**, *9*, 850–856.
4. Seo, B.; Baek, D. S.; Sa, Y. J.; Joo, S. H. *CrystEngComm.* **2016**, *18*, 6083–6089.
5. Yu, Y.; Huang, S.-Y.; Li, Y.; Steinmann, S. N.; Yang, W.; Cao, L. *Nano Lett.* **2014**, *14*, 553–558.
6. Morales-Guio, C. G.; Stern, L. A.; Hu, X. *Chem. Soc. Rev.* **2014**, *43*, 6555–6569.
7. Sanchez Casalongue, H. G.; Benck, J. D.; Tsai, C.; Karlsson, R. K. B.; Kaya, S.; Ng, M. L.; Pettersson, L. G. M.; Abild-Pedersen, F.; Nørskov, J. K.; Ogasawara, H.; Jaramillo, T. F.; Nilsson, A. *J. Phys. Chem. C* **2014**, *118*, 29252–29259.
8. Lassalle-Kaiser, B.; Merki, D.; Vrubel, H.; Gul, S.; Yachandra, V. K.; Hu, X.; Yano, J. *J. Am. Chem. Soc.* **2015**, *137*, 314–321.
9. Deng, Y.; Ting, L. R. L.; Neo, P. H. L.; Zhang, Y.-J.; Peterson, A. A.; Yeo, B. S. *ACS Catal.* **2016**, *6*, 7790–7798.
10. Breysse, M.; Furimsky, E.; Kasztelan, S.; Lacroix, M.; Perot, G. *Catal. Rev. Sci. Eng.* **2002**, *44*, 651–735.
11. Chianelli, R. R.; Berhault, G.; Raybaud, P.; Kasztelan, S.; Hafner, J.; Toulhoat, H. *Appl. Catal. A* **2002**, *227*, 83–96.
12. Ma, Y.; Wang, X.; Jia, Y.; Chen, X.; Han, H.; Li, C. *Chem. Rev.* **2014**, *114*, 9987–10043.
13. Kudo, A.; Sekizawa, M. *Catal. Lett.* **1999**, *58*, 241–243.
14. Chen, J.; Wu, X.; Yin, L.; LI, B.; Hong, X.; Fan, Z.; Chen, B.; Xue, C.; Zhang, H. *Angew. Chem. Int. Ed.* **2015**, *54*, 1210–1214.
15. Liu, J.; Liu, Y.; Liu, N.; Han, Y.; Zhang, X.; Huang, H.; Lifshitz, Y.; Lee, S.-T.; Zhong, J.; Kang, Z. *Science* **2015**, *347*, 970–974.
16. Maeda, K.; Domen, K. *J. Phys. Chem. Lett.* **2010**, *1*, 2655–2661.
17. Lu, Q.; Yu, Y.; Ma, Q.; Chen, B.; Zhang, H. *Adv. Mater.* **2016**, *28*, 1917–1933.
18. Linic, S.; Christopher, P.; Ingram, D. B. *Nat. Mater.* **2011**, *10*, 911–921.
19. Zhou, N.; Lopez-Puente, V.; Wang, Q.; Polavarapu, L.; Pastoriza-Santos, I.; Xu, Q. H. *RSC Adv.* **2015**, *5*, 29076–29097.
20. Zhang, P.; Fujitsuka, M.; Majima, T. *Nanoscale* **2017**, *9*, 1520–1526.
21. Matousek, R. C.; Hill, D. W.; Herwig, R. P.; Cordell, J. R.; Nielsen, B. C.; Ferm, N. C.; Lawrence, D. J.; Perrins, J. C. *J. Ship Prod.* **2006**, *22*, 160–171.

BORA SEO

CURRICULUM VITAE

Personal Information

Nanomaterials and Catalysis Lab.
Department of Chemistry
Ulsan National Institute of Science and Technology (UNIST)
50 UNIST-gil, Ulsan 44919, Republic of Korea
E-mail: brseo@unist.ac.kr
Cellphone: +82-10-2607-2858

Education

2013 – 2017	**M.S.-Ph.D. Course** in Chemistry, UNIST
	Advisor: Prof. Sang Hoon Joo
2013	**B.S.** in Nano Chemical Science, UNIST, Summa Cum Laude

Awards & Honors

2014	**Excellent Poster Award** in Fall Meeting of Korean Chemical Society
2013	**Global Ph.D. Fellowship**, NRF of Korea

Research Interests

Synthesis of Nanomaterials as Electrocatalysts for Water Electrolyzer (Hydrogen Evolution Reaction, Oxygen Evolution Reaction) and Hydrogen Fuel Cell (Oxygen Reduction Reaction, Hydrogen Oxidation Reaction)

Publications

1. Sunmi Kim, Kamran Qadir, Sookyoung Jin, A. Satyanarayana Reddy, **Bora Seo**, B. S. Mun, Sang Hoon Joo, and Jeong Young Park* Trend of Catalytic Activity of CO Oxidation on Rh and Ru Nanoparticles: Role of Surface Oxide. *Catal. Today* **2012**, *185*, 131–137.
2. Jeong Wook Kim, Sang Hoon Joo, **Bora Seo**, Seong-Soo Kim, Dae-Hyun Shin, Sung Hoon Park, Jong-Ki Jeon, and Young-Kwon Park* Bio-Oil Upgrading *via* Catalytic Pyrolysis of Waste Mandarin Residue Over SBA-15 Catalysts. *J. Nanosci. Nanotechnol.* **2013**, *13*, 2566–2572.
3. Hyung Won Lee, Jong-Ki Jeon, Kwang-Eun Jeong, Soon-Yong Jeong, Jeongsik Han, **Bora Seo**, Sang Hoon Joo, and Young-Kwon Park* Effect of Pt Particle Size on the Hydroisomerization of n-Dodecane Over Pt/Al-SBA-15 Catalysts. *J. Nanosci. Nanotechnol.* **2013**, *13*, 6074–6078.
4. Sun Mi Kim, Kamran Qadir, **Bora Seo**, Hu Young Jeong, Sang Hoon Joo, Osamu Terasaki, and Jeong Young Park* Nature of Rh Oxide on Rh Nanoparticles and Its Effect on the Catalytic Activity of CO Oxidation. *Catal. Lett.* **2013**, *143*, 1153–1161.

5. Eun Hwa Lee, Mi-Jin Jeon, Jong-Ki Jeon, Dong Jin Suh, Sung Hoon Park, **Bora Seo**, Sang Hoon Joo, and Young-Kwon Park* *In Situ* Catalytic Pyrolysis of Miscanthus Over Modified SBA-15 Catalysts Using Py-GC/MS. *J. Nanosci. Nanotechnol.* **2014**, *14*, 2343–2351.

6. **Bora Seo**†, Gwan Yeong Jung†, Young Jin Sa, Hu Young Jeong, Jae Yeong Cheon, Jeong Hyeon Lee, Ho Young Kim, Jin Chul Kim, Hyeon Suk Shin, Sang Kyu Kwak,* and Sang Hoon Joo* Monolayer-Precision Synthesis of Molybdenum Sulfide Nanoparticles and Their Nanoscale Size Effects in the Hydrogen Evolution Reaction. *ACS Nano* **2015**, *9*, 3728–3739.

7. **Bora Seo**, Hu Young Jeong, Sung You Hong, Alla Zak, and Sang Hoon Joo* Impact of a Conductive Oxide Core in Tungsten Sulfide-Based Nanostructures on the Hydrogen Evolution Reaction. *Chem. Commun.* **2015**, *51*, 8334–8337.

8. **Bora Seo**, and Sang Hoon Joo* Noble-Metal Free Electrocatalysts for the Hydrogen Evolution Reaction. *Catalysis* **2015**, *31*, 25–42.

9. Jiha Choi, D. Amaranatha Reddy, M. Jahurul Islam, **Bora Seo**, Sang Hoon Joo, and Tae Kyu Kim* Green Synthesis of the Reduced Graphene Oxide–CuI Quasi-Shell–Core Nanocomposite: A Highly Efficient and Stable Solar-Light-Induced Catalyst for Organic Dye Degradation in Water. *Appl. Surf. Sci.* **2015**, *358*, 159–167.

10. Fabiano Bernardi*, Michael E. Grass, Young P. Hong, Rui Chang, Naila Jabeen, Chunjuan Zhang, Bryan W. Eichhorn, **Bora Seo**, Selim Alayoglu, Zahid Hussain, Sang Hoon Joo, and Zhi Liu* Control of the Surface Atomic Population of $Rh_{0.5}Pd_{0.5}$ Bimetallic Nanoparticles Supported on CeO_2. *Catal. Today* **2016**, *260*, 95–99.

11. Donghwan Yoon†, **Bora Seo**†, Jaeyoung Lee†, Kyoung Sik Nam, Byeongyoon Kim, Suhyun Park, Hionsuck Baik, Sang Hoon Joo*, and Kwangyeol Lee* Facet-Controlled Hollow Rh_2S_3 Hexagonal Nanoprisms as Highly Active and Structurally Robust Catalysts toward Hydrogen Evolution Reaction. *Energy Environ. Sci.* **2016**, *9*, 850–856.

12. **Bora Seo**†, Young Jin Sa†, Jinwoo Woo, Kyungjung Kwon, Jongnam Park, Tae Joo Shin, Hu Young Jeong,* and Sang Hoon Joo* Size-Dependent Activity Trends Combined with *in Situ* X-Ray Absorption Spectroscopy Reveal Insights into Cobalt Oxide/Carbon Nanotube-Catalyzed Bifunctional Oxygen Electrocatalysis. *ACS Catal.* **2016**, *6*, 4347–4355.

13. **Bora Seo**†, Du San Baek†, Young Jin Sa, and Sang Hoon Joo* Shape Effects of Nickel Phosphide Nanocrystals on Hydrogen Evolution Reaction. *CrystEngComm.* **2016**, *18*, 6083–6089.

14. Sungeun Jeoung, **Bora Seo**, Jeong Min Hwang, Sang Hoon Joo, and Hoi Ri Moon* Direct Conversion of Coordination Compounds into Ni_2P Nanoparticles Entrapped in 3D Mesoporous Graphene for Efficient Hydrogen Evolution Reaction. *Mater. Chem. Front.* **2017**, *1*, 973–978.

15. **Bora Seo**, and Sang Hoon Joo* Recent Advances in Unveiling Active Sites in Molybdenum Sulfide-Based Electrocatalysts for the Hydrogen Evolution Reaction. *Nano Convergence* **2017**, *4*, 19.

16. Donghwan Yoon†, Jaeyoung Lee†, **Bora Seo**†, Byeongyoon Kim, Hionsuck Baik, Sang Hoon Joo*, and Kwangyeol Lee* Cactus-Like Hollow $Cu_{2-x}S$@Ru Nanoplates as Excellent and Robust Electrocatalysts for the Alkaline Hydrogen Evolution Reaction. *Small* **2017**, *13*, 1700052.